JOHANNES GUTENBERG
UNIVERSITÄT MAINZ

Production of Z Bosons in Proton-Proton Collisions at $\sqrt{s} = 10$ TeV: Expectations for Early Measurements at the ATLAS Experiment

Markus Bendel
geboren in Limburg an der Lahn

Dissertation
zur Erlangung des Grades

DOKTOR DER NATURWISSENSCHAFTEN

dem Fachbereich Physik vorgelegt

Dezember 2010

Institut für Physik
Johannes-Gutenberg-Universität Mainz

CERN-THESIS-2010-358

Dekan: *)
1. Gutachter: *)
2. Gutachter: *)
Datum der mündlichen Prüfung: 17. Dezember 2010

*) Aufgrund datenschutzrechtlicher Bestimmungen in der elektronischen Fassung gelöscht.

Abstract

The production of the Z boson in proton-proton collisions at the LHC serves as a standard candle at the ATLAS experiment during early data-taking. The decay of the Z into an electron-positron pair gives a clean signature in the detector that allows for calibration and performance studies. The cross-section of ~ 1 nb allows first LHC measurements of parton density functions.

In this thesis, simulations of 10 TeV collisions at the ATLAS detector are studied. The challenges for an experimental measurement of the cross-section with an integrated luminositiy of 100 pb^{-1} are discussed. In preparation for the cross-section determination, the single-electron efficiencies are determined via a simulation based method and in a test of a data-driven ansatz. The two methods show a very good agreement and differ by $\sim 3\%$ at most.

The ingredients of an inclusive and a differential Z production cross-section measurement at ATLAS are discussed and their possible contributions to systematic uncertainties are presented. For a combined sample of signal and background the expected uncertainty on the inclusive cross-section for an integrated luminosity of 100 pb^{-1} is determined to

$$\frac{\Delta\sigma^{pp\to\gamma^*/Z+X\to e^+e^-+X}}{\sigma^{pp\to\gamma^*/Z+X\to e^+e^-+X}} = 1.5\%_{\text{stat}} \pm 4.2\%_{\text{syst}} \pm 10\%_{\text{lumi}}\,.$$

The possibilities for single-differential cross-section measurements in rapidity and transverse momentum of the Z boson, which are important quantities because of the impact on parton density functions and the capability to check for non-pertubative effects in pQCD, are outlined.

The issues of an efficiency correction based on electron efficiencies as function of the electron's transverse momentum and pseudorapidity are studied. A possible alternative is demonstrated by expanding the two-dimensional efficiencies with the additional dimension of the invariant mass of the two leptons of the Z decay.

Kurzfassung

Die Produktion von Z Bosonen in Proton-Proton-Kollisionen am LHC dient als Standardkerze beim ATLAS-Experiment in der ersten Phase der Datennahme. Der Z-Zerfall in ein Elektron-Positron-Paar weist eine eindeutige Signatur im Detektor auf, was Leistungsstudien und dessen Kalibrierung ermöglicht. Der Wirkungsquerschnitt von ~ 1 nb erlaubt erste LHC-Messungen von Parton-Dichteverteilungen.

In der vorliegenden Arbeit werden Simulationen von 10-TeV-Kollisionen studiert. Es werden die Herausforderungen einer experimentellen Messung des Wirkungsquerschnitts mit einer integrierten Luminosität von 100 pb^{-1} diskutiert. In Vorbereitung auf die Wirkungsquerschnittsmessung werden die Einzelelektron-Effizienzen auf Simulationsbasis und im Test einer datenbasierten Methode bestimmt. Beide Vorgehensweisen zeigen eine sehr gute Übereinstimmung und unterscheiden sich höchstens um $\sim 3\%$.

Die einzelnen Bestandteile einer inklusiven und differentiellen Z-Produktions-Wirkungsquerschnitts-Messung bei ATLAS werden diskutiert und deren möglichen Beiträge zu systematischen Unsicherheiten präsentiert. Für eine Selektion aus Signal- und Untergrundereignissen wird die zu erwartende Unsicherheit auf den inklusiven Wirkungsquerschnitt für eine integrierte Luminosität von 100 pb^{-1} bestimmt zu

$$\frac{\Delta\sigma^{pp\to\gamma^*/Z+X\to e^+e^-+X}}{\sigma^{pp\to\gamma^*/Z+X\to e^+e^-+X}} = 1.5\%_{\text{stat}} \pm 4.2\%_{\text{syst}} \pm 10\%_{\text{lumi}} \,.$$

Die Möglichkeiten für einfach-differentielle Wirkungsquerschnittmessungen in Rapidität und transversalem Impuls des Z-Bosons, welche wichtige Parameter in Bezug auf Parton-Dichteverteilungen und bezüglich des Studiums nicht-pertubativer Effekte im Rahmen der pQCD sind, werden dargelegt.

Die Schwierigkeiten einer Effizienzkorrektur basierend auf Elektron-Effizienzen, die Funktionen von Transversalimpuls und Pseudorapidität des Elektrons sind, werden studiert. Eine mögliche Alternative durch Hinzufügen einer weiteren Dimension – nämlich der invarianten Masse des Leptonpaars – wird aufgezeigt.

Acknowledgements

For my parents and grandparents

(The detailed acknowledgements are not included in the electronical version of this thesis due to data protection issues.)

Danksagung

Meinen Eltern und Großeltern in Dankbarkeit gewidmet

(Die ausführliche Danksagung ist aufgrund datenschutzrechtlicher Bestimmungen in der elektronischen Fassung dieser Arbeit nicht enthalten.)

Contents

Abstract i

Kurzfassung iii

Acknowledgements v

Danksagung vii

Contents ix

I Overview and Basics 1

1 Introduction 3

2 Theoretical Groundwork 7
- 2.1 Introduction . . . 7
- 2.2 The Standard Model . . . 7
  - 2.2.1 History . . . 7
  - 2.2.2 The Electroweak Interaction . . . 11
  - 2.2.3 The Higgs Mechanism . . . 13
  - 2.2.4 The Cabibbo-Kobayashi-Maskawa Matrix . . . 14
  - 2.2.5 Quantum Chromodynamics (QCD) . . . 15
- 2.3 Proton-Proton Interactions . . . 17
  - 2.3.1 Deep Inelastic Scattering . . . 19
  - 2.3.2 Parton Distribution Functions . . . 21
  - 2.3.3 The Matrix Element of the Hard Process . . . 22
  - 2.3.4 Fragmentation Functions . . . 22
  - 2.3.5 The Underlying Event . . . 23
- 2.4 Discovery and History of the Z Boson . . . 23
- 2.5 Z Production in Proton-Proton Interactions . . . 26
- 2.6 Motivation for the Measurement . . . 28

II Experiment and Simulation 29

3 The ATLAS Experiment 31

3.1 Introduction 31
3.2 The Large Hadron Collider (LHC) 32
3.3 The ATLAS Detector 34
 3.3.1 Inner Detector – Tracking System 37
 3.3.2 Calorimeter 40
 3.3.3 Muon System 44
3.4 The Trigger System 46
 3.4.1 Level-1 Trigger (L1) 47
 3.4.2 Level-2 Trigger (L2) 49
 3.4.3 Event Filter (EF) 49
3.5 The ATLAS Computing Model 50
3.6 Luminosity Determination 52

4 The Monte Carlo Simulation 55

4.1 Introduction 55
4.2 Event Generation 55
4.3 Detector Simulation – `GEANT4` 57
4.4 Samples Used in this Analysis 58

5 Electrons in the ATLAS Experiment 61

5.1 Introduction 61
5.2 Electron Signature in ATLAS 61
 5.2.1 Tracking System 62
 5.2.2 Calorimeter 62
5.3 Triggering on Electrons 63
 5.3.1 First Level Trigger 64
 5.3.2 Second Level Trigger 65
 5.3.3 Event Filter 65
 5.3.4 Trigger Menus 66
5.4 Electron Reconstruction 66
5.5 Electron Identification 69

III Analysis 73

6 Single-Electron Efficiencies 75

6.1 Introduction 75

6.2 Electron Resolution and Binning . . . 76
  6.2.1 Energy Resolution . . . 76
  6.2.2 Spatial Resolution . . . 78
  6.2.3 Electron Binning . . . 80
6.3 Different Methods to Determine Efficiencies . . . 81
6.4 The “Truth Efficiency” . . . 81
  6.4.1 Cluster Seeding . . . 82
  6.4.2 Reconstruction Efficiency . . . 82
  6.4.3 Identification Efficiency . . . 83
  6.4.4 Trigger Efficiency . . . 83
6.5 The “Tag and Probe” Method . . . 84
  6.5.1 Basic Ideas . . . 84
  6.5.2 “Truth Matched” Tag-and-Probe Efficiencies . . . 87
6.6 Event Selection . . . 87
  6.6.1 Truth Efficiencies . . . 87
  6.6.2 Tag-and-Probe Method . . . 90
6.7 Efficiency Determination . . . 93
  6.7.1 The Fitting Procedure . . . 94
  6.7.2 Inclusive Electron Efficiencies . . . 97
  6.7.3 Single Differential Electron Efficiencies . . . 98
  6.7.4 Double Differential Electron Efficiencies . . . 101
6.8 Systematic Uncertainties . . . 104
  6.8.1 Truth Single-Electron Efficiency . . . 105
  6.8.2 Monte Carlo Generator . . . 105
  6.8.3 Variation of the Matching Criterion . . . 107
  6.8.4 Final State Radiation . . . 108
  6.8.5 Tag-and-Probe Cut Variation . . . 109
6.9 Summary . . . 110

7 Cross-Section Determination 111
7.1 Introduction . . . 111
7.2 Event Selection . . . 112
7.3 Binning for Differential Cross-Sections . . . 113
7.4 Z Acceptance . . . 115
7.5 Correction for Inefficiencies . . . 117
7.6 Special Aspects for Simulated Samples . . . 118
  7.6.1 Scaling of QCD Background . . . 118
  7.6.2 Relative Normalisation . . . 120
  7.6.3 Filter Efficiency . . . 121

7.7 Signal Extraction 122
7.8 Corrected Event Numbers 125
  7.8.1 Inclusive Event Numbers 125
  7.8.2 Differential Distributions 127
7.9 Systematic Uncertainties 128
  7.9.1 Impact of the Energy Scale 130
  7.9.2 Bin Migration 132
  7.9.3 Parton Density Functions 135
  7.9.4 Background Estimation 139
  7.9.5 Luminosity Uncertainty 139
  7.9.6 Treatment of Systematic Uncertainties 139
7.10 Expected Accuracy of the Cross-Section(s) 141
  7.10.1 Total Cross-Section 141
  7.10.2 Single Differential Cross-Sections 142
  7.10.3 Double Differential Cross-Section 143
7.11 Summary 144

8 Calculation of the Efficiency Correction 147
8.1 Introduction 147
8.2 Standard Approach 147
8.3 4 Dimensional Efficiencies 149
8.4 Correction Factors Including the Invariant Mass 153
8.5 Comparison and Summary 156

9 Summary and Outlook 163

List of Figures 167

List of Tables 175

Bibliography 177

Part I

Overview and Basics

≪Wer von Anfang an genau weiß, wohin sein Weg ihn führt, wird es nie weit bringen.≫

Napoleon Bonaparte (^{*1769}, $^\dagger 1821$)

1

Introduction

The defining purpose of science is the quest for the answer of a simple question: Why is everything the way it is, the way, how we experience our world? Scientists in their attempt to close in to the answer were always dependent on the given circumstances and tools. Nevertheless, they always managed to expand the knowledge to new levels, sometimes beyond human imagination: Isaac Newton (1642-1742) equalised the force that lets things fall down to earth with the motions of planets around the sun, James Clerk Maxwell (1831-1879) unified the electric and magnetic forces to a common theory named "electromagnetism", Albert Einstein (1879-1955) revolutionised our understanding of time and space with his theory of relativity and Werner Heisenberg (1901-1976) introduced the principle of probability into physics, abandoning the thought that everything is predictable once the initial state of a system is known.

But these are just a few milestones in the long history of science contributing to the answer of the central question. It converges in the effort to find the 'Master Formula", a single "Theory of Everything", covering all forces acting in nature. Four of them are known: the electromagnetism, the weak force (responsible for the radioactive decay), the strong force (glues the nucleons together) and gravity. A further unification, binding the first two together to the "electroweak force", has already been achieved. With the exception of gravity, a theoretical framework called the "Standard Model of Particle Physics" describes all elementary particles and forces of nature. Matter (and hence anti-matter) consists of *fermions* (quarks q and leptons ℓ), the force-carriers are *bosons* (gluon g, photon γ, $W^\pm$ and Z). The last particle predicted by the Standard Model that is not discovered so far is the *Higgs* boson, as the manifestation of the Higgs field. Particles acquire their masses by interacting with this field.

In particle physics and astrophysics, completely different objects are studied, which are separated by many orders of magnitude. In the twentieth century, however, the two disciplines started to complement each other whilst studying the very early universe. With better optical instruments available, astronomers discovered that the universe is expanding, thus it must have an origin: the idea of the "Big Bang" was born. With today's instruments and natural phenomena like gravitational lenses, astrophysicists and astronomers are able to look into the very early stage of the universe, as close as some hundred thousand years after its birth 14 billion years ago. Those studies brought a great understanding of the structure of our world. Unsatisfying, though, is what astrophysicists and astronomers actually *can see* as matter in the universe only makes up as little as 4% of it. Due to the lack of gravitational force, galaxies would not exist as we see them, if they would only consist of visible matter.

A quite elegant explanation for the missing (“dark”) matter in our universe would be a new stable, yet undiscovered, elementary particle. As there is no candidate within the Standard Model remaining, a completely new theory-model that has been developed since the 1970’s, called “Supersymmetry” (SUSY), was tuned to account for a particle with the needed properties.

But particle physics might not only be able to answer the question in which kind of universe we live in now, but also answer the question what was at the very beginning, at the Big Bang itself. As already mentioned, the universe might have expanded from a single point with almost infinite energy and density (the era of “quantumgravity”, where all forces of nature were expected to be unified), expanding and cooling down for billions of years. By approaching energies as they were close to the Big Bang, the conditions back then can be simulated in the laboratory, reproducing the way in the opposite direction that nature has gone from the one single force at the beginning, separating to the forces we know today.

One goal of particle accelerators is to create new, so far unseen particles like SUSY particles or the Higgs boson. The latter is the “Holy Grail” of particle physics these days, since it is the one missing piece in the Standard Model. The *Large Hadron Collider* (LHC) at CERN in Geneva as the most sophisticated machine ever being built is designed to accomplish this goal. Once fully operational, it will collide mainly[1] protons at an unprecedented centre-of-mass energy of 14 TeV at four interaction points along its ring of 27 km circumference. Located at one interaction point is the ATLAS experiment as a multi-purpose detector. It is designed to detect the described new particles.

While approaching a new energy regime with the LHC, the instruments and tools to detect and study the produced particles need to be calibrated and checked for consistency with “well known” physics first. Therefore, the original idea for this analysis was to measure the cross-section of the production of the Z boson and its subsequent decay into an electron-positron pair with the first data from the ATLAS experiment. Unfortunately, delays in the construction of the very complex LHC machine and an accident soon after its start-up left no choice but to stick to simulations. This prevents contributions to the calibration of the detector itself, but opens the possibility to study the tools that will also be used in the data-based studies to come.

---

[1] a smaller fraction of operation time is dedicated to heavy-ion collisions

This analysis outlines the challenges and the necessary steps to measure the production cross-section of the Z with $100\,\text{pb}^{-1}$ of data. The statistical and systematic uncertainties on the measurement are estimated for the inclusive and the differential cross-sections. The event selection itself reflects the criteria that will also be applied in the early period of ATLAS running. The aim is to develop a robust fitting algorithm that accounts for signal as well as for background contributions. However, not every Z boson that is produced within ATLAS can be reconstructed due to the fiducial detector acceptance and inevitable inefficiencies. These factors have to be known precisely in order to correct for them. The acceptance correction can only be determined in simulations. Efficiencies for each lepton from the Z decay, on the other hand, can also be extracted by a data-driven ansatz. The challenge is to derive an overall efficiency correction factor per event that can be calculated from the variety of single-electron efficiencies via the data-driven method.

Following this Introduction, in the next Chapter presented is the theoretical groundwork by giving an overview of the Standard Model and the basics of proton-proton interactions at machines like the LHC. The latter is introduced in Chapter 3, together with an overview of the ATLAS detector with a detailed discussion of the detector components relevant for this analysis. In addition, the reconstruction software is briefly outlined. The event generation within Monte Carlo simulations is discussed in Chapter 4, along with the detector simulation and the simulated samples used within this analysis. The more general part of the thesis is concluded by Chapter 5, in which the detector response in terms of trigger, reconstruction and identification for an electron that traverses ATLAS is described.

The actual analysis starts in Chapter 6, where the inclusive and differential single-electron efficiencies for the $\gamma^*/Z \rightarrow e^+e^-$ decay are determined via two different approaches. The techniques are introduced and possible sources of systematic uncertainties are discussed. In Chapter 7, the various steps to measure the inclusive and differential cross-sections are presented and the results for this simulation-based approach are shown, including the discussion of systematic uncertainties. A discussion of the problems arising from the use of the standard factorisation ansatz using two-dimensional efficiencies in order to calculate an efficiency correction for the cross-section determination concludes the analysis. Finally, a summary and an outlook is given in Chapter 9.

≪Wer sich der Praxis hingibt ohne Wissenschaft ist wie der Steuermann, der ein Schiff ohne Ruder und Kompass besteigt und nie weiß, wohin er führt.≫

Leonardo da Vinci (*1452, †1519)

2

Theoretical Groundwork

2.1 Introduction

Since the discovery of the first elementary particle, the electron, at the end of the 19th century, theory and experimental knowledge of the processes at the atoms-scale and below have come a long way. Today, more than hundred particles are known, which are composed of very few elementary constituents. The latter are described in *the* fundamental framework of particle physics, the "Standard Model" (SM). This overwhelmingly successful model earned its glory not only from describing already known phenomena at the time it was formulated, but also from leading to predictions of yet undiscovered particles, which then were discovered at later experiments.

In the following section, the details of the Standard Model will be outlined, framed by a brief history as well as known issues and its future. The details include a description of the theoretical fundamentals on which this analysis is based on. The chapter is then concluded by describing the Z-boson production at hadron colliders and the motivation for this analyis.

2.2 The Standard Model of Particle Physics

2.2.1 History

With the discovery of the electron in 1897 by J. J. Thomson (Nobel Prize 1906) it became clear that the atom[1] also has a sub-structure. In 1911, E. Rutherford improved the picture of the atom in his experiments with a beam of positively charged α-particles onto a gold foil as target, where he concluded from the angular distribution of the scattered particles that the positive charge of the gold atom is located in its centre, while electrons surround this nucleus.

---

[1] after the Greek word α-$\tau\varepsilon\mu\nu\omega$, "indivisible"

This lead, as many discoveries in physics did, to another difficulty: how could the nucleus, and hence atoms as a whole, be stable as the repelling electromagnetic force between positively charged nucleons should prevent stability? The discovery of a second nucleon, the *neutron*, at the beginning of the 1930's did not solve this mystery, since—as their name already suggests—neutrons do not carry any net[2] charge.

The contradiction was solved by H. Yukawa (Nobel Prize 1949), who postulated a new kind of particle, called *meson*, as the carrier of a force causing nuclei to "glue" together. With the size of the nucleus as a measure for the range of the force, he estimated the meson's mass[3] to be ≈ 100 MeV. A few years later, the *pion* was found as the particle carrying the attractive force between the nucleons. It was a great confirmation of the predictions from the mathematical framework[4], where a new particle was postulated in theory and has been discovered in the experiment afterwards.

Another example of a successful prediction of a particle is the *neutrino*, whose discovery led to a whole new discipline of particle physics. In 1930, the fundamental physical law of energy conservation seemed to be violated in the decay of an atomic nucleus[5], $X^0 \rightarrow p + e^-$. Since this two-body decay implies a discrete energy spectrum of the electron with respect to the proton, its continuous distribution came as a surprise. W. Pauli (Nobel Prize 1945) suggested a neutral, light-weight spin-$\frac{1}{2}$ particle, called *neutron* at first, which in the end was named *neutrino*. It was experimentally discovered in 1953 via the induced β-decay of the proton (see Reference [41]).

The sub-structure of proton and neutron was postulated by Gell-Mann (Nobel Prize 1969) in 1964, when he considered the constituents of nucleons and mesons as *quarks*, with the underlying symmetry group to be $SU(3)$ (see Reference [54]). He also correctly predicted the charges of the quarks, thus leading to the observed three-quark multiplets as well as to the meson-octet.

Not only the particle themselves have been investigated, but also their interactions were objects of interest. However, gravity as the most commonly known interaction does not play a role on particle level, since the particles have very small masses. Very well understood at this point of history was *electromagnetism*, which unifies phenomena of electricity, magnetism and optics and was formulated by J. C. Maxwell in 1864. Its counterpart in relativistic quantum field theory, Quantum Electrodynamics (QED), describes generally the way, how light (i.e. photons) interacts with matter (like electrons).

The two remaining forces of nature were yet relatively unknown in the early 1960's. These are the weak force, which is responsible for the radioactive decay and the strong

---

[2] their later discovered constituents (quarks), on the other hand, do carry charge

[3] in this analysis the simplification $\hbar \equiv c \equiv 1$ as it is commonly used in particle physics is applied; hence, all masses are given in units of energy

[4] manifested in the "Yukawa potential"

[5] as shown above, the neutron was not yet discovered, thus only the neutral initial state was known

		Generation		
		1	2	3
Fermions	Leptons (ℓ, ν)	e	μ	τ
		ν_e	ν_μ	ν_τ
	Quarks (q)	u	c	t
		d	s	b
Bosons	electromagnetic	Photon (γ)		
	weak	$W^{\pm}, Z$		
	strong	Gluon (g)		

Table 2.1: Listing of all Standard Model particles. For each particle exists an anti-particle.

force, which glues the (positively charged) constituents of the nuclei together. Since further progress in understanding these interactions came along with the formulation of the Standard Model, details will be outlined in the next section.

The "Standard Model of Particle Physics" describes our today's knowledge of the elementary particles and their interactions. It is based on the three fundamental publications by S. L. Glashow [55], S. Weinberg [75] and A. Salam [70], who became awarded the Nobel Prize in 1979.

Overview

Within the Standard Model, the fundamental particles are categorised in two groups: *fermions*, which form matter[6], and *bosons*, which transmit forces. Fermions are subdivided into *leptons* and *quarks*. The criterion for this distinction is whether they participate in the strong interaction (quarks) or not (leptons). So far, no experiment has shown any hint that quarks and leptons are anything but point-like particles without a sub-structure and hence represent the fundamental constituents of everything. However, it seems curious that the fermions can be organised in three "generations", with increasing masses from first to second and second to third generation, but repeating characteristics of the particles across. This might imply an underlying symmetry and be thus an indication that fermions are not the most fundamental particles.

Table 2.1 shows the six leptons and quarks categorised in generations. Fermions of the second and third generation decay into lighter ones, thus only particles from the first generation are stable and build the conventional matter in the universe.

Since the quarks respond to the strong interaction, they cannot be observed free, but are always "confined" (see Section 2.2.5) in two- or three-quark states, called *hadrons*.

---

[6] in particle physics, anti-matter is usually included when matter is mentioned in general

The two-quark states $q\bar{q}$ are called *mesons*, whilst the three-quark states qqq (or $\bar{q}\bar{q}\bar{q}$, respectively) are called *baryons*, with protons and neutrons as their best known representatives.

Interactions of fermions are mediated by the coupling of their *fermion fields* to the *gauge bosons*, which are also shown in Table 2.1. Whilst gravity is not considered within the Standard Model, three interactions matter in particle physics and thus three different types of gauge bosons. The photon (γ) is the force carrier of the electromagnetic interaction, thus all fermions (except for the uncharged neutrinos) respond to it. The $W^{\pm}$ and Z bosons on the other hand mediate the weak force and couple to leptons as well as to quarks and affect therefore all fermions. By coupling to the *colour charge* of the quarks, the strong force is carried by the *gluons* (g). Glashow, Weinberg and Salam unified the weak and the electromagnetic force and formulated the electroweak theory, which laid the foundation to formulate the Standard Model.

Known Issues

Even if the Standard Model has been very successful over the past decades, it also has some inaccuracies that are addressed in current experiments and by theories describing physics beyond the Standard Model. In this context, two aspects will briefly be discussed.

Shortly after the discovery of neutrinos, experiments targeted to understand the sun's physics by detecting the solar neutrino flux on earth. In their experiment, R. Davis (Nobel Price 2002) and J. N. Bahcall discovered that the measured flux of electron neutrinos disagrees with the predictions from the Standard Solar Model. This discrepancy was resolved by allowing the neutrinos to have a small mass, which results in the ability to perform oscillations between their flavour eigenstates, and hence give an explanation for the deficit of electron neutrinos due to the oscillation on their way to earth. According to the Standard Model, neutrinos are massless and thus cannot oscillate.

From the observations of the universe it is a known fact that only 4% of it is made of "visible matter". The existence of galaxies indicates, however, that another form of matter, called "dark matter", is necessary to ensure their stability. A possible candidate for dark matter is the "lightest supersymmetric particle" (LSP), which is part of a new framework of particle physics, called *Supersymmetry* (SUSY). Within this theory, each fermion in the Standard Model has a corresponding boson in the SUSY framework and vice versa. All other properties are the same for SM and SUSY particles. Since none of the SUSY particles has been observed so far, it is considered to be a broken symmetry with masses of the SUSY particles approaching the TeV scale. The search for these particles is one of the main purposes of the ATLAS experiment at the LHC.

2.2.2 The Electroweak Interaction

In order to formulate the electroweak theory in an elegant way, a new quantum number is introduced, the *weak isospin*, $\boldsymbol{T}$. Each generation of left-handed fermions builds a doublet with $T = \frac{1}{2}$ and $T_3 = \pm\frac{1}{2}$, which reflects the coupling to the charged current. The charged current does not interact with right-handed fermions, thus they build an isospin singlet, $T = T_3 = 0$.

The terms "left handed" and "right handed", which denote the *chirality* of a massive particle, are essential to understand the weak force: For massless (highly relativistic) particles, chirality and *helicity* are (almost) equal. Helicity h is defined as the projection of the spin vector $\boldsymbol{s}$ of a particle onto its momentum vector $\boldsymbol{p}$:

$$h = \frac{\boldsymbol{s} \cdot \boldsymbol{p}}{s \cdot p} \,. \tag{2.1}$$

If the spin of a particle points in the direction of its trajectory, the helicity is right-handed, and left-handed if they point in opposite directions. For massive particles, the chirality is defined by eigenvectors of $(1 \pm \gamma^5)$, with $\gamma^5 = i\gamma^0\gamma^1\gamma^2\gamma^3$ and γ^i ($i = 0 \ldots 3$) as the Dirac matrices. In case of the leptons of the first generation, the projection of the left-handed doublet onto its left-handed component is (cf. Reference [75]):

$$L \equiv \frac{1}{2}(1 - \gamma^5) \begin{pmatrix} e \\ \nu_e \end{pmatrix} \,. \tag{2.2}$$

For the right-handed singlet one has

$$R \equiv \frac{1}{2}(1 + \gamma^5)\, e \,. \tag{2.3}$$

The theory is invariant under rotations in the space of the weak isospin, i.e., invariant under $SU(2)_L$ transformations. L denotes the acting on left-handed fermions only. Another invariance of the electroweak interaction arises for $U(1)_Y$ phase-transitions of the *weak hypercharge* Y. Like the Gell-Mann-Nishijima formula in the theory of the strong force, the hypercharge in the electroweak theory links the electrical charge Q to the third component of the weak isospin T_3:

$$Y = T_3 + \frac{1}{2}Q \,. \tag{2.4}$$

By requiring not only global but also local gauge invariance for the combined group $SU(2)_L \times U(1)_Y$, four additional vector fields have to be introduced, namely W_i^μ with $i = 1, 2, 3$ and B^μ. In order to guarantee gauge invariance, the fields have to transform correctly:

$$\begin{aligned} \boldsymbol{W}_\mu &\rightarrow \boldsymbol{W}_\mu + \partial_\mu \boldsymbol{\theta}(x) + g\boldsymbol{\theta}(x) \times \boldsymbol{W}_\mu \\ B_\mu &\rightarrow B_\mu + \partial_\mu \lambda(x) \;, \end{aligned} \tag{2.5}$$

where $\boldsymbol{\theta}(x)$ are arbitrary functions of space-time. The Lagrangian of the electroweak interactions then reads as follows:

$$\mathcal{L}_{\text{ew}} = -\frac{1}{4}\boldsymbol{W}_{\mu\nu}\boldsymbol{W}^{\mu\nu} - \frac{1}{4}B_{\mu\nu}B^{\mu\nu} + i\bar{\psi}'\gamma_\mu\partial^\mu\psi' - g\bar{\psi}'\gamma_\mu\partial^\mu\boldsymbol{T}\cdot\boldsymbol{W}^\mu\psi' - g'\frac{Y}{2}\bar{\psi}'\gamma_\mu\partial^\mu B^\mu\psi' \tag{2.6}$$

Here, the vector fields are composed of gauge-invariant field-tensors, which are given by $\boldsymbol{W}_{\mu\nu} = \partial_\mu\boldsymbol{W}_\nu - \partial_\nu\boldsymbol{W}_\mu - g\boldsymbol{W}_\mu \times \boldsymbol{W}_\nu$ and $B_{\mu\nu} = \partial_\mu B_\nu - \partial_\nu B_\mu$, respectively. These fields are not to be confused with the particles or fields mediating the actual interaction (see below). In Equation 2.6, ψ represents the Dirac spinor[7] of all fermion fields, hence left-handed and right-handed quarks and leptons. The $SU(2)_L \times U(1)_Y$ structure is represented by their operators $\boldsymbol{T}$ and Y, and the associated coupling constants g and g'.

The actual weak interactions are mediated by superpositions of the $\boldsymbol{W}_\mu$ and B_μ fields. The "charged current" $W^{\pm\mu}$ is composed of linear combinations of W_1^μ and W_2^μ, whereas the "neutral current" Z^μ and the "photon field" A^μ of the electromagnetic interaction consists of superpositions of W_3^μ and B^μ:

$$W^{\pm\mu} = \frac{1}{\sqrt{2}}(W_1^\mu \pm iW_2^\mu) \tag{2.7}$$

$$\begin{pmatrix} Z^\mu \\ A^\mu \end{pmatrix} = \begin{pmatrix} \cos\theta_W & -\sin\theta_W \\ \sin\theta_W & \cos\theta_W \end{pmatrix} \begin{pmatrix} W_3^\mu \\ B^\mu \end{pmatrix} \tag{2.8}$$

In Equation 2.8, the "weak mixing angle" or "Weinberg angle" θ_W has been introduced. It can be expressed as

$$\sin\theta_W = \frac{g'}{\sqrt{g^2 + g'^2}} = \frac{e}{g} \ . \tag{2.9}$$

Its value cannot be determined within the Standard Model. The coupling strengths of the physical particles $W^\pm$, Z and γ can be derived by combining Equations 2.7, 2.8 and Equation 2.6. With the $W^\pm$ only coupling to left-handed fermion-fields, the coupling is given by

$$\frac{G_F}{\sqrt{2}} = \frac{g^2}{8M_W^2} \ . \tag{2.10}$$

Here, G_F denotes the Fermi constant. The coupling of the photon to fermions does not distinguish between left-handed and right-handed fields. It is given by

$$e = g\sin\theta_W = g'\cos\theta_W \ . \tag{2.11}$$

Although the Z boson, like the photon, couples to both fields, it discriminates axial and vector couplings, known as the "$V - A$ theory". Its coupling strength, ξ_Z can be expressed in terms of the third component of the weak isospin and charge of the fermion as

$$\xi_Z = T_3 - Q\sin^2\theta_W \ . \tag{2.12}$$

---

[7] the " $'$ " denotes that the constituents of the spinors are not necessarily mass eigenstates, but rather gauge eigenstates

When going back to the Lagrangian defined in Equation 2.6 it becomes obvious that a mechanism is missing that allows particles to acquire mass. This mechanism is the subject of the following section.

2.2.3 The Higgs Mechanism

In order to allow for mass-generating terms within the electroweak Lagrangian (Equation 2.6), quadratical terms like $M_W^2 W_{\mu\nu} W^{\mu\nu}$, which violate the invariance under gauge transformations, would have to be added. P. Higgs et al. restored the invariance of the Lagrangian by introducing a scalar doublet ϕ (see References [60], [58] and [47])

$$\phi = \begin{pmatrix} \phi^0 \\ \phi^- \end{pmatrix} , \tag{2.13}$$

whose non-vanishing vacuum expectation-value will spontaneously break the given $SU(2)_L \times U(1)_Y$ symmetry. With this scalar field ϕ and its coupling to the vector fields $\boldsymbol{W^\mu}$, Equation 2.6 can be extended by the contribution from the Higgs field:

$$\mathcal{L}_{\text{Higgs}} = D^\mu \phi^\dagger D_\mu \phi - \underbrace{\left[\mu^2 \phi^\dagger \phi + \lambda(\phi^\dagger \phi)^2\right]}_{V(\phi)} , \tag{2.14}$$

with the covariant derivative $D^\mu = \partial^\mu - ig\boldsymbol{T} \cdot \boldsymbol{W}^\mu - ig' \frac{Y}{2} B^\mu$. Since the minimum at $\phi^\dagger \phi = -\frac{\mu^2}{2\lambda}$ of the potential $V(\phi)$ in Equation 2.14 is non-zero for $\mu^2 > 0$ and $\lambda < 0$, the ground state is degenerated. With the vacuum expectation value, $v \equiv |\langle \phi \rangle| = \left(-\frac{\mu^2}{2\lambda}\right)^{\frac{1}{2}}$, the mass of the charged spin-1 boson can now be generated,

$$M_W = \frac{1}{2} v g , \tag{2.15}$$

whereas the masses of the neutral vector-fields read as

$$M_Z = \frac{M_W}{\cos\theta_W} = \frac{1}{2} v \sqrt{g^2 + g'^2} , \tag{2.16}$$

$$M_A = 0 . \tag{2.17}$$

Obviously, A^μ can be identified as the photon field with zero mass.

With the same considerations the masses of the fermions can be generated, too. The interaction of the fermion field with the gauge field and therefore the Higgs field, can be expressed as follows:

$$\mathcal{L}_{\text{Fermions}} = \bar{\psi}' \gamma_\mu D^\mu \psi' + G_\psi \bar{\psi}' \phi \psi' . \tag{2.18}$$

In this Langrangian, the parameter G_ψ denotes the Yukawa couplings of the fermions to the Higgs field. Via the non-vanishing vacuum expectation value of the Higgs field after the spontaneous symmetry breaking, $\phi \rightarrow \phi + v$, the second term allows fermions to acquire their masses:

$$\begin{aligned}\mathcal{L}_{\text{mass}} = & -(\bar{u}', \bar{c}', \bar{t}')_R \boldsymbol{M}_u \begin{pmatrix} u' \\ c' \\ t' \end{pmatrix}_L - (\bar{d}', \bar{s}', \bar{b}')_R \boldsymbol{M}_d \begin{pmatrix} d' \\ s' \\ b' \end{pmatrix}_L \\ & -(\bar{e}', \bar{\mu}', \bar{\tau}')_R \boldsymbol{M}_\ell \begin{pmatrix} e' \\ \mu' \\ \tau' \end{pmatrix}_L + \text{h.c.}\end{aligned} \tag{2.19}$$

The mass matrices M_u and M_d for the quarks and M_ℓ for the leptons are composed of G_ψ and v. Since neutrinos do not have a right-handed component, no mass term is being generated in Equation 2.19. Thus neutrinos stay massless within the Standard Model and $\boldsymbol{M}_\ell$ becomes diagonal, i.e., the mass-eigenstates $\ell_{L,R}$ equal the gauge eigenstates $\ell'_{L,R}$ of the weak interaction.

With the Higgs mechanism for the gauge bosons of the weak interaction and the Yukawa coupling to the Higgs field, the mass generation within the Standard Model is explained. But the theory not only manifests itself by the predictions of particle masses and interaction strengths, but the excitation of the Higgs field itself give rise to a new, yet undiscovered, particle of the Standard Model: the Higgs boson. Its detection is one of the main goals of the LHC and would complete the Standard Model of Particle Physics.

2.2.4 The Cabibbo-Kobayashi-Maskawa Matrix

In order to ensure the universality of the weak interaction, N. Cabibbo introduced a new mixing angle[8] θ_C that allows the transition between quark generations (see Reference [35]), since processes like $\Lambda \rightarrow p\, e^- \bar{\nu}$ have already been observed experimentally at that time. Thus, he postulated a mixing matrix in a way that flavour-changing charged currents (FCCC) like, for instance, $s \xrightarrow{W^-} u$ are possible:

$$\begin{pmatrix} d' \\ s' \end{pmatrix} = \begin{pmatrix} \cos\theta_C & \sin\theta_C \\ -\sin\theta_C & \cos\theta_C \end{pmatrix} \begin{pmatrix} d \\ s \end{pmatrix} . \tag{2.20}$$

In this equation, d and s are the mass eigenstates (and hence the eigenstates of QCD) and d' and s' are the eigenstates of the weak interaction. Since each s quark is a superposition of d' and s' eigenstates of the weak interaction, the coupling to the $W^\pm$ allows for transitions between generations.

However, in the model of Cabibbo another phenomenon was not addressed that was experimentally found shortly after Cabibbo's proposal: $\mathcal{CP}$ violation[9]. In order to allow $\mathcal{CP}$ violation in their models, M. Kobayashi and T. Maskawa suggested an additional interaction term in the hadronic parts of the electroweak Lagrangian and thus extended the fermion multiplets to include three quark-generations (see Reference [62]). The mixing between the weak eigenstates doublet-partners of the up-type quarks and the mass eigenstates of down-type quarks can then be realised as follows (see Reference [67]):

---

[8] today referred to as *Cabibbo angle*

$$\begin{pmatrix} d' \\ s' \\ b' \end{pmatrix} = \begin{pmatrix} c_{12}c_{13} & s_{12}c_{13} & s_{13}e^{-i\delta} \\ -s_{12}c_{23} - c_{12}s_{23}s_{13}e^{-i\delta} & c_{12}c_{23} - s_{12}s_{23}s_{13}e^{-i\delta} & s_{23}c_{13} \\ s_{12}s_{23} - c_{12}c_{23}s_{13}e^{-i\delta} & -c_{12}s_{23} - s_{12}c_{23}s_{12}e^{-i\delta} & c_{23}c_{13} \end{pmatrix} \begin{pmatrix} d \\ s \\ b \end{pmatrix}, \tag{2.21}$$

where $s_{ij} = \sin\theta_{ij}, c_{ij} = \cos\theta_{ij}$ and θ_{ij} as the three Euler angles. The phase δ as the fourth free parameter in Equation 2.21 is responsible for $\mathcal{CP}$ violation and the reason for introducing a third generation of quarks. The prediction was confirmed by the discovery of the bottom quark (1977) and the top quark (1995) and led to the Nobel Prize for Kobayashi and Maskawa in 2008.

2.2.5 Quantum Chromodynamics (QCD)

When the basic structure of nature was explored in the 1960's, M. Gell-Mann proposed the "eightfold way" as the fundamental symmetry for the constituents of hadrons (see Reference [54]). He gave rise to the term "quark" and claimed that they are the constituents of baryons and mesons. The idea, which became advanced by G. Zweig (see Reference [77]), led to the concept of baryon and meson multiplets in which the triplets (doublets) of the three (two) lightest quarks u, d, s and anti-quarks $\bar{u}, \bar{d}, \bar{s}$ can be arranged as new particles or resonances.

But as a consequence, this very elegant formalism resulted in a new problem: the baryon decuplet[10] allows the combinations $|uuu\rangle$ and $|sss\rangle$ and therefore totally symmetric wave functions, which is forbidden by the *Pauli principle*. In order to save the theory and to yield an anti-symmetric wave function a new quantum number, called "colour", was introduced.

The structure of QCD is represented by the $SU(3)$ symmetry group with the colour as the representative of the three dimensions[11] and eight generators ("gluons") of the group. They are represented as 3×3 matrices $\boldsymbol{T}$ in colour space and fulfil the commutator relationship

---

[9] the laws of physics should stay the same if space coordinates are swapped (parity $\mathcal{P}$) and a particle becomes exchanged by its anti-particle (charge $\mathcal{C}$). The violation of the $\mathcal{CP}$ principle might explain the excess of matter over anti-matter and hence the existence of the universe in its current state

[10] the decuplet represents three-quark states with aligned spin (e.g. $|\uparrow\uparrow\uparrow\rangle$, $J^- = \frac{3}{2}^-$), whilst the octet includes $J^- = \frac{1}{2}^-$ states (e.g. $|\uparrow\downarrow\uparrow\rangle$)

[11] referred to as "red", "blue" and "green"

$$[T_a, T_b] = i f_{abc} T_c \ , \tag{2.22}$$

where the f_{abc} are the structure constants of $SU(3)$ and the indices a, b, c refer to the gluon index. Since leptons are colour singlets, their fields do not change under rotations in colour space. For colour-carrying quarks whose fields ψ_q are $SU(3)$ triplets, a rotation yields:

$$\psi_q \to e^{-ig_s \boldsymbol{T}\cdot\boldsymbol{\theta}(x)} \psi_q \ . \tag{2.23}$$

It is obvious that with this transformation the invariance of the free-fermion field has to be restored by introducing a gauge invariant, gluonic field-strength tensor $G^a_{\mu\nu}$ that can be written as

$$G^a_{\mu\nu} = \partial_\mu G^a_\nu - \partial_\nu G^a_\mu - g f_{abc} G^b_\mu G^c_\nu \ . \tag{2.24}$$

With this information, the QCD Lagrangian can be formulated as follows:

$$\mathcal{L}_{\text{QCD}} = i\psi^\dagger_q \gamma^\mu D_\mu \psi_q - m_q \psi^\dagger_q \psi_q - \frac{1}{4} \boldsymbol{G}_{\mu\nu} \cdot \boldsymbol{G}^{\mu\nu} \ . \tag{2.25}$$

In parallel to the considerations given in Section 2.2.3, the following abbreviation for the covariant derivative has been used:

$$D_\mu = \partial_\mu + i g_s \boldsymbol{T} \cdot \boldsymbol{G}_\mu \ . \tag{2.26}$$

One important aspect of QCD has not been discussed so far, which has an important impact on the nature of the theory. The $SU(3)$ gauge group is *non-abelian*, meaning that the product of two elements is not commutative. Thus, the self-interacting terms of the gluons do not cancel and hence lead not only to self-coupling of the gluons, but also to the effects called *confinement* and *asymptotic freedom*.

Impacts from the $SU(3)$ Structure of QCD

The gluon self-interaction is an important difference to the nature of the electromagnetic theory, which is represented by $U(1)_Y$, and manifests itself in the behaviour of the coupling constant of the strong interaction, α_s.

In QED, for instance, the strength of the interaction of a photon with a charged particle is given by the coupling constant $\alpha \approx \frac{1}{137}$. However, this is only true for low-energy, $\mathcal{O}$(1 GeV), interactions. If with increasing energy smaller structures can be resolved, an effect known as *vacuum polarisation* becomes important: each charged[12] particle is surrounded by fermion anti-fermion fluctuations of the vacuum, distorting the effective strength of the boson field of that particle. With this weakening of the interaction field, the effective coupling of a photon carrying a sufficient amount of energy to resolve these vacuum effects becomes larger.

---

[12] in this context, “charge” is not restricted in any sense and can thus even stand for colour

In QCD the same effect occurs: with increasing energy, a gluon can resolve smaller structures. But because of the self coupling of the gluons, the probe itself interacts with the vacuum fluctuations, thus the coupling constant α_s decreases with higher energies. This effect, called *asymptotic freedom*, was first described by H. D. Politzer [68] and independently by D. J. Gross and F. Wilczek [57], who became awarded the Nobel Prize in 2004. A possible parametrisation of α_s as it is used in Reference [67] is

$$\mu \frac{\partial \alpha_s}{\partial \mu} = 2\beta(\alpha_s) = -\frac{\beta_0}{2\pi}\alpha_s^2 - \frac{\beta_1}{4\pi^2}\alpha_s^3 - \mathcal{O}(\alpha_s^4) - \dots \ , \tag{2.27}$$

with $\beta_0 = 11 - \frac{2n_f}{3}$, $\beta_1 = 51 - \frac{19n_f}{3}$ and n_f as the number of quarks with masses less than the energy scale μ. Within the Standard Model this always leads to a decreasing coupling strength at higher energy. By solving the differential equation 2.27 one obtains:

$$\alpha_s(\mu) = \frac{4\pi}{\beta_0 \ln \frac{\mu^2}{\Lambda^2}} \left[1 - \frac{2\beta_1}{\beta_0^2} \frac{\ln\ln \frac{\mu^2}{\Lambda^2}}{\ln \frac{\mu^2}{\Lambda^2}} + \mathcal{O}(\ln^2(\mu^2)) - \dots \right] . \tag{2.28}$$

The dimensional parameter Λ can be chosen freely. Expressing the solution of Equation 2.27 in inverse powers of $\ln \mu^2$ gives a meaning to Λ: in case of $\mu \to \infty$ the coupling vanishes ($\alpha_s \to 0$). Thus QCD becomes strongly coupled at $\mu \sim \Lambda$ (see Reference [67]).

Equation 2.27 shows the opposite behaviour at lower energies with an increasing coupling strength. This leads to the other aspect of QCD, which is called *confinement*, and causes quarks to exist always in bound states as mesons or baryons.

In the left panel of Figure 2.1, the current α_s measurements from various experiments are shown at $\mu = M_Z$. The scale dependency of the “running coupling constant” α_s is shown in the right panel of the same figure. The confinement is expressed by the increasing coupling strength at low Q, which is mirrored by the fact that free quarks do not exist in nature. The higher the energy in the scattering process is, the smaller becomes the coupling strength so that the interaction seems to happen on a free particle. This is the reason for the previously introduced term “asymptotic freedom”.

2.3 Proton-Proton Interactions

The phenomenology of proton-proton interactions depends on the energy scale of the interaction. At low collision energies ($\lesssim 1$ GeV), the interaction can be approximated by an elastic scattering process of two charged objects. When it comes to higher energy regimes, however, the sub-structure of the proton becomes visible and the interaction gets much more complicated.

A physical process H can be described with its initial state, an interaction and a final state. In technical terms, this can be written as

$$H = \langle \psi_f | M_{if}^2 | \psi_i \rangle \ , \tag{2.29}$$

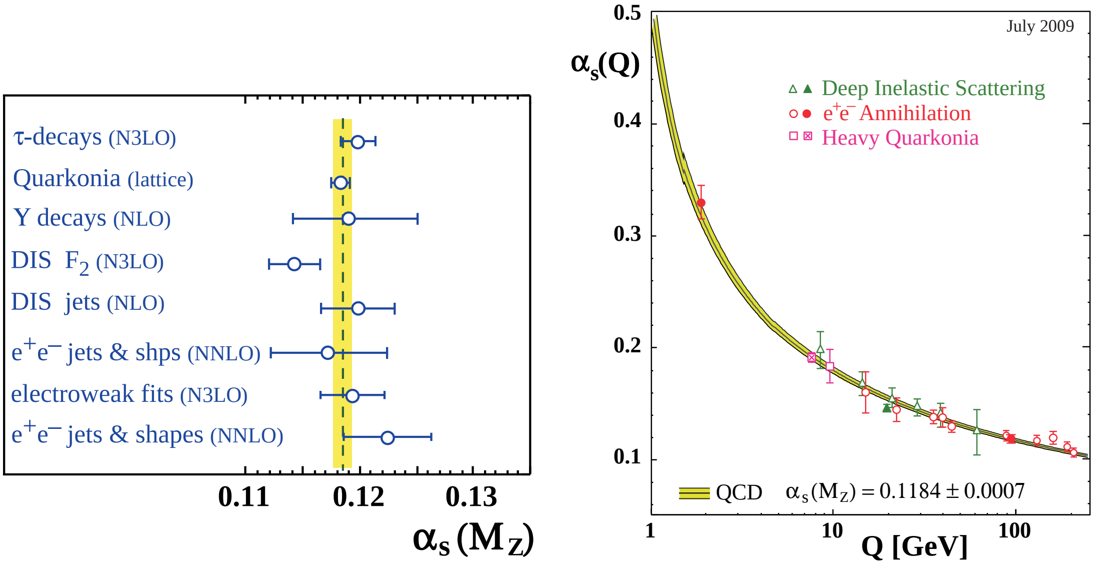

Figure 2.1: Combination of α_s measurements. Left: Measurements and world average at $\mu = M_Z$. Right: Measurements of $\alpha_s(\mu)$ at different energy regimes. Results are obtained from the τ width, Υ decays, deep inelastic scattering, JADE and TRISTAN experiments, Z width and further e^+e^- event shapes. A fit on the data and its $\pm 1\sigma$ error band is included. Figures taken from [67].

where ψ_f (ψ_i) is the final (initial) state and M_{if}^2 is the matrix element of the interaction. In order to determine the overall cross-section of a QCD process, a similar factorisation into the description of initial, intermediate and final state can be made (“factorisation theorem”):

$$\sigma_{\text{tot}} = \text{PDFs} \otimes \hat{\sigma} \otimes \text{FF} \; . \tag{2.30}$$

Here, the initial state is represented by the *parton distribution functions* (PDFs) of the incoming protons, which cannot be calculated but have to be determined from experiment, e.g., via deep inelastic scattering (see Section 2.3.1). The cross-section $\hat{\sigma}$ of the hard process describes the interaction of the particles involved, like $qg \rightarrow qg$ and $q\bar{q} \rightarrow q\bar{q}$. Also not exactly computable is the *fragmentation* of the remaining partons, which do not directly participate in the interaction. Their contribution to the total cross-section in Equation 2.30, denoted as FF, is described in *fragmentation functions*.

The three contributing terms will be discussed in the following, with the focus on the determination of the PDFs. Today’s knowledge of the PDF is almost completely based on information gained from *deep inelastic scattering* (DIS) experiments. Thus, the concept of DIS is introduced beforehand.

2.3.1 Deep Inelastic Scattering

With the items discussed so far, it is known that protons have a sub-structure and that their constituents[13]—referred to as *partons*—participate in the electroweak interaction. It is clear that electrons are an obvious choice to probe the inner structure of hadrons, as electrons are stable and it is easy to tune their energy to suitable values. In order to scatter on partons, high electron energies are necessary, since free quarks do not exist in nature and the principle of asymptotic freedom of the quarks has to be utilized in order to achieve electron-quark scattering.

Not only electrons were taken as incoming particles in the early phase of DIS experiments. In the 1970's and early 1980's, muons were also used to probe hydrogen, deuterium or neutron at fixed-target experiments like BCDMS [31], E665 [12] and NMC [20]. Their results as well as the electron approach at SLAC [76] are also shown in Figure 2.2, covering the regime at low Q^2 and high values of x.

The difficulty at hadron-colliders lies in the ignorance of the initial state when a collision takes place. This sounds surprising as the initial energy of the protons—at least in the transverse plane relative to the beam axis—is precisely defined. But because of the sub-structure of the protons, the actual interaction takes place on parton level. Therefore it is necessary to know the parton behaviour within the proton.

At the HERA[14] experiment, the proton structure has been investigated via electron-proton scattering. The energy of the proton (electron) beam was 920 GeV (27.5 GeV). Obviously, each parton only carries a fraction of the proton's momentum. This fraction is given by a scaling variable, called *Bjorken* x, which is restricted to $0 < x < 1$:

$$x = \frac{Q^2}{2M\nu} \ , \tag{2.31}$$

where $Q^2 = -\boldsymbol{q}^2$ is the four-momentum transfer, M the mass of the incoming proton and $\nu = \frac{\boldsymbol{q}\cdot\boldsymbol{P}}{M}$ the energy loss of the lepton in the rest frame of the proton with momentum P. In order to find a measure for the scattering in terms of the transferred momentum or energy, *structure functions* were defined which are directly related to the differential cross-section (see Reference [32]):

$$\frac{d^2\sigma}{dE'\,d\Omega} = \frac{\alpha^2}{4E^2\sin^4\frac{\theta}{2}}\left(\frac{F_2(x,q^2)}{\nu}\cos^2\frac{\theta}{2} + \frac{2F_1(x,q^2)}{M}\sin^2\frac{\theta}{2}\right) \ . \tag{2.32}$$

Here, E (E') is the energy of the incident (scattered) electron and θ is the electron's scattering angle. The structure functions F_1, F_2 depend on the momentum transfer q^2 and the scaling variable x. They cannot be deduced from theory due to non-pertubative effects within QCD, and must be measured at dedicated facilities like HERA, instead.

---

[13] in this context, only valence quarks are considered—a deeper discussion would also have to deal with sea-quark and gluon contributions

[14] HERA stands for "Hadron-Elektron-Ring-Anlage" at the DESY facility in Hamburg, Germany

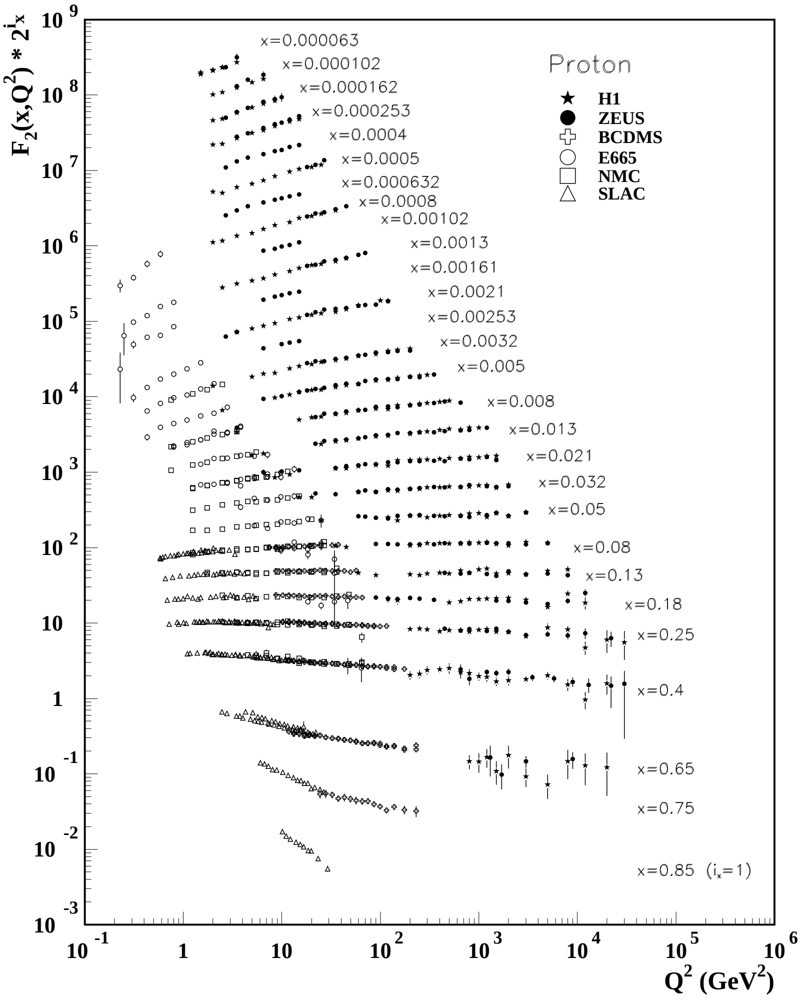

Figure 2.2: Proton structure function $F_2^p(x, Q^2)$ as a function of the momentum transfer, $Q^2 = -\boldsymbol{q}^2$, with data from fixed-target experiments (SLAC, BCDMS, E665, NMC) and collider experiments (H1, ZEUS). See text for details. Figure taken from [67].

Figure 2.2 shows an example of the proton structure function $F_2^p(x, q^2)$ for the accessible kinematic regime of HERA and other experiments. The moderate change, which is known as “scale independence”, in the experimentally determined values for F_2 over a broad range of Q^2 in a certain scale regime ($0.05 \lesssim x \lesssim 0.4$) is evidence for the scattering at point-like partons. By probing lower values of x, a scale violation becomes observable as gluon radiation causes an evolution in the structure functions.

As one cannot make use of discrete data points from the experimentally found structure functions within a simulation, several groups put a huge effort into the modelling of the structure functions. An overview of their work is subject of the next section.

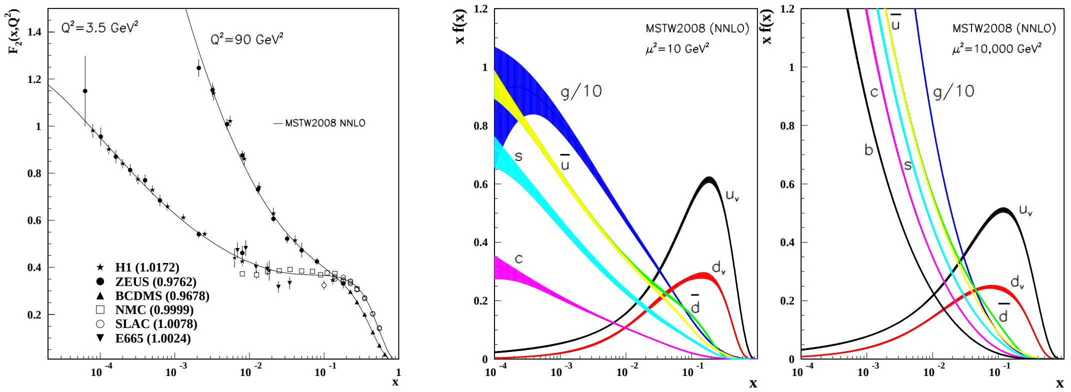

Figure 2.3: Parametrisation of the parton distributions by the MRST group. Left: Proton structure function $F_2^p(x, Q^2)$ for two given values of $Q^2 = -\boldsymbol{q}^2$ versus the scaling variable x. Right: Contributions of the gluons and different quark flavours to the structure functions for $\mu^2 = 10$ GeV^2 and $\mu^2 = 10$ TeV^2. All figures taken from [67].

2.3.2 Parton Distribution Functions

In order to simulate an interaction of hadrons accurately, the momentum-distribution of the partons within the hadron have to be reflected in the Monte-Carlo simulation. This is done by parametrising the structure functions in *parton distribution functions* (PDFs). The difficulty for groups like MRST [65] and CTEQ [66]—besides the modelling of the structure functions given by experiments—is the extrapolation of the PDFs to yet inaccessible kinematic regimes of Q^2. The extrapolation as well as the PDFs are based on the DGLAP[15] equations (see References [56], [44] and [18]).

In their current form, the MRST collaboration performs fits at leading order (LO), next-to leading order (NLO) and next-to next-to leading order (NNLO) by starting at a reference input scale ($Q^2 = 1$ GeV^2), determined from a global analysis of data. With sum rules as boundary conditions, like the number of valence quarks of a given type[16] a total of 30 free parameters remain in the fit.

Some exemplary results for the parametrisation of the structure functions via PDFs are shown in the left panel of Figure 2.3. It shows a very good agreement between the data points given by various experiments and the fits. Additionally, the contribution of different quark-flavours and gluons to the structure functions can be modelled for different energy regimes, mirroring the increasing gluon contribution at higher energies in proton-proton interactions at the LHC.

---

[15] “DGLAP” stands for the authors of the different papers, who are Dokshitzer, Gribov, Lipatov, Altarelli and Parisi

[16] e.g. for the number of up-quarks within a proton one has $\int_0^1 dx\, u_v(x, Q^2) = 2$

The PDFs included in the simulations that were used in this analysis will be introduced in Chapter 4.

2.3.3 The Matrix Element of the Hard Process

The cross-section $\hat{\sigma}$ of the hard process in proton-proton interactions is exactly calculable, in principle. However, when going to higher order diagrams the calculation quite soon becomes very complex. As of today, the cross-sections are known at NNLO level.

At leading order the cross-sections of processes relevant for the LHC can be calculated precisely. Such processes are, for instance, $qq \rightarrow qq$, $q\bar{q} \rightarrow q\bar{q}$ and, in contrast to non-existent triple-photon couplings in QED, processes with three-gluon coupling, $q\bar{q} \rightarrow gg$, and the crossed reactions $qg \rightarrow qg$ and $gg \rightarrow q\bar{q}$.

The available Monte-Carlo generators can roughly be distinguished in LO, NLO and NNLO generators. The implementation of the hard process' matrix element is already possible at NNLO with ZWPROD (see References [59] and [74]) and FEWZ[17] (see Reference [19]), which calculates the cross-sections of hadron-hadron collisions in pertubative QCD, including full spin-correlations and effects like γ^*/Z interference, in case of the leptonic decay channels. At NLO, generators like MC@NLO or MCFM[18], which also includes spin-correlations of the decay products, are available.

With this in mind it seems a bit anachronistic to rely on a LO generator like `PYTHIA` for the majority of the samples used in this analysis, especially for the signal sample. The reasons for using `PYTHIA` nevertheless are practical issues: the vast majority of centrally produced samples are generated with `PYTHIA` including the PHOTOS[19] extension; additionally, most of the detector studies relied on the use of this generator. However, by considering the QED final-state radiation via PHOTOS, `PYTHIA` already emulates some aspects of higher-order behaviour.

2.3.4 Fragmentation Functions

The fragmentation functions (FF) can be seen as final-state analogon to the PDFs and hence have to deal with the transition of partons emerging from the hard process to the final-state hadrons. The non-pertubative nature of this transition forces a splitting into pertubative and non-pertubative aspects, which is realised in the FFs. Since the deduction of FFs in pp-scattering always suffers from effects like the underlying event (see next section), fragmentation functiones can best be studied in e^+e^- annihilation, in processes like $e^+e^- \rightarrow \gamma^*/Z \rightarrow h + X$. The total fragmentation function $F^h(x, s)$, which can be deduced from the cross-section observables in the process quoted, is given by (see Reference [67]):

---

[17] "Fully Exclusive W, Z Production through NNLO in pQCD"

[18] "Monte Carlo for FeMtobarn processes"

[19] calculates the final-state photon radiation

$$F^h(x,s) = \sum_i \int_x^1 \frac{dz}{z} C_i \left(z, \alpha_s(\mu), \frac{s}{\mu^2} \right) D_i^h \left(\frac{x}{2}, \mu^2 \right) + \mathcal{O}\left(\frac{1}{\sqrt{2}} \right) , \tag{2.33}$$

with $x = \frac{2E_h}{\sqrt{2}} \leq 1$, C_i as observable-dependent coefficient functions and i as placeholder for the respective (anti) quark or for the gluon. The functions D_i^h denote the *parton fragmentation functions* (or *fragmentation densities*) and give the probability that a parton i fragments into a hadron h carrying a fraction z of the parton's momentum. The scale parameter μ^2 of the factorisation can be identified with the renormalisation scale.

The downside of using e^+e^- scattering to determine the FFs lies in the insensitivity to gluon-like fragmentation densities and the investigation of charge asymmetries, $D^h_{q_i} - D^h_{\bar{q}_i}$, where studies of ep and pp scattering deliver complementary results to the one's from e^+e^- scattering.

2.3.5 The Underlying Event

In hadron-collider physics, the description of the final state always has to deal with the remnants of the initial state protons that have not participated in the hard process. This additional particle flow is called *underlying event* (UE).

In simulations, the UE is usually implemented by including additional $2 \rightarrow 2$ scatterings ("multiple parton interactions"). An independent treatment of the UE and the actual hard-interaction process is difficult due to their correlation in terms of colour, as both share a common, neutral-colour initial state.

2.4 Discovery and History of the Z Boson

The outstanding success of the Standard Model was underlined by the discovery of particles whose properties—like masses and interactions—matched exactly their prediction by Glashow, Weinberg and Salam (see Section 2.2).

One of those particles, the *weak neutral current* or Z boson, was indirectly[20] discovered at CERN' *Gargamelle* bubble chamber in 1973. The experiment used a neutrino beam from the Proton Synchrotron (PS) to induce the scattering process

$$\overset{(-)}{\nu}_\mu + e^- \rightarrow \overset{(-)}{\nu}_\mu + e^- \tag{2.34}$$

that can only take place via the neutral current.

---

[20] for a direct search, the center-of-mass energy provided by an experiment has to reach $M(Z)$ for an on-shell production

After the commissioning of the Super Proton Synchrotron (SPS) in 1976, the energy for an on-shell production, and hence a direct observation of the Z, became technically available. However, since the cross-section to create $W^{\pm}$ and Z bosons is significantly larger if the required $q\bar{q}$ pair is provided by valence quarks rather than using contributions from sea quarks, the possibility to use the SPS as a $p\bar{p}$ collider (called "S$p\bar{p}$S") from 1981 to 1984 allowed the discovery of the two electroweak gauge-bosons. The experiments UA1 and UA2 directly measured the Z along with the W in 1983. For the discovery, C. Rubbia and S. van der Meer become awarded the Nobel Prize in 1984.

In the following years, the experiments at LEP (ALEPH, DELPHI, OPAL and L3), and at the Tevatron (D∅ and CDF) measured the properties of the Z very precisely (see Reference [67]):

$$\begin{aligned} M_Z &= (91.1876 \pm 0.0021)\ \text{GeV}\ , \\ \Gamma_Z &= (2.4952 \pm 0.0023)\ \text{GeV}\ . \end{aligned} \tag{2.35}$$

The decay width of the Z boson is theoretically determined by Equation 2.9. In terms of axial g_A^i and vector g_V^i coupling constants, the common width for a Z boson decaying into a pair of fermions i is given by

$$\Gamma(Z \to \psi_i \bar{\psi}_i) = \frac{N_C \sqrt{2} G_F M_Z^3}{12\pi} \cdot \left({g_V^i}^2 + {g_A^i}^2 \right) , \tag{2.36}$$

where N_C is 1 for leptons and 3 for quarks[21], G_F is the Fermi constant, M_Z is the mass of the Z, $g_V^i = T_3(i) - 2Q_i \sin\theta_W$ and $g_A^i = T_3(i)$, respectively. Due to the lepton universality, the Z couples equally to each lepton generation. In particular, the decay modes and branching ratios are

$$\begin{aligned} \frac{\Gamma_{Z\to\ell^+\ell^-}}{\Gamma_{\text{total}}} &= (3.3658 \pm 0.0023)\%\,, \\ \frac{\Gamma_{Z\to\text{invisible}}}{\Gamma_{\text{total}}} &= (20.00 \pm 0.06)\%\,, \\ \frac{\Gamma_{Z\to\text{hadrons}}}{\Gamma_{\text{total}}} &= (69.91 \pm 0.06)\%\,. \end{aligned}$$

Additionally, the ALEPH experiment proved the concept of the three generations of matter by measuring the width of the Z with the required precision (see Reference [36]). This experimental results excluded a possible fourth generation of neutrinos and once more confirmed the predictions of the Standard Model.

The total cross-sections of a variety of processes are given in Figure 2.4. The overall pp cross-section is ~ 7 orders of magnitude higher than the inclusive Z cross-section. The difficulty for this analysis is the enormous number of produced jet-events. As it is shown

---

[21] the factor $N_C = 3$ denotes the presence of the colour, without higher-order corrections in α_s

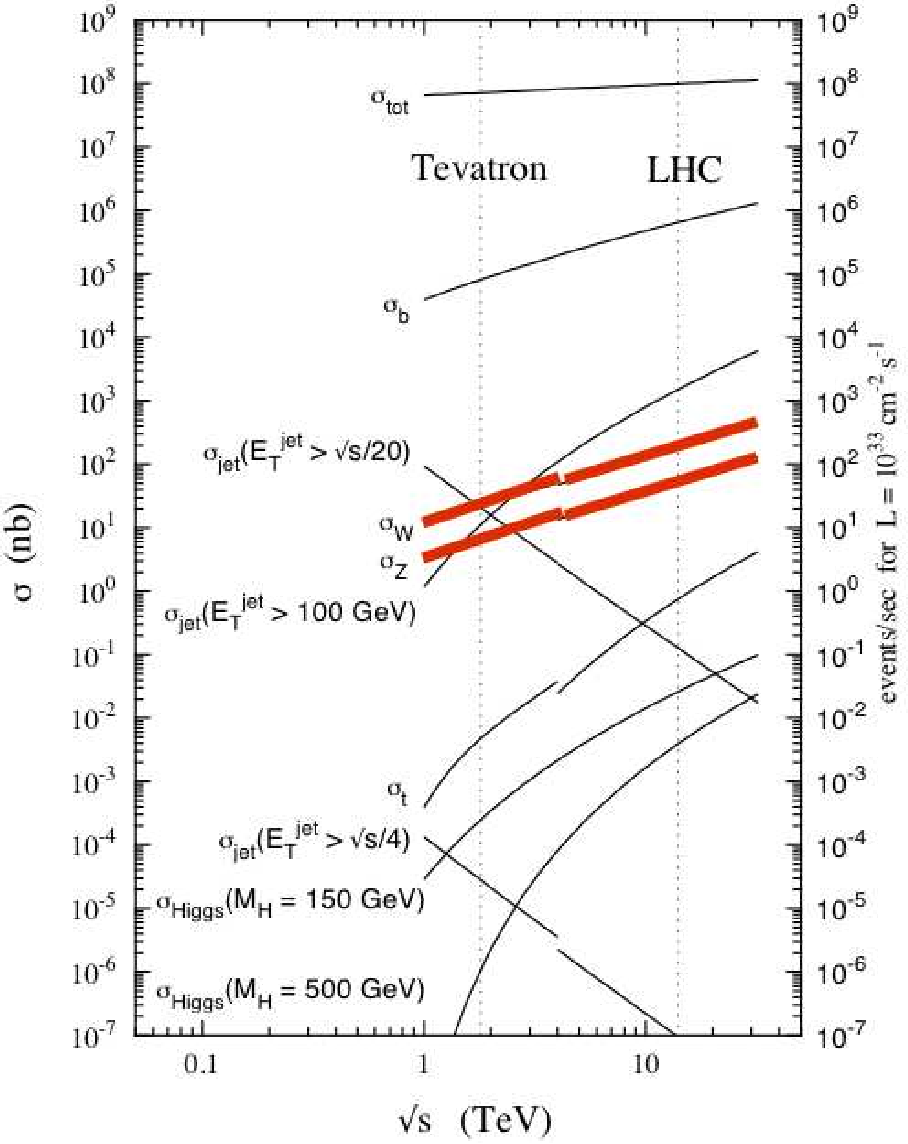

Figure 2.4: Illustration of the expected cross-sections for various processes versus centre-of-mass energy. The evolutions for the weak gauge bosons are highlighted.

in Figure 2.4, the jet cross-section with $E_T^{\text{jet}} > 100$ GeV already exceeds the inclusive Z cross-section for energies reached at the LHC. Furthermore, the jet cross-section increases exponentially for lower E_T thresholds, such that $\sigma_{\text{jets}}(E_T^{\text{jet}} > 20\ \text{GeV}) \sim \mathcal{O}(10^7\ \text{nb})$. This is a huge challenge for the ATLAS trigger system (see Chapter 3). In comparison, the LO cross-section as given by the `PYTHIA` generator as well as the LO and higher order cross-sections from FEWZ are shown in Table 2.2. It is obvious that only a sufficient jet-rejection allows the extraction of a clean Z boson signal by the offline selection.

Generator	Order in pertubation theory	$\sigma_{pp\to Z+X\to e^+e^-+X}$ / nb
PYTHIA+PHOTOS	LO	1.47
FEWZ	LO	1.66
FEWZ	NLO	2.03
FEWZ	NNLO	2.02

Table 2.2: Leading order (LO) and higher order ((N)NLO) cross-sections for Z production in pp collisions at 14 TeV and its subsequent decay into an electron-positron pair. The invariant mass of the lepton-pair is restricted to $M_{\ell\ell} > 60$ GeV.

2.5 Z Production in Proton-Proton Interactions

In 1970, S. D. Drell and T.-M. Yan discussed the possibility of producing large-mass lepton-pairs in inelastic hadron-hadron scattering (see Reference [45]). They claimed that the creation of a massive dilepton-pair within the “infinite momentum frame”[22] can only take place via annihilation of a parton and an antiparton from each incoming hadron rather than producing this final state from one of the hadrons by just exchanging low-x partons between them, in order to fulfil momentum and energy conservation requirements.

The paper by Drell and Yan had two implications: the theoretical description of the experimentally discovered rapid fall-off of the (differential) cross-section when producing $\mu^+\mu^-$ pairs in hadron-hadron collisions (see Reference [37]), and the explanation of high-mass dilepton systems via an intermediate—and at that time yet unknown—state. The available energy for the final state,

$$Q^2 = x_1 x_2 s \ , \tag{2.37}$$

is composed of the total collision energy squared, s, and the fractions of the longitudinal moment of each parton, $x_{1,2}$ ($0 < x_{1,2} < 1$). The intermediate state turned out to be an interference of a virtual photon and a virtual Z boson, as the available energy still was insufficient to produce Z bosons on the mass shell.

At the LHC, the Z production is dominated by the Drell-Yan process (see Figure 2.5), with the subsequent decay into a fermion-anti-fermion pair

$$q\bar{q} \to \gamma^*/Z \to f\bar{f} \ . \tag{2.38}$$

With the same collision energy, the LHC’s cross-section for this process would be slightly lower than the one at the Tevatron, since the latter is a $p\bar{p}$ collider with the required $\bar{q}$ as valence quark already in the initial state. However, the higher center-of-mass energy more than compensates for the required contribution of sea quarks at the LHC.

---

[22] the *infinite momentum frame*, $P \to \infty$, allows to treat the constituents of hadrons as collinear, free particles, whereas their momentum is slowed by time dilation (see Reference [49])

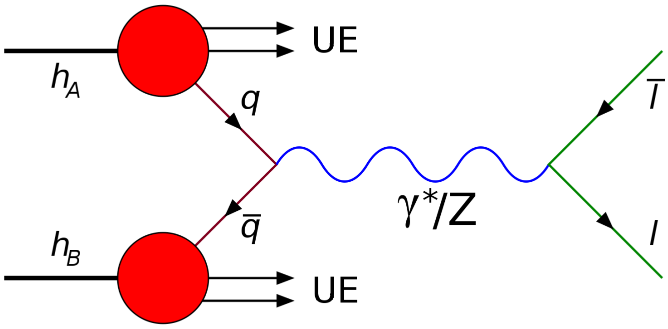

Figure 2.5: Illustration of the Drell-Yan process: hadron-hadron (h_A and h_B) interaction via quark anti-quark annihilation, intermediate γ^*/Z state and its subsequent decay into a lepton anti-lepton pair (cf. Reference [61]).

In order to produce on-shell Z bosons at the LHC, the collision energy in Equation 2.37, $\sqrt{s} = 10$ TeV ($\sqrt{s} = 14$ TeV) must provide $Q^2 \approx M_Z^2$, so that each quark carries on average $x \sim 0.91\%$ ($x \sim 0.85\%$) of the proton's momentum. The production cross-section for the process $pp \to \gamma^*/Z + X$ can be calculated in leading-order[23] expansion of α_s within the electroweak theory as follows (see Reference [42], Chapter 10):

$$\sigma(q\bar{q} \to Z; Q^2) \sim M_Z^2 G_F \left(\xi_{Z,L}^2 + \xi_{Z,R}^2\right) \delta(Q^2 - M_Z^2) \, , \tag{2.39}$$

with the Z coupling, ξ_Z, as defined in Equation 2.12. The involvement of quarks in the Z production, however, leads to a modification of Equation 2.39 in order to account for the relevant PDFs of this process. By using the factorisation theorem (see Reference [39]), the parton-level interaction from the previous equation can be separated from the terms arising from the PDF contributions:

$$\sigma(pp \to Z) = \int dx_1 dx_2 \sum_q \{f_q(x_1,\mu) f_{\bar{q}}(x_2,\mu)\} \, \sigma(q\bar{q} \to Z; Q^2) \, . \tag{2.40}$$

Here, μ denotes the factorisation scale and can be chosen arbitrarily, e.g., $\mu \approx M_Z$ in order to reflect the underlying physical process. This free parameter shows the uncertainty that arises from non-pertubative QCD contributions and can be minimised by adding higher-order corrections for α_s in the formula to calculate the cross-section. The implementation of the PDFs is part of the discussion of the Monte-Carlo simulation in Chapter 4.

---

[23] the leading-order approximation can be justified by the decreasing of α_s at high energy scales (see Section 2.2.5)

2.6 Motivation for the Measurement

The Drell-Yan production of a Z boson and its subsequent decay into a $\ell\bar{\ell}$ pair serves as a standard candle for the electron and muon channel. The cross-section of ~ 1 nb is sufficiently large in order to collect enough statistics for various purposes in the early data-taking period. The decay into a pair of isolated leptons leaves a clean signature in the detector, which allows for calibration and performance studies. Once the experimental uncertainties have been minimised, the Drell-Yan process could also be used to measure the luminosity at the LHC.

The central parameter in order to measure the Z production is the cross-section of the process. With Monte Carlo simulations (FEWZ, see Reference [19] and ZWPROD, see References [59] and [74]), the cross-section has been computed at NNLO level. In addition to an inclusive measurement, the production of Z events can also be determined with respect to the rapidity of the Z or with respect to its transverse momentum. At leading order, the relation between the rapidity of the Z and the involved partons' momentum fractions x_1 and x_2 can be expressed as follows:

$$y^Z = -\frac{1}{2}\ln\frac{x_2}{x_1}\,.$$

The measurement of $d\sigma/dy_Z$ thus is a probe for the PDFs of the proton. In addition, measuring the Z production with respect to its transverse momentum, $d\sigma/dp_T$, yields information about non-pertubative effects in pQCD.

The aim of this study is therefore to estimate the expected uncertainties on the inclusive and differential cross-sections for an integrated luminosity of 100 pb^{-1}, hence an early stage of the experiment. The methods and tools, which can also be applied to data in studies to come, are introduced and tested whether or not they allow for a reproduction of the cross-section that was used to generate the given samples.

Part II

Experiment and Simulation

≪Nur ein Narr macht keine Experimente.≫

Charles Darwin (*1809, †1892)

3

The ATLAS Experiment

3.1 Introduction

After World War II, the restart in European science lead to the foundation of an international laboratory for nuclear research. Named after the initial council, *Conseil Européen pour la Recherche Nucléaire*, CERN as the “European Organization for Nuclear Research” with 12 member states was brought to life in 1954. It is located on the outskirts of Geneva on the Franco-Swiss border.

The first particle accelerator, the Synchrocyclotron (SC), brought protons to an energy of 600 MeV and started operation in 1957. Two years later, the Proton Synchrotron (PS) provided proton beams with an energy of 28 GeV. Over the years, the PS fed many experiments with particle beams and was used as pre-accelerator for subsequent machines—and is in use even today, as one of the pre-accelerators of the LHC.

Another milestone in CERN’s history was the first proton-proton collider, ISR[1]. Rather than focussing a particle beam onto a fixed target, the collider technology allows to increase the available collision-energy by a factor of two, leading to a significant increase in the centre-of-mass energy of the reaction. Of course, new techniques had to be developed in order to control the beam within the ring and to focus it at the interaction point.

The experiences obtained with the ISR went directly into the development of the Super Proton Synchrotron (SPS), which became operational in 1976. It was built in a tunnel with a circumference of 7 km and initially[2] accelerated protons to an energy of 300 GeV. Today, the SPS still delivers its 450 GeV proton-beam to experiments and acts as pre-accelerator for the LHC.

In 1989, the Large Electron-Positron collider (LEP) was commissioned in a new tunnel with a circumference of 27 km, which also hosts today’s LHC. In a first phase, LEP operated with a design energy of 100 GeV, being increased to 200 GeV in a second phase of operation from 1996 until the year 2000, when the LEP was shut-down in order to build

---

[1] “ISR” stands for *Intersecting Storage Rings*

[2] later on, anti-protons and heavy ions were also accelerated within the SPS

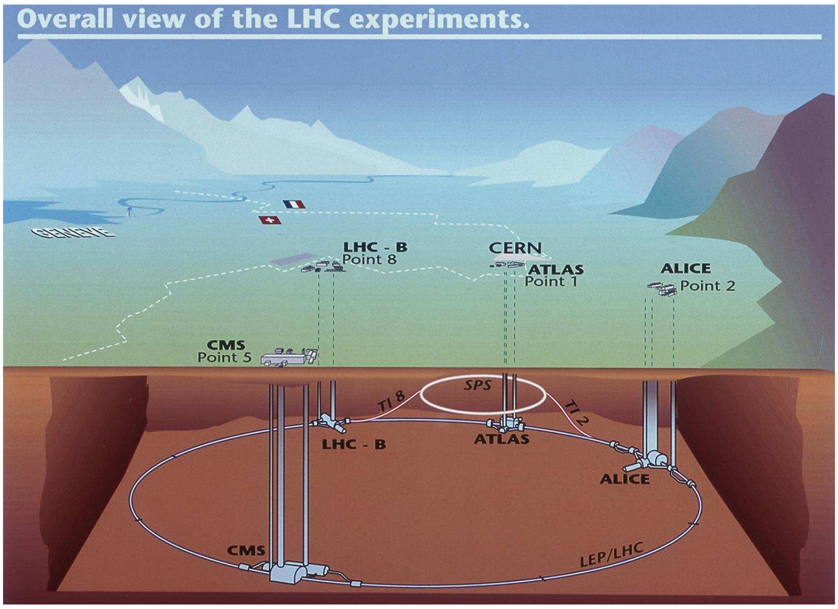

Figure 3.1: Schematic view of the Large Hadron Collider and its four major experiments. Figure taken from [24].

the LHC.

In the history of CERN, many discoveries have been made, which either confirmed given theories or gave rise to new questions about nature. One important step to verify the Standard Model was the detection of the heavy electroweak bosons $W^{\pm}$ and Z in 1983. The Higgs-Boson as the very last, yet undiscovered, piece of the Standard Model waits for its discovery at the LHC.

In the following sections, the ATLAS[3] experiment will be discussed in detail. First, an overview of the LHC is given with a brief summary of the other major experiments besides ATLAS. After a detailed discussion of each for this analysis relevant part of the detector, the trigger system, the reconstruction software and the computing model are being explained. The chapter is concluded by a brief outlook on the luminosity measurement at ATLAS.

3.2 The Large Hadron Collider (LHC)

The construction of the LHC was approved in 1994. Together with its four major experiments ATLAS, CMS, LHCb and ALICE it is located in the former LEP-tunnel (see Figure 3.1). Its main purpose[4] is to provide proton-proton collisions with an unprece-

---

[3] “**A** **T**oroidal **L**HC **A**pparatu**s**”

[4] alternatively, the LHC is also used for dedicated heavy-ion (Pb) runs, with energies up to 2.8 TeV per nucleon.

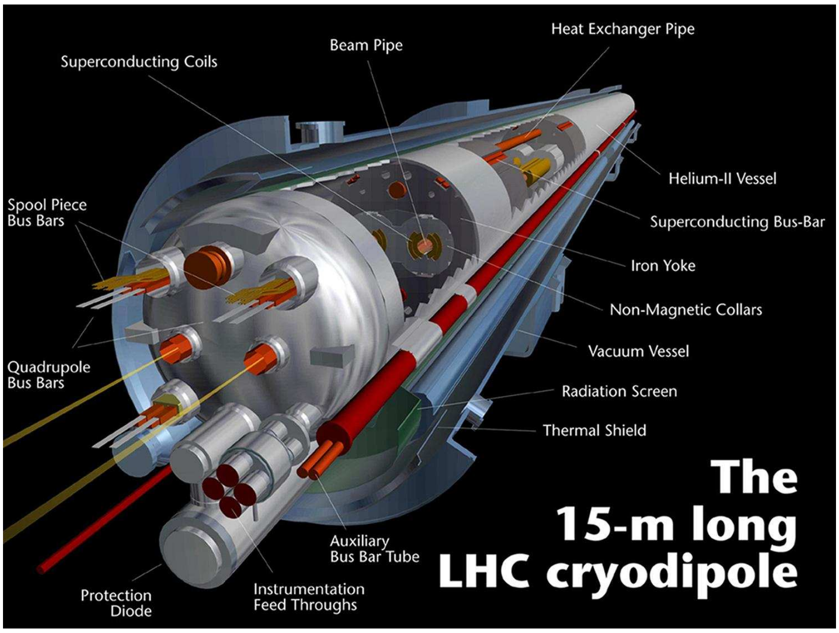
Superconducting Coils
Beam Pipe
Heat Exchanger Pipe
Helium-II Vessel
Superconducting Bus-Bar
Iron Yoke
Non-Magnetic Collars
Vacuum Vessel
Radiation Screen
Thermal Shield
Spool Piece Bus Bars
Quadrupole Bus Bars
Auxiliary Bus Bar Tube
Instrumentation Feed Throughs
Protection Diode
The 15-m long LHC cryodipole

Figure 3.2: Illustration of a LHC dipole-magnet and its components. Figure taken from [24].

dented centre-of-mass energy of 14 TeV at specified interaction points. As many, yet undiscovered, processes come with very low cross-sections, the main focus in the development of the LHC was on achieving a sufficiently high (instantaneous) luminosity ($\mathscr{L} = 10^{34}$ cm^{-2}s^{-1}) in order to produce rare events with an acceptable rate. The relation between the expected event rate and the luminosity is as follows:

$$\frac{dN}{dt} = \sigma \mathscr{L} \,, \tag{3.1}$$

with σ as the (total) cross-section and $\mathscr{L}$ as the machine—or instantaneous—luminosity. The latter can be derived only from machine parameters (see Reference [34]):

$$\mathscr{L} = \frac{N_b^2 n_b f_{\text{rev}} \gamma_r}{4\pi \varepsilon_n \beta^*} F \,, \tag{3.2}$$

where N_b is the number of protons per bunch, n_b is the number of bunches per beam, f_{rev} the revolution frequency of the LHC, $\gamma_r = (1-\beta^2)^{-\frac{1}{2}}$ the relativistic gamma-factor, ε_n the normalised transverse beam emittance. In Equation 3.2, β^* is the beta-function and F the geometric luminosity reduction factor, both at the interaction point. A symmetrical setup for both beams is assumed in Equation 3.2.

In order to reach the desired luminosity as well as the design energy of 14 TeV, superconducting magnets at a temperature of 1.9 K are used throughout the entire ring to bend the protons around their trajectory within the LHC and to focus each proton beam. Figure 3.2 shows an illustration of a bending dipole, with its almost symmetrical structure in order to host both beam pipes.

Once the LHC has become fully operational, each bunch of protons will carry $\sim 10^{11}$ particles and each fill[5] will consist of 2,808 bunches. This leads to a bunch crossing each 25 ns and an expected interaction rate of 1 GHz at ATLAS.

Apart from ATLAS, three other major experiments are detecting the collisions at the LHC: the CMS[6] detector is like ATLAS a multipurpose detector that covers the same goals in terms of physics. In some way, CMS with its better muon system at the cost of a worse tracking system and calorimeter is complementary to ATLAS. The results of both experiments, CMS and ATLAS, can therefore be used for cross-checking purposes. LHCb[7], on the other hand, is dedicated to the investigation of $\mathcal{CP}$ violation in the b sector. LHCb concentrates on scattered particles in the forward region, hence it is not build symmetrically around the interaction point. Also built for a special purpose was ALICE[8], a detector that is designed to study the quark-gluon plasma that existed shortly after the big bang via heavy-ion collisions.

The LHC started its operation with the first circulating proton-beams on 10 September 2008. Nine days later, however, an incident at one dipole-intersection caused a leak in the cooling system and a major damage to several adjacent magnets. The inevitable shutdown and repair period of 11 months forced this analysis to deal with simulated events, rather than analysing the very first data from the ATLAS detector.

Since 20 November 2009 the LHC operates again with a collision energy of currently 7 TeV. After another shutdown in 2012, the LHC will presumably reach its design energy of 14 TeV in the year 2013.

3.3 The ATLAS Detector

The ATLAS detector is located in a cavern at CERN's "Point 1" site, opposite to the main entrance. It is the largest multi-purpose particle detector built so far, with a diameter of 25 metres and a length of 44 metres. An illustration of the detector is shown in Figure 3.3.

The coordinate system of the experiment is defined as follows: the origin is the nominal interaction point of the beams, the x axis points from the origin to the centre of the LHC ring, the y axis points upwards. With the right-handed orientation of the coordinate system, the z axis, which is defined by the beam pipe, becomes its orientation. The azimuthal angle ϕ is measured around the z axis, the polar angle θ is the angle from the z axis.

In hadron colliders, however, the polar angle is most commonly expressed as the *pseu-*

---

[5] after injecting the SPS beam(s) into the LHC and accelerating them to the targeted intensity, the beams circulate for many hours to provide luminosity to the experiments

[6] "Compact Muon Solenoid"

[7] "Large Hadron Collider beauty"

[8] "A Large Ion Collider Experiment"

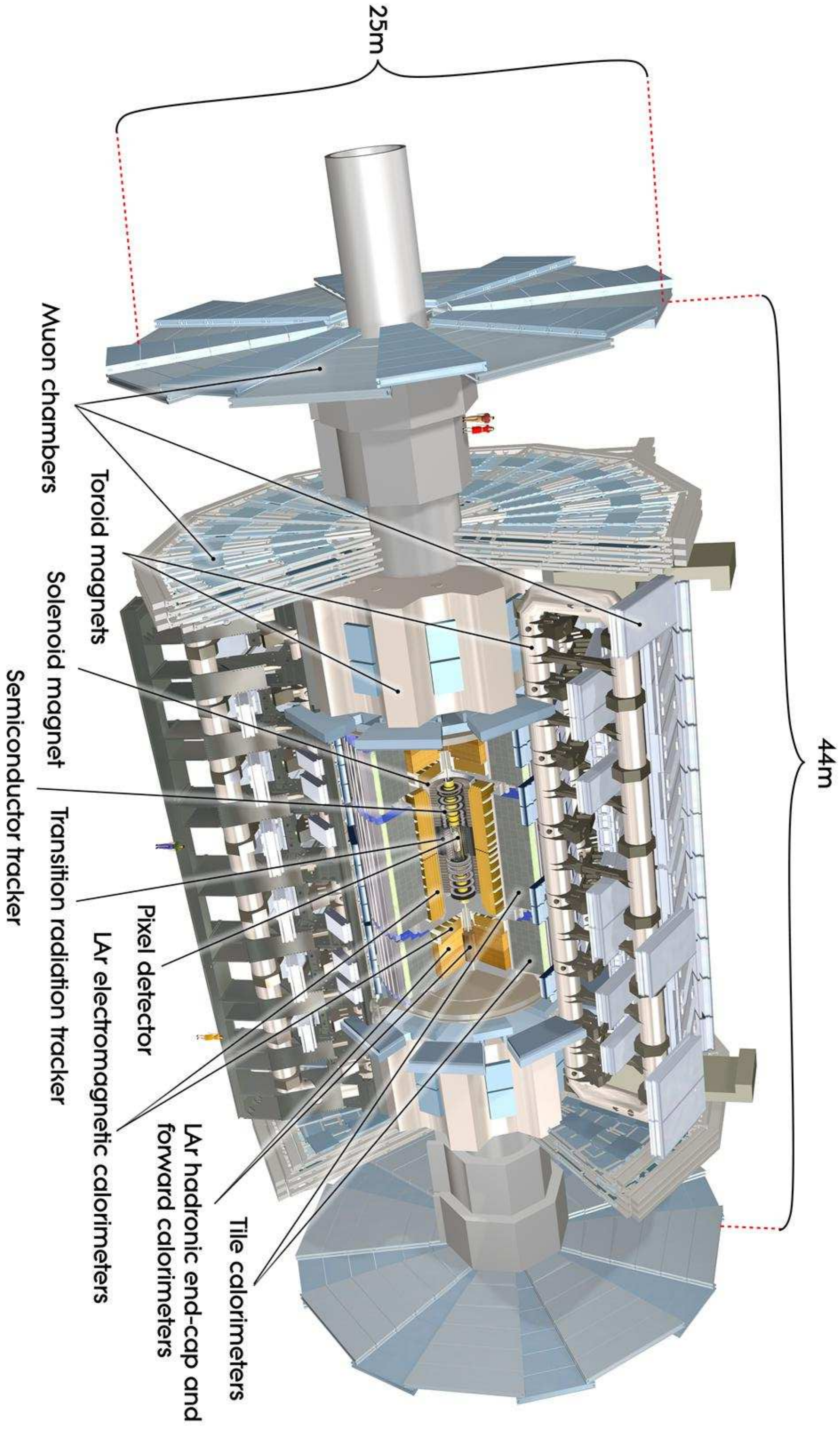
25m
44m
Muon chambers
Toroid magnets
Solenoid magnet
Semiconductor tracker
Transition radiation tracker
Pixel detector
LAr electromagnetic calorimeters
LAr hadronic end-cap and forward calorimeters
Tile calorimeters

Figure 3.3: Illustration of the ATLAS detector. Figure taken from [24].

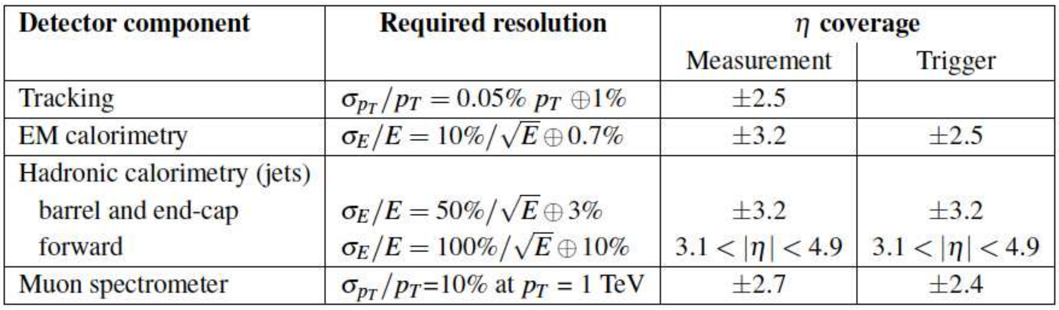

Detector component	**Required resolution**	**η coverage**	
		Measurement	Trigger
Tracking	$\sigma_{p_T}/p_T = 0.05\%\ p_T \oplus 1\%$	±2.5	
EM calorimetry	$\sigma_E/E = 10\%/\sqrt{E} \oplus 0.7\%$	±3.2	±2.5
Hadronic calorimetry (jets)			
barrel and end-cap	$\sigma_E/E = 50\%/\sqrt{E} \oplus 3\%$	±3.2	±3.2
forward	$\sigma_E/E = 100\%/\sqrt{E} \oplus 10\%$	$3.1 < \lvert\eta\rvert < 4.9$	$3.1 < \lvert\eta\rvert < 4.9$
Muon spectrometer	σ_{p_T}/p_T=10% at p_T = 1 TeV	±2.7	±2.4

Table 3.1: Performance goals of the ATLAS experiment for the different detector parts. The performance of the muon spectrometer is given for high-p_T muons without taking the Inner Detector into account. The unit of p_T and E is GeV. Table taken from [3].

dorapidity,

$$\eta = -\ln\tan\frac{\theta}{2} \,. \tag{3.3}$$

As this equation only holds for massless particles, the rapidity for massive particles is defined as

$$y = \frac{1}{2}\,\ln\frac{E+p_z}{E-p_z} \,, \tag{3.4}$$

where E is the particle's total energy and p_z its momentum component in z direction. Radial distances are given by $R = \sqrt{(x^2+y^2)}$.

In order to cover as many disciplines of particle physics from precision measurements of well-known processes to the discovery of new ones, the requirements on the design of the ATLAS detector were manifold (see Reference [3] for a more detailed description):

- fast, radiation-hard electronics and sensor elements
- large acceptance in η
- good charged-particle momentum resolution and reconstruction efficiency as well as the ability to resolve secondary vertices in the tracking system
- very good electromagnetic calorimetry for electron and photon identification and measurements
- complementary full-coverage of the hadronic calorimeter in order to find jets and missing transverse energy
- good muon identification and momentum resolution
- highly efficient trigger system, i.e. maximised background suppression by minimised signal loss

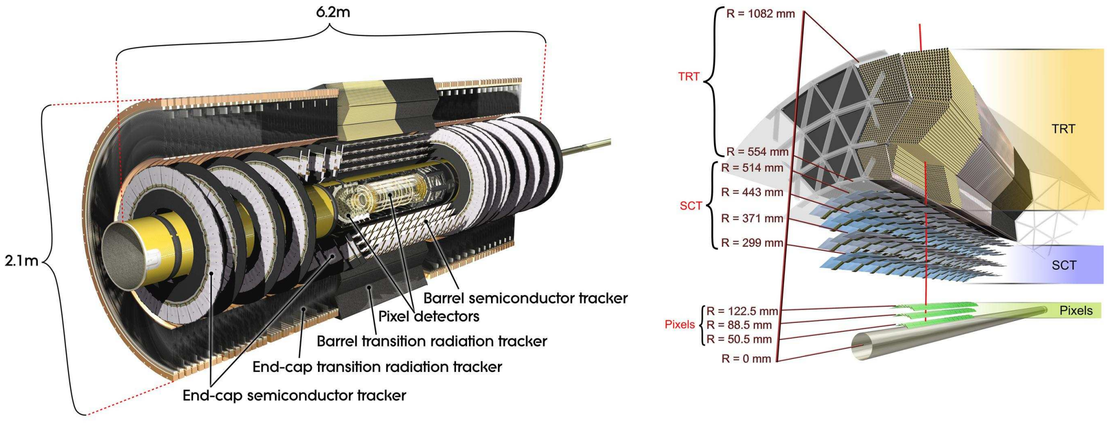
6.2m
2.1m
Barrel semiconductor tracker
Pixel detectors
Barrel transition radiation tracker
End-cap transition radiation tracker
End-cap semiconductor tracker
R = 1082 mm
TRT
R = 554 mm
R = 514 mm
R = 443 mm
SCT
R = 371 mm
R = 299 mm
R = 122.5 mm
Pixels
R = 88.5 mm
R = 50.5 mm
R = 0 mm
TRT
SCT
Pixels

Figure 3.4: Illustrations of ATLAS' Inner Detector. Figures taken from [24].

The overall performance goals deduced from these requirements on the ATLAS components are given in Table 3.1.

In the following, the different parts and sub-detectors of ATLAS will be discussed—more detailed when related to the analysis, and more briefly, if not (like the muon system).

3.3.1 Inner Detector – Tracking System

The Inner Detector (ID) of ATLAS (see References [26] and [3]) has to deal with $\mathcal{O}(1000)$ particles per bunch crossing, hence, a very fine detector granularity is required, especially close to the interaction point. Closest to the beam pipe is the Pixel Detector (PD), followed by the Semi-Conductor Tracker (SCT) and the Transition-Radiation Tracker (TRT). An overview of the Inner Detector is given in Figure 3.4.

In order to perform momentum measurements and to determine the charge of a particle, the ID region is embedded in a 2 T solenoidal magnetic field. The solenoid itself is located between the ID and the electromagnetic calorimeter. The coverage of the whole ID is $0 < |\eta| < 2.5$.

Pixel Detector (PD)

An important requirement for the innermost detector-component (see Reference [1]) is the capability to find secondary vertices, e.g., for decays of the τ lepton or the b and c quarks. Therefore, the inner pixel-layer, called "b-layer", is located directly at the beam pipe. The nominal pixel size is 50 μm in ϕ and 400 μm in z (barrel region) or R (disk region), which are located on more than 1,700 modules providing $\approx 80 \cdot 10^6$ channels.

Even though the design of the PD complies with the requirement of radiation hardness, the luminosity within ATLAS forces the b-layer to be replaced after three years of LHC operation. The remaining layers do not suffer from this extremely high particle flux and have an expected lifetime of ~ 10 years.

In order to protect the Pixel Detector from a possibly misguided beam, the Beam Conditions Monitor (BCM) is installed (see Reference [1]) within the PD. It consists of two diamond sensors that produce coincident signals if interactions originate from the nominal interaction point. Out-of-time events might indicate a misplaced beam and thus trigger the LHC to dump the beam. Furthermore, the BCM signals can be also used to monitor the luminosity.

Semi-Conductor Tracker (SCT)

Within the Semi-Conductor Tracker (for details, see References [9] and [10]), each track crosses eight[9] strip layers, which leads to four resulting space points. Within the barrel region, both coordinates are measured by using small-angle (40 mrad) stereo strips. One set of strips is parallel to the beam pipe, measuring $R - \phi$ with an accuracy of 17 μm. In the endcap, the detector has strips running radially as well as a set of small-angle stereo strips. The accuracy in $R - \phi$ is the same as in the barrel region.

For both, barrel and endcap, the resolution in the orthogonal coordinates, z and R, is worse ($\approx 580\ \mu$m) due to the use of ambiguity-reducing stereo strips. The SCT has a total of more than $6 \cdot 10^6$ read-out channels.

Transition Radiation Tracker (TRT)

As its name already says, the TRT (see Reference [8]) makes use of low-energy transition radiation (photons) from ultra-relativistic particles (like electrons) passing through numerous dielectric boundaries[10]. This is achieved by polypropylene-polyethylene fibres in the barrel (see Reference [6]) and polypropylene foils in the endcaps (see Reference [7]), which are interleaved with drift tubes (“straws”). These straws are 4 mm in diameter and filled with a xenon-based gas mixture to enhance the signal when photons from transition radiation pass through. The intrinsic accuracy for of each straw providing $R - \phi$ measurements within the barrel is $130\ \mu$m. In total, the TRT has more than 350,000 read-out channels.

Due to external constraints, the coverage of the TRT is limited to $|\eta| < 2.0$. Another difference to the PD and the SCT is the inability to measure the z coordinate within the TRT in the barrel region, which is compensated by its electron-identification capability. However, generating transition radiation comes at the cost of introducing additional material in the particle’s trajectory. This item will be discussed in the ID summary.

---

[9] for some regions of η the number is less than eight

[10] as the number of TRT hits strongly depends on η, an electron gives ~ 30 hits

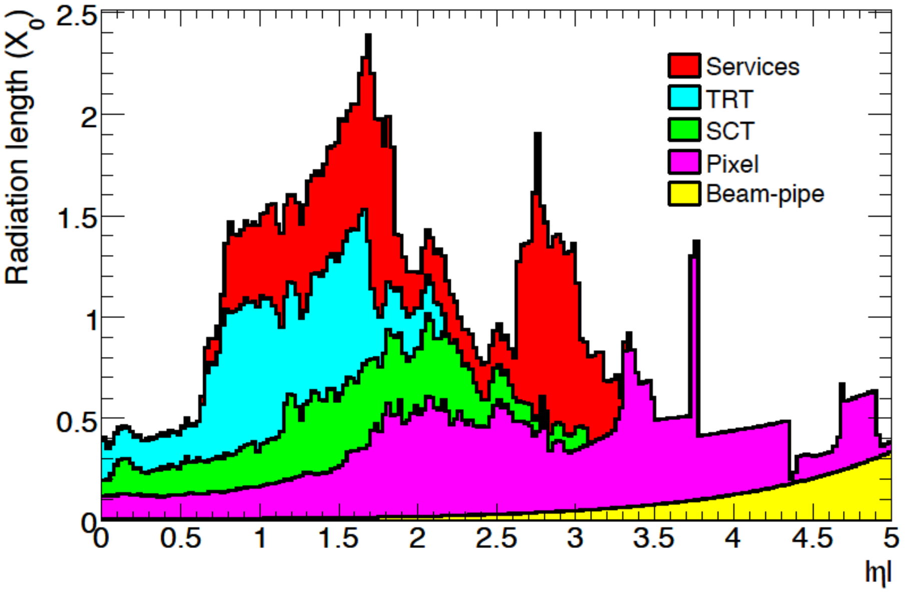

Figure 3.5: Simulated material distribution in terms of radiation length (X_0) at the exit of ATLAS' Inner Detector envelope. Figure taken from [3].

Summary of the Inner Detector

Every kind of material a particle traverses is a possible source of conversions, bremsstrahlung and multiple scattering. Each effect distorts the measurement of the particle's trajectory or its energy, and thus has severe consequences (see Reference [3]):

- many electrons loose most of their energy due to bremsstrahlung before even entering the calorimeter
- $\sim 40\%$ of the photons do not reach the calorimeter but convert to electron-positron pairs
- a significant amount of (charged) pions interact inelastically with the material in the ID

In order to describe and to reproduce the effects within the Inner Detector, a detailed modelling of its material has been implemented in the simulation. Figure 3.5 shows the impact of different kinds of material on a particle exiting the ID's envelope. Especially trajectories within the transition region from barrel to endcap at $|\eta| \approx 1.5$ face a large amount of material.

With the requirements on the accuracy of the spatial measurements within the ID, the alignment of the sub-detector parts is another crucial element. In order to correct the alignment and to mirror possible irreversible misalignments in the simulation, cosmic rays were studied prior LHC operation.

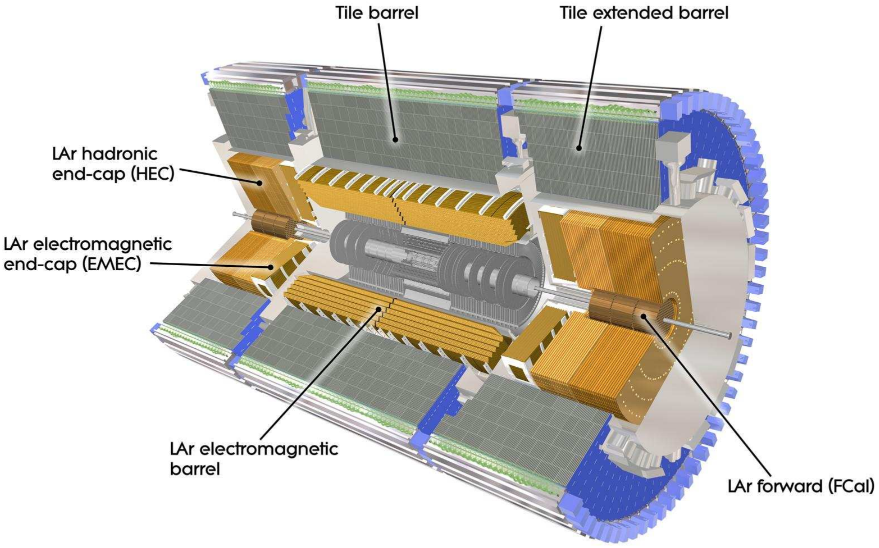
Tile barrel
Tile extended barrel
LAr hadronic end-cap (HEC)
LAr electromagnetic end-cap (EMEC)
LAr electromagnetic barrel
LAr forward (FCal)

Figure 3.6: Cut-away view of the ATLAS calorimetry. Image taken from [24].

In routine LHC running, the alignment is checked by a dedicated stream of tracks selected at a rate of $\sim$ 10 Hz, giving almost 10^6 events to fix the alignment constants daily, and to ensure a precision of 10 μm on the module positions of the SCT.

The solenoid field of the ID, which can also be a source of uncertainties, has been checked during the installation phase of ATLAS. Before the installation of the ID, the magnetic field strength has been measured by movable Hall probes within its volume in order to map the magnetic field and to find inhomogeneities. During running, four permanent probes to monitor any long term drifts in the magnetic field are installed at $z = 0$.

Whilst discussing the different sub-detectors of the ID, the individual numbers of readout channels were stated. It is obvious that, due to the need of a high granularity of the ID, the first trigger stage is not capable of handling that much information within ~ 2 μs. Hence, the (digitised) ID information is buffered during the level-1 latency, and is passed to the High Level Trigger system in case of a level-1 accept.

3.3.2 Calorimeter

An illustration of the ATLAS calorimetry is given in Figure 3.6. As it is common to multi-purpose detectors, ATLAS' calorimeter system is divided into an electromagnetic and a hadronic part (see Reference [3]). Both have to cover a wide range of physics requirements over a large rapidity region of $|\eta| < 4.9$.

Another similarity of both parts is to stop the measured particles completely. Apart from the obvious reason in containing the whole energy of the particle, this requirement also reduces leakage into the following detector-parts (hadronic calorimeter or muon system). Thus, calorimeter depth is an important consideration in the construction phase. For the electromagnetic calorimeter the radiation length X_0 exceeds 20 in all parts of it, as well as 10 interaction lengths[11] λ in barrel and endcap of the hadronic calorimeter.

Electromagnetic Calorimeter

The electromagnetic calorimeter (for details, see References [25], [30] and [17]) is a LAr[12]-lead detector with an accordion-shaped geometry for the electrodes and lead absorber-plates. The accordion structure guarantees azimuthal symmetry, whilst the thickness of the lead absorbers changes as a function of η in order to optimise performance and energy resolution of the calorimeter.

The calorimeter covers a total range of $|\eta| < 4.9$ and is divided into a barrel part ($0 \leq |\eta| < 1.475$), two endcaps ($1.375 < |\eta| < 3.2$) and a compartment in the forward calorimeter ($3.1 < |\eta| < 4.9$). The barrel is composed of two identical half-barrels, leading to a 4 mm gap at $\eta = 0$. The endcaps also consist of two parts, an outer wheel covering $1.375 < |\eta| < 2.5$ and an inner wheel for the region $2.5 < |\eta| < 3.2$. In order to correct for energy losses of electrons and photons in front of the calorimeter, an active LAr-layer, named “presampler”, is used in the region of $|\eta| < 1.8$.

Since the analysis will only deal with central objects (i.e. $|\eta| < 2.5$), the inner wheel will not be discussed here. In the central region, the electromagnetic calorimeter is segmented in three sections in depth, called “samplings” or “layers”, which is shown in Figure 3.7. The layers clearly have different purposes: the first layer consists of strip cells with $\Delta\phi \times \Delta\eta = 0.98 \times (3.1 \cdot 10^{-3})$ and $X_0 \gtrsim 4$. The very fine granularity in the η coordinate helps to differentiate photons coming from neutral pions ($\pi^0 \to \gamma\gamma$), and hence to identify the mother particle. The second layer with its almost quadratic shape ($\Delta\phi \times \Delta\eta = 0.0245 \times 0.025$) absorbs most of the electromagnetic showers ($X_0 \gtrsim 16$), whilst the third layer ($\Delta\phi \times \Delta\eta = 0.0245 \times 0.05$, $X_0 \gtrsim 2$) is used to estimate possible energy leakage into the hadronic calorimeter. The values for the radiation lengths depend on η of the particle and vary between $22 \leq X_0 \leq 33$ in the barrel region.

The transition from the barrel to the endcap at $1.37 < |\eta| < 1.52$ is a special case in the description of the detector, as it hosts a large amount of dead material (like cables etc.). This leads to an increased effort to estimate losses and material distribution correctly. Early analysis with data—and hence this thesis—will thus not rely on data from this region.

The read-out of the electromagnetic calorimeter with its $\approx 182{,}000$ channels is sep-

---

[11] mean path length to reduce the hadronic interacting particles by a factor of $\frac{1}{e}$

[12] LAr stands for liquid argon

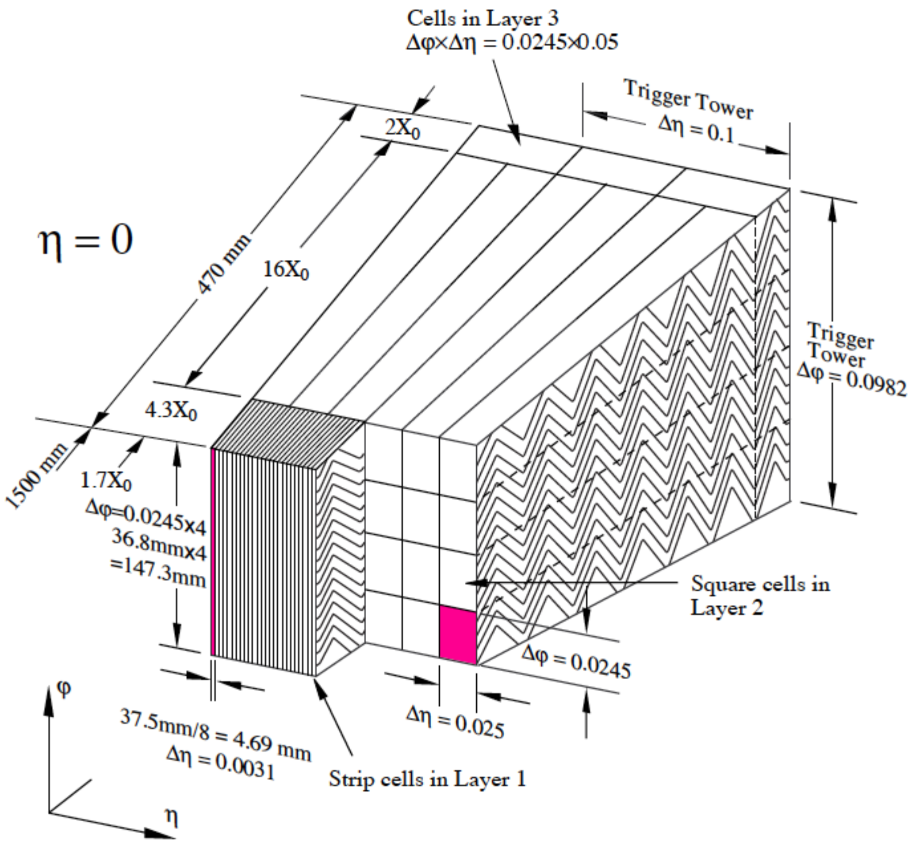
Cells in Layer 3
Δφ×Δη = 0.0245×0.05
Trigger Tower
Δη = 0.1
2X0
η = 0
470 mm
16X0
Trigger Tower
Δφ = 0.0982
4.3X0
1500 mm
1.7X0
Δφ=0.0245x4
36.8mmx4
=147.3mm
Square cells in Layer 2
Δφ = 0.0245
φ
37.5mm/8 = 4.69 mm
Δη = 0.0031
Δη = 0.025
Strip cells in Layer 1
η

Figure 3.7: Sketch of the three-layer structure (and the granularity of each layer) of the electromagnetic calorimeter. Also shown is the size of the *trigger towers* that will be discussed in Section 3.4. Image taken from [3].

arated in on-detector (front-end) and off-detector (back-end) electronics. Though front-end electronics need to be radiation-tolerant, it is necessary to avoid picking up additional noise during long analogue signal-transport in order to deal with $\mathcal{O}(10\ \text{MeV})$ signals. Thus, amplification and digitisation of the analogue cell-information happens on-detector. Furthermore, the front-end electronics builds *trigger towers* as the analogue sums of all 4×4 cells on which the Level-1 decision (see Section 3.4) will be based on. Both, digital and analogue information is then driven to the back-end electronics, located in a cavern ("USA15") 70 m away from the detector.

The back-end electronics buffers the digitised, full-granularity information from the calorimeter, whilst the analogue trigger-towers are digitised and a Level-1 decision is computed. In case the event is accepted, buffered information is processed to the High Level Trigger stages. A detailed description of the trigger system will be given in Section 3.4. The performance of the electromagnetic calorimeter with respect to electrons will be discussed in Chapter 5.

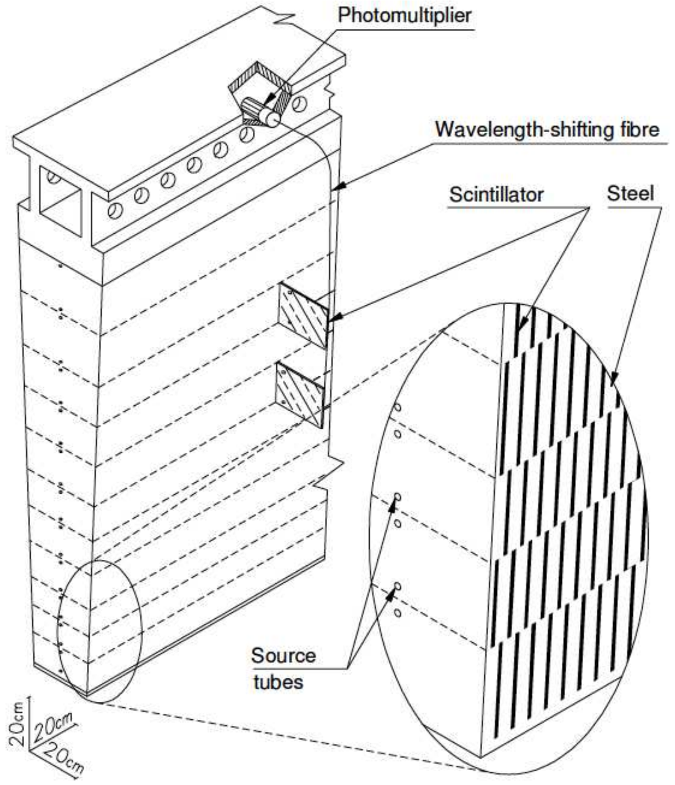

Figure 3.8: Sketch of the mechanical assembly of the tile calorimeter. Image taken from [3].

Hadronic Calorimeter

The heterogeneous hadronic calorimeter consists of three parts: the central tile calorimeter (TileCal, covering $|\eta| < 1.7$, see References [3] and [15]), the hadronic end-cap calorimeter (HEC, $1.5| < \eta| < 3.2$, see References [3] and [25]), and the forward calorimeter (FCal, $3.1 < |\eta| < 4.9$, see Reference [21]). The main purpose of each sub-part of this calorimeter is to completely absorb the energy of hadrons and jets, which should be fulfilled as the interaction length exceeds 10 in all parts of it. For the reconstruction of electrons, however, the hadronic calorimeter acts as a veto if an electromagnetic shower deposits energy above a given threshold also there.

The TileCal is a sampling calorimeter with steel as absorber and scintillating tiles as active medium. The arrangement of absorbers and tiles as well as the optical read-out is shown in Figure 3.8.

When a hadronically interacting particle enters the TileCal, it causes scintillator light that becomes modulated by wave-length shifting fibres, before it gets detected by photomultiplier tubes adjacent to each module. In order to mirror the particle's (or jet's) trajectory, the fibres are grouped to form read-out cells with respect to the nominal interaction point.

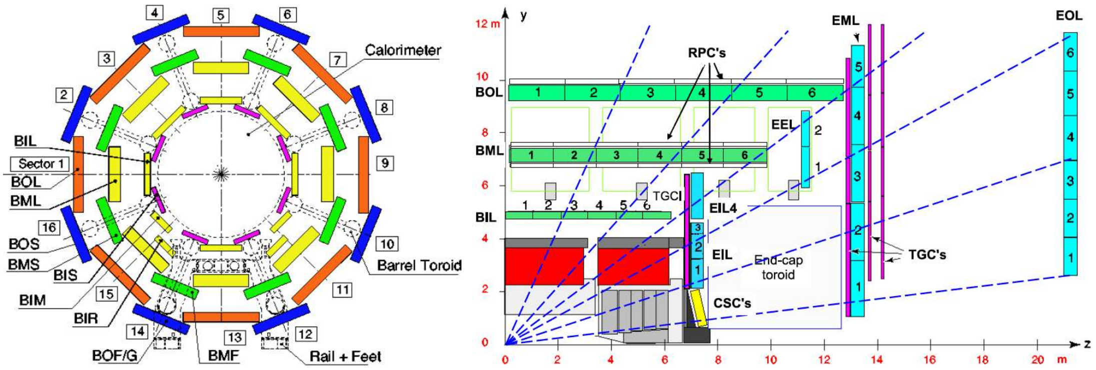

Figure 3.9: Cross-section of the muon spectrometer. Left: x-y plane perpendicular to the beam axis (non-bending plane). Right: x-z plane (bending plane). Images taken from [3].

With the expected high rate of jets in the intermediate region that is covered by the HEC as well as for geometric reasons, LAr is used as active medium and copper as absorber material within the hadronic endcaps. The latter choice, which is different from the one in the electromagnetic calorimeter, is due to the fact that copper has a higher density for hadron interactions. As can be seen in Figure 3.6, the HEC consists of two longitudinal layers on either side.

The FCal is segmented into three parts, FCal1, FCal2 and FCal3. Although they also use the LAr technology, FCal1 is dedicated to measure electromagnetic particles and uses copper as absorber material. FCal2 and FCal3, on the other hand, have tungsten absorbers and measure hadronic energy deposits, primarily.

The electronic read-out of the hadronic calorimeter follows almost exactly the one of the electromagnetic calorimeter, with the front-end components as well as with the signal paths to the back-end electronics. Details of the further signal treatment will be given in Section 3.4.

3.3.3 Muon System

The muon spectrometer (MS, see References [27], [3]) in ATLAS is essentially a tracking detector that is in the barrel (endcaps) embedded in a toroidal magnetic field of ≈ 0.5 T (≈ 1 T). The magnetic fields lead to field gradients up to 1 mT per mm, yielding bending powers as shown in Figure 3.10. The fact that muons pass matter with minimal interaction provides the possibility to study them with all other particles being stopped in front of the muon system.

An overview of the muon system gives Figure 3.9. It has a (high precision) coverage of $|\eta| < 2.7$ ($|\eta| < 2.4$) and aims on a stand-alone, i.e. without relying on information from other detector parts, transverse momentum resolution of 10% for 1 TeV muons,

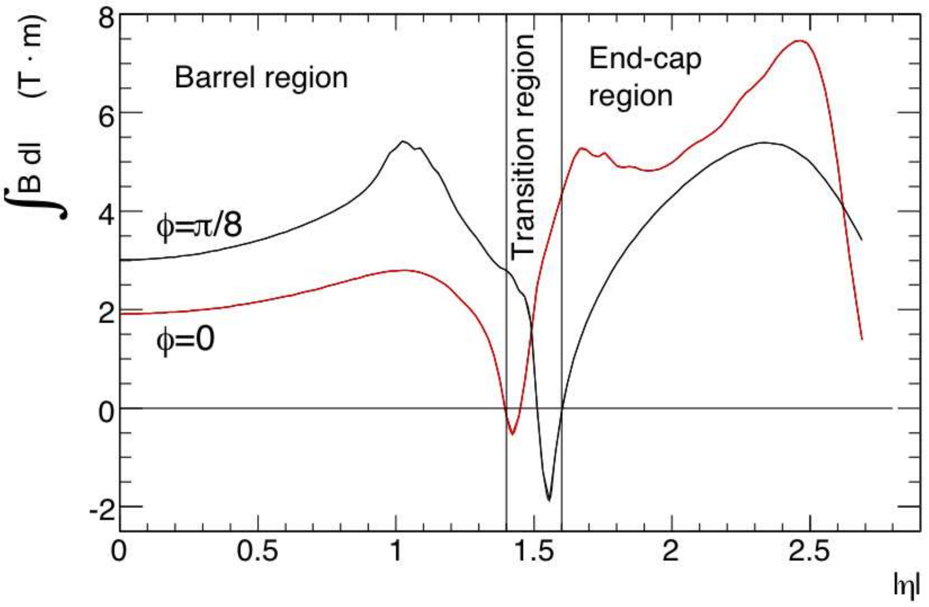

Figure 3.10: Predicted bending power of the muon spectrometer versus rapidity for two different azimuthal angles ϕ. Image taken from [3].

which gives a direct constraint to the spatial resolution ($\leq 50~\mu$m) of the spectrometer. The trigger system, however, only covers trajectories up to $|\eta| < 2.4$.

In the barrel region, the precision-tracking chambers are located between the superconducting toroid-coils, whereas the endcap chambers are in front and behind the endcap toroids. The symmetry in ϕ of the magnetic field is mirrored in the octet-structure of the muon chambers, which minimises possible gaps in detector coverage due to the overlap on the edges (see Figure 3.9). The three consecutive layers of chambers are aligned projectively with respect to the nominal interaction point in both, barrel and endcap. Only in the forward region ($2.0 < |\eta| < 2.7$) where the occupancy is high, Cathode Strip Chambers are used in the inner segment, whilst for the rest Monitored Drift Tubes (MDTs) measure the muon position.

Similarly to the considerations from Section 3.3.1, precision measurements of the muon's momentum require a precise alignment and a well-understood magnetic field. In order to achieve an alignment to comply with the constraints, a complex optical alignment system that forms a dense, stable grid for monitoring (barrel) or reconstructing (endcaps) the positions of the MDTs (see Reference [3]) has been used. The magnetic field, which should be known at the per-mille level for each track's path, is monitored by $1{,}800$ Hall probes sitting on the MDTs and on the endcap cryostats, whilst long-term drifts are monitored by two NMR tubes.

Dedicated trigger chambers[13] within the muon system feed the back-end electronics

---

[13] Resistive Plate Chambers (RPCs) are used in the barrel region as well as Thin Gap Chambers (TGCs)

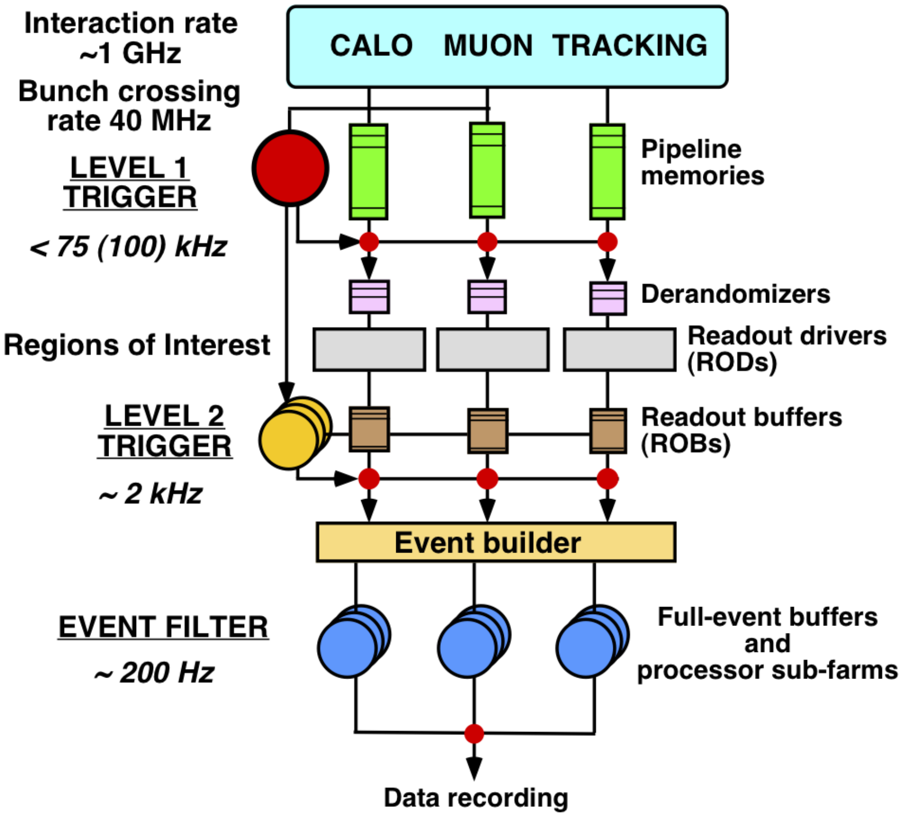
Interaction rate
~1 GHz
Bunch crossing
rate 40 MHz
LEVEL 1
TRIGGER
< 75 (100) kHz
Regions of Interest
LEVEL 2
TRIGGER
~ 2 kHz
EVENT FILTER
~ 200 Hz
CALO MUON TRACKING
Pipeline
memories
Derandomizers
Readout drivers
(RODs)
Readout buffers
(ROBs)
Event builder
Full-event buffers
and
processor sub-farms
Data recording

Figure 3.11: Schematic overview of the ATLAS trigger system that consists of three stages: Level 1, Level 2 and Event Filter.

with a fast-signal about the event to derive a trigger decision, measure the ϕ position of the muon and to provide bunch-crossing information.

3.4 The Trigger System

The main parameter defining the requirements on the trigger system is the amount of data that can be written to disk per second. A particle detector like ATLAS with its $\mathcal{O}(10^8)$ read-out channels operating at 40 MHz and a—already zero suppressed—raw event size of ~ 1.5 MB, would produce an overwhelming ~ 60 TB/s of data if no preceding instance, called “trigger”, selects the events—based on a flexible set of criteria—that actually will be written to disk and, hence, can be analysed afterwards.

With a manageable output of ~ 300 MB/s, the trigger rate is set to ~ 200 Hz. Hence, a suppression factor of $\gtrsim 10^5$ has to be achieved by the trigger, with an overall latency in the order of seconds.

In order to meet these requirements, a three-staged trigger system is implemented in

---

in the endcaps

ATLAS. The first trigger level is completely hardware-based, since software-based algorithms would not meet the timing requirements. The second and third trigger stage, also commonly referred to as High Level Trigger (HLT), is software-based and consists almost entirely of commercially available networking hardware and computers, in contrast to the custom-build hardware of the first trigger stage (see Reference [3]). A detailed overview of the ATLAS trigger system gives Figure 3.11.

3.4.1 Level-1 Trigger (L1)

The ATLAS L1 trigger receives the analogue sums of 4×4 calorimeter cells (Trigger Towers, TT) with a granularity of $\Delta\phi \times \Delta\eta = 0.1 \times 0.1$ for the calorimetry and the information of the muon trigger-chambers from the front-end electronics of the detector (see Reference [28]). Its purpose is to look for high-p_T muons, jets, electrons, photons and τ leptons. Additionally, it calculates the possible imbalance in the transverse energy within an event, called missing energy, $\not{E}_T$ as well as $\sum E_T$ and $\sum E_T^{\text{jet}}$. The overall latency is 2.5 μs during which the raw data is buffered on the front-end electronics that have a maximum acceptance rate of 75 kHz[14].

The muon trigger information is separated in streams from the RPCs and the TGCs, with a total of $\sim 8{\cdot}10^5$ input signals. The trigger algorithm tries to identify high-p_T muons originating from the nominal interaction point, with six independently-programmable p_T thresholds whose multiplicity is passed to the Central Trigger Processor (CTP).

A more detailed description of the operating principle of the calorimeter signal path will be given in the following, since one part of the thesis concentrated on the software development for and testing of the Jet Energy Modules (JEMs) of the L1 trigger.

After receiving the 4×4 energy sums from the front-end electronics of the calorimeters, Pre-Processor Modules (PPMs) digitise the data stream. In order to calculate energy sums and to find large objects like jets, the digitised information of the TTs is summed in a coarser granularity ($\Delta\phi \times \Delta\eta = 0.2 \times 0.2$), called "jet elements". The TTs are passed to the Electromagnetic Cluster Processor Modules (CPM) to find electromagnetic objects, and the jet elements are passed to the JEMs, in order to run jet, $\sum E_T$ and $\not{E}_T$ algorithms.

The various—electromagnetic and hadronic—trigger towers are distributed by the PPMs over 64 CPMs, whilst some TTs are duplicated[15] in order to handle cluster sharing between adjacent CPMs correctly. Via a sliding-window algorithm (described in Section 5.3.1), a local maximum of a 2×2 TT-window is sought. If one of the 16 programmable thresholds[16] is passed, the corresponding multiplicity bit is increased. As this procedure

---

[14] upgradeable to 100 kHz

[15] a part of the TTs are duplicated by the PPMs, another part by the Cluster or Jet Processor via the backplane of the crate

[16] divided in 8 thresholds for electron/photon objects and 8 for τ/hadron objects. τ signatures include

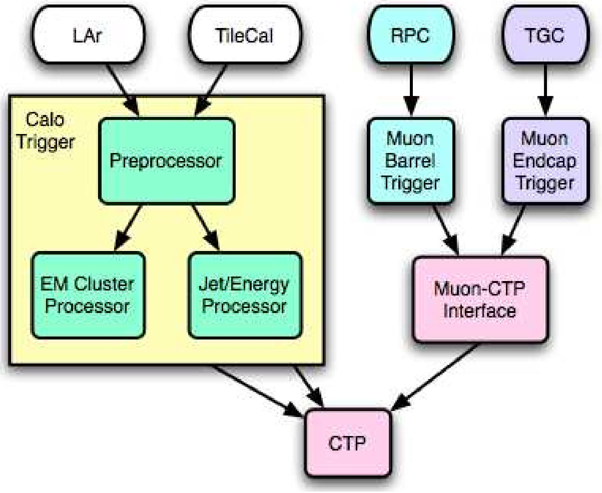

Figure 3.12: Block diagram of the ATLAS L1 trigger. Image taken from [22].

happens for each of the CPMs, Common Merger Modules (CMMs) combine the multiplicities into one overall multiplicity for each threshold. This information as well as the location of these objects passing one or more thresholds (“Regions of Interest”, RoI) are then passed to the Central Trigger Processor (CTP).

The operation of the JEMs is quite similar to the one of the CPMs, but one difference is that half of the numbers of modules are necessary in order to cover the whole detector due to the doubled granularity of the jet elements with respect to the trigger towers. Additionally, the jet-finding happens within a customisable window-size of 2×2, 3×3 or 4×4 jet elements. The JEMs provide the sums of the transverse energy, $\sum E_T$, $\sum E_T^{\text{jet}}$ as well as E_x and E_y to Sum Merger Modules (SMMs) and the number of jet clusters passing each threshold to Jet Merger Modules (JMMs). In a final step, the missing transverse energy is computed, and the individual threshold multiplicities are passed to the CTP.

The CTP combines the information of the two calorimeter trigger parts and the muon trigger to make the final L1 decision, whether an event is rejected or becomes accepted (L1A). The latter happens if at least one of the conditions[17] for each stream is fulfilled. In case of a L1A, a signal is sent to the front-end electronics to initiate the read-out. Moreover, the CTP has to handle timing differences between arriving information from different parts of the calorimeter and muon trigger and, hence, from different parts of the detector.

The Central Trigger Processor provides information to the data acquisition system (DAQ) that is used for offline-monitoring purposes of events that become rejected by the

---

processes like $W \to \tau\nu_\tau$ and $Z \to \tau^+\tau^-$.

[17] each condition is an item of the *trigger menu*, an abundant set of requirements to satisfy various physics demands

second trigger stage, as well as—via a separate path—to the level-2 trigger. This data stream contains information about why the event has been accepted and the locations of the RoIs.

3.4.2 Level-2 Trigger (L2)

The first part of the HLT is the L2 trigger (see Reference [29]), which receives the RoIs and the multiplicities of the trigger-menu items from the previous trigger stage. Within a latency of 40 ms, the incoming event rate of $\gtrsim 75$ kHz has to be reduced to 2 kHz, in order to comply with the input rate of the last trigger stage.

As stated earlier, the HLT is realised in software algorithms running on a computer farm. This allows a maximum of scalability and flexibility. The algorithms used at L2 have been written especially for this trigger stage to accomplish the available latency, but emulate some aspects from the offline reconstruction (see Section 3.5).

Unlike the L1 trigger, L2 has access to the full granularity of the detector, though this access is limited to the RoIs delivered by L1. Additionally, information from the Inner Detector can be used, allowing track-cluster matching and improved particle identification, like electron and photon separation.

In case the event is accepted at this stage, its information from the various detector parts becomes processed into one coherent structure. This is done by the Event Builder [33], before the stream is passed to the last trigger stage.

3.4.3 Event Filter (EF)

The final stage of the ATLAS trigger system is the Event Filter. Although it uses L2-based seeds, it has potential access to the full detector information and runs ATLAS standard event reconstruction algorithms (see Reference [3]). This is possible due to the relaxed time constraint of 4 s for each event to become processed. This is sufficient to guarantee an overall output rate of 200 Hz on which the data is finally written to tape.

Another tasks of the EF is the classification of the events within the accepted data stream, according to the ATLAS physics streams. These are, currently, streams for electrons, photons, muons, jets, missing (transverse) energy and tauons, as well as a dedicated stream for B-physics. In addition to that, the EF also delivers streams for detector calibration, monitoring and data-quality purposes, similar to L2.

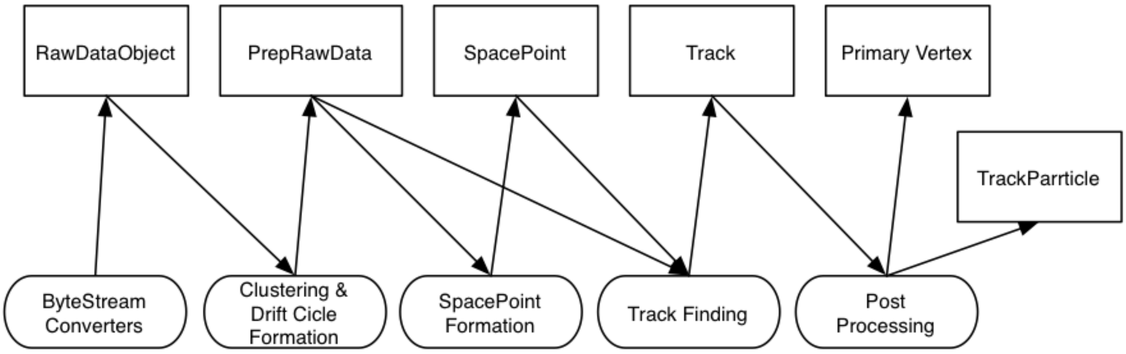

Figure 3.13: Tracking reconstruction chain. The boxes in the top represent data objects, whilst the second-row boxes show the algorithms working on the them. Figure taken from [11].

3.5 The ATLAS Computing Model

With the raw-output[18] of the Event Filter, the offline reconstruction software now prepares the different streams for analysis (see References [46] and [11]). However, an important instrument in particle physics is the ability to simulate both, physics processes and detector responses, hence also obtaining the raw data only from simulation. This will be discussed separately in Chapter 4.

In order to analyse the data from the detector, several different datasets corresponding to the stage of reconstruction will be produced, so that the following data will be available:

- *Byte-Stream (Raw) Data Object, RDO:* persistent (C++ object) representation of event data from the HLT ~ 1.5 MB per event
- *Event Summary Data, ESD:* contains detailed output of the detector reconstruction, hence particle identification, track re-fitting, jet calibration etc. Still possible is calibration and algorithm tuning ~ 0.5 MB per event
- *Analysis Object Data, AOD:* derived from the ESD, containing sufficient information for most analysis' purposes, can be adjusted to deliver different AODs in order to fit specific analysis-paths ~ 0.1 MB per event

Starting from AODs, even smaller representations of the data can be derived (*Derived Physics Data, DPD*), which, roughly speaking, correspond to the common n-tuples.

The reconstruction of the RDOs derives the particle parameters like four-momenta for electrons, photons, muons, jets etc., as well as auxiliary information (like the primary vertex, missing transverse energy) for each event. In order to optimise the determination of

---

[18] the *raw* data is a C++ object representation of the *byte-stream* that is the actual output of the EF

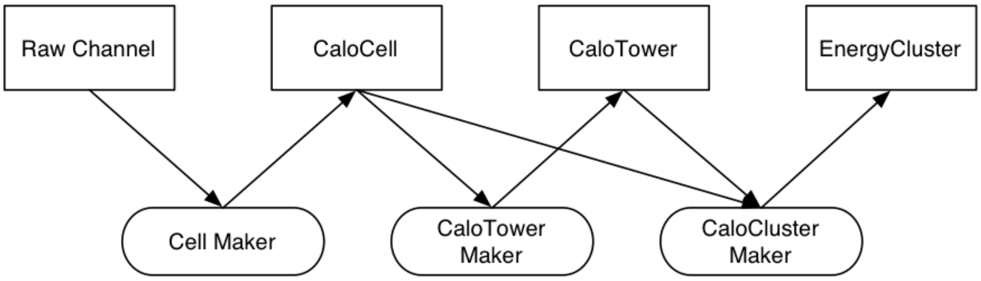

Figure 3.14: Cluster finding scheme with the data objects on the top and the algorithms in the second row. Figure taken from [11].

the four-momentum, information from all detector parts is combined, without restrictions on particle's momentum or rapidity. First, tracking system and calorimeter reconstruction are independent steps, followed by, second, combined reconstruction algorithms. The identification of some of the physical objects is part of the reconstruction, as well.

The track reconstruction has to deal with a variety of different detector parts from the Inner Detector as well as the Muon Spectrometer, accompanied by different coordinate systems from measurements on their various surfaces. An illustration of the track-finding algorithm is shown in Figure 3.13, where, after the determination of space points, a preliminary track is tried to be found. The last step in the track reconstruction is the post processing, which determines the primary vertex and results in "track particle" objects.

As the hadronic and electromagnetic calorimeters have different data formats, a "cell maker" (see Figure 3.14) algorithm is run in order to form common objects for the calorimetry. In the following, two different kinds of algorithms are used to find the output ("energy clusters"): the *sliding window* algorithm (see Sections 5.3.1 and 5.4) and a *topological cluster* algorithm.

Subsequent to the determination of the objects that form a track or a cluster individually, the combination of the results yields in the identification of physical objects. High-p_T electrons ($p_T \geq 10$ GeV), for example, become identified by associating tracks to clusters found by the sliding-window algorithm as well as by computing shower-shape and other variables. Soft-elecctrons ($p_T < 10$ GeV), on the other hand, are found by extrapolating the track to the calorimeter, where the topological-cluster algorithm is run. This gives a higher efficiency for low-p_T electrons than to start from two objects, a track in the ID and a cluster given by the sliding-window algorithm. The very same considerations hold for the photon search, with a track veto if an associated cluster is found.

Similar algorithms are run to identify muons, jets, tauons etc., but are not to be discussed in this context. More details on the electron reconstruction algorithms will be given in Chapter 5.

3.6 Luminosity Determination

An important parameter for each particle accelerator experiment is the instantaneous luminosity, which is a measure for the number of particles per unit area per unit time times the opacity of the target. With this parameter, the expected interaction rate can be calculated for an experiment. During one fill, the number of particles per bunch varies significantly due to collisions and imperfect beam quality. The instantaneous luminosity follows an exponential decay function with a lifetime of about 15 hours (see Reference [48]). By dividing each fill in short time periods of “luminosity blocks”, in which the instantaneous luminosity is assumed to be constant, ATLAS tracks these changes and makes them available for following analysis. The blocks cover a period on the order of minutes.

The primary luminosity measurement system in ATLAS is LUCID[19], which is the only detector primarily dedicated to online luminosity monitoring (see Reference [3]). It uses Cerenkov radiation to detect inelastic pp scattering in the forward direction. Since its purpose is to provide charged particle multiplicity for online monitoring, a part of LUCID events will also be used for detailed offline luminosity studies.

The LUCID detectors are placed around the beam pipe (radial distance ≈ 10 cm) at both sides of the ATLAS interaction point at $z \approx 17$ m. Each detector consists of aluminium drift tubes, filled with C_4F_{10}. The tubes are 15 mm in diameter, and each detector contains 20 of them. The online monitoring criteria can sufficiently be fulfilled by simply counting the number of tubes with a signal above a given threshold.

Further methods like BCM (see Reference [38]) and ALFA (see Reference [3]) complement the LUCID measurements and help to improve the initial accuracy of the instantaneous luminosity measurement from ≈ 20–30% to $\sim 5\%$ in later stages of the ATLAS experiment. However, this accuracy can only be reached by counting events relative to an already known, “reference” cross-section, like the one from the γ^*/Z production. An high-precision absolute measurement is not possible.

A completely different technique that does not take into account reference cross-sections is the *van der Meer* method, also known as “beam separation” or “luminosity” scans. The basic idea—as it is described in *van der Meer’s* initial proposal (see Reference [73]) for the ISR—is to determine the “effective beam height”,

$$h_{\text{eff}} = \frac{\int \rho_1(z)\,dz \cdot \int \rho_2(z)\,dz}{\int \rho_1(z)\rho_2(z)\,dz}\,, \tag{3.5}$$

with ρ_i as the beam-densities as a function of the vertical coordinate z. By displacing one of the beams vertically with respect to the other, the counting rate that can be measured within ATLAS is plotted versus the beam displacement, which results in a Gaussian-shaped curve with a maximum at zero displacement. The point is that the effective beam height is equal to the area under the Gaussian divided by the ordinate at zero displacement. This measure is completely independent of the beam shape itself.

---

[19] LUminosity measurement using Cerenkov Integrating Detector

Transferring this method to ATLAS, the instantaneous luminosity can be calculated by:

$$\mathscr{L} = \frac{\mu \cdot n_b \cdot f_r \cdot I_1 \cdot I_2}{2\pi \cdot \Sigma_x \cdot \Sigma_y}\,, \tag{3.6}$$

with $I_{1,2}$ as the beam intensities and $\Sigma_{x,y}$ as the standard deviations of the Gaussian distributions in the transverse x, y plane. By measuring the rates in the previously described ways within ATLAS, the beam intensities can be derived.

Each luminosity scan in ATLAS consists of 27 steps, where a total range of $\pm 6\sigma_{\text{beam}}$ in beam separation is covered horizontally and vertically (σ_{beam} is the nominal transverse size of the beams in ATLAS). With this method, the systematic uncertainty of $\approx 20\%$, which results from the imperfect knowledge of the inclusive inelastic cross-section in the simulation, is reduced by a factor of two.

> *≪Durch bloßes logisches Denken vermögen wir keinerlei Wissen über die Erfahrungswelt zu erlangen; alles Wissen über Wirklichkeit geht von der Erfahrung aus und mündet in ihr.≫*
>
> Albert Einstein (*1879, †1955)

4

The Monte Carlo Simulation

4.1 Introduction

In the early days of particle physics, the only way to study particles was either via exclusive counting experiments or by visualising the particles' paths in, e.g., bubble chambers.

With the increasing performance of accelerators and detectors, however, it became more and more important to be able to simulate already discovered physics processes and to implement new theoretical developments within the simulation in order to mirror physics in computer models. Over the years, many different simulations have been developed, some to describe processes at Leading Order (LO), some at Next-to Leading Order (NLO) or even Next-to Next-to Leading Order (NNLO). The variety of event generators also allows for cross-checking results and to estimate systematic uncertainties.

Translated to ATLAS, the aim is to reach the byte-stream (or raw) level with the simulation, meaning that the simulation chain (see Figure 4.1) has to take care of the event generation with a suitable Monte Carlo simulator as well as the detector simulation.

Within this brief chapter, the event generation with the `PYTHIA` generator will shortly be introduced (see Section 4.2), followed by an overview of the ATLAS detector simulation (see Section 4.3). At the end, the different signal and background samples being used in this analysis will be shown.

4.2 Event Generation

With the hundreds of particles being created in each event at the LHC, it is absolutely essential to model these complex physics processes with event generators (see Reference [3]). They deliver valuable input for analysis strategies (e.g., optimising signal-to-background ratios), estimate acceptance corrections and, even at the planning stage of detectors, requirements on their construction.

As the generated events serve as input for the detector simulation (see next section), the output of the various generators has to be compatible to the common format

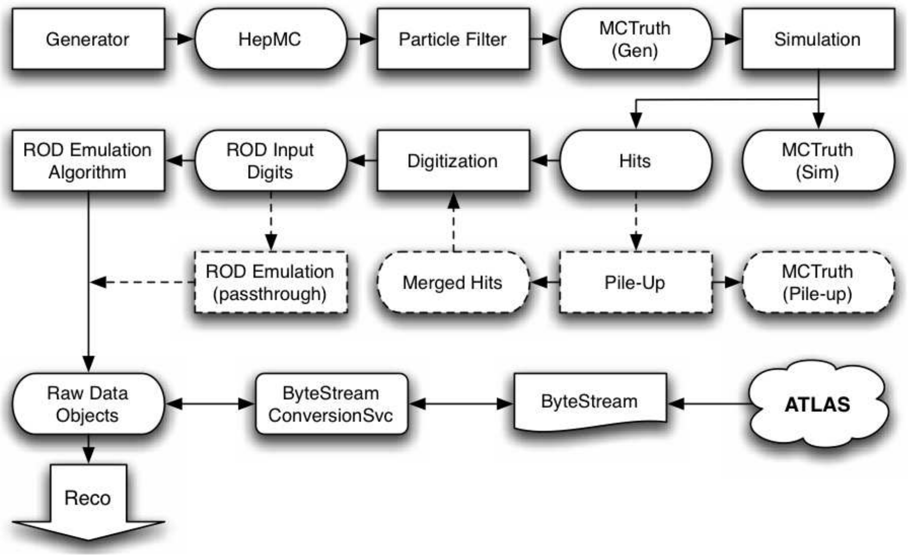
Generator
HepMC
Particle Filter
MCTruth (Gen)
Simulation
ROD Emulation Algorithm
ROD Input Digits
Digitization
Hits
MCTruth (Sim)
ROD Emulation (passthrough)
Merged Hits
Pile-Up
MCTruth (Pile-up)
Raw Data Objects
ByteStream ConversionSvc
ByteStream
ATLAS
Reco

Figure 4.1: Data flow in the simulation chain. Rounded rectangles show objects in the event data model, whilst rectangles represent processing stages. Figure taken from [3].

("HepMC", see Reference [43]).

Monte Carlo generators like `PYTHIA` [72], `HERWIG` [40], `AlpGen` [64] and others, have to model in particular:

- Initial State Radiation (ISR), where one of the partons radiates a gluon ($q \rightarrow qg$) before the actual interaction
- the actual hard process, where the interacting partons are described by the PDFs
- possible multiple interactions from the remaining partons and showers originating from beam remnants
- intermediate states, such as $W^{\pm}/Z$ resonances
- decays of particles produced in the hard process
- Final State Radiation (FSR), characterising the energy loss of a (stable) decay product, like $e \rightarrow e + \gamma$
- hadronisation of the resulting partons and gluons and the proper description of their possible subsequent decays
- final state parton showers

Since it only simulates the hard-process itself, hadronisation and final state parton showers cannot be simulated alone within `AlpGen`.

As on of the underlying principles in particle physics is quantum mechanics, randomness plays an important role. In order to simulate a process given by nature that is described by a function $f(x)$ (where $f(x)$ can stand for anything like a fragmentation function or a differential cross-section), the task is to select a random x in a way that the probability in a small intervall dx around x is proportional to $f(x)dx$ (see Reference [72]).

One important difficulty for Monte Carlo simulations are limitations in the phase space of certain processes. If, for instance, a multi-dimensional function $f(x)$ could be factorised in order to pick phase-space variables for each dimension separately, the impact on the simulation is small. If the factorisation is not possible, however, the simulation can become quite inefficient due to the randomly chosen x, which has to satisfy the phase-space conditions now in an n-dimensional hyperspace.

In Chapter 2, the PDFs $f_q(x, Q^2)$ have been introduced as the parametrisation of the probability for finding a parton q with the energy fraction x of the beam's energy at a virtually scale Q^2, with the normalisation condition $\sum_q \int_0^1 dx\, x f_q(x, Q^2) \equiv 1$. Within `PYTHIA`, many different PDFs can be chosen. The standard is the LO implementation by the CTEQ group (see Reference [63]), CTEQ6L, and is therefore also the parametrisation of the samples used in this analysis (see Section 4.4).

In terms of event generation via `PYTHIA`, the production of the γ^*/Z interference is a $2 \to 1$ process, even if additional jets arise from ISR. The cross-section is given by Equation 2.40, when the decay of the interference is not considered. Apart from `PYTHIA` and `AlpGen`, the `MC@NLO` generator that is also used in this analysis is the only one above the LO level. Its advantages are a modified subtraction method in order to deal with divergences such that a cut-off is no longer needed and that the leading-p_T emission in the initial state is calculated precisely.

With the decay width of the Z and the known branching ratio of its decay to two electrons, the event simulation of the process $pp \to \gamma^*/Z + X \to e^+e^- + X$ is complete. After translating the generator-specific event-information into the common HepMC format, the detector simulation can take place.

4.3 Detector Simulation – `GEANT4`

The depiction of a complex machine like ATLAS within a software framework needs a great effort and is done within the `GEANT4` toolkit (see Reference [13]). It has to meet at least the following requirements:

- mirror ATLAS' geometry and its material distribution
- track particles through the detector and through external magnetic fields

- handle particle interactions within the detector geometry correctly
- simulate the detector response of sensitive parts
- store the event data in a format that is compatible with the actual detector output

The input of the detector simulation is the HepMC output of an event generator (see previous section) and contains primary particles and primary vertices of the event, after an additional filtering stage. Hits produced by the simulation can directly be digitised and transformed into RDOs, or can be sent to the pile-up algorithm, first (see Figure 4.1, Reference [69]). The digitisation also includes the simulation of channel-by-channel response variations as well as electronic noise. Afterwards, the digitised information is passed to the Read-Out-Driver (ROD) emulation algorithm in order to form RDOs. The ROD emulation might be skipped, however, to directly form RDOs in passthrough mode. By building RDOs, the simulation chain is completed and the event can be analysed by the reconstruction software.

Even after optimisation of the ATLAS simulation it is still very time-consuming to simulate events, with $\gtrsim 10$ min per event. Therefore, most of the simulations are a centralised effort by the ATLAS collaboration.

Apart from dedicated test-beams, the uncertainties on the implementation of the ATLAS detector can be estimated by intentionally adding material in the simulation or by misaligning detector parts.

4.4 Samples Used in this Analysis

For the purpose of this analysis, the simulation of six different physics processes have been used, all of them generated and reconstructed by the ATLAS collaboration, due to the heavily time-consuming process of event reconstruction. The event generators in use were `PYTHIA`, version 6.4, `AlpGen`+`HERWIG` (LO) and `MC@NLO`. The ATLAS reconstruction software used version 14.2.20. At the beginning of this analysis, a center-of-mass energy of 10 TeV was anticipated for early running of the LHC. Therefore, an increased effort was made to produce Monte Carlo samples for this energy. As it turned out, only an energy of 3.5 TeV per beam could be realised for the early phase of ATLAS operation. Since 7 TeV samples had not yet been produced, this analysis uses the 10 TeV samples for signal and background channels that will now be introduced, and their impact on the analysis will be discussed briefly. An overview of all samples gives Table 4.1.

Almost each generator output runs through a *filter* that sorts out events that most likely would not become reconstructed at all, hence reducing the amount of events entering the time-consuming reconstruction beforehand. To avoid possible bias, the filter criteria are quite loose, mostly concentrating on objects that miss the Inner Detector. For instance,

Sample	Generator	σ_{tot} / nb	Events	$\int dt\,\mathscr{L}$ / pb^{-1}	ε_F
$Z \to e^+e^-$	`PYTHIA`	1.147	3,023,412	$2{,}846.9$	0.956
QCD	`PYTHIA`	$1{,}458{,}000.$	8,608,768	0.0787	0.075
$t\bar{t}$	`MC@NLO`	0.2029	321,306	$1{,}583.7$	$1.$
$W + 1$ jet	`AlpGen+`	2.112	60,741	31.96	0.9
$W + 2$ jets	`AlpGen+`	0.676	107,920	159.6	$1.$
$W \to e\nu$	`PYTHIA`	11.76	59,995	5.793	0.88

Table 4.1: Summary of the Monte Carlo samples used within this analysis. Each sample is generated for $\sqrt{s} = 10$ GeV.

the filter criterion for events to enter the detector simulation for the signal sample is that at least one of the generated particles has to be within $|\eta| < 2.8$.

The simulation of the signal channel was generated with a total (LO) cross-section $\sigma_{\text{tot}} = 1.147$ nb. After the filter, the “Monte Carlo truth” sample contains more than 3 Million $\gamma^*/Z \to e^+e^-$ events, corresponding to an integrated luminosity of 2.85 fb^{-1}. Besides the “on-shell” Z intermediate state, the sample includes the off-shell photon part as well as the γ^*/Z interference. In order to remove the lower-mass Drell-Yan component, the invariant mass of the lepton pair must exceed 60 GeV[1].

QCD events with jets in the final state contribute dominantly to the background for the signal channel. Even though the jet suppression works very well in ATLAS, the enormous cross-section ($\sigma_{\text{tot}} = 1.46 \cdot 10^6$ nb) leads to a large amount of events where jets become misidentified as electrons and thus fake a Z boson. With the computing limitations described earlier, the sample contains ≈ 8.6 Million events or 0.079 pb^{-1} of data. The filter removes most of the events on generator level, since many QCD[2] events do not result in concentrated jets or the jets’ energies are too low. The event is kept if at least one stable particle (excluding electrons and muons) with $p_T > 17$ GeV is inside an energy deposition in a window $\Delta\eta \times \Delta\phi = 0.12 \times 0.12$. In this way, 7.5% of the generated events enter the detector simulation.

The production of top pairs in ATLAS is expected to contribute significantly to the background, with high-p_T electrons originating from the semi-leptonic decay of each top particle $t \to bW \to be\nu$. Hence, if the $W^\pm$ bosons from the decay of the $t\bar{t}$ pair both decay via the electron channel, the final state contains an electron-positron pair. A sufficiently large sample is available, with an integrated luminosity of ≈ 1.6 fb^{-1}.

---

[1] in particle physics, masses and momenta of particles are commonly given in units of energy, with $c \equiv \hbar \equiv 1$

[2] strictly speaking, the sample also contains other processes with electrons in the final state, like $t\bar{t}$, W and Z production. These events are removed in the selection process in order to clean up the sample

Two additional samples are used in order to estimate the background contribution to the $\gamma^*/Z \to e^+e^-$ analysis: $pp \to W + n$ jets, with $n = 1, 2$. Here, one electron originates from the decay $W \to e\nu$ and the other one from a misidentified jet. For the 1 (2) jet(s) sample, $\approx 60{,}000$ ($\approx 110{,}000$) simulated events are available. Because of the cross-sections that are comparable to the one from the signal sample and the jet suppression factor, they are not expected to contribute significantly to the background.

In order to study possible biases arising from correlations between the electron and the positron of the final state when determining single electron efficiencies, a $W \to e\nu$ sample containing $\approx 60{,}000$ events is used.

≪Die ≪Bahn≫ des Elektrons entsteht erst dadurch, dass wir sie beobachten. ≫
Werner Heisenberg (*1901, †1976)

5

Electrons in the ATLAS Experiment

5.1 Introduction

In this chapter, the way a physical object like an electron is defined within the ATLAS experiment, is being discussed. When an actual electron passes the detector, it usually leaves discrete information in the inner detector as well as some energy at a certain spot in the electromagnetic calorimeter. This interaction is described in Section 5.2.

As there are many particles and particle-like objects within one single event, the trigger system (see Section 3.4) has to merge the information provided by the various detector parts to reconstruct these objects. Thus, many of the algorithms of the offline reconstruction are also implemented in the trigger. A clean separation between trigger and (electron) reconstruction done by the offline software is thus not possible. In the following, the chronological order is being kept, meaning that, first, the different trigger stages are described (Section 5.3), which provide, second, an event that the reconstruction software can analyse afterwards. If there are parallels between the two parts, the trigger description will refer to the detailed reconstruction walk-through (Section 5.4).

Not only during the start-up phase of the ATLAS experiment, but also in later stages with higher energies and luminosities, high-p_T electrons are important objects to trigger on, as they appear not only in well-known processes, such as the one discussed in this analysis, but also in final states of, yet unseen, “new physics” like SUSY. Therefore it is necessary to trigger on electrons reliably.

5.2 Electron Signature in ATLAS

On its way through the ATLAS detector, the electron passes two different kinds of subdetectors: the Inner Detector (ID) with the tracking system where it ideally should loose none of its energy, and the electromagnetic calorimeter, where, again ideally, the electron should be stopped, i.e. all of its energy should be deposited here. It is obvious that these idealised requirements cannot be fulfilled in an experiment. The different deviations from

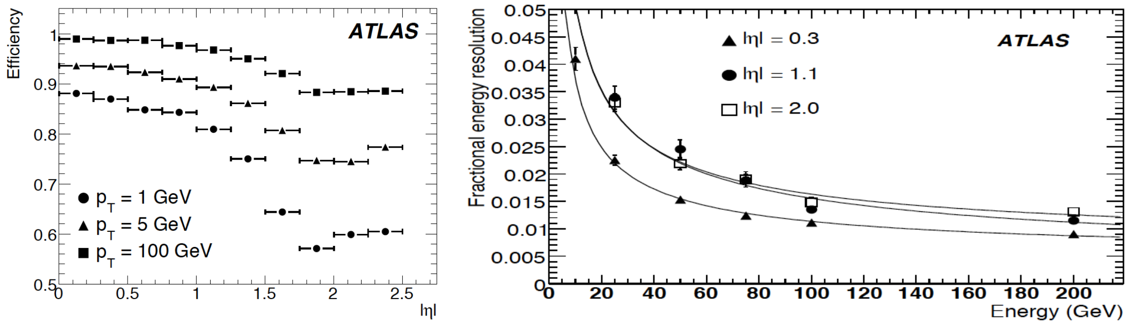

Figure 5.1: Left: track reconstruction efficiencies for electrons with a given p_T as functions of $|\eta|$. Right: energy resolution of electrons in the electromagnetic calorimeter for different values of $|\eta|$. Figures taken from [4].

this idealised detector have to be known precisely to ensure a high-precision measurement within ATLAS.

5.2.1 Tracking System

As described in Section 3.3, the inner detector consists of a Pixel Detector (PD), a Semi Conductor Tracker (SCT) and a Transition Radiation Tracker (TRT). An electron leaves track points in each of these sub-detectors; the number of hits at least required to qualify for a possible track reconstruction can be adjusted individually. The solenoidal magnetic field bends the trajectory of charged particles, allowing it to determine the momentum and the sign of the charge.

Even if the resolution of the tracking system improves with higher-E_T electrons, the effects from electron bremsstrahlung and photon conversions have negative impact on the resolution and the track reconstruction efficiency of electrons. The latter is shown in Figure 5.1: for low-p_T electrons, the amount of material is mirrored in the lower efficiency, as the effect of bremsstrahlung becomes important here. The more significant drop at larger $|\eta|$ underlines this as more material has to be traversed.

5.2.2 Calorimeter

When an electron passes the electromagnetic calorimeter (see Section 3.3), it initially loses energy due to bremsstrahlung[1]. The radiated photon loses energy by electron-positron pair creation whilst the initial electron can make bremsstrahlung again. The result is an electromagnetic shower that consists of photons, electrons and positrons. Each process comes along with a loss of energy, that is absorbed by the detector. The energy deposit in the detector is measured and it is therefore the intention to completely stop the electron within the calorimeter, so that its total energy can be recorded.

---

[1] at energies $\gtrsim$ 1 GeV the fraction is $\approx 100\%$

But even if this succeeds, one does not know its *original* energy. While traveling *to* the calorimeter, the electron has to pass varying amounts of material, mostly within the ID. Furthermore, the position measurement might also not be exact due to the limited granularity and effects of the accordion geometry of the electromagnetic calorimeter etc. Therefore, corrections have to be applied to the information delivered by the calorimeter, to ensure uniformity in both, position and energy measurement.

Figure 5.1 shows the resulting energy resolution for electrons in the electromagnetic calorimeter. It reflects the better resolution when smaller amounts of material have to be traversed by the particle, usually at lower $|\eta|$.

5.3 Triggering on Electrons

The technical implementation of the ATLAS trigger system is shown in Section 3.4. In a nutshell, the three trigger stages sort out events with useless or uninteresting information. While the understanding of the detector will increase over time, it will happen that interesting information during early running will become unattractive, making it mandatory to be flexible with trigger signatures. The leptonic decay of the Z boson, for example, is used as a “standard candle” for detector calibration as it has clean final states ($ee, \mu\mu$), allowing studies of the detector response. Later on, the experiment will start concentrating on the search for new signatures and handle the former standard candle as background.

The need for flexibility in trigger signatures is mirrored in the trigger menus (see Section 5.3.4), which are configurable sets of trigger *items* (L1) and *chains* (HLT). The naming scheme for a Level-1 item is composed of the RoI multiplicity N (omitted if N=1), the trigger purpose (“EM” for electrons and photons), the E_T threshold cut XX (in GeV) and the suffix ”I” if the RoI has to fulfil the isolation requirements: L1_NEMXXI. For this analysis, the trigger item L1_EM7[2] is being used. In case of the HLT, the naming pattern is similar, e.g., EF_e10_medium. The suffix “loose”, “medium” or “tight” denotes the selection cuts which have been applied (see Section 5.5). The collection of related trigger items and chains are called *signatures*, e.g., `e10_medium` signature, which includes the items (chains) L1_EM7, L2_e10_medium and EF_e10_medium.

At first, the general way ATLAS triggers on electrons (and on photons, for the first trigger stage) is explained.

---

[2] only information from the first-level trigger has been used, as the corresponding HLT information was not available in the centrally produced sample

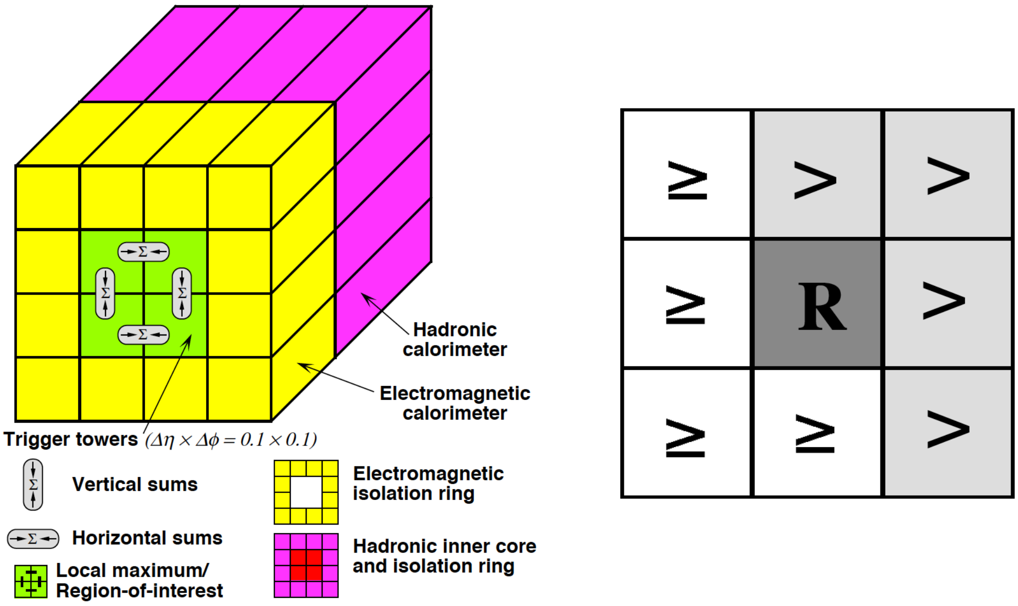
Hadronic calorimeter
Electromagnetic calorimeter
Trigger towers ($\Delta\eta \times \Delta\phi = 0.1 \times 0.1$)
Vertical sums
Horizontal sums
Local maximum/ Region-of-interest
Electromagnetic isolation ring
Hadronic inner core and isolation ring
Σ
≥
>
>
≥
R
>
≥
≥
>

Figure 5.2: L1 trigger towers. Left: representation of a 4×4 window of trigger towers; right: sliding-window algorithm to find a “region of interest”. Figure taken from [4].

5.3.1 First Level Trigger

The first, hardware based trigger stage has to reduce the incoming event-rate by many orders of magnitude in only a few microseconds time. In contrast to the following trigger stages it is therefore impossible to use data from the whole detector to base the trigger decision on. For the search for electromagnetic objects, only information from the calorimeters is available, at the cost of a coarser granularity. This implies that a separation of photons and electrons is not possible within L1.

Figure 5.2 shows a sketch of the L1 trigger towers: in each η-ϕ direction, four of the calorimeter cells are summed up in E_T, building one trigger tower with a resulting $\Delta\eta \times \Delta\phi = 0.1 \times 0.1$ granularity for $|\eta| < 2.5$. In the next step, a sliding-window algorithm tries to find a local maximum (“region of interest”, RoI) in the transverse energy of a 2×2 window with the comparison operators also shown in Figure 5.2.

Once such a local maximum has been found, a variety of other E_T-sums is calculated in order to compare them to given thresholds. These sums are as follows:

- four sums of adjacent trigger towers within the region of interest: at least one of these 2×1—or 1×2, respectively— sums has to pass a pre-defined energy threshold
- electromagnetic isolation: the ring of 12 trigger towers surrounding the RoI is used to veto on energy depositions close to the core region

- hadronic core: the 2×2 trigger towers in the hadronic calorimeter corresponding to the RoI; if a certain threshold is exceeded, the object will be rejected to be an electron or a photon
- hadronic isolation: ring of 12 trigger towers around the hadronic core, also used to veto on electromagnetic objects

To get an object to be accepted as an electromagnetic object at L1, the transverse energy of the first sum has to pass the given threshold, while the other three sums must not exceed their individual values.

The importance of a perfectly working L1 trigger manifests in the fact that—in order to enable the following stages to use the full detector-information—only the regions of interest are passed to the second trigger-stage. Thus, if L1 fails to provide the RoI information, it will not be investigated by level 2 and the whole event might be lost.

5.3.2 Second Level Trigger

As described in the previous section, the software-based L2 trigger works with the RoI information provided by the L1 trigger. For these regions, the full detector-information is accessible (see Reference [4]). Within this $\Delta\eta \times \Delta\phi = 0.4 \times 0.4$ window, the trigger scans the cells of the calorimeter's middle layer to find the one with the highest E_T, which, in the following, is used as a seed to build a new cluster with an area of $\Delta\eta \times \Delta\phi = 0.075 \times 0.175$. To account for electron bremsstrahlung and photon conversions, the window size in ϕ is coarser than in η.

When trying to differentiate electromagnetic particles from other objects, such as jets, the L2 trigger takes advantage of the fact that they are different in the amount of energy they deposit in the calorimeters as well as their distinguishable shower width. As electromagnetic showers are smaller than hadronic showers, the finer granularity at the L2 stage allows to cut on this quantity.

Another huge advantage over the L1 trigger is the comprehension of the tracking information of the inner detector at L2. When an object has passed all calorimeter-based cuts, a track-finding algorithm is run, followed by a loose track-RoI matching. In a second step, the track-position is extrapolated to the calorimeter and compared to the one of the cluster to tighten the matching criteria even further.

The detailed algorithms that are applied by the second and third trigger stage will be discussed in Section 5.4.

5.3.3 Event Filter

The last trigger stage is the Event Filter (EF). Like L2, the EF mainly adopts the algorithms of the offline reconstruction; thus, the same remarks as for the L2 hold for the explanation of these. While the algorithms are almost the same, their technical application is different between reconstruction and EF.

Once an event has been recorded, the offline software accesses the whole detector-information for it, where the EF, similar to L2, makes use of the seeds of the previous trigger stage. It therefore runs the same algorithms for each given seed and only for this specific part of the detector. The window size used for clusters in the EF is $\Delta\eta \times \Delta\phi = 0.125 \times 0.125$.

Compared to L2, the track reconstruction in the EF is greatly enhanced. Whilst L2 only used rudimentary track-finding algorithms, EF algorithms come close to the ones from offline reconstruction. However, some time-consuming steps have been skipped in the trigger. Another advantage of the EF over L2 is the more detailed calibration and alignment information at this stage. Finally, the electron identification is improved at the EF stage: the classification in *loose*, *medium* and *tight* electrons has been adopted from the offline reconstruction, as well as most of the cuts that will be introduced in Section 5.5.

5.3.4 Trigger Menus

Since this analysis concentrates on simulations of very early data, trigger menus will be discussed for this early period. This means low trigger thresholds and menus dedicated to examine Standard Model physics. With higher luminosities later on, lower trigger thresholds will not be kept in order to comply with the fixed overall output rate. The menus will then allow to select specific signatures of rare processes and physics beyond the Standard Model.

Trigger menus consist of various trigger chains (or "signatures"), to allow the selection of different processes. The choice of items in the menu has to respect the overall output rate of each trigger stage. Thus, the sum of all contributing rates must not exceed ≈ 75 kHz for L1 and ≈ 200 Hz for the HLT, respectively. An excerpt of a trigger menu for early running ($L = 10^{31}$ cm^{-2}s^{-1}) is shown in Table 5.3.

When looking at the relevant trigger items for early analysis at ATLAS, `e10` and `2e5`, it is obvious that such low thresholds cannot be kept for higher luminosities in later LHC-operation, as the output rate of the trigger would be too high. As the di-electron trigger uses lower threshold and is also used to trigger on J/Ψ events, the `e10` trigger chain is preferred.

5.4 Electron Reconstruction

Within ATLAS, objects named as "reconstructed electrons" have to be separated from the term "identified electrons". Latter are a subset of reconstructed electrons and are going

Signature	**L1 rate (Hz)**	**HLT rate (Hz)**	**Comments**
Minimum bias	Up to 10000	10	Pre-scaled trigger item
e10	5000	21	$b, c \to e$, W, Z, Drell-Yan, $t\bar{t}$
2e5	6500	6	Drell-Yan, J/ψ, Υ, Z
γ20	370	6	Direct photons, γ-jet balance
2γ15	100	< 1	Photon pairs
μ10	360	19	W, Z, $t\bar{t}$
2μ4	70	3	B-physics, Drell-Yan, J/ψ, Υ, Z
μ4 + J/$\psi(\mu\mu)$	1800	< 1	B-physics
j120	9	9	QCD and other high-p_T jet final states
4j23	8	5	Multi-jet final states
τ20i + xE30	5000 (see text)	10	W, $t\bar{t}$
τ20i + e10	130	1	$Z \to \tau\tau$
τ20i + μ6	20	3	$Z \to \tau\tau$

Figure 5.3: Trigger menu for an instantaneous luminosity of 10^{31} cm^{-2}s^{-1} during early data taking at ATLAS. Table taken from [3].

to be discussed in the next section. Here, the (standard) algorithm for the reconstruction process is explained, which is used for non-low-p_T electrons.

Seed clusters. The electron reconstruction uses the—already described—sliding window algorithm to look for local E_T-maxima in the calorimeter ($E_T > 3$ GeV). The window size is $\Delta\eta \times \Delta\phi = 0.125 \times 0.125$, as five cells in the second sampling are combined in each direction[3]. Each of the so found clusters is used as a seed to look for a loosely matching track from the Inner Detector. Additionally, the $E_{\text{cluster}}/p_{\text{track}}$ ratio is required to be less than 10. Even if these criteria are quite weak, a few percent of real electrons are lost at this stage due to the traversed material in the ID.

If the loose track-cluster matching fails, the cluster is considered to be a photon, rather than an electron. However, this might also happen for electrons which emit hard bremsstrahlung and is one source of possible inefficiencies.

The track reconstruction works in three steps (see Reference [3] for details): the preprocessing, where the raw information is transformed to space-points within the subdetectors; the track-finding itself; the post-processing, where primary and secondary vertices are reconstructed and possible photon conversions are being considered.

Track finding. The track-finding algorithm uses an inside-out and, like the cluster-finding, a seeded approach: starting with the hits in the Pixel Detector and a hit in the first SCT-layer, a proto-track is formed and propagated through the rest of the SCT. If further space-points from the pre-processing can be assigned to it, a track-candidate is found. Now, fits are applied, ambiguities are removed and the algorithm tries to reject fake tracks. With the surviving track-candidates, an extrapolation into the TRT tries to associate hit-points with them and, if successful, a fit with information of all three sub-detectors is run to ensure the quality of the track.

---

[3] this is only valid for the detector's central region, $|\eta| < 2.5$.

Final cluster reconstruction. Subsequent to the track-matching and, hence, after the classification as electron or photon, the full cluster reconstruction is run in order to apply specific algorithms for the given particle.

In this final step of particle reconstruction, the algorithm has to account for all corrections that have to be applied, since both, position and energy measurements are distorted by different factors, which now will be briefly discussed (see Reference [4] for details).

The *position* of a cluster, measured in η and ϕ, is defined as the ϕ-coordinate of the second sampling and a weighted average of the η-coordinate of the first and second sampling, *after* corrections. In η, a particle would have a fixed value in each of the calorimeter samplings, if its vertex is the origin of the detector. As this is generally not the case, a “depth” has to be assumed for each sampling. Due to the finite granularity, the energy measurement in each cell is biased, dependent on where the particle actually hits a cell. This leads to an effect referred to as “S-shape” and has to be parametrized for each region of the calorimeter specifically, as the shape of the cells varies. In ϕ, the “S-shape” effect would also occur, but in this coordinate, the accordion structure of the calorimeter diminishes it due to the increased energy sharing between adjacent cells. The bias in ϕ that is introduced by the (η dependent) shower-depth is symmetric.

For the *energy* of a cluster, it is not sufficient to simply add the energy depositions within the electromagnetic calorimeter, but also account for energy losses *before* and remaining energy *after* it. Currently, two competing methods can be used to apply the energy-corrections: the default “4-weight method” and the “calibration hit method”.

The *4-weight method* is named after the number of free parameters in the fit to get the reconstructed cluster energy[4]:

$$E_{\text{reco}} = A(B + W_{\text{PS}} E_{\text{PS}} + E_1 + E_2 + W_3 E_3)\,, \tag{5.1}$$

with E_{PS}, E_1, E_2 and E_3 as the measured energy in the Presampler (PS) and the three samplings of the electromagnetic calorimeter, respectively. For each η region, defined by the granularity of the second sampling, a minimisation of the term

$$\chi^2 = \frac{(E_{\text{true}} - E_{\text{reco}})^2}{\sigma^2(E_{\text{true}})} \tag{5.2}$$

---

[4] the formula shown here is slightly altered for the transition region between barrel and endcap, but as the principle of the method stays the same, it is not discussed, here.

is used to determine the overall scale A, the offset due to fatal energy-loss before the PS, B, the weight to account for losses before the PS, W_{PS} and the correction for energy that leaves the calorimeter, W_3, applied to the energy measured in the third sampling. In Equation 5.2, single particle simulations (for electrons and photons separately) have been used, with $\sigma^2(E_{\text{true}})$ as the expected energy resolution.

To understand the impact of the ϕ position on the measured energy, one has to recall the accordion structure of the calorimeter: the amount of passive absorber material the particle encounters fluctuates periodically with the position it hits. Thus, the reconstructed energy varies, too. In η, the situation is much the same as for the formerly discussed correction of the position: as the cells (in the second sampling) have quadratic layout, the more energy is deposited in a single cell the closer the impact is to the cell's center. It is obvious that a correction can be done by a quadratic function.

Once arrived at this point, an electron in ATLAS is *reconstructed*, while in the next step, quality criteria can be applied to categorise it. This is necessary due to the fact that the signal to background ratio is still bad at this point.

5.5 Electron Identification

The electron identification is divided in three classes to allow for different requirements on signal efficiency and background suppression. Each class consists of a set of various cuts that are changeable within the reconstruction software.

An electron is either identified as *loose*, *medium* or *tight*, where the medium criterion includes the loose cuts as well as the tight identification includes both, loose and medium cuts. Whilst medium and tight criteria use information from the whole detector, the loose identification makes only use of cuts on calorimeter variables due to latency restrictions and the complexity of the tracking system. When discussing these classes, one has to keep in mind that with tighter cuts the background suppression improves, but at the cost of a worse signal efficiency, meaning that also real electrons might be rejected.

As QCD events are the main source of background, the three classes are optimised to give the best signal efficiency and jet rejection:

- *loose* selection: cuts on shower shapes in the second sampling of the electromagnetic calorimeter and cut on hadronic leakage

- *medium* selection: track-quality cuts, improved cuts on shower-shapes, inclusion of first sampling (important for π^0-suppression)

- *tight* selection: cuts on the number of TRT-hits, the E/p-ratio and vertex-layer hit, $\Delta\phi$-cut between track and cluster

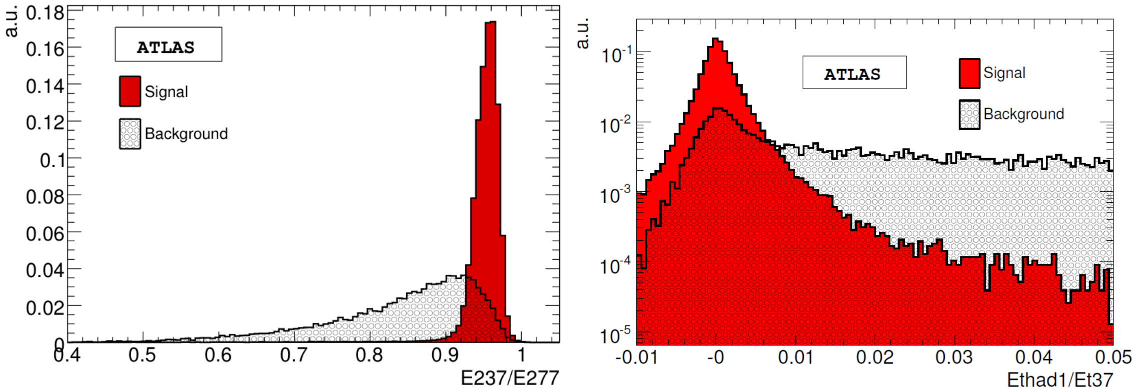

Figure 5.4: Signal ($Z \to e^+e^-$ sample with $E_T > 15$ GeV and $|\eta| < 2.4$) and hadronic-background separation for two discriminating variables. Left: cluster-width in second sampling of the electromagnetic calorimeter. Right: leakage of electromagnetic clusters in the first compartment of the hadronic calorimeter. Figures taken from [2].

Most of the cuts have an η and/or ϕ dependency to account for the varying amount of material in different regions of the detector. As the flexibility of the reconstruction software allows the changing of the ingredients of the classes, Table 5.1 shows the implementation of the electron identification that has been used within this analysis. Due to the geometric dependency of most of the criteria, no specific cut values can be given in this context (see Reference [14] for details).

Figure 5.4 shows the discrimination of signal and background for two variables given in Table 5.1. The left plot shows the ratio of the energy[5] deposite in the second compartment of the electromagnetic calorimeter in 3×7 cells and 7×7 cells around the barycenter of the cluster, denoted as R_η in the table. If an object causes only small lateral showers, the distribution should peak near zero as almost all of the total cluster energy is contained already in the smaller window. Since electrons fulfil this criterion whilst hadrons usually cause broader showers, background suppression is possible by introducing a cut-off at a ratio where almost none of signal-electrons are located.

The plot on the right in Figure 5.4 gives the energy deposition in the first compartment of the hadronic calorimeter divided by the total energy-deposit in the electromagnetic calorimeter, given as h_{leak} in Table 5.1. As it is the purpose of the electromagnetic calorimeter to completely contain the energy of electrons and photons, the leakage of their showers into the hadronic calorimeter should be small compared to the energy deposit of hadrons. As it is shown, the distribution peaks at zero for signal electrons and drops sharply with increasing energy contributions in the hadronic part of the calorimeter. This allows a sufficient discrimination to hadronic objects, for which the distribution is almost

---

[5] in this section, the expression “energy” always means transverse energy, E_T

	Description	Variable
loose	overall acceptance: $\|\eta\| < 2.47$	acc
	hadronic leakage: ratio of E_T deposition in the first compartment of the hadronic calorimeter (HAD) and E_T deposition in the electromagnetic calorimeter (EM)	h_{leak}
	shower shape: rapidity ratio of cell energies in 3×7 over 7×7 cells	R_η
	shower shape: azimuthal ratio of cell energies in 3×3 over 3×7 cells	R_ϕ
	shower shape: lateral width of the shower	weta2
medium	EM: energy fraction in the first layer	f_1
	EM: energy difference of 2nd largest energy deposition and the minimum between the 1st and 2nd maximum	ΔE_s
	EM: shower width in first layer	wtots1
	EM: shower width in first layer around most energetic cell	weta1
	EM: second largest energy deposition, normalised to cluster energy	Rmax2
	EM: total shower width	wstot
	EM: shower width of 3 strips around central one	ws3
	EM: energy fraction outside 3-strip core but within 7 strips	F_{side}
	Track Quality (TQ): number of hits in the PD	n_{px}
	TQ: sum of hits in the PD and SCT	n_{si}
	TQ: closest approach of track and vertex	A_0
tight	b layer: number of hits	n_{bl}
	Track Matching (TM): difference in rapidity of cluster and track	$\Delta\eta$
	TM: azimuthal difference of cluster and track	$\Delta\phi$
	TM: ratio cluster energy over track momentum	$\frac{E_{\text{clus}}}{p_{\text{track}}}$
	TRT: number of hits	n_{TRT}

Table 5.1: Listing of the electron-identification criteria, leading to the classification *loose*, *medium* and *tight*. The given set of definitions is applicable to release 14 of the ATLAS reconstruction software. The specific cut criteria are mostly η and/or ϕ dependent, see Reference [14] for details.

ID level	Signal Efficiency (%)	Jet Rejection Factor
loose	87.9 ± 0.5	570 ± 10
medium	76.7 ± 0.5	$2{,}200 \pm 20$
tight	61.3 ± 0.5	$(8 \pm 1) \cdot 10^4$

Table 5.2: Signal efficiency (from a simulated $Z \rightarrow e^+e^-$ sample) for electrons with $E_T > 17$ GeV, and jet rejection. Numbers taken from [3].

constant.

Again, requiring certain conditions to be fulfilled for electron identification is always a trade-off between signal efficiency and background rejection. Table 5.2 shows the two variables for (reconstructed) electrons with $E_T > 17$ GeV: each electron from the signal sample pass the medium identification cut in 87.5% of all cases, leading to a total identification efficiency of 76.7% for the Z event. The very good jet suppression of $\approx 2{,}200$ for the medium criterion, however, has an eminent negative impact on this analysis. Since two mis-identified jets are needed to survive the signal selection criteria (see Chapter 7), a total of $\gtrsim 4 \cdot 10^6$ events need to be generated in order to let one QCD background event survive the selection.

With a simulation rate of $\gtrsim 10$ min per event, it is obvious that a sufficiently large QCD sample cannot be simulated. Hence, the analysis will skip the identification cuts and perform a re-weighting instead.

Part III

Analysis

6

Single-Electron Efficiencies

6.1 Introduction

In Chapter 5, the way an electron[1] traverses ATLAS, being triggered on and, in the end, becoming reconstructed by the software, has been discussed in detail. But even with the most sophisticated trigger-algorithms and reconstruction software, a part of these electrons will not fire the trigger or be dismissed in the reconstruction or identification process. These falsely rejected electrons cause *inefficiencies*, which have to be known precisely in order to be able to account for them by applying corrections, e.g., for the cross-section determination.

The reasons that lead to inefficiencies are manifold and depend on their location within the reconstruction chain. For example, the reason for the identification of an electron to fail can be just one more hit required in the TRT or an insufficient E/p ratio due to fatal bremsstrahlung. All of the criteria that are applied by the trigger or the reconstruction software have in common that they should accept the signal whilst rejecting as much background as possible. Thus, it is always a trade-off between these two quantities: signal efficiency versus background rejection.

Within this chapter, some of the methods, which can be used to determine the inefficiencies that might occur, are described, with the focus on a data-driven approach called the *tag and probe* method. It is suitable to study inefficiencies on single-particle level and hence helps to determine systematic uncertainties on the efficiencies that can be derived only from simulation. As a start, energy and spatial resolutions for electrons within ATLAS and their impact on the binning will be analysed, followed by general ideas and concepts for the determination of efficiencies and the specific cuts that were applied within the analysis. The chapter will be concluded by the presentation and discussion of the results and the systematic uncertainties, which have been considered.

---

[1] if not explicitly stated otherwise, the term “electron” always accounts for both, electron and positron

6.2 Electron Resolution and Binning

If one imagines a perfect detector for particle physics, it would be able to measure parameters like energy and trajectory of a particle almost perfectly without any differences to its truth values. But in real life there are many factors that limit the precision of the measurement, thus contributing to a worse resolution in the variable of interest. Energy measurement suffers from effects like energy loss in front of the calorimeter, whereas impacts on the spatial resolution are such as multiple scattering, cell granularity, limited read-out channels (and hence limited granularity as well) and so on.

The resolution has a direct impact on the binning that will be used throughout the main part of this analysis, as the resolution gives a lower limit to the reasonable size of a bin in the variable of interest. In order to study the resolution for electrons, the $Z \rightarrow e^+e^-$ signal sample that was introduced in Chapter 4 has been used exclusively. In the following, resolution studies are presented for the transverse energy (E_T) and the pseudorapidity (η) of the reconstructed electron. The resolution of each variable is determined in bins of E_T^{truth} and $|\eta^{\text{truth}}|$.

6.2.1 Energy Resolution

The energy resolution is a measure of how strong the measurement of the energy fluctuates around the truth[2] value. It is conventionally parametrised as

$$\frac{\sigma(E)}{E} = \frac{a}{E} \oplus \frac{b}{\sqrt{E}} \oplus c\,. \tag{6.1}$$

The three parameters are as follows: a is the *noise term* that gives a constant contribution due to effects from the electronics or from radioactive decays. It dominates for low energies and usually becomes negligible for higher energies. The *sampling term* b accounts for statistical fluctuations in the shower development as well as sampling fluctuations within the calorimeter. Not dependent on the energy is the parameter c, which is therefore called *constant term*. Effects like imperfect cell-calibration, non-linearities or inter-cell smearing contribute to this term. It dominates the resolution at high energies.

The energy resolution of the detector is determined as the difference between measured and truth energy divided by the latter:

$$\frac{\Delta E}{E^{\text{truth}}} = \frac{E^{\text{calo}} - E^{\text{truth}}}{E^{\text{truth}}}\,. \tag{6.2}$$

With only statistical effects contributing, the resulting distribution would be a Gaussian. For the energy response this is far from being true. As the electrons make bremsstrahlung

---

[2] when referring to “truth” parameters in this analysis, usually the particle’s properties on generator-level before detector simulation are meant. For data-taking, this information is given by the real parameters of the particles and thus inaccessible.

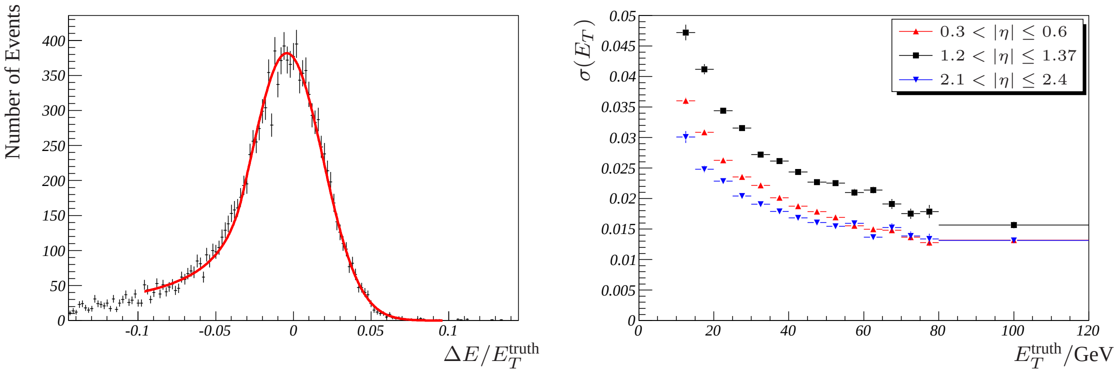

Figure 6.1: Left: example of a fit within a certain E_T^{truth}-η^{truth} bin with the Crystal-Ball function; $\sigma = (2.327 \pm 0.025) \times 10^{-2}$, reduced $\chi^2 = 101.3/86$. Right: resulting E_T resolution for different values of $|\eta|$.

in front of the calorimeter, the distribution becomes asymmetric due to the systematic measurement of lower energies for the electrons. Thus the longer tail towards lower energies.

Fitting Procedure, Crystal-Ball Function

To account for the asymmetry of the distribution, a "Crystal Ball" function[3] has been used to describe the spectrum. It consists of a Gaussian component with a power-law tail to low energies to parametrise the energy response of the detector (see Reference [52]):

$$f(x) = \begin{cases} N \cdot e^{\frac{(x-\bar{x})^2}{2\sigma^2}}, & \text{if } \frac{x-\bar{x}}{\sigma} > -\alpha \\ N \cdot \left(\frac{n}{|\alpha|}\right)^n \cdot e^{-\frac{\alpha^2}{2}} \cdot \left(\frac{n}{|\alpha|} - |\alpha| - \frac{x-\bar{x}}{\sigma}\right)^{-n}, & \text{otherwise} \end{cases} \tag{6.3}$$

Here, N is the normalisation factor and α the breaking point of the function. The breaking point is responsible for the transition between the two components. The left panel of Figure 6.1 shows an example for the fit to the distribution within 25 GeV $< E_T^{\text{truth}} \leq 30$ GeV and $0.3 < |\eta^{\text{truth}}| \leq 0.6$. The fit is performed for the whole E_T^{truth}-$|\eta^{\text{truth}}|$ plane, with the width σ being extracted as the resolution for the region.

Results

In order to visualise differences in the E_T resolution for different regions of the detector, results from the fits in the right panel of Figure 6.1 are displayed separately for a set of $|\eta|$ ranges. Common for each region is the characteristic improvement in resolution

---

[3] named after the Crystal Ball collaboration at *SLAC*

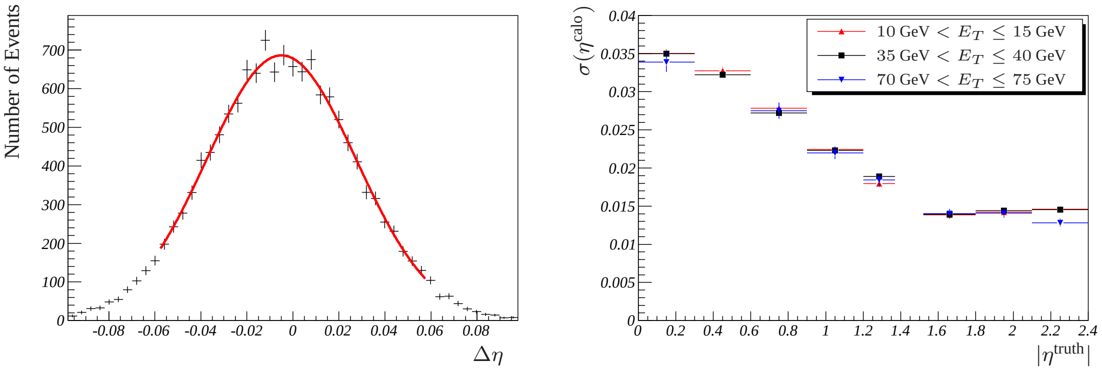

Figure 6.2: Spatial resolution for electrons in the electromagnetic calorimeter. Left: example of a resolution fit with the normal distribution; $\sigma = (3.255 \pm 0.038) \times 10^{-2}$, reduced $\chi^2 = 20.8/26$. Right: η^{calo} resolution for different E_T.

with increasing E_T, since fluctuations become less important at high energies. For low-E_T electrons the noise from the detector is of the order of their momentum, thus the resolution is worse. Clearly visible is the impact of the amount of material in front of the calorimeter: the energy resolution in the η-region close to the barrel-endcap transition ($|\eta^{\text{calo}}| \approx 1.3$) suffers the most from effects related to the material (see Figure 3.5) the particle has to pass before hitting the calorimeter.

The results show a very good agreement with the studies presented in Reference [4], which were also shown exemplarily in Figure 5.1.

6.2.2 Spatial Resolution

The second variable, which is important for this analysis, is the pseudorapidity η that denotes the polar angle of the particle's trajectory relative to the beam axis (see Equation 3.3). Each electron within ATLAS can be measured in two different ways regarding η: from the position of the track in the Inner Detector and from the position of the cluster in the calorimeter. In the following, the two η measurements are denoted as η_{track} and η_{calo}, respectively. Thus, the resolution will be determined independently for the two different parts of the detector, whilst the deviation of each measured η from the truth value is in both cases determined as:

$$\Delta\eta = \eta_{\text{measured}} - \eta_{\text{truth}} \,. \tag{6.4}$$

Like for the energy resolution, $\Delta\eta$ is calculated in bins of E_T^{truth} and $|\eta^{\text{truth}}|$.

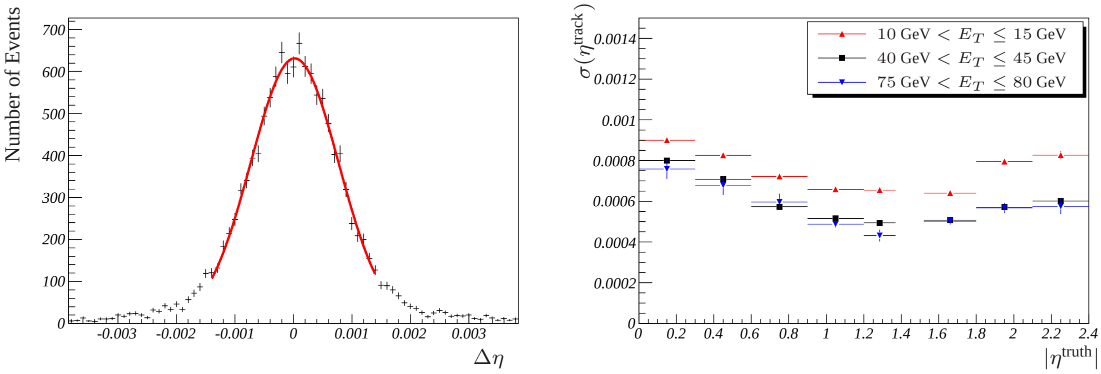

Figure 6.3: Spatial resolution for electrons in the tracking system. Left: example of a resolution fit with the normal distribution; $\sigma = (7.512 \pm 0.093) \times 10^{-4}$, reduced $\chi^2 = 27.1/24$. Right: η^{track} resolution for different E_T.

Fitting Procedure

As already mentioned, effects like bremsstrahlung do not distort the distributions obtained from Equation 6.4. Thus, the function used to fit the spectra is the normal distribution,

$$f(x) = N \cdot e^{\frac{(x-\bar{x})^2}{2\sigma^2}} , \tag{6.5}$$

with N as the normalisation factor. The width σ of the Gaussian thus gives the resolution of the bin.

The left panel of Figure 6.2 shows an example of the agreement between the fit and the $\Delta\eta$ distribution for 20 GeV $< E_T^{\mathrm{truth}} \leq 25$ GeV and $0.3 < |\eta^{\mathrm{truth}}| \leq 0.6$. The shift of the location of the maximum that can be observed in Figure 6.2 is caused by the granularity of the calorimeter. In comparison, a fit to the $\Delta\eta$ distribution in the same E_T^{truth}-$|\eta^{\mathrm{truth}}|$ bin is shown in the left part of Figure 6.3. No shift between the maximum of the distribution and the truth information of the particle is visible.

Results

When comparing Figures 6.2 and 6.3, the granularity of the electromagnetic calorimeter is mirrored in the resolution for the electrons. The resolution in the tracking system is $\sigma(\eta^{\mathrm{track}}) \approx 6 \times 10^{-4}$, whilst within the calorimeter the resolution is worse by almost two orders of magnitude, $\sigma(\eta^{\mathrm{calo}}) \approx 2 \times 10^{-2}$.

In addition to the different overall resolutions, the distributions show significant differences in shape and in their E_T dependence. In the Inner Detector, the resolution improves for higher values of $|\eta|$, reflecting the better track measurement with the growing length of the particle's trajectory in this area. At $|\eta| \gtrsim 1.0$, the increasing amount of material prevents a further improvement in the resolution, before it gets worse since the coverage of the TRT ends at $|\eta| = 2.0$. The transverse momentum of the electron has also an impact on the resolution (see Section 6.2.1). Low-E_T electrons ($E_T \lesssim 25$ GeV) face a constantly lower resolution due to multiple scattering and/or bremsstrahlung.

A different behaviour than the Inner Detector shows the η resolution for the calorimeter: as already mentioned, the coarser granularity of the calorimeter cells prevents a comparable resolution in η and is therefore almost two orders of magnitudes worse than the one from the tracking. As there is apparently no E_T dependence for electrons with $E_T > 10$ GeV, the resolution improves with higher values of $|\eta|$ and becomes constant at $|\eta| \gtrsim 1.5$ due to the fact that the amount of (dead) material in front of the calorimeter drops sharply for this region.

The very good spatial resolution of the inner detector makes it obvious to use the tracking variables instead of taking into account the calorimeter position of a cluster. However, when considering objects that can be detected in different parts within the detector—such as electrons with their tracking and calorimeter information—it is preferable to have a common set of variables, *all* particles that may cause a cluster can be described with. Thus, position and energy measurement from the calorimeter are generally used in this analysis, rather then mixing calorimeter and tracking information in case of electrons. As it will be shown in the next section, this does not have a negative impact on the analysis.

6.2.3 Electron Binning

In the following sections, many results will be presented in bins of cluster (electron) E_T or cluster (electron) η or in both, respectively. Choosing an appropriate binning in either variable depends on the expected amount of statistics per bin and the resolution for each variable.

With the results from the previous section, a lower limit can be set for the bin-sizes in E_T and η, as it would not be reasonable to enhance effects like bin migration, where a particle becomes reconstructed in another bin than it was originally generated due to imperfect detector resolution. This lower limit is given at $\gtrsim \sigma_{E_T,\eta}$, where σ is the resolution in the specific E_T or η bin, that has been determined in Section 6.2.

Although this analysis can revert to a sufficient amount of statistics from the signal sample, the artificial restriction to 100 pb^{-1} in order to “simulate” the feasibility of measurements in a very early phase of the ATLAS experiment has a huge impact on the bin sizes. As it turns out, this restriction forces bin sizes, which always fulfil the lower limit given above. In parallel to Reference [16], which also includes contributions from this analysis, the bin boundaries were chosen as follows:

$$\begin{aligned} E_T &= \{15, 20, 25, 30, 35, 40, 45, 50, 60, 120\}\ \text{GeV}\ , \\ |\eta| &= \{0, 0.4, 0.8, 1.37, 1.52, 2.01, 2.37\}\ . \end{aligned} \tag{6.6}$$

This results in a total of nine bins in E_T as well as five[4] $|\eta|$ bins.

6.3 Different Methods to Determine Efficiencies

As mentioned before, neither a detector recording nor a software analysing events from an experiment work with 100% accuracy. This trivial statement transferred to this analysis results in the fact that not every electron originating from a Z decay is detected or correctly reconstructed by the software to enter the analysis. If this happens for just one of both leptons, the whole Z event cannot be reconstructed.

These occurring (in)efficiencies have to be known precisely in order to account for them via corrections. In order to determine the inefficiencies appropriately, two methods that are completely independent from each other can be used. One is based on information taken from the simulation of the detector and is therefore named “Monte Carlo truth”. The other one is a data-driven approach and does not rely on the simulation, called “tag and probe” method.

With the arrival of data and hence in future analysis, the tag-and-probe method will be used to validate the simulation and/or estimate the systematic uncertainties on the efficiencies derived from the simulation. In the following sections, both approaches are first introduced in general. In a second step, their implementations and specific selection criteria will be shown in detail.

6.4 The “Truth Efficiency”

When simulating a physics event, all of the information about each participating particle can be saved and is therefore accessible within the analysis. As discussed in Chapter 4, the whole simulation chain is divided into three parts: the event simulation itself, the simulation of the detector response and the event reconstruction by the software. Important for the determination of the “truth” efficiency is the data from the first and the last step.

The data from the event simulation shows, which particles were created by the simulation, including the complete information about their vertices, momenta, etc. Furthermore, effects like initial or final state radiation can be studied. This information of what has been created can then be compared to what the simulated detector-response gives, and whether, for example, a “truth electron” has also been reconstructed by the software. In this way each efficiency like for the reconstruction, identification or trigger is accessible from the simulation.

---

[4] the bin at $1.37 \leq |\eta| \leq 1.52$ is not counted in this context as it represents the transition region from the barrel to the endcap region within the detector. All clusters (electrons) reconstructed in this region will not be taken into account for the rest of this analysis.

The starting point for each truth-efficiency determination are the clusters in the electromagnetic calorimeter in order to compare data-driven methods with simulation-based results later on. Otherwise, truth variables without detector-related effects would become compared to reconstructed variables.

6.4.1 Cluster Seeding

In Section 5.4 the way an electron is being reconstructed within ATLAS has been described. The starting point is a cluster, loosely matched to a track from the Inner Detector. In order to determine the truth efficiencies, one can also use the cluster objects to start from if one assumes that almost every truth particle causes a cluster object.

The verification that one truth electron has an associated cluster—or electron—object is done within the whole analysis via a cut on the distance between the objects in the η-ϕ plane. It is calculated as follows:

$$\begin{aligned} \Delta R &= \sqrt{(\Delta\eta)^2 + (\Delta\phi)^2}\,, \text{ with (in this case)} \qquad (6.7) \\ \Delta\eta &= \eta^{\text{clus}} - \eta^{\text{truth}}, \\ \Delta\phi &= \phi^{\text{clus}} - \phi^{\text{truth}}, \end{aligned}$$

If the distance between truth object and, in this case, cluster lies within 0.15, the cluster counts as matched to the truth electron. Figure 6.4 shows the probability, that a cluster object is matched to one of the two truth electrons. The overall probability, $\varepsilon_{\text{clus}} = \frac{N^{\text{clus}}}{N^{\text{truth}}}$, is 99.2%, with a decreasing matching-efficiency at lower E_T due to bremsstrahlung, which causes cluster to fail the minimal E_T criterion at 15 GeV. Even if the deviations from 100% are small, they have to be taken into account when discussing systematics at the end of this chapter.

At first glance, the matching of truth particles to clusters might not be necessary, as the efficiencies that will be discussed in the next sections could also be derived directly by a matching between truth electron and, for example, a reconstructed object. The reason for this “detour” is the fact that once clusters are associated to the truth particle, the parameters of interest can be expressed in cluster variables and hence are comparable to quantities that do not rely on information from the simulation, i.e., truth variables.

As the specific cuts will be shown in Section 6.6, only a brief overview of the efficiencies of interest is given here.

6.4.2 Reconstruction Efficiency

In order to avoid introducing a possible source for bias, each truth-electron will be considered separately for efficiency determination. Thus, the truth reconstruction efficiency

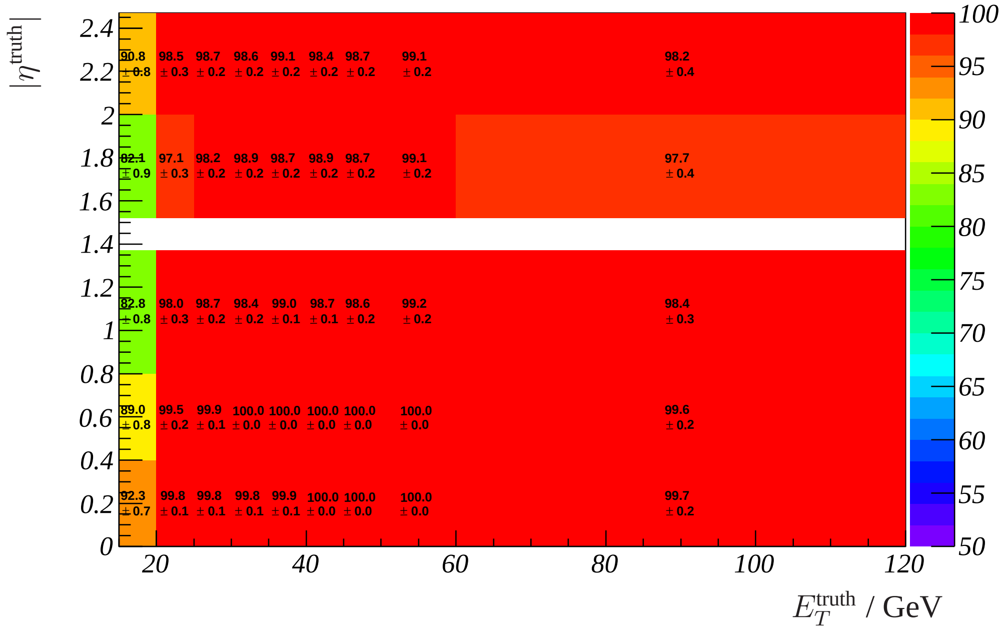

Figure 6.4: Probability that a cluster is matched to a truth electron from the $Z \rightarrow e^+e^-$ decay, including statistical errors. All values are given in per cent.

is defined as the ratio between objects that are reconstructed electron-candidates matched to the given cluster seed N^{reco} and all seed-clusters N^{clus}:

$$\varepsilon_{\text{truth}}^{\text{reco}} = \frac{N^{\text{reco}}}{N^{\text{clus}}} \,. \tag{6.8}$$

6.4.3 Identification Efficiency

Once an electron has been reconstructed, the algorithm categorises each electron with pre-defined cuts either as loose, medium or tight (see Section 5.5). Therefore, the identification efficiency is calculated with respect to the reconstructed electron:

$$\varepsilon_{\text{truth}}^{\text{ID, x}} = \frac{N^{\text{ID,x}}}{N^{\text{reco}}} \,, \tag{6.9}$$

where $N^{\text{ID,x}}$ can stand for each of the three identification categories.

6.4.4 Trigger Efficiency

Similar to the reconstruction efficiency, the trigger efficiency can be determined by a matching between the objects that build the quantity $N^{\text{ID,x}}$ and the positions of trigger-objects. Thus, if a trigger object is matched to the already identified electron, it contributes to the numerator of the following equation:

$$\varepsilon_{\text{truth}}^{\text{trig (ID), x}} = \frac{N^{\text{trig,x}}}{N^{\text{ID,x}}} \,. \tag{6.10}$$

Like for the various identification criteria, $N^{\text{trig,x}}$ can stand for each trigger stage, L1, L2 and EF. Due to the previously mentioned limitations of the used Monte Carlo sample, only the L1 efficiency can be determined in this way.

In order to determine efficiencies for single electrons, the trigger efficiency is commonly given with respect to the offline reconstruction:

$$\varepsilon_{\text{truth}}^{\text{trig (offline), x}} = \frac{N^{\text{trig,x}}}{N^{\text{reco}}} \,. \tag{6.11}$$

It depends on the problem whether to use the method given by Equation 6.10 or the one given by Equation 6.11.

6.5 The “Tag and Probe” Method

The ATLAS detector is fully simulated within the reconstruction software, so that the detector response of a simulated event is, in principle, fully predictable. Thus, the description of well-understood physics processes as well as, for example, the determination of efficiencies could naively be done completely within the simulation framework.

However, a particle detector, especially one of the size of ATLAS, cannot be build *perfectly*, with all parts at their planned location on the sub-millimeter level. Any possible offset has to be transferred to the simulation and might not be obvious until first data arrives. Beyond misalignment, missing or additional material in the detector can also lead to inaccurate results from the detector simulation.

During the phase of early data taking, misaligned detector-parts may not be reflected within the simulation, making it mandatory to derive such relevant information like the efficiencies also from data-driven methods, rather than having to rely on (maybe inaccurate) information from the simulation. For this reason, the tag-and-probe method is being used. With this method, trigger, reconstruction and identification efficiencies can be determined without taking the simulation into account.

The downside of a data-driven method is that a sufficient amount of data has first to be taken. Especially during the early period of the experiment the results from the data-driven approach will be used to estimate the systematic uncertainties on simulation-based analysis.

6.5.1 Basic Ideas

As the name of the method already suggests, two objects are needed to make this method work. The decay of the γ^{*}/Z interference into an electron-positron pair provides such objects: while one of them acts as the “tag”, the other one is used as the “probe” that will be tested for the condition(s) of interest.

An intrinsic “feature” of data is the lack of truth information. Thus, it is unclear whether a reconstructed electron originates from the decay of a Z boson or not. It is therefore important to tune the selection in a way that a sufficiently clean sample of two-electron events can be selected, whereas “clean” means that background-suppression should be as good as possible.

The first step is to select a “tag” object. For all reconstructed electrons, stringent cuts are applied in order to maximise the probability that it is in fact an electron. In anticipation of the sections to follow, the quality of background suppression is given by the tag selection, since the criteria for the second object have to be quite weak in order to prevent possible biases.

In a second step, for each of the tag electrons an object to “probe” is being looked for. The starting points are the cluster objects: when an electron traverses ATLAS, it almost certainly ($\geq 99\%$) leads to an associated cluster object, which becomes reconstructed by the software. The cluster has to pass a *preselection*, where kinematic and geometric requirements have to be fulfilled. The preselection is concluded by a cut on the invariant mass of the tag electron and the cluster: if the invariant mass is not within a window around the mass of the Z boson, the cluster is not considered to originate from an electron. Otherwise, the combination of tag and preselected probe enters the denominator to determine the efficiency. If it also fulfils the *probe requirement* that separates the different efficiencies (as discussed below), the combination of the tag and the probe enters the numerator as well. The tag-and-probe efficiency is then simply defined as

$$\varepsilon_{\text{tag and probe}} = \frac{N^{\text{tag+probe condition}}}{N^{\text{tag+probe preselection}}} \;. \tag{6.12}$$

As already mentioned, one has to account for background, too. Even if the tag-and-probe method is only applied to a simulated signal-only sample, in more than half of all events more than the two electrons from the Z decay are available after reconstruction. Thus, the tag-and-probe method cannot be used to naively “count” events that fulfil the criteria, but, in order to account for background, it uses the combined invariant mass of the tag and the preselected probe to fit the resulting spectra, where a separation of signal and background is possible. Then Equation 6.12 reads as follows:

$$\varepsilon_{\text{tag and probe}} = \frac{N^{\text{condition}}_{\text{selected}} - N^{\text{condition}}_{\text{background}}}{N^{\text{preselection}}_{\text{selected}} - N^{\text{preselection}}_{\text{background}}} \;. \tag{6.13}$$

This method is not restricted to inclusive spectra, it can also be used to determine the efficiencies in bins of E_T or $|\eta|$, or even double-differentially in E_T *and* $|\eta|$ of the probe. The limiting factor is the available amount of statistics, which should be large enough to ensure a stable fit.

The following paragraphs show the definitions of the efficiencies, similarly to the previously defined truth efficiencies.

Reconstruction Efficiency

In case of the reconstruction efficiency, the preselected probe is tried to be matched to an electron object. If the reconstructed electron is reasonably close to the preselected cluster, the probe requirement is fulfilled. The reconstruction efficiency is then defined as:

$$\varepsilon^{\text{reco}}_{\text{tag and probe}} = \frac{N^{\text{reco}}_{\text{sel}} - N^{\text{reco}}_{\text{bg}}}{N^{\text{preselection}}_{\text{sel}} - N^{\text{preselection}}_{\text{bg}}} \,. \tag{6.14}$$

Identification Efficiency

Reconstruction and trigger efficiencies can be defined with respect to the preselected cluster. Since an object that becomes identified either as “loose”, “medium” or “tight” is already reconstructed, the identification efficiency is necessarily defined with respect to the reconstructed electron:

$$\varepsilon^{\text{ID,x}}_{\text{tag and probe}} = \frac{N^{\text{reco+ID,x}}_{\text{sel}} - N^{\text{reco+ID,x}}_{\text{bg}}}{N^{\text{reco}}_{\text{sel}} - N^{\text{reco}}_{\text{bg}}} \,. \tag{6.15}$$

The “x” denotes the identification criterion. For the purposes of this analysis and to reflect the conditions during early data-taking, the medium identification-level will be used, if not stated otherwise.

Trigger Efficiency

With the very same procedure like for the reconstruction efficiency, the trigger efficiencies can be determined. In this case, the probe requirement is a ΔR-matched object at a certain trigger stage that passes an E_T-threshold which corresponds to the applied trigger chain. In anticipation of the part of this analysis that will be presented in Chapter 8, the trigger efficiencies are defined with respect to identified electrons:

$$\varepsilon^{\text{trig (ID), x}}_{\text{tag and probe}} = \frac{N^{\text{reco+ID+trig,x}}_{\text{sel}} - N^{\text{reco+ID+trig,x}}_{\text{bg}}}{N^{\text{reco+ID}}_{\text{sel}} - N^{\text{reco+ID}}_{\text{bg}}} \,, \tag{6.16}$$

where “x” denotes the trigger stage (L1, L2 or EF). The efficiencies for L2 and EF might also be calculated with respect to the previous trigger stage, where the denominator in Equation 6.16 has to be adjusted accordingly. However, due to limitations in the available Monte Carlo sample this analysis can only access the information obtained by the level-1 trigger. With respect to the offline reconstruction, Equation 6.16 reads as follows:

$$\varepsilon^{\text{trig (offline), x}}_{\text{tag and probe}} = \frac{N^{\text{reco+trig,x}}_{\text{sel}} - N^{\text{reco+trig,x}}_{\text{bg}}}{N^{\text{reco}}_{\text{sel}} - N^{\text{reco}}_{\text{bg}}} \,. \tag{6.17}$$

6.5.2 “Truth Matched” Tag-and-Probe Efficiencies

When only dealing with the signal sample, one might assume that background is not involved in this kind of analysis. However, as the simulation of the process within the Monte Carlo generator also considers effects like bremsstrahlung and hence not only passes the e^+e^- pair to the detector simulation, there are usually more than two electrons that become reconstructed by the software. Thus, it can happen that at least one of those additional electrons might pass the selection criteria, either for the tag or for both, the tag and the probe. In this case, they contribute to the, so called, “combinatorial background” of the signal sample, which is of the order of $\sim 1\%$.

In order to study possible impacts, the selection of tag-and-probe pairs can artificially be “cleaned” by matching the positions of the tag-and-probe objects to the η-ϕ parameters of the truth particles via a ΔR cut ($\Delta R < 0.15$). In this way only pairs that actually originate from the simulated Z decay survive the selection of the tag-and-probe pair.

6.6 Event Selection

In this section the algorithms to determine the various efficiencies will be explained in detail. The common part is first to define a denominator for the given efficiency, followed by applying a criterion to create a subset that defines the numerator. As mentioned earlier, using the same variables with cluster-E_T and cluster-η for truth and tag-and-probe efficiencies gives the advantage of much better comparability between the resulting distributions.

For the tag-and-probe study, each distribution is available either as inclusive (i.e. not binned in any variable), single differential (versus E_T or $|\eta|$), and double differential (in bins of E_T and $|\eta|$) spectra in the invariant mass of the tag-and-probe pair. In order to comply with the restriction to an integrated luminosity of 100 pb^{-1} when applying data-driven techniques within this analysis, a symmetry in the pseudorapidity variable is assumed, which allows to use only its absolute values.

6.6.1 Truth Efficiencies

After the general discussion in Section 6.4 of how to determine the truth efficiencies, the specific cuts are now presented. Since the efficiencies are determined on single-electron level, the electrons will be treated independently from each other, no matter if they are coming from the same Z boson or not. Possible biases that might be introduced due to kinematic entanglement of the particles coming from the same mother particle, are going to be discussed at the end of this chapter.

cut	requirement
barcode	$< 10^5$
particle ID	± 11
mother ID	± 23
status flag	1 or 3

Table 6.1: Cuts to select the electron-positron pair on generator level.

Within the simulation, the information about the generated particles before entering the detector simulation is accessible. Since this data not only contains information about the Z boson and the electron-positron pair but also includes many other particles ($\sim 1{,}000$) involved in the simulation, the pair of leptons from the Z decay has first to become selected. This selection follows the same procedure within the whole analysis and is described in the following paragraph, before the further discussion of the efficiencies continues.

Selection of the Truth Pair. The first step is to loop over all possible pairs of truth objects. Each particle has to have a *barcode*—which keeps track of the particle's history within a generated event—less than 10^5, meaning that later stages of a particle's history are rejected. The *particle's ID* must be ± 11, which is the PDG[5] code for an electron $(+11)$ or a positron (-11) in Monte Carlo generators like `PYTHIA`, as described in Reference [53]. Since these objects could originate from other processes or might come from photon conversions, the *mother's ID* must equal ± 23, which stands for a Z boson.

The *status flag* of a particle denotes whether or not it is stable. This is particularly important for the invariant mass spectrum of the two (truth) leptons, as events affected by final state radiation (FSR) have their invariant mass, $M(e^+e^-)$, shifted towards lower masses. Thus, the distinction can be made between a status flag of 3 (FSR possible) and 1 (stable). It depends on the purpose of the specific analysis, which value needs to be chosen.

With these criteria, the two leptons from the Z decay can be selected for each event on truth level. A summary of these cuts is shown in Table 6.1.

After selecting the truth electrons, the corresponding calorimeter objects have to be found. In order to find the cluster "belonging" to a truth object, the distance in the η-ϕ plane that is calculated via Equation 6.8 must not exceed 0.15. This happens to be the case for $\sim 99\%$ of the truth electrons (see Figure 6.4) when applying the following criteria: The matched cluster must have a minimal transverse momentum of 15 GeV,

---

[5] PDG: Particle Data Group

cut	requirement
matching	$\Delta R(\text{truth, clus}) < 0.15$
minimal momentum	$E_T^{\text{clus}} > 15$ GeV
maximal momentum	$E_T^{\text{clus}} < 120$ GeV
central object	$\lvert\eta^{\text{clus}}\rvert < 2.47$
crack exclusion	$1.37 < \lvert\eta^{\text{clus}}\rvert < 1.52$
reconstruction	$\Delta R(\text{clus, reco}) < 0.01$
identification	medium
Level-1 trigger	$\Delta R(\text{clus, RoI}) < 0.2$

Table 6.2: Cuts and requirements to determine the truth efficiencies.

while satisfying the condition for a central object, $|\eta^{\text{clus}}| < 2.47$. It must not be located within the transition region between barrel and end-cap hence $1.37 < |\eta^{\text{clus}}| < 1.52$ is excluded. The cutoff for high-E_T objects at 120 GeV ensures that no bias is introduced from clusters outside the highest-E_T bin and that always the same set of objects is being considered.

Once a cluster passes these criteria, it enters the denominator for the (truth) reconstruction efficiency, N^{clus}. In the next step, the cluster is studied to determine the various efficiencies.

By looping over all objects that have been reconstructed by the software as electrons, the distance of the cluster and the current electron has to fulfil the condition $\Delta R < 0.01$ in order to find the associated object. Since the electron and its associated cluster position is obviously the same[6], the cut value is chosen in a way that allows for possible rounding errors. Once a matching electron is found, it enters the numerator for the truth reconstruction efficiency, N^{reco}.

Based on these reconstructed electrons, which form the denominator (N^{reco}) of the identification efficiency, only one criterion has to be applied: by requiring the loose, medium or tight flag to be set, the electron enters the numerator of the appropriate identification efficiency, $N^{\text{ID},x}$, where x is a placeholder for the given flag. For the purpose of this analysis, the identification stages, which are shown with all entering criteria in Chapter 5, are treated as "black boxes", i.e. that effects from individual constituents of a certain flag are not considered.

Again, with the numerator of the previously described efficiency now acting as the denominator, $N^{\text{ID},x}$, a loop over all level-1 "regions of interest" (RoIs) that exceed the en-

---

[6] the position of the shower in the electromagnetic calorimeter can also be used as the one of the electron (see Section 6.2.2)

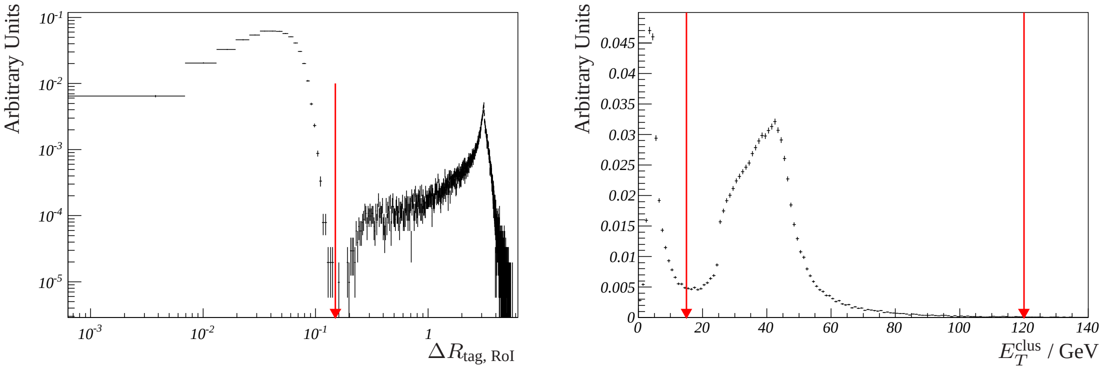

Figure 6.5: Examples of cuts to select a tag-and-probe pair, signal-only case. Left: distance between probe cluster and the regions of interest (RoIs). Right: E_T spectrum of the probe cluster.

ergy threshold of 7 GeV for the `e10_medium` trigger-chain compares their position to the successfully identified electron. To account for the coarser granularity of the first trigger stage, the matching criterion is relaxed to $\Delta R < 0.2$. If a level-1 object is successfully matched to the electron, it enters the numerator N^{trig} as well.

It should be emphasised again in this context that the determination of the truth efficiencies does not necessarily have to take the detour via the cluster matching. However, the advantage of the presented method is that all efficiencies of interest can be expressed in cluster variables and therefore in the same way as for the efficiencies determined from data-driven techniques, making comparisons more comfortable. The results for the truth efficiencies will be shown in Section 6.7.

6.6.2 Tag-and-Probe Method

As described in Section 6.5, the tag-and-probe method requires two objects to work. A tightly constrained tag object and a probe object that, together with the tag, originates most likely from a Z boson. That gives a high probability that both objects are indeed electrons.

The first step to find such a pair is to look for a tag object by looping over all offline reconstructed electrons. As each electron might be available twice within the event to account for analysis that include soft electrons, the *electron author* flag must be either 1 or 3 to avoid double counting. In order to comply with hard selection criteria, the trigger must have fired for this electron. This is assured by requiring a $\Delta R < 0.15$ cut between the tag candidate and a RoI that exceeds the transverse energy threshold of 7 GeV, which corresponds to the selected trigger item. Figure 6.5 shows the clean separation between level-1 objects associated to reconstructed electrons and other objects.

The second maximum at $\approx \pi$ indicates the preferred back-to-back topology of the decay.

The most important, since background-rejecting, cut is the electron identification requirement, which has to fulfil the “tight” criterion. In case of the QCD-sample, however, this cut is skipped as it would simply kill nearly all available events due to insufficient statistics in the initial sample (see Chapter 4). Instead, a suppression factor θ is calculated as the ratio of events with and without the ID cut, $\theta = \frac{N_2^{\text{tight}}}{N_1}$. The resulting distributions for the QCD-sample will be rescaled with this factor after applying the remaining criteria.

The transverse momentum cuts $E_T > 25$ GeV and $E_T < 120$ GeV, the limitation to the central part of the detector, $|\eta| < 2.47$, and the exclusion of the transition region, $1.37 < |\eta| < 1.52$ conclude the selection of the tag object. The minimal transverse-momentum cut can also be varied to reduce background even further, but at the cost of reduced statistics.

If the algorithm finds more than one tag electron within an event, all of them are kept to look for an adequate probe cluster, since this analysis focuses on possible studies with real data. A differentiation between signal and additional background electrons would only be possible in simulated samples. For each given tag a set of cuts is applied to each of the clusters within the event to find the probe. The only difference to the previously discussed kinematic and geometric cuts for the tag selection is the minimal E_T cut, which is relaxed to 15 GeV in order to cover as much phase-space as possible but to reject low-E_T electrons (see Figure 6.5).

The last step in the pre-selection process is the cut on the invariant mass of the tag and the probe, $M_{\text{tag, probe}}$. Whilst the probability for a cluster to be in fact an electron is highest for invariant mass pairs close to the Z mass, the window has to be chosen wide enough in order to allow a sufficient amount of background to enter the distribution. The latter assures an appropriate description of the background shape via fitting. Therefore, the invariant mass has to be in a window of 40 GeV $< M_{\text{tag, probe}} < 140$ GeV. Figure 6.6 shows the inclusive invariant mass spectrum after the pre-selection cuts. Whilst the contribution of combinatorial background to the signal is almost negligible, the QCD background dominates most of the spectrum.

After the selection of the probe cluster, the distributions obtained will be fitted (see Section 6.7) and the results enter the denominator in Equation 6.14. To get the distribution for the numerator, the cluster will now be “probed” for the appropriate condition.

For the reconstruction efficiency, all offline reconstructed electrons are tried to be matched to the cluster. This again happens via a ΔR cut, where the distance between electron and probe must not exceed 0.01. Responsible for this ostensibly tight criterion is the fact that the cluster position is also taken as the electron position in the calorimeter. The reconstructed events from the previous step are checked whether or not they pass the identification criterion. If the certain flag is set, the electron is identified as loose, medium or tight and enters the numerator Equation 6.15.

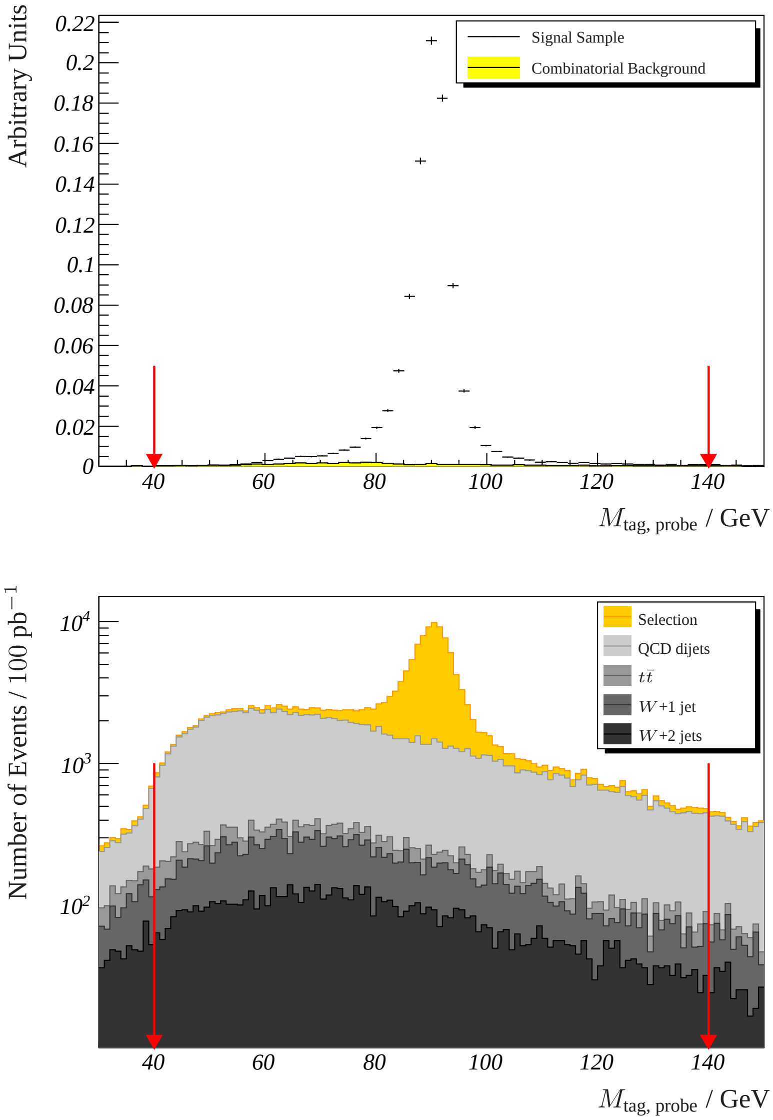

Figure 6.6: Invariant mass of the tag-and-probe pair after preselection. Top: signal-only sample. Bottom: combined sample with contributions from different backgrounds.

The ΔR matching is also applied to determine the trigger efficiency: here, the distance between RoI and the identified electron is required to fulfil $\Delta R < 0.2$ to account for the coarser granularity of the trigger information. The remaining, hence triggered, events enter the numerator in Equation 6.16.

A summary of all applied cuts is given in Table 6.3. Each invariant mass distribution is available inclusively, single-differentially (in bins of E_T and in bins of $|\eta|$) and double-differentially in bins of E_T and $|\eta|$. The truth efficiencies that have been derived from the signal-only sample make use of the whole statistics, whereas the combined sample, which consists of signal and background events, is limited (or scaled) to 100 pb^{-1}, in order to

	cut description	requirement
tag selection	electron author	1 or 3
	Level-1 matching	$\Delta R(\text{tag, RoI}) < 0.15$
	Level-1 threshold	$E_T^{\text{RoI}} > 7$ GeV
	min. momentum	$E_T^{\text{tag}} > 25$ GeV
	max. momentum	$E_T^{\text{tag}} < 120$ GeV
	central object	$\lvert\eta^{\text{tag}}\rvert < 2.47$
	crack exclusion	$1.37 < \lvert\eta^{\text{tag}}\rvert < 1.52$
	identification	tight
probe presel.	min. momentum	$E_T^{\text{clus}} > 15$ GeV
	max. momentum	$E_T^{\text{clus}} < 120$ GeV
	central object	$\lvert\eta^{\text{clus}}\rvert < 2.47$
	crack exclusion	$1.37 < \lvert\eta^{\text{clus}}\rvert < 1.52$
	invariant mass	40 GeV $< M_{\text{tag, probe}} <$ 140 GeV
condition	reconstruction	$\Delta R(\text{clus, reco}) < 0.01$
	identification	medium
	Level-1 trigger	$\Delta R(\text{clus, RoI}) < 0.2$

Table 6.3: Cuts to determine the efficiencies with the tag-and-probe method.

reflect an early stage of data taking in the ATLAS experiment.

6.7 Efficiency Determination

With the algorithms, which were presented in the previous section, the task is now to derive the efficiencies from the output. This output consists of the numerators and denominators of the considered method, namely truth, truth-matched tag-and-probe for the signal-sample and standard tag-and-probe for the signal-only and the combined sample. In case of the tag-and-probe method, each nominator and denominator is represented by the invariant-mass spectrum determined by the algorithms described in the previous section. For each method, the event numbers (truth) or invariant-mass spectra (tag-and-probe) are available inclusively, single- and double-differentially.

To calculate the efficiencies, two different approaches are considered, a trivial one and the standard way. When considering truth (or truth-matched) efficiencies, they are calculated just by building the ratios of the counted number of events. This can be justified by the total absence of background and the sufficient amount of statistics for the signal sample. This trivial approach cannot be applied to the tag-and-probe method, not even in the signal-only case: As it has been shown before, combinatorial background from additionally reconstructed electrons contributes to the invariant-mass spectra and has to be described adequate in order to determine the efficiencies correctly. The implications might be quite small while considering inclusive distributions (like shown for the signal-only case in Figure 6.6), but this does not necessarily have to be the case when looking at single- or double-differential distributions, where the impact of (combinatorial) background might change quite drastically depending on the transverse energy or η of the probe. Thus, a fit has to account for signal and background events separately.

After introducing the fitting procedure, the efficiencies and their comparisons will be presented for the inclusive case, for the single differential cases and as double differential distributions. In anticipation of Chapter 8 it should be emphasised in this context that the essential results are the one's from the double differential analysis, as they might be used later on as "look-up tables" for a re-weighting on event basis for the cross-section determination (see Chapter 7).

6.7.1 The Fitting Procedure

As mentioned before, many distributions have to be considered to derive an efficiency. A representative overview of them gives Figure 6.7, which shows the double-differential distributions for numerator and denominator of the reconstruction efficiency for the combined sample.

With the amount of distributions to fit, it is clear that one does not want to adjust fit parameters for each distribution individually, but to find a common description for almost all of them to minimise the need of subsequent fine-tuning. The basic idea is to add a function that describes the shape of the signal to a function for the varying background. The challenge is that the peak in the invariant mass is not only distorted by the detector response but might also be influenced for kinematic and geometric reasons. This is due to the breakdown of the (inclusive) invariant mass spectrum into certain E_T-$|\eta|$ areas, which has to be accounted for in the parametrisation of the fit.

Furthermore, as the line shape of the γ^*/Z resonance has three contributions (photon, interference and Z term), the contribution of the Drell-Yan continuum in the sidebands of the (on-shell) Z peak might be indistinguishable from background. In order to describe the shape over a broad range in the invariant-mass spectrum correctly, the fits cover a window of 60 GeV$< M_{\text{tag, probe}} < 120$ GeV, whilst the integral to determine the number of events has a range of 70 GeV to 110 GeV. The latter can be justified by the fact that the sidebands of a Z distribution below and above these thresholds contain less than 1% of the total number of events.

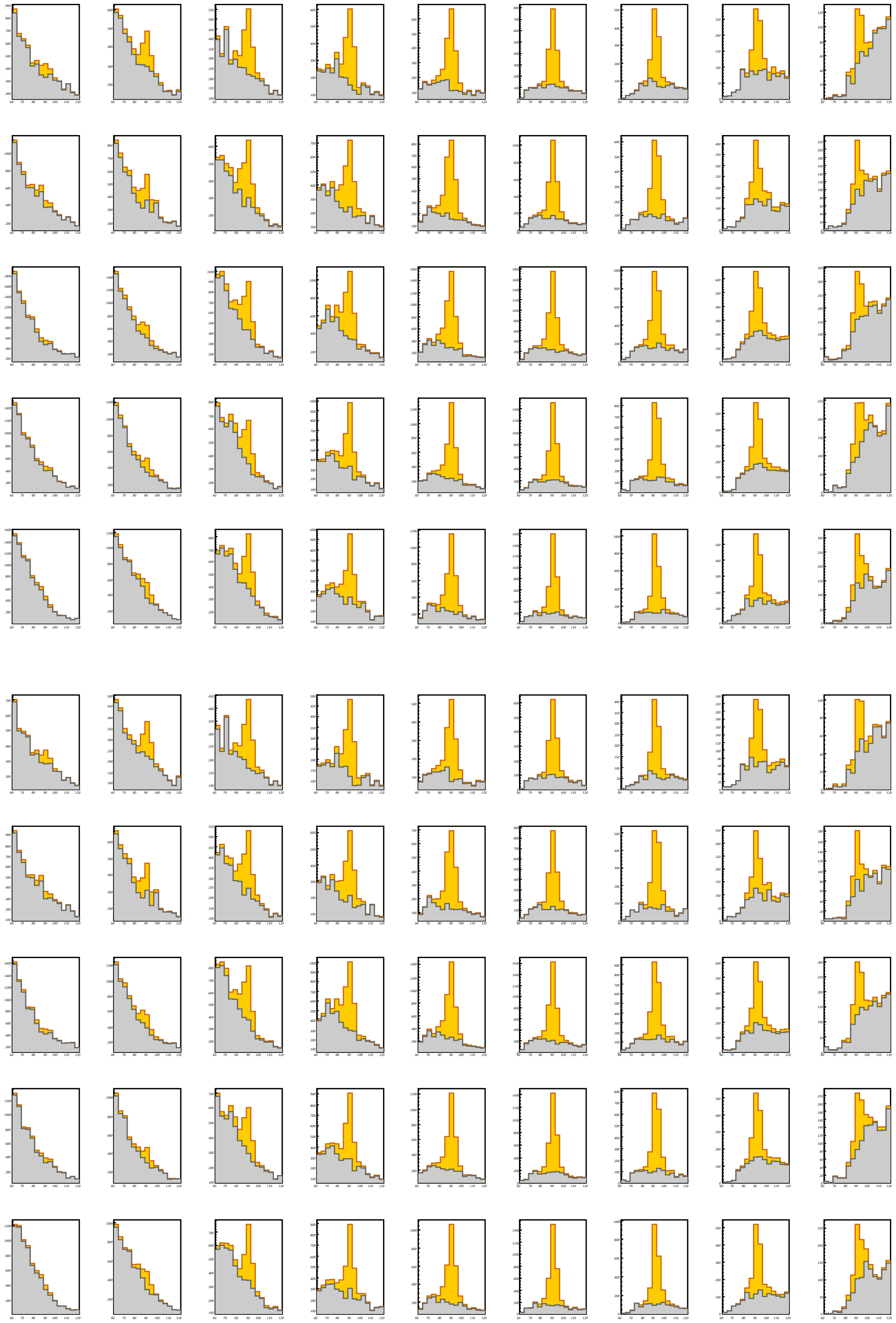

Figure 6.7: Invariant mass spectra (60 GeV $< M_{\text{tag,probe}} < 120$ GeV) in bins of E_T (horizontal) and $|\eta|$ (vertical) to determine the reconstruction efficiency via the tag-and-probe method. By fitting, the contribution of signal (orange) and background (grey) in each bin is determined (cf. Equation 6.14). Top: double-differential denominator. Bottom: double-differential numerator.

Signal Parametrisation

The accurate description of the invariant-mass spectra obtained from the analysis given in the previous sections in a fitting algorithm has to take care of the γ^*/Z lineshape and the treatment of the detector response. The implementation of the fitting algorithm follows closely Reference [50], which includes a similar analysis for the determination of the inclusive cross-section of the process $pp \to \gamma^*/Z \to e^+e^-$.

The line shape of the γ^*/Z can theoretically be described with the following formula (cf. Reference [42]):

$$\sigma(\hat{s}) \sim A \cdot \frac{1}{\hat{s}} \left(\frac{m_0}{\sqrt{\hat{s}}} \right)^{\beta} \left(f_{\frac{u}{d}} I_u(\hat{s}) + I_d(\hat{s}) \right) . \tag{6.18}$$

In this equation, $\hat{s} = x_1 x_2 s$ is the energy of the interacting partons, m_0 is the energy scale and β parameterises the impact of the PDFs on the line shape. The factor $f_{\frac{u}{d}}$ handles the ratio of up and down quark contributions to the cross-section and A is a normalisation constant. The physics of the process, including all three terms previously mentioned, is represented in the functions I_q (with $q = u, d$ either for the up or the down type quark):

$$I_q(\hat{s}) = \Xi_q^{\gamma} + \frac{\hat{s} M_Z^2}{(s - M_Z^2)^2 + \Gamma_Z^2 M_Z^2} \left[(\hat{s} - M_Z^2) \Xi_q^{\gamma Z} + \hat{s} M_Z^2 \Xi_q^{Z} \right] , \tag{6.19}$$

M_Z and Γ_Z represent the invariant mass and the width of the Z boson, where the Ξ_q^x are the coupling constants for photon, interference and Z term. They are defined as follows:

$$\begin{aligned} \Xi_q^{\gamma} &= Q_q \, , \\ \Xi_q^{\gamma Z} &= 2 Q_e Q_q (\xi_Z^{e_L} + \xi_Z^{e_R})(\xi_Z^{q_L} + \xi_Z^{q_R}) \kappa \, , \\ \Xi_q^{Z} &= 4 \left({\xi_Z^{e_L}}^2 + {\xi_Z^{e_L}}^2 \right) \left({\xi_Z^{q_L}}^2 + {\xi_Z^{q_L}}^2 \right) \kappa^2 \, , \end{aligned}$$

with $\kappa = \frac{\sqrt{2} G_F}{4 \pi \alpha} = \left(4 M_W^2 \sin^2 \theta_W \right)^{-1}$ and the fundamental quark and electron couplings defined in Section 2.2.2. It is not obvious that all parameters in Equation 6.18 are fixed except for two, the normalisation A and β, where the latter can be determined from fitting the invariant- mass distribution on generator level, to use it as another fixed parameter later on.

In order to account for the response of the detector, the “clean” description of the invariant mass distribution gets distorted by a convolution with a Crystal Ball function that has been introduced in Equation 6.3. This function is preferred over a simple Gaussian, as the power-law tail accounts for bremsstrahlung.

Background Parametrisation

As it has already been mentioned before, the varying shape of the background is a great challenge. Without an accurate estimation of background events in an invariant-mass distribution, the uncertainty on the efficiency grows large, as the underestimation would become compensated by the signal description and hence contributes twice.

The Landau distribution guarantees sufficient flexibility to describe the background in every bin and can numerically be expressed as:

$$p(x) = \frac{1}{\pi} \int_0^\infty e^{-t \ln t - xt} \sin(\pi t) \, dt \; . \tag{6.20}$$

Characteristic for this distribution is a turn-on behaviour and, after a maximum, an exponential decline. This is usually the case for the present invariant-mass spectra.

Even though background and signal can be accessed separately in this simulation-based analysis, the focus lies on the clean separation when taking the combined sample into account.

6.7.2 Inclusive Electron Efficiencies

Without differentiating in transverse momentum or direction of the electron, the inclusive distributions found with the criteria from Section 6.6 describe the total efficiencies, integrated over all E_T and η. In order to determine an efficiency, the distributions have to be fitted for denominator and numerator via the fitting functions presented in the previous section. The resulting fits for all efficiencies of interest are shown in Figure 6.8 for the signal-only case and in Figure 6.9 for the combined sample.

With a reduced $\chi^2 \approx 1$ for each of the fits it is clear that the superposition of Equation 6.18 and Equation 6.20 describes the invariant-mass spectra very well. However, even with strict limitations on most of the parameters, the contribution of the background can be difficult to estimate in data if it does not dominate in the sidebands. Examples for this case are the numerator of the identification efficiency as shown in Figure 6.9[7] as well as the signal-only samples with their combinatorial background. Alternatives on how to deal with this problem in data will be discussed in Section 7.7.

Also visible in this panel of Figure 6.9 as well as in Figure 6.8 is the impact of the restriction on the invariant mass, $M(ee) \geq 60$ GeV, on generator level. The fitting window was therefore chosen to cover invariant masses only above that threshold.

The results for the inclusive efficiencies are calculated according to Equations 6.14, 6.15 and 6.17, and are shown in Table 6.4. The deviations between the different methods are on the level of $\lesssim 1\%$ in case of the reconstruction and the level-1 efficiencies and thus show a good agreement. However, the inclusive identification efficiency derived with the tag-and-probe method for the combined sample shows a significant deviation. A possible source for this behaviour will be discussed in the next section. The given uncertainties in

---

[7] this distribution yields $\chi^2_{\text{selection}}/\text{ndf} = 1.21 \pm 0.10$ and $\chi^2_{\text{background}}/\text{ndf} = 1.31 \pm 0.12$, respectively. Even if this is the worst description of the selected and background event spectra, it is sufficient not to dominate the statistical uncertainty for the efficiencies

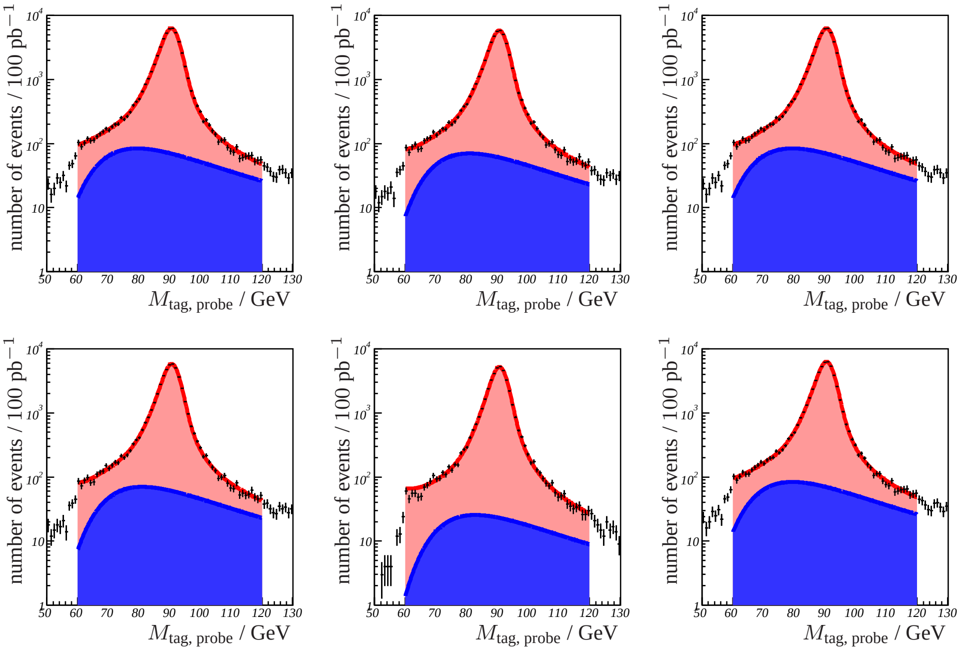

Figure 6.8: Fits to determine the inclusive efficiencies via the tag-and-probe method (signal-only case). From left to right: electron reconstruction, medium identification and level 1. First row: denominator. Second row: numerator.

		tag-and-probe method		
efficiency	truth	truth-matched	signal-only	combined sample
reconstruction	88.82 ± 0.02	90.02 ± 0.02	89.42 ± 0.28	90.00 ± 0.53
medium ID	87.25 ± 0.02	87.90 ± 0.02	88.35 ± 0.30	84.44 ± 0.61
level 1	99.88 ± 0.01	99.94 ± 0.01	99.94 ± 0.18	99.86 ± 0.49

Table 6.4: Inclusive electron efficiencies. The truth and truth-matched efficiencies utilise the full statistics of the signal sample, the signal-only (including combinatorial background) and the combined samples are limited to 100 pb^{-1}. The errors are statistical errors, only. All values are given in per cent.

Table 6.4 are calculated using Bayesian statistics and additionally via error propagation including uncertainties from the fitting parameters, if applicable.

6.7.3 Single Differential Electron Efficiencies

To demonstrate the behaviour of the efficiencies in dependence of one variable or another, the invariant-mass distributions are split into partial ranges of these variables. After fitting

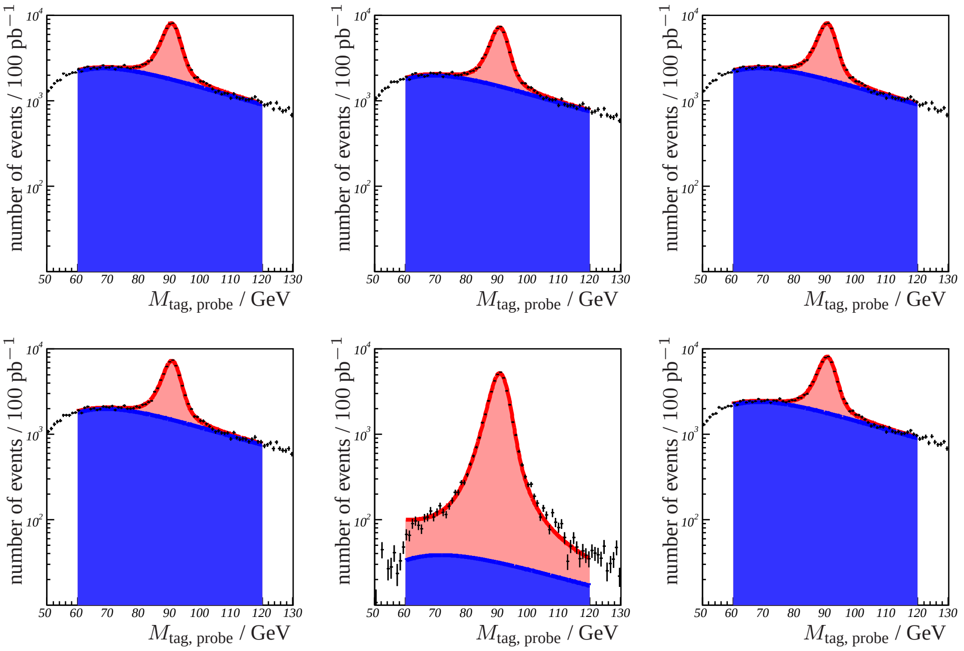

Figure 6.9: Fits to determine the inclusive efficiencies via the tag-and-probe method for the combined sample (first row: denominator, second row: numerator). From left to right: electron reconstruction, medium identification and level 1. In order to demonstrate the background-suppression for the ID criterion, the range of the y axis has been kept constant for all plots.

the eight[8] E_T and five $|\eta|$ distributions according to the approach outlined before, the resulting efficiencies are shown[9] in Figures 6.10, 6.11 and 6.12, where only statistical errors are given. Possible sources of deviations between the methods are going to be discussed in Section 6.8.

The reconstruction efficiency for single-electrons increases with the transverse energy of the particle, starting at $\varepsilon^{\text{reco}} \gtrsim 85\%$ and reaches a plateau at $\approx 90\%$. For central objects at $\eta \sim 0$ the reconstruction efficiency is excellent ($\approx 95\%$) and decreases due to (dead) material in front of the calorimeter. The different methods to determine the reconstruction efficiency show a very good agreement, especially with respect to $|\eta|$. However, the truth efficiency is $\lesssim 3\%$ lower for $E_T \geq 35$ GeV than the efficiencies derived via either of the tag-and-probe methods.

---

[8] due to the dominating background at the lowest-E_T bin (see Figure 6.7), it is hardly possible to differentiate between signal and background contributions in this kinematic region. Thus, this bin was not included in the single- and double-differential tag-and-probe analysis.

[9] like motivated before, the lowest-E_T bin, 15 GeV $< E_T \leq 20$ GeV, is not taken into account to determine efficiencies via the tag-and-probe method; nevertheless, the truth efficiency for this bin is given for reference

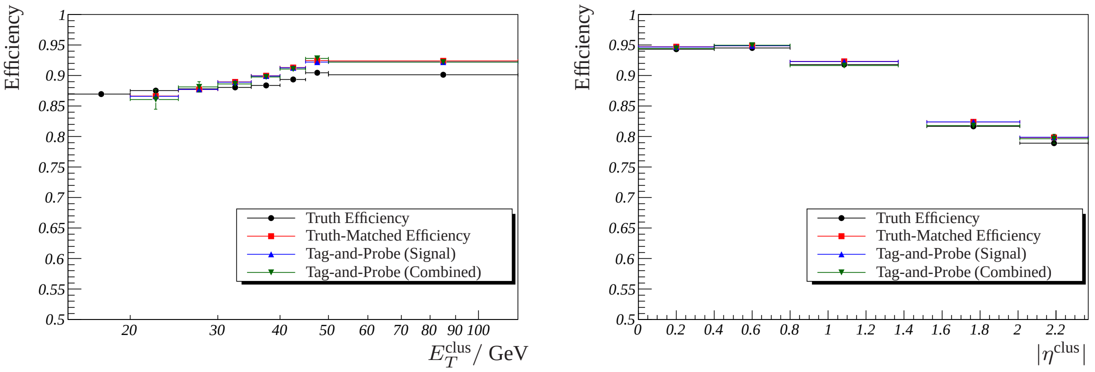

Figure 6.10: Single-differential reconstruction efficiencies for truth, as well as for the tag-and-probe method with and without truth-matching. Left: versus cluster-E_T (logarithmic scale). Right: versus $|\eta|$ of the cluster.

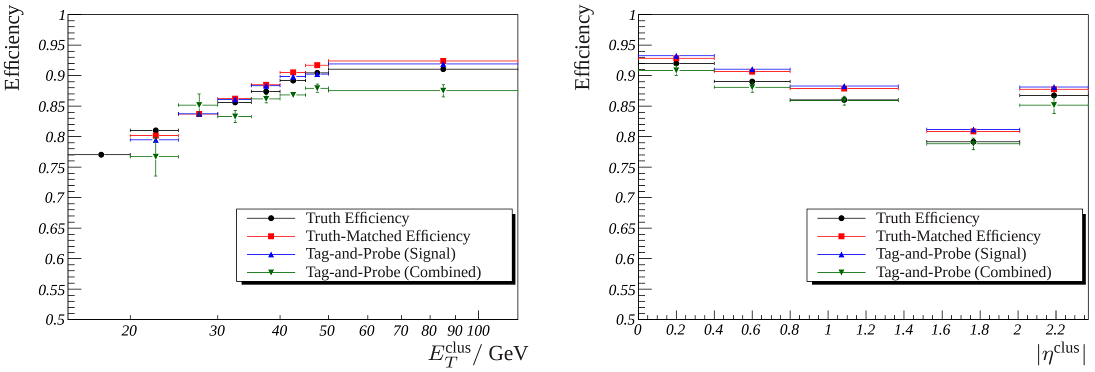

Figure 6.11: Single-differential medium identification efficiencies for truth, as well as for the tag-and-probe method with and without truth-matching. Left: versus cluster-E_T (logarithmic scale). Right: versus $|\eta|$ of the cluster.

The identification efficiency shows a similar behaviour as the reconstruction efficiency. With an increasing transverse energy of the electron, the efficiency improves. However, the turn-on of the efficiency starts at $\approx 75\%$ and reaches its plateau at $\approx 90\%$. When integrating over all energies and studying the identification efficiency versus $|\eta|$, it drops towards the forward region except for the outermost bin, where the efficiency is at the same level as before the crack region. The identification efficiency for the combined sample deviates significantly (up to 5%) from the other methods, clearest visible in the single-differential presentation versus E_T. Since this seems to be a unique behaviour of the combined sample without truth matching, the cause might be the improper description of the background shape after the rescaling (see Section 6.6.2).

The level-1 efficiency with respect to reconstructed electrons shows no differences for

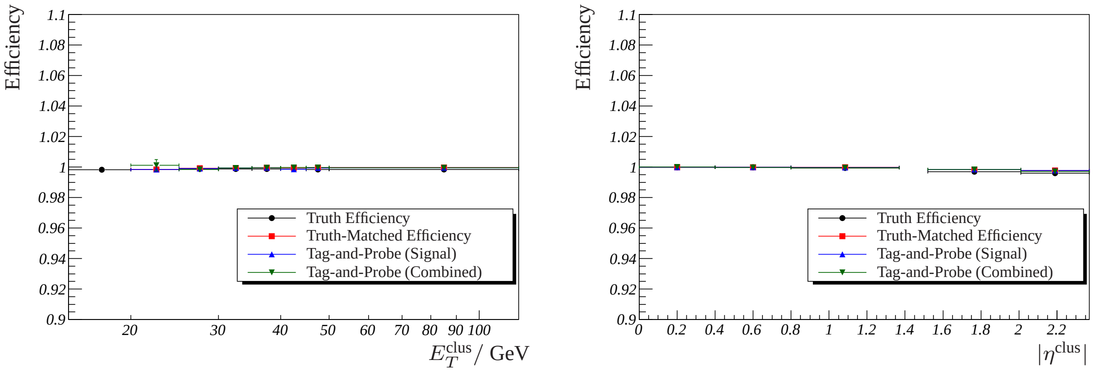

Figure 6.12: Single-differential level-1 trigger-efficiencies for truth, as well as for the tag-and-probe method with and without truth-matching. Left: versus cluster-E_T (logarithmic scale). Right: versus $|\eta|$ of the cluster.

the methods, it is approximately 100% for each distribution and agrees with the previously determined inclusive efficiency.

6.7.4 Double Differential Electron Efficiencies

The double-differential truth reconstruction efficiency is given in the top panel of Figure 6.13. The efficiency increases for high-E_T electrons and decreases from central to forward parts of the detector. Shown in the middle panel of the same Figure is the relative deviation of the truth-matched tag-and-probe method to the truth efficiency. As for the majority of bins in the E_T-$|\eta|$ plane the fluctuations are covered by the statistical uncertainties, it seems that the discrepancies increase with higher values of E_T and $|\eta|$.

The challenge for the limited combined sample is the low amount of the statistics per bin. As this analysis is restricted to an integrated luminosity of 100 pb^{-1}, the available number of events per bin drops to $\sim \mathcal{O}(10^3)$. Furthermore, the shape of the background varies extremely in the E_T-$|\eta|$ plane (cf. Figure 6.7), which makes it difficult to describe its contribution correctly in order to derive the correct efficiency for each bin. Nevertheless, the comparison to the truth efficiency works reasonably well for most bins (see bottom panel in Figure 6.13). The fluctuation lies within $\lesssim 2\%$. Significant deviations can only be observed in the two lowest-E_T bins and the highest E_T-$|\eta|$ bin.

The truth medium identification efficiency is shown in the top panel of Figure 6.14. It increases with higher transverse energies of the electron and decreases for higher pseudo-rapidity-regions. In agreement with the discussion of the single-differential distribution, however, the identification efficiency improves for the most forward bin, $2.0 \leq |\eta| < 2.47$. Obviously, the most distinct efficiency-minima occur for low-E_T electrons.

In comparison to the truth information, the tag-and-probe method seems to systemati-

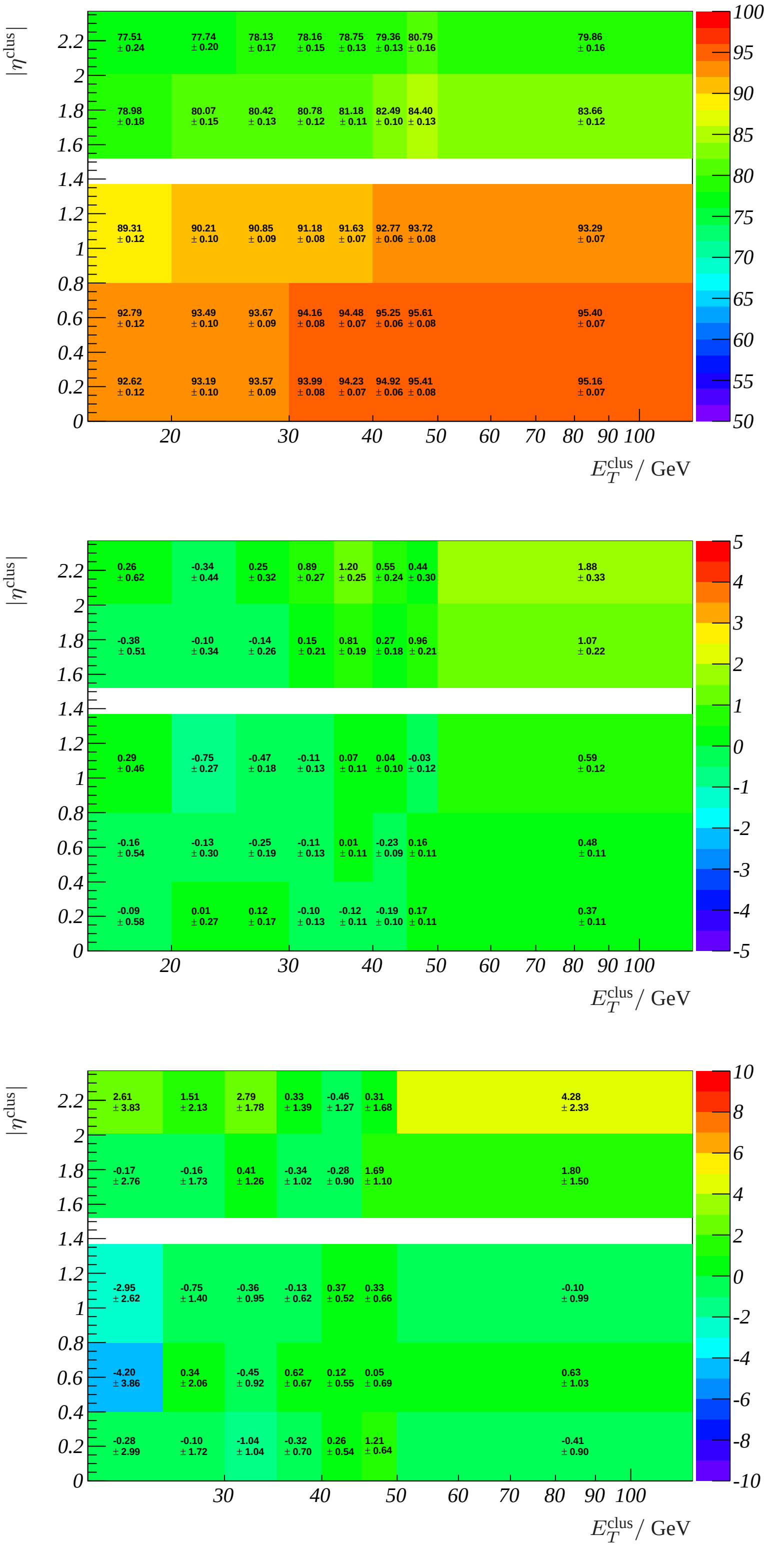

Figure 6.13: Double differential reconstruction efficiencies. Top: truth efficiency. Middle: relative deviation of the truth-matched tag-and-probe method (full statistics) and the truth efficiency. Bottom: relative deviation of the tag-and-probe method (combined sample, $100\ \mathrm{pb}^{-1}$) and the truth efficiency. All values are given in per cent.

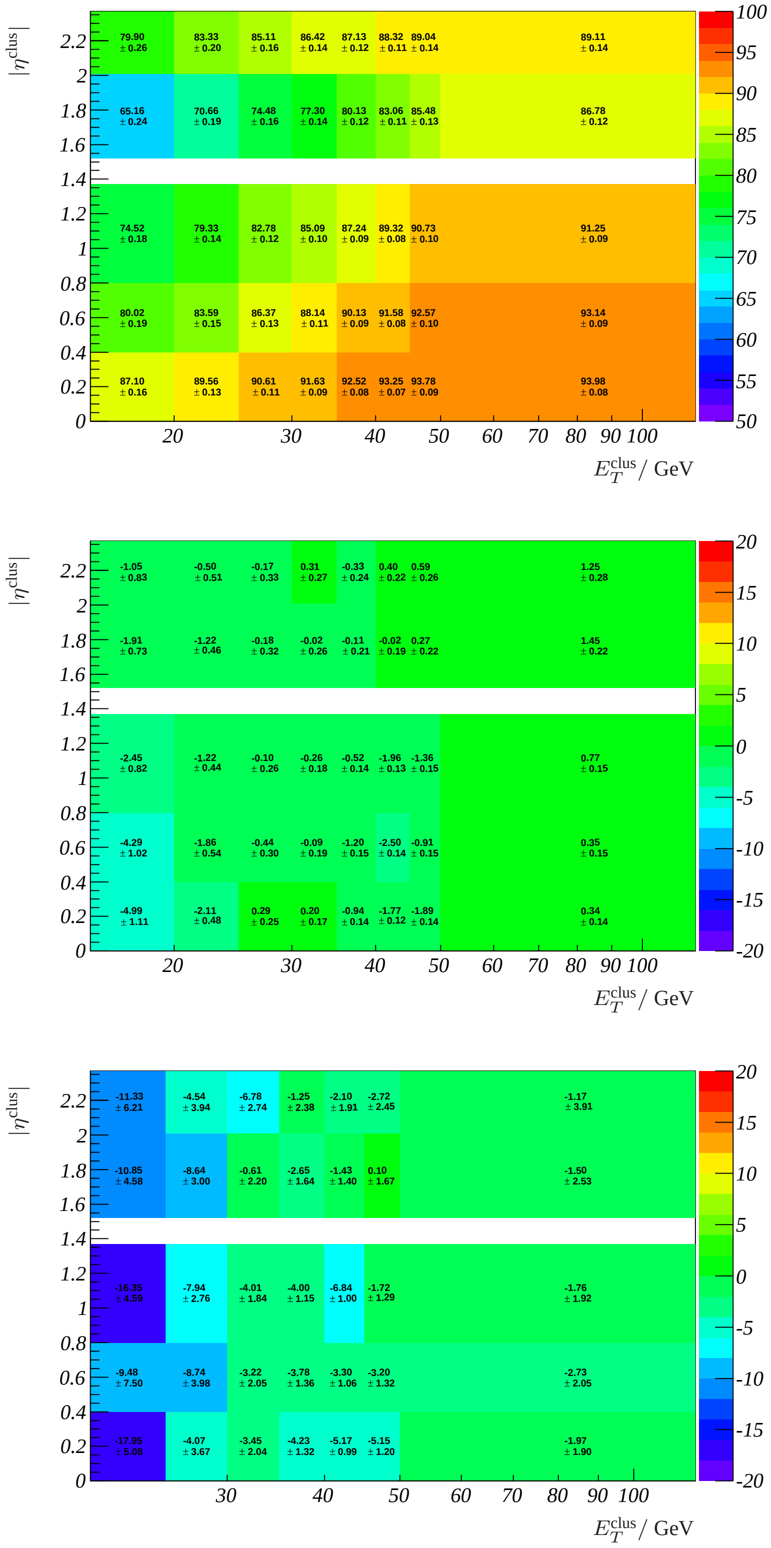

Figure 6.14: Double differential identification efficiencies. Top: truth efficiency. Middle: relative deviation of the truth-matched tag-and-probe method (full statistics) and the truth efficiency. Bottom: relative deviation of the tag-and-probe method (combined sample, $100\ \mathrm{pb}^{-1}$) and the truth efficiency. All values are given in per cent.

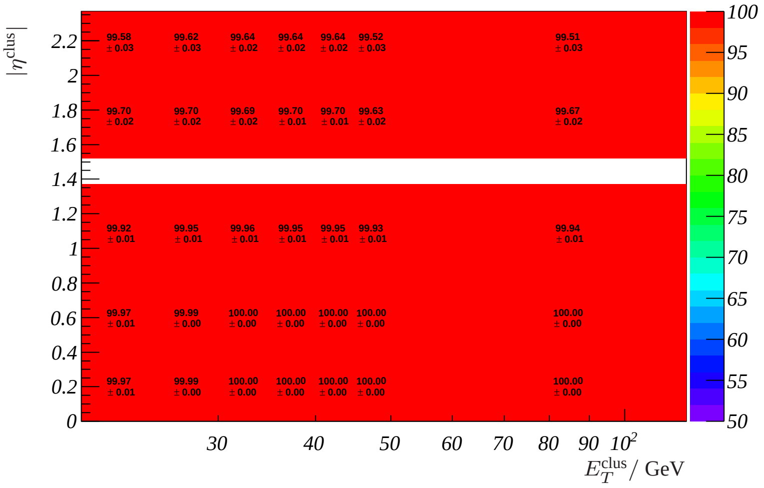

Figure 6.15: Double differential level-1 trigger-efficiency. All values are given in per cent.

cally underestimate the efficiency. In the truth-matched case this is the dominating effect, except for the highest-E_T bin, where the truth-efficiency becomes over-estimated beyond statistical fluctuations. Significantly with up to 5% difference is the under-estimation for central electrons with 15 GeV $< E_T \leq 20$ GeV. With this bin skipped for the combined sample, the bottom panel in Figure 6.14 shows the same behaviour for low-E_T electrons. Their identification efficiency is lower throughout the E_T-η plane, with a maximum difference of up to 16% at the lowest E_T bin. Possible explanations for the discrepancies are going to be discussed in the next section.

As it can be seen in Figure 6.15, the level-1 truth efficiency is essentially 100% in each bin of the E_T-η plane. A study of the related tag-and-probe efficiencies showed no significant deviations apart from statistical fluctuations.

6.8 Systematic Uncertainties

Within this section, the impact on the efficiencies of several factors that might have an effect on the determination of the single-electron efficiencies are going to be discussed. In the first part, the uncertainty on the truth efficiency is estimated by using a slightly different release of the reconstruction software and another Monte-Carlo generator, respectively. The latter, however, has not been analysed within this thesis due to unavailability of a suitable sample. Apart from that, cut variations are studied in order to estimate their impact on the efficiencies of interest. In this context, possible biases arising from FSR are considered, as well.

The results are shown as distributions versus E_T and η. An overview of the inclusive systematic effects is given at the end of Chapter 7.

6.8.1 Truth Single-Electron Efficiency

The determination of the single-electron truth efficiencies as described in Section 6.4 is essential in order to determine an overall efficiency correction factor to determine the cross-sections (see Chapters 7 and 8). Thus, they should be determinable in other processes with electrons in the final state, in principle. In this case, the $W \rightarrow e\nu$ sample has been chosen to cross-check the truth efficiencies independently from the $Z \rightarrow e^+e^-$ signal sample. Due to different hadronic contributions in both samples, the difference in the efficiencies is expected to be of the order of $\lesssim 1\%$.

The process $pp \rightarrow W \rightarrow e\nu$ has been simulated with the `PYTHIA` generator and has a single electron in the final state since the neutrino cannot be detected and contributes thus to the missing energy of the event. The sample was introduced in Chapter 4 and includes $\approx 60{,}000$ events.

In order to derive the efficiency for the electron from the W decay, the same procedure has been applied as for the Z sample (see Section 6.4). The resulting efficiencies are then compared to the truth efficiencies that have been presented in the previous section.

As long as both processes were generated with `PYTHIA`, no meaningful systematic studies can be performed, especially if the reconstruction used the same software release. One would expect no significant differences for the truth single-electron efficiencies in this case. Figure 6.16 shows the ratio of the efficiencies of the given samples. Especially for electrons with low transverse energy the reconstruction efficiency seems to be lower (up to 2%) when coming from the W boson. This might be caused by the recoil-jet of the W interfering with the electron. However, the identification efficiency shows a different behaviour, as it is higher for medium E_T electrons (~ 40 GeV) from the W decay, where the stringent criteria for the medium identification quality reduce the probability for both electrons to pass. The picture is slightly different when the efficiency ratios are plotted versus the pseudorapidity, where the electrons from the Z decay show slightly higher identification probability at high-$|\eta^{\text{clus}}|$ (see right panel of Figure 6.16).

6.8.2 Monte Carlo Generator

Rather than being dependent on a single Monte-Carlo generator, the extraction of truth efficiencies can be cross-checked by using a different generator that simulates the process $pp \rightarrow \gamma^*/ + X \rightarrow e^+e^- + X$. Up to this point, all efficiencies were determined by using the `PYTHIA` generator. By comparing the results to the efficiencies derived from a `MC@NLO` sample, the systematics introduced by the generator can be estimated.

The `MC@NLO` generator is in principle superior to the (LO) `PYTHIA` generator, as

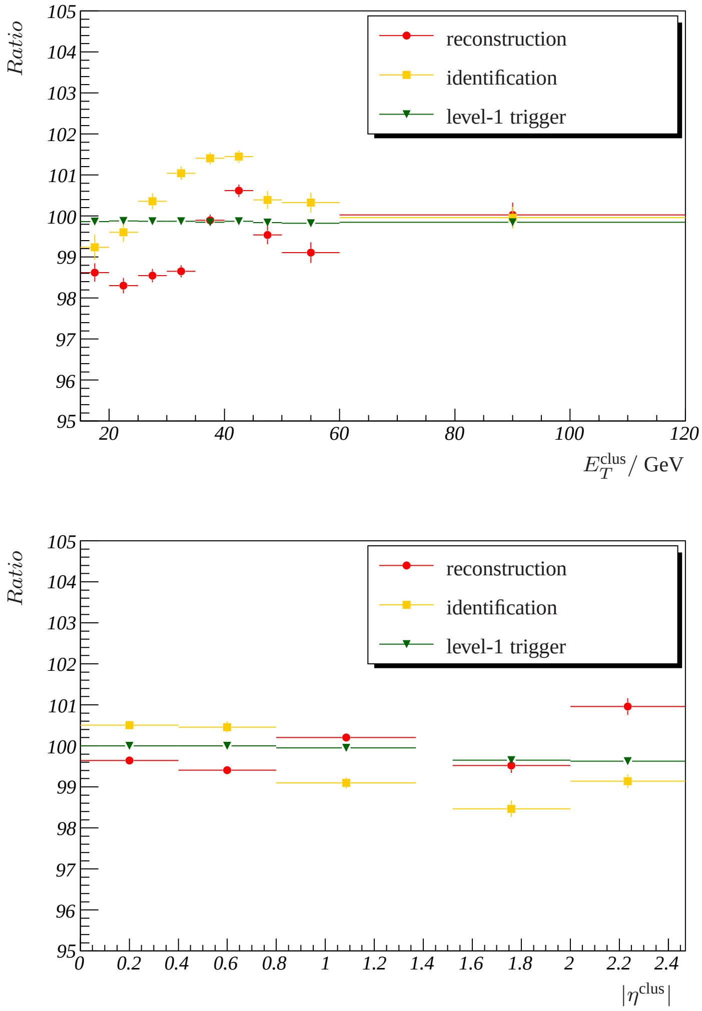

Figure 6.16: Ratio of truth efficiencies derived from the $Z \to e^+e^-$ and the $W \to e\nu$ sample, $\frac{\varepsilon_{W\to e\nu}}{\varepsilon_{Z\to e^+e^-}}$, versus E_T (top) and $|\eta|$ (bottom). Both samples were reconstructed with the same software release (14.2.20.4). All values are given in per cent.

it includes full NLO matrix elements in order to calculate the hard cross-sections with parton showers. On the downside, the event record is not as detailed as in `PYTHIA`, making it harder to study FSR related issues, for instance.

As already mentioned before, some of the centrally produced Monte Carlo samples were no longer available for this analysis. The results of a similar analysis (see Reference [16]), which also contains contributions from this thesis, are therefore described in this context.

The event selection and the determination of the truth efficiencies in Reference [16] comply largely with their counterparts presented in this chapter, and the binning is the same as shown in 6.6. One minor difference in this thesis is the exclusion of the crack re-

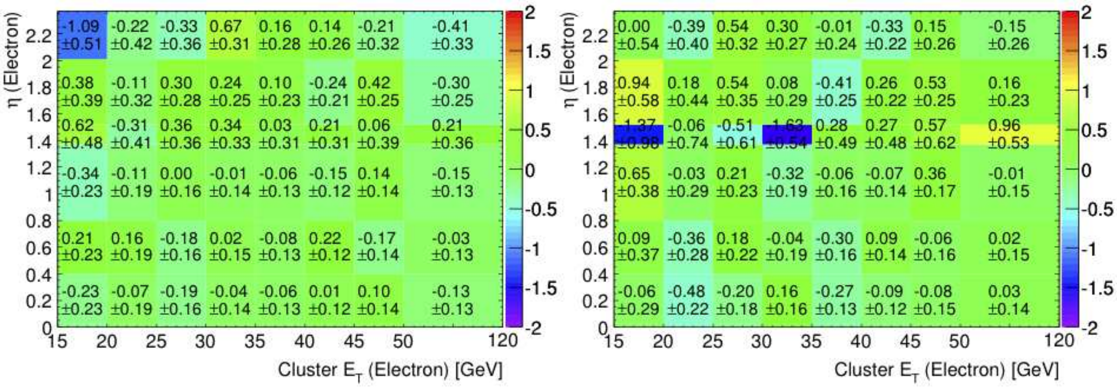

Figure 6.17: Relative deviation between `MC@NLO` and `PYTHIA` generators. Left: Single electron truth reconstruction efficiency. Right: Single electron truth identification efficiency. All values are given in per cent. Figures taken from [16].

gion. The ratio of the single-electron reconstruction (identification) efficiency determined with the `MC@NLO` sample and the one derived from the `PYTHIA` sample is presented in the left (right) panel of Figure 6.17. It shows an excellent agreement between the two generators, so that with the given statistical uncertainties no systematic bias can be observed.

6.8.3 Variation of the Matching Criterion

In order to decide whether or not a truth-level electron caused an associated object within the calorimeter, the distance in the η-ϕ plane between the truth parameters and the cluster position is the defining criterion. It is calculated as follows (cf. 6.8):

$$\Delta R = \sqrt{(\Delta\eta)^2 + (\Delta\phi)^2} \,, \tag{6.21}$$

where $\Delta\eta = \eta_{\text{truth}} - \eta_{\text{cluster}}$ and $\Delta\phi = \phi_{\text{truth}} - \phi_{\text{cluster}}$, respectively. As this matching is the link between truth and reconstructed object, biases introduced by the choice of the specific cut value will directly effect most of the truth efficiencies presented in this analysis.

The standard cut of $\Delta R = 0.15$ is varied by ± 0.10 in order to study the impact of the choice. The result is shown in Figure 6.18. With the good separation between clusters caused by truth electrons and additional energy deposits in the calorimeter, a more conservative choice does not affect the capability of reconstructing or identifying electrons. With an aggressive choice, however, some of the clusters predominantly originating from low-E_T electrons, fail the matching due to the impact of bremsstrahlung. This worsens the efficiencies in this E_T regime by $\lesssim 0.5\%$. The impact of the ΔR cut versus the η position of the cluster is negligible.

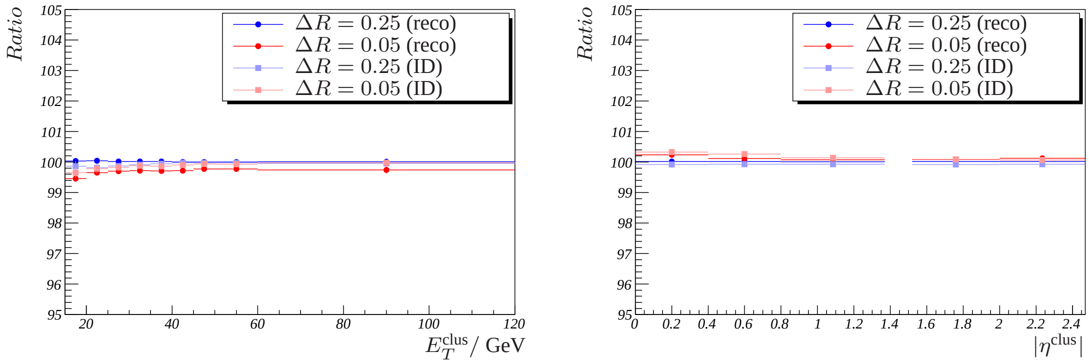

Figure 6.18: Ratio of the reconstruction (identification) efficiency determined with a varied ΔR cut and the according efficiency derived with the standard cut-value, versus E_T (left) and versus η (right). All values are given in per cent.

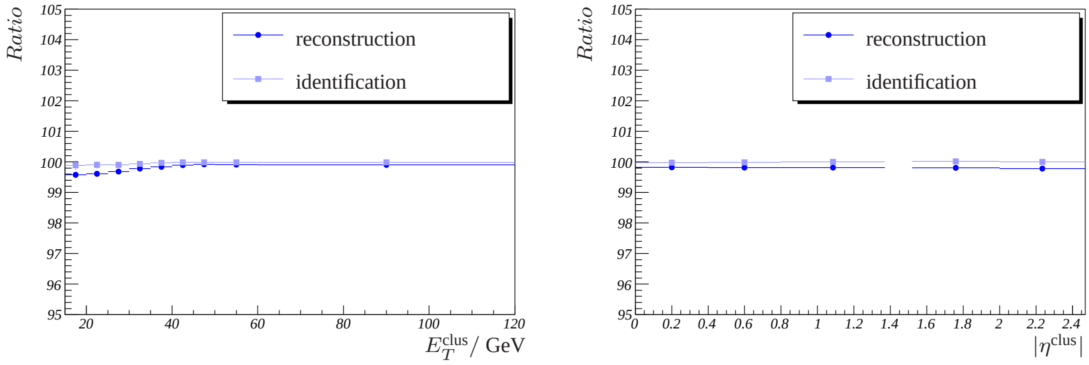

Figure 6.19: Ratio of single-electron efficiencies with and without final-state radiation versus E_T and $|\eta|$. All values are given in per cent.

6.8.4 Final State Radiation

Unlike initial-state radiation where an incoming quark emits a photon, final state radiation distorts the reconstructed invariant-mass distribution of the Z boson, since the electron's energy is measured systematically lower, leading to a lower invariant-mass tail for the Z boson. In order to study the impact of FSR, the electrons are flagged on truth level as stable particles or as electrons making bremsstrahlung. Afterwards, the single-electrons efficiencies are determined for both classes separately.

The result is shown in Figure 6.19. As expected, low-E_T electrons have a slightly lower reconstruction efficiency ($\lesssim 1\%$) than electrons not radiating photons. The effect shows no dependence on η.

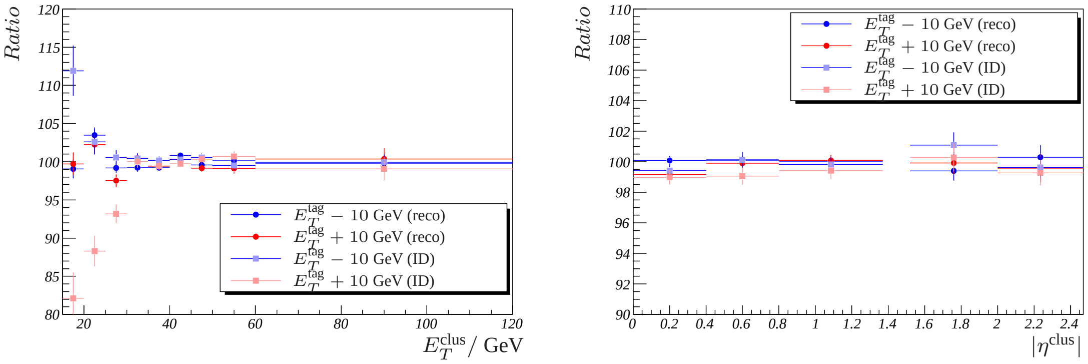

Figure 6.20: Ratio of the modified single-electron tag-and-probe efficiencies and the standard tag E_T-cut versus E_T and $|\eta|$. All values are in per cent.

6.8.5 Tag-and-Probe Cut Variation

The choice of a specific value in the selection process as shown in Section 6.6.2 might have an impact on the resulting efficiencies. Whilst most of the selection criteria for a tag-and-probe pair are pretty much forced due to geometric considerations (detector acceptance, crack region), the main free parameter is the minimal E_T cut for the tag electron. Its purpose is to reject as much low-E_T background as possible while leaving a sufficient amount of signal events untouched.

In order to study the effect of the minimal E_T cut on the efficiencies themselves, the tag-and-probe pairs are matched to the truth particles in order to reject possible impact of (combinatorial) background in this context. This is being done in order to demonstrate the influence of the cut on the method itself.

With a variation of the transverse-momentum requirement by ± 10 GeV for the tag object, the effect on the resulting efficiencies can be studied. The results are shown in Figure 6.20 for the reconstruction and the identification efficiency. Within statistical uncertainties, the efficiencies with a varied E_T cut show an acceptable agreement with the efficiencies derived with the nominal E_T cut. In case of the identification efficiency, however, there is a large effect visible at the low-E_T bins. Obviously, the harder the E_T condition on the tag electron is, the less electrons become identified as medium electrons and vice versa. The differences in the low-E_T region could explain the deviations shown in the previous section, the choice of the tag E_T has therefore a huge impact on the identification efficiency.

6.9 Summary

In this chapter, two of the commonly used methods to determine efficiencies for single electrons were shown. One of them, the truth efficiency, can only be derived from Monte Carlo simulations and therefore needs a very good understanding of the detector. Another method, which is also applicable to data, is the tag-and-probe method. In the early stages of the ATLAS experiment, it can be used to estimate systematic uncertainties for efficiencies derived with the truth method. Once a sufficient amount of statistics is available, the efficiencies derived by the tag-and-probe method might even replace the simulation-based approach.

Both methods show a very good agreement for almost all applications. Especially the truth reconstruction and trigger efficiencies can be reproduced accurately with the data-driven tag-and-probe method. However, the tag-and-probe method seems to have an issue at the low-E_T part of the identification efficiency. As it is shown in Reference [16], the effect also occurs in similar analysis and should be subject of further investigations.

7

Cross-Section Determination

7.1 Introduction

The inclusive cross-section of a given process can simplified be written as

$$\sigma = \frac{N - B}{\mathcal{A} \cdot \varepsilon \cdot \int dt\, \mathscr{L}} \,. \tag{7.1}$$

Here, N is the total number of selected events and B the number of estimated background events. The acceptance, $\mathcal{A}$, for Z bosons and the efficiencies[1], ε, reduce the number of signal events and hence enter the denominator. The integrated luminosity $L = \int dt\, \mathscr{L}$, which reflects the available amount of data, enters the denominator as well. The precise knowledge of the instantaneous luminosity is essential for the correct determination of cross-sections. The expected uncertainty on the luminosity for the early period of data taking will be discussed in Section 7.9.5.

Equation 7.1 holds for data as well as for simulation-based analysis. However, since the simulation is optimised to ignore non-relevant events, not every generated event automatically enters the detector simulation but rather gets filtered out due to minimal kinematic or geometric requirements. In this case the filter efficiency ε_F has to be included in the denominator of Equation 7.1.

In this context it should be noted that the corrections are applied differently. Since the acceptance of a Z boson does not depend on the specific kinematic topology of the leptons per event, the correction can be applied after the selection of all events. The efficiencies, however, may depend on the kinematics of the electron-positron pair and have therefore to be corrected on event-basis. It is obvious that these aspects have to be disentangled in order to derive the correct cross-section in the end.

In order to put all the ingredients together to calculate a cross-section, the general selection strategy to find a Z candidate will first be discussed in the following section. The resolution of the invariant mass and the impact on the binning is then shown in Section 7.3, followed by the discussion of the Z-acceptance in Section 7.4 and the efficiency correction in Section 7.5. After demonstrating the techniques necessary when dealing only with simulated samples (Section 7.6), the fitting strategy and the results are shown in Section 7.7 and Section 7.8. This is followed by the discussion of the systematic uncertainties of the measurements (Section 7.9) and the presentation of the results for the cross-sections (Section 7.10).

---

[1] this factor includes the several efficiencies involved like, for instance, reconstruction efficiency and trigger efficiency of the electrons

7.2 Event Selection

Each event has to have at least two reconstructed electrons. All possible combinations of reconstructed electron-pairs are in the following tested whether or not they fulfil a set of criteria. To exclude soft electrons from the selection process, the *electron author* variable must not be equal to 2. Soft electrons are particles with a low E_T and are mainly used in J/Ψ analysis.

Even if it has already been assured that the event has successfully passed the trigger, one of both electrons must have caused the trigger to fire. This can be checked by matching the electrons to the trigger objects (RoIs) at each stage. Within the available samples, however, the required information is not accessible for L2 and EF. Thus, at least one electron has to be matched via $\Delta R < 0.15$ to a RoI on the first trigger-stage. This RoI must also exceed the level-1 momentum threshold for the `e10_medium` trigger chain, $E_T^{\text{L1}} \geq 7$ GeV.

In order to reject low-momentum electrons and to work within the same kinematic boundaries as in Chapter 6, the transverse momentum is chosen to be in the range of 15 GeV$\leq E_T^{\text{el}} \leq 120$ GeV. The geometrical limitations discussed in Chapter 6 also hold for the event selection. Thus, only central electrons ($|\eta^{\text{el}}| < 2.47$), which are outside the transition region ($1.37 < |\eta^{\text{el}}| < 1.52$) pass.

The remaining lepton-pairs have to fulfil the medium identification requirement and must have an opposite charge. When an electron-positron pair of an event has passed all given selection criteria, the four-vector of the lepton-pair is calculated. The allowed invariant mass window for the selected Z candidate is 60 GeV $< M_{\text{el1, el2}} < 120$ GeV. This range allows for a sufficient amount of events from the sidebands in order to fit signal and background appropriately. The selection of the Z candidates is concluded by the restrictions on the Z's phase space, $p_T^{\text{el1, el2}} < 100$ GeV and $|y^{\text{el1, el2}}| < 2.5$. In addition to these criteria, a cut on the primary vertex of the two leptons can be applied in order to suppress contributions from pile-up in data. Moreover, each event will be required to have passed a certain trigger chain in order to enter the event selection. Since the trigger chains were simulated incompletely in the present samples, the criterion could not be applied in

cut description	requirement
reconstructed electrons	≥ 2
electron author	1 or 3
L1 matching (≥ 1 $e^{\pm}$)	$\Delta R(\text{el, RoI}) < 0.15$
associated L1 threshold	$E_T^{\text{RoI}} > 7$ GeV
min. momentum	$E_T^{\text{el}} > 15$ GeV
max. momentum	$E_T^{\text{el}} < 120$ GeV
central object	$\lvert\eta^{\text{el}}\rvert < 2.47$
crack exclusion	$1.37 < \lvert\eta^{\text{el}}\rvert < 1.52$
identification	*medium*
charge of the leptons	opposite
invariant mass	60 GeV $< M_{\text{el1, el2}} < 120$ GeV
max. four-momentum	$p_T^{\text{el1, el2}} < 100$ GeV
max. rapidity	$\lvert y^{\text{el1, el2}}\rvert < 2.5$

Table 7.1: Cut requirements for two reconstructed electrons to select Z-boson candidates.

this analysis.

A summary of all criteria is given in Table 7.1. By applying these cuts to data, this would yield inclusive, single and double differential invariant-mass spectra, reflecting the amount of signal and background events in each mass bin at a given integrated luminosity. With appropriate descriptions (see Section 7.7) of signal and background shapes the numerator of Equation 7.1 can be determined. With this approach, however, one would lose the opportunity to apply the efficiency correction ε in dependence of each event's kinematic topology. The inclusion of the efficiency correction on event-basis is going to be discussed in Section 7.5.

As this analysis deals with different sets of individual physical processes rather than dealing with a data sample, some additional steps need to be done in order to "fake" the combined invariant-mass spectra after selection. This will be discussed in Section 7.6.

7.3 Binning for Differential Cross-Sections

The determination of the resolution for the Z boson follows closely the procedure for single electrons from Chapter 6. Very similar to the arguments given there, it does not make sense to choose bin sizes smaller than the resolution for a variable. Since this kind of resolution studies are based on Monte-Carlo simulation exclusively, the whole statistics available is used, rather than to restrict to 100 pb^{-1}.

With the event selection discussed in the previous section, suitable Z candidates are selected in order to study their resolution in the detector. The first step to get the p_T^Z or $|y^Z|$ resolution is to choose a fine binning in both variables, such that each bin still contains a sufficient amount of events to allow for a fit. In p_T^Z, the granularity is 1 GeV up to 15 GeV and somewhat coarser above to account for the decreasing statistics coming with higher p_T^Z. The granularity in $|y|$ is 0.3, except for the outermost bin, which covers $2.1 < |y| < 2.5$.

In a second step, for each p_T^Z-$|y^Z|$ bin the relative (p_T) or absolute (y) deviation between reconstructed and truth value is calculated:

$$\frac{\Delta p_T^Z}{p_T^{Z,\,\text{truth}}} = \frac{p_T^{Z,\,\text{reco}} - p_T^{Z,\,\text{truth}}}{p_T^{Z,\,\text{truth}}}\,, \tag{7.2}$$

$$\Delta y^Z = y^{Z,\,\text{reco}} - y^{Z,\,\text{truth}}\,. \tag{7.3}$$

The distributions, which have been obtained in this way are fitted in order to determine the width as a measure for the resolution. The various $\Delta p_T^Z/p_T^{Z,\,\text{truth}}$ distributions show a similar shape with the tail below the nominal Z mass due to final-state radiation as shown in Figure 6.1. Thus, the same function (see Equation 6.3) is used to fit the distributions. Regarding the fitting function, the same applies for the determination of the rapidity resolution. As the distributions are not distorted by effects like bremsstrahlung, the normal distribution (see Equation 6.5) is used. All fits describe the distributions well, the reduced χ^2 does not exceed 1.25 for any of the fits.

Figure 7.1 shows the result for the whole p_T^Z-$|y^Z|$ plane. The transverse-momentum resolution drastically improves with increasing Z momentum and is worst for Z bosons with low transverse momenta. This is due to the fact that high p_T Z's decay preferably to high-E_T electrons, which have a better resolution than electrons with lower energy. Hence, the resolution for the Z bosons improves, too. The p_T^Z resolution shows no y^Z dependency and varies between $\sim 1\%$ for high-p_T^Z and $\approx 60\%$ for low p_T^Z. In case of the rapidity, the variation of the resolution is smaller than for the transverse momentum. The resolution is worst ($\sigma(y^Z) \sim 0.1$) for Z bosons with medium rapidity ($|y^Z| \sim 1$) and low p_T^Z. The resolution improves with increasing rapidity of the Z and reaches $\sigma(y^Z) \approx 10^{-2}$ for $2.1 \leq |y^Z| < 2.5$.

The results suggest to choose bin-sizes of $\gtrsim 1$ GeV for the transverse momentum variable and $\gtrsim 0.1$ for the rapidity of the Z. Besides this lower limit, the binning in p_T and in Z rapidity is oriented on the expected statistics of Z events within a certain area of the p_T^Z-$|y^Z|$ plane. With these results, the bins in terms of transverse momentum and rapidity of the Z boson are chosen as follows:

$$\begin{aligned} p_T^Z &= \{0.0, 3.0, 5.5, 8.0, 11.0, 17.0, 25.0, 40.0, 100.0\}\ \text{GeV}\,, \\ |y^Z| &= \{0.0, 0.4, 0.8, 1.3, 1.9, 2.5\}\,. \end{aligned} \tag{7.4}$$

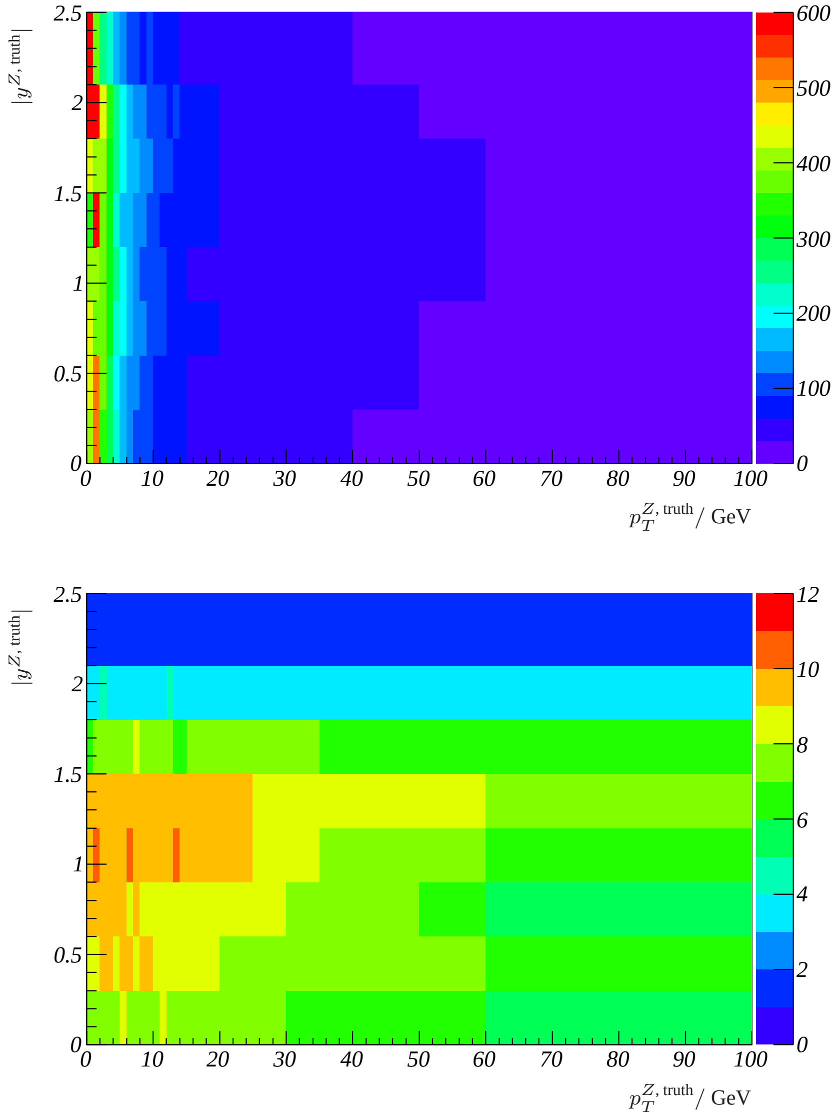

Figure 7.1: Resolution for the reconstructed Z bosons after selection in bins of truth p_T^Z and $|y^Z|$. Top: relative transverse momentum resolution, $\sigma(p_T^Z) \times 10^3$. Bottom: absolute rapidity resolution, $\sigma(y^Z) \times 10^2$.

7.4 Z Acceptance

There are several limiting factors that reduce the number of Z events to pass the selection criteria. One is the rejection of Z bosons due to kinematic and geometric cuts on the leptons. If only one of them fails a criterion, the initial state could not be reconstructed anymore and is therefore lost for the remaining stages of the cross-section measurement.

The acceptance studies have to be done completely on Monte-Carlo generator level, since the acceptance cannot be obtained from data. As this analysis is based on recon-

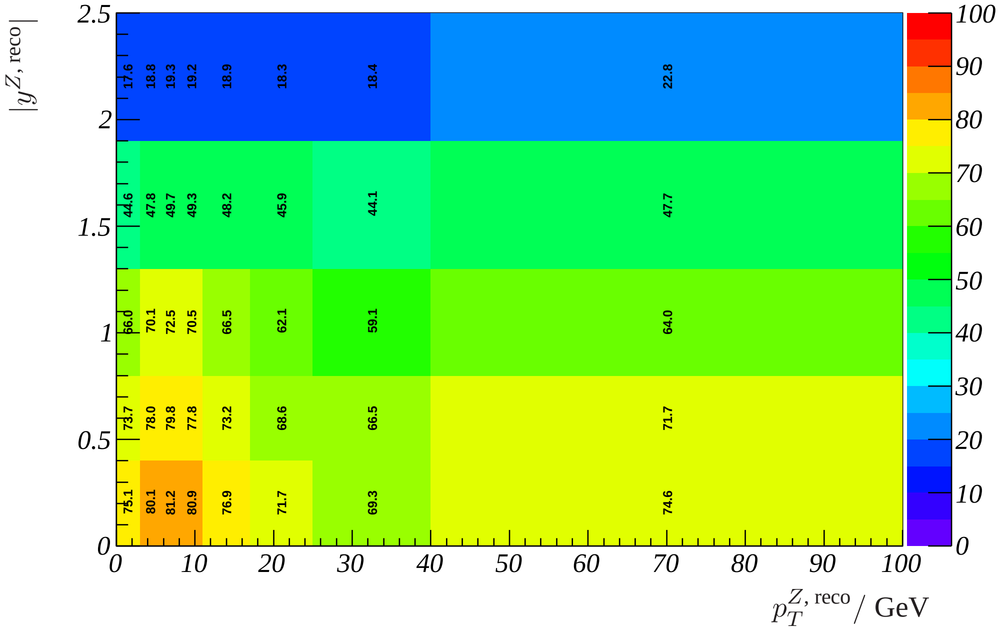

Figure 7.2: Kinematic and geometric acceptance for two clusters in bins of p_T^Z and $|y^Z|$, errors are statistical. All values are given in per cent.

structed variables rather than using variables on truth or generator level, the kinematic and geometric criteria are applied to the cluster variables. As it has been shown in Figure 6.4, the probability of finding a cluster associated to a truth electron from the Z decay is approximately 100%. This provides the possibility to cut on and express distributions in reconstructed quantities.

In order to estimate the loss of Z bosons due to the restriction to kinematic and geometric ranges, the ratio of the amount of cluster-pairs before and after the specific cuts gives the acceptance in the appropriate p_T^Z-$|y^Z|$ bin. The criteria to find a cluster-based Z are already given in Section 7.2: the transverse momentum of the clusters is limited to 15 GeV$< E_T < 120$ GeV, and as the analysis concentrates on objects in the central detector, the pseudo-rapidity has an upper bound, $|\eta| < 2.47$. The transition region $1.37 < |\eta| < 1.52$ is excluded. The nominal invariant-mass cut as given in Table 7.1 is modified to 70 GeV$< M_Z < 110$ GeV since this mass window will be used to determine the background-subtracted number of signal events in the later stages of this analysis.

The result of this study is shown in Figure 7.2. Whilst the acceptance is fairly constant over the whole p_T^Z range, it drops sharply for higher rapidity values of the Z. This is due to the fact that the probability for loosing at least one lepton from the Z decay because of the limitation to the central part of the detector increases with the Z's rapidity. Overall, the acceptance varies between 17.6% and 81.2% within the kinematic and geometric limits of $p_T^Z < 100$ GeV and $|y^Z| < 2.5$. Without these limits and the restricted invariant-mass window, the inclusive acceptance is $\mathcal{A} = (40.05 \pm 0.01)\%$. For the remainder of this chapter it makes sense to split the different aspects and factorise the inclusive acceptance:

$$\mathcal{A} = a_l \cdot A_{\text{cluster}} \, , \tag{7.5}$$

where $a_l = (74.62 \pm 0.01)\%$ accounts for the restrictions on the Z's transverse momentum and rapidity and $A_{\text{cluster}} = (53.67 \pm 0.02)\%$ reflects the criteria on the clusters including the cut on the invariant-mass. The double-differential representation of A_{cluster} (see Figure 7.2) has already been discussed.

7.5 Correction for Inefficiencies

After the selection of a signal candidate, one could simply add the unweighted event to the invariant-mass distribution and apply the corrections (like for the efficiency) after the fitting procedure. But this would not account for the efficiency that may vary in dependence of the kinematic topology of an event. As it was shown in Section 6.7.4, the various efficiencies for single-electrons vary quite strongly over the E_T-$|\eta|$ plane. Thus, the correction should be done per event, rather than applying one overall correction factor.

For the purpose of this analysis, a correction factor for each $p_T^Z, |y^Z|$ bin has been used. This is a compromise between using only one overall correction-factor and a correction-factor calculated from the two-dimensional single-electron efficiencies introduced in Chapter 6. The *factorisation ansatz*[2],

$$\varepsilon = \varepsilon_{\text{el1}}^{\text{reco}} \cdot \varepsilon_{\text{el2}}^{\text{reco}} \cdot \varepsilon_{\text{el1}}^{\text{ID}} \cdot \varepsilon_{\text{el2}}^{\text{ID}} \cdot \varepsilon_{\text{el1}}^{\text{q}} \cdot \varepsilon_{\text{el2}}^{\text{q}} \cdot \left(\varepsilon_{\text{el1}}^{\text{L1}} + \varepsilon_{\text{el2}}^{\text{L1}} - \varepsilon_{\text{el1}}^{\text{L1}} \cdot \varepsilon_{\text{el2}}^{\text{L1}} \right) \, , \tag{7.6}$$

which has been used in former analysis (cf. References [71] and [50], for instance) does not work. This will be discussed in Chapter 8.

The correction factor ε_Z that will be used within this analysis is simply determined as follows. The denominator N^{acc} is given by the accepted cluster-pairs from the previous Section. The numerator N^{sel} consists of a subset of N^{acc} where both clusters have been reconstructed as electrons that are matched to them, and these electrons fulfil the selection critera given in Table 7.1. Thus, the correction factor is

$$\varepsilon_Z(p_T^Z, |y^Z|) = \frac{N^{\text{sel}}(p_T^Z, |y^Z|)}{N^{\text{acc}}(p_T^Z, |y^Z|)} \, . \tag{7.7}$$

This results in an efficiency map in p_T^Z and $|y^Z|$, which is shown in Figure 7.3 and will be used for each selected Z candidate to get the appropriate weight $\varepsilon_Z(p_T^Z, |y^Z|)$. Its application for each Z event will be shown in the following section.

---

[2] apart from the reconstruction, identification and trigger efficiency, the charge identification efficiency ε^q has also to be taken into account if it is not $\sim 100\%$. With $\varepsilon^q > 98\%$ in each E_T-$|\eta|$ bin, the charge identification efficiency has been neglected in this analysis

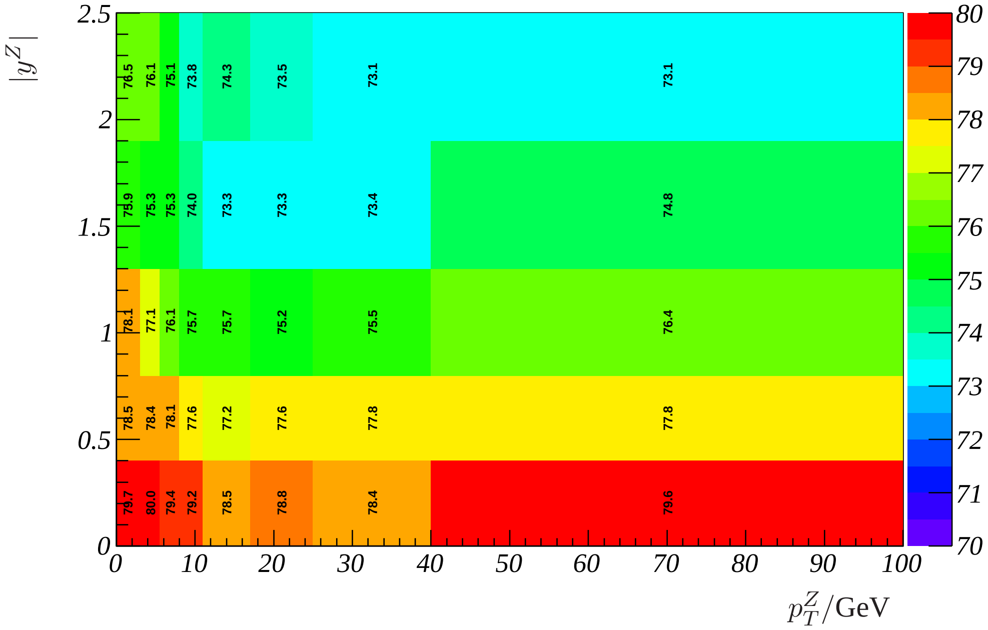

Figure 7.3: Correction factor $\varepsilon_Z(p_T^Z, |y^Z|)$. The statistical uncertainties vary between 0.2% and 0.6% All values are given in per cent.

7.6 Special Aspects for Simulated Samples

Within this study the signal sample and four background channels have been taken into account (see Chapter 4). The latter are hadronic QCD background, $t\bar{t}$, $W + 1$ jet and $W + 2$ jets and each of them might lead to an electron-positron pair in the final state. Unfortunately, they all come with a different amount of statistics, whereas the QCD sample, which happens to be the biggest source of background, suffers from a lack of simulated events in the order of ~ 1000 (see Section 4.4). The impact of this issue and an alternative way to estimate the contribution of this sample to the total background will be demonstrated in the following section, along with the method to create a combined sample of signal and background. In addition to this method, which is basically faking the expected detector output for $100\,\text{pb}^{-1}$ of real data, the selection criteria are also applied to the full signal-sample in order to cross-check the results from the combined sample and to compare the full-statistics results for the cross-section with the generator cross-section.

7.6.1 Scaling of QCD Background

With the excellent jet suppression in ATLAS (see Section 5.5) and the poor statistics available for the QCD sample (see Section 4.4) it is obvious that by requiring two medium identified electrons not enough events remain to describe the background appropriately.

$\int dt\,\mathcal{L}\,/\,\mathrm{pb}^{-1}$	$2{,}847$	0.079		$1{,}584$	32.0	160.0
Cut	Signal	QCD		$t\bar{t}$	$W+1\,$jet	$W+2\,$jets
$\geq 2e^{\pm}$	1,700,168	6,274,145		317,201	32,122	84,359
Author	1,589,800	3,776,137		313,571	28,085	78,276
E_T^{min}	1,242,890	104,272		172,522	4,421	20,001
E_T^{max}	1,237,210	103,836		169,503	4,274	19,191
$\lvert\eta^{\mathrm{max}}\rvert$	1,209,816	102,073		168,448	4,188	18,848
Crack	1,079,789	91,114		157,626	3,717	16,932
ID	788,173	—	48	3,527	36	83
Charge	781,604	44,581	30	3,296	27	65
L1	781,330	8,628	30	3,289	27	22
$M_{\mathrm{e1,\,e2}}$	768,187	2,850	25	1,515	11	22
$p_T^{Z,\,\mathrm{max}}$	760,017	2,843	25	1,366	11	22
$\lvert y^{Z,\,\mathrm{max}}\rvert$	760,017	2,843	25	1,366	11	22

Table 7.2: Remaining number of events after applying the given cut criteria. The QCD sample is split-up into flows with and without the identification criterion. All numbers given are with respect to the available statistics of each sample and therefore not normalised to a common integrated luminosity.

Table 7.2 shows the remaining number of events after each selection step for the signal and background samples. By applying the medium-identification criterion, only 48 events remain for the QCD sample. In order to preserve a sufficient amount of statistics, this cut is skipped and each event becomes re-weighted instead. The low statistics after applying the identification cut is not an issue for the W+jet(s) samples, since their initial integrated luminosity is at least ($W+1$jet) comparable to $100\mathrm{pb}^{-1}$. Thus, the remaining number of events roughly reflects the expectations for data.

The re-weighting is done by applying each of the cuts given in Table 7.2 separately to the electron candidates within the QCD sample to determine a background-electron efficiency. The number of electrons before and after applying the medium-identification criterion are counted in bins of E_T and $|\eta|$, rather than using an overall scaling-factor. The result is a look-up table with an efficiency

$$\varepsilon_{\mathrm{QCD}}^{\mathrm{ID,\,medium}}(E_T, |\eta|) = \frac{N^{\mathrm{ID}}(E_T, |\eta|)}{N^{\mathrm{reco}}(E_T, |\eta|)} \tag{7.8}$$

for each bin. The weight for each pair of electrons that survives the standard signal-selection is then simply approximated by

$$w(E_T^{\mathrm{el1}}, |\eta^{\mathrm{el1}}|, E_T^{\mathrm{el2}}, |\eta^{\mathrm{el2}}|) = \varepsilon_{\mathrm{QCD}}^{\mathrm{ID,\,medium}}(E_T^{\mathrm{el2}}, |\eta^{\mathrm{el2}}|) \cdot \varepsilon_{\mathrm{QCD}}^{\mathrm{ID,\,medium}}(E_T^{\mathrm{el2}}, |\eta^{\mathrm{el2}}|)\,. \tag{7.9}$$

The factor w is used to adjust the invariant mass spectrum of the QCD sample by applying it as a weight for each event entering the spectrum. For the other samples one has $w \equiv 1$. With the considerations from Section 7.5, the re-weighting on event-basis can be written as

$$N_{\text{corr}} = \sum_{\text{Events}} \frac{w(E_T^{\text{el1}}, |\eta^{\text{el1}}|, E_T^{\text{el2}}, |\eta^{\text{el2}}|)}{\varepsilon_Z(p_T^Z, |y^Z|)} \,. \tag{7.10}$$

7.6.2 Relative Normalisation

At this stage, the inclusive, both single-differential and the double-differential invariant mass distributions come in five variations, namely one for each sample. It is obvious that the summing up of these to a combined sample that fakes data-like distributions can only work if they all represent the same amount of data. Except for the QCD and the $W + 1$ jet sample, which suffer from insufficient statistics, this can be achieved in different ways:

- consider only events up to a corresponding integrated luminosity of 100 pb^{-1}. The advantage is that the statistical uncertainty of the resulting distributions is correct, but always the same events are used. The latter might result in adjusting fit parameters for one set of distributions, rather then ensuring stable fits even if statistical fluctuations might lead to slightly different distributions

- use all available events. Making use of all events smoothes out the spectra, but, after downscaling to the desired amount of data, the statistical fluctuations will not be mirrored in this case

- choosing events randomly. Each event is considered with a probability that corresponds to the desired integrated luminosity with respect to the full amount of events within the sample. This method ensures that a different set of events is picked each time the analysis is run, mirroring statistical fluctuations. Furthermore, the distributions do not have to be heavily re-scaled, as they intrinsically contain ≈ 100 pb^{-1}

For this analysis, the third method was chosen. Thus, after applying the selection criteria in 7.2, the signal sample as well as two of the background samples ($t\bar{t}$ and $W + 2$ jets) contain the number of events corresponding to ≈ 100 pb^{-1}. By running the analysis ≈ 30 times, the stability of the fits for the targeted integrated luminosity was verified.

There are two samples, which have an integrated luminosity of less than 100 pb^{-1}, so they need to be scaled. The scaling factor for each $W + 1$ jet spectrum is simply $f_{\text{W+1 jet}} = \frac{100\text{ pb}^{-1}}{32\text{ pb}^{-1}}$. The calculation of the scaling factor f_{QCD} for the QCD sample is of course the same as for the $W + 1$ jet sample. With $f_{\text{QCD}} > 1200$, however, the need of re-weighting the sample beforehand becomes clear.

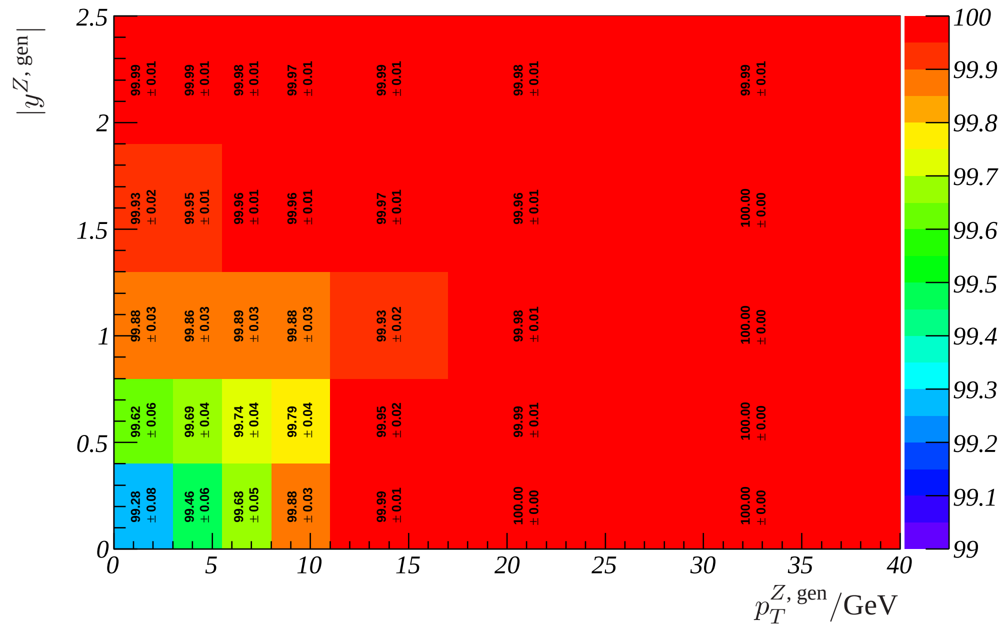

Figure 7.4: Filter efficiency on Monte Carlo generator level. One particle has to fulfil the requirement $|\eta| < 2.8$. For better illustration, the highest E_T-bin was not drawn, its efficiency is essentially 100%. All values are given in per cent.

After re-scaling the spectra are added up in order to “fake” combined distributions of signal and background. These combined samples are now used to determine the number of selected and background events via fitting procedures.

7.6.3 Filter Efficiency

The filter efficiency ε_F is a technical factor that is only relevant for simulated events. It denotes the ratio of all events that were generated within the Monte Carlo simulation and the events that actually enter the detector simulation. Many criteria might be applied on generator level to prevent events from entering the sample in order to reduce the rather time-consuming process of detector simulation.

In case of the signal sample, the only criterion on generator level is the requirement to have at least one particle within $|\eta| < 2.8$. Thus, most generated events pass this criterion, which can be seen in Figure 7.4. Here, the filter efficiency was determined with an independently produced Monte Carlo sample that used the very same options and parameters as the signal-sample on which this analysis is based on. Without running the detector simulation on this “flat” sample, the filter efficiency could be reproduced as

$$\varepsilon_F = \frac{N^{\text{gen}+|\eta^{1\text{p}}|<2.8}}{N^{\text{gen}}}, \tag{7.11}$$

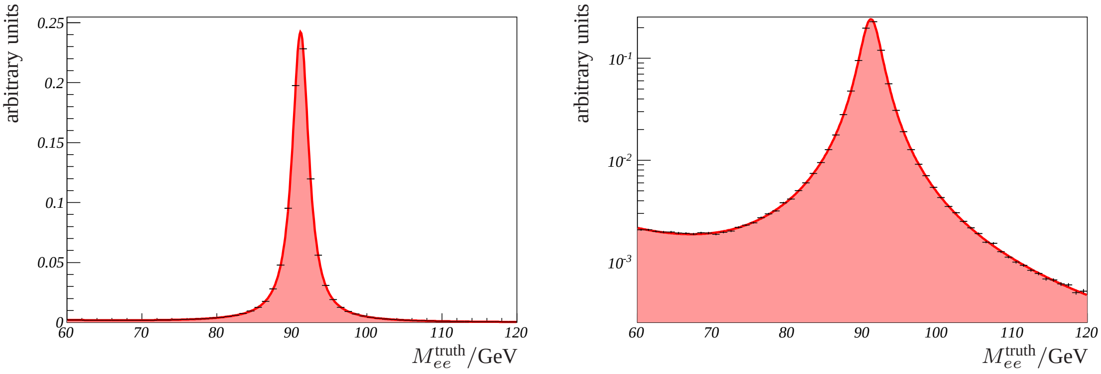

Figure 7.5: Fit of the inclusive, truth e^+e^- invariant mass before reconstruction, linear (left) and logarithmic illustration (right). See text for details.

where $N^{\rm gen}$ is the total number of generated Z events and $N^{{\rm gen}+|\eta^{\rm 1p}|<2.8}$ is the number of events with the additional η-cut. Even though Figure 7.4 shows almost no impact of the filter criterion on Z events to enter the reconstruction within the kinematic ($p_T^Z \leq 100$ GeV) and geometric ($|y^Z| \leq 2.5$) window of interest, the cut leads to a rejection of 4.4% of all (i.e., without restrictions on p_T^Z and $|y^Z|$) generated Z bosons.

7.7 Signal Extraction

The fitting algorithm as described in Section 6.7.1 is also applicable to the combined signal and background distributions, which have been derived in the previous section. Furthermore, as in this case the algorithm targets exclusively on Z selection, rather than applying specific criteria for the tag-and-probe method, the line shape to describe the whole process—including FSR[3] and Drell-Yan continuum—should work perfectly, at least for the inclusive spectrum.

As mentioned earlier, the description of the signal comes in two parts. One is the pure γ^*/Z line shape and the other one is a function to account for the detector resolution. In order to demonstrate the description of the signal with the fitting function, the invariant-mass spectrum of the two truth-leptons is fitted with the formulae that were introduced in Section 6.7.1. The result is shown in Figure 7.5. It shows excellent agreement between simulation and fit, with $\chi^2/\text{ndf} = 1.03$. The Z mass and the width are found to be $M_Z = (91.17 \pm 0.06)$ GeV and $\Gamma_Z = (2.51 \pm 0.02)$ GeV. They agree perfectly with the generator input ($M_Z = 91.19$ GeV, $\Gamma_Z = 2.50$ GeV).

In order to test the behaviour of the function when the detector resolution enters the signal, all selected electron-positron pairs, which form a Z candidate, are tried to be

---

[3] final state radiation

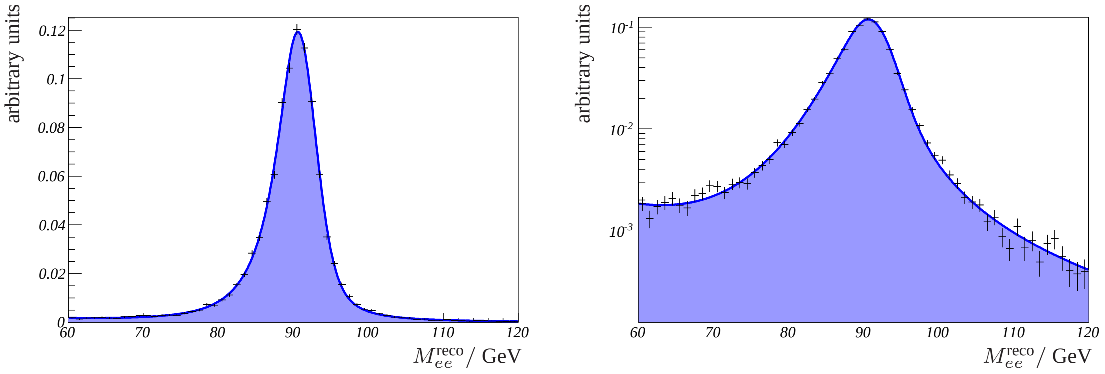

Figure 7.6: Fit of the inclusive, reconstructed e^+e^- invariant mass, linear (left) and logarithmic illustration (right). In order to clean the sample from combinatorial background, the reconstructed leptons were matched to the truth particles. See text for details.

matched to the truth particles. The result is a background-free invariant-mass spectrum of Z candidates, that is distorted by the effects of the electron resolution. With the fit-parameters taken from the previous fit, the second part of the fitting algorithm, the convoluted Crystal-Ball, can be included. Figure 7.6 shows the resulting distributions as well as the description by the fit.

The convolution not only accounts for the broadening of the Z resonance, but also allows for shifts in the location of the maximum of the peak, which might occur if the electron's energy-scale is incorrect. The fit in Figure 7.6 gives a reconstructed mass of the Z boson of $M_Z = (89.90 \pm 1.21)$ GeV. The resolution that can be derived from the fit is 1.50 ± 0.12 GeV and is in good agreement with the expectations for the ATLAS experiment (cf. Table 3.1). The good agreement between fit and reconstructed events is confirmed by a value for χ^2/ndf of 1.12.

In this context it should be emphasised again that the precise description of the Z line shape comes with a high price: the parametrisation is quite vulnerable to background events, which simply means that a differentiation of signal and background becomes difficult. It is therefore necessary to limit as many signal-parameters as possible before fitting a combined spectrum of signal and background. Within the scope of this analysis with its focus on single and double differential representations of distributions, many different approaches to face this difficulty have been tested. Some of them will now be briefly discussed.

Fitting Strategies for a Combined Sample

The difficulties in fitting a combined sample of signal and background events were already discussed before (cf. Section 6.7.1): Firstly, if the background in the lower-mass tail of the invariant mass spectrum is on the order of the Drell-Yan continuum, a differentiation between signal and background events becomes impossible. Secondly, the shape of the background changes quite dramatically with p_T^Z (cf. Figure 6.7); this matters only for the single or double-differential spectra, obviously.

In order to reach a sufficiently stable fit for each binned or inclusive distribution, two different approaches have been taken into account, where the basis is either the background or the signal description.

Background Based Approaches. One standard method to determine the background contribution to a distribution is the side-band method: the amount of background in a narrow window around the peak region is estimated by the number of events to the left and to the right of the window, given that these sidebands only consist of background events and the background itself is approximately linear in the peak region of the signal. Since the differential distributions given by the event-selection show a similar behaviour as the tag-and-probe distributions (see Figure 6.7), this method cannot be applied.

One possible workaround is to make use of the Monte Carlo simulation, once data is available. The background distribution can be used to constrain the shape of the background in data. With the normalisation as the free parameter, the contribution of the background to the invariant-mass spectrum can be estimated appropriately. This method depends on simulation and data, as the QCD cross-section applied for the simulation still suffers from a large uncertainty.

Signal Based Approach. Similarly to the previous approach, this one uses the simulation in order to constrain one part of the fit, before dealing with the combined distribution (or data). As the theory and hence the cross-section of the γ^*/Z process is well known, the signal part of the fit parameters can be taken from fits on the simulated distributions that are “cleaned” from possible combinatorial background. One has to be very careful, though, not to introduce any bias by restricting the parameters too much.

With these constraints on the signal-fit, the whole distribution can then be fitted, where the background-part has to account for most of the remaining events that exceed the predefined signal contribution.

Both of the introduced methods were applied to determine the number of signal and background events from the (non-)inclusive distribution(s). If they showed a significant difference in the result, the method with the best χ^2 of the fit has been chosen.

7.8 Corrected Event Numbers

With the selection criteria, the fitting algorithms and the different fitting approaches discussed so far, it is now possible to show the results of the different fits, i.e., inclusive and binned number of signal and background events. Since the numbers do not represent the actual number of selected events, but the number of events *after* efficiency correction, Equation 7.10 can be written as

$$(N-B)_{\text{corr}} = \sum_{\text{events}} \frac{w(E_T^{\text{el1}}, |\eta^{\text{el1}}|, E_T^{\text{el2}}, |\eta^{\text{el2}}|)}{\varepsilon_Z(p_T^Z, |y^Z|)} \,. \tag{7.12}$$

Here, N is the total number of events, B the number of background events, both determined by the fit and w and ε_Z are the applied corrections for each Z candidate, i.e., for signal and background events. In the following, the results are shown for the fit of the combined sample with an amount of data equal to 100 pb^{-1} and for the signal-only case with truth-matching, i.e., with rejection of combinatorial background with all statistics available. Additionally, the event numbers will be corrected by the cluster acceptance A_{cluster}. Both results are compared to the expected number of events given by the Monte-Carlo generator within the limited Z acceptance ($p_T^Z < 100$ GeV, $|y^Z| < 2.5$).

7.8.1 Inclusive Event Numbers

Within the allowed geometric and kinematic acceptance of the Z boson, $p_T^Z < 100$ GeV and $|y^Z| < 2.5$, $760{,}017$ events have been selected in case of the signal-only sample. Including the corrections, this translates to a resulting, corrected number of signal events of $(N-B)_{\text{corr}}/A_{\text{cluster}} = (2.329 \pm 0.002_{\text{stat}}) \times 10^6$. The excellent agreement with the number of generated event within the allowed Z rapidity and transverse momentum is expected since the correction factor ε_Z mirrors the event selection. The uncertainty is given by the statistics. In case of the combined sample, the uncertainty is calculated by error propagation of the fit-uncertainty and the uncertainty on the number of events.

As this analysis targets on providing useful information on the feasibility of a cross-section determination at the very early stage of data taking, the corrected number of events of the combined sample is compared to the expected number of events given by the generator for 100 pb^{-1}. With the event-based corrections, a total number of $(N-B)_{\text{corr}} = (82.91 \pm 1.28_{\text{stat}}) \times 10^3$ has been derived from the fit, whilst on generator level, $N_{\text{gen}} = 81{,}823$ were produced. The deviation of $\approx 1\sigma$ shows a good agreement between the corrected number of events and the expected value. Table 7.3 summarises the numbers.

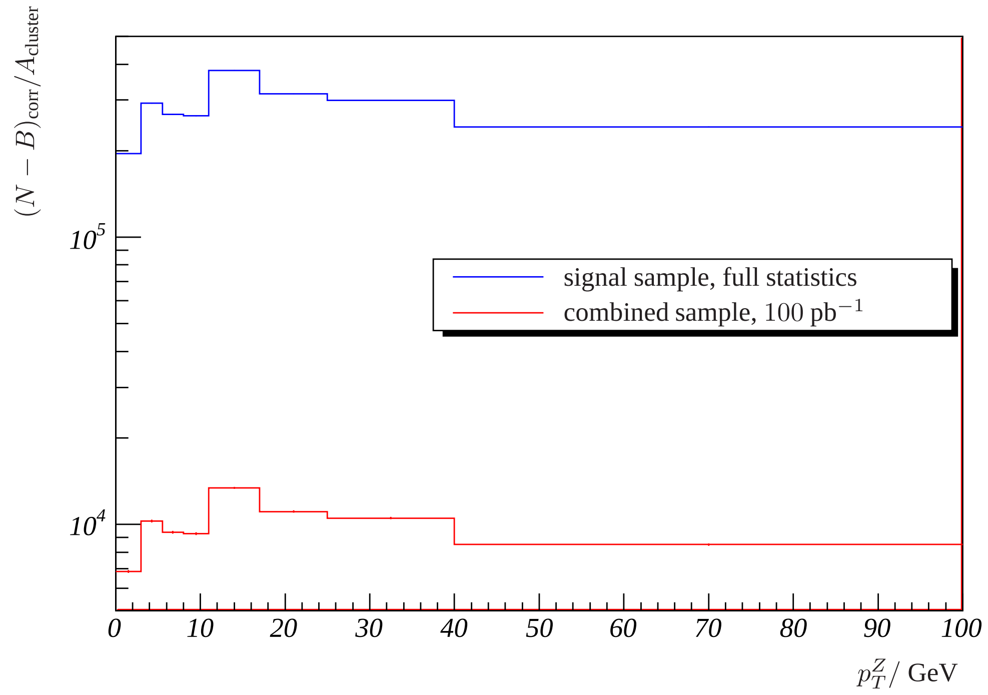

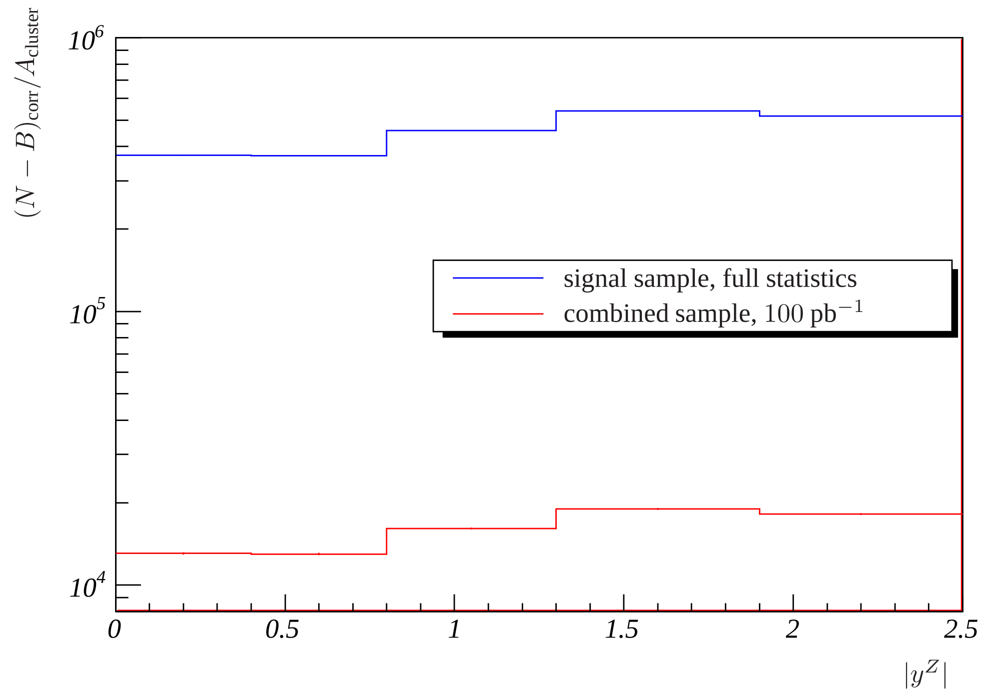

Figure 7.7: Number of reconstructed signal events after efficiency and acceptance correction for the signal-only sample (full statistics) and for the combined sample (100 pb^{-1}). Top: versus the transverse momentum of the Z. Bottom: versus Z rapidity.

Expectation, $N_{\text{gen}} \cdot a_l$	2.329×10^6	$81{,}823$
	Signal-only (full stat.)	Combined sample (100 pb^{-1})
$(N-B)_{\text{corr}}/A_{\text{cluster}}$	$(2.329 \pm 0.002) \times 10^6$	$(82.91 \pm 1.28) \times 10^3$
Relative deviation	–	1.32%

Table 7.3: Comparison of the total numbers of generated events and reconstructed Z events after corrections. In order to study the stability of the fitting algorithm and minimise the uncertainty on the fit parameters, the corrected number of events for the combined sample is averaged over 30 runs (see Section 7.6.2 for details).

7.8.2 Differential Distributions

Even if the agreement would be perfect for the inclusive number of events, the corrections applied might lead to systematic effects. Especially the impact of, e.g., parton distributions on single differential Z distributions can only be studied if their current implementation in the simulation can be reproduced.

Figure 7.7 shows the number of signal events for Equation 7.12 as derived from the fits, divided by the cluster acceptance A_{cluster}. The ratios between the results and the expected number of events per bin never exceed 5% and can be read of the final results for the single-differential cross-sections in Section 7.10. From the distributions in Figure 7.7 one can also draw the conclusion that the binning was chosen appropriately in order to guarantee a sufficient amount of statistics per bin.

The double-differential binning in p_T^Z and $|y^Z|$ allows to study the Z production in both variable at once, but comes at the cost of lower statistics per bin. This is even more crucial if the integrated luminosity is low. In Figure 7.8 the expected number of events within the acceptance per p_T^Z-$|y^Z|$-bin is shown on generator level. The occupancy per bin varies between $\gtrsim 30{,}000$ events for low-momentum ($p_T^Z \lesssim 3$ GeV) and central ($|y^Z| \lesssim 0.8$) Z bosons and $\approx 90{,}000$ events for 11 GeV $< p_T^Z \leq 17$ GeV and $1.3 < |y^Z| \leq 2.5$. In comparison to these numbers, the top panel of Figure 7.9 shows the ratio between the expected number of events and the corrected number of events for the signal-only sample with full statistics divided by the cluster acceptance A_{cluster}, $[(N-B)_{\text{corr}} \cdot A_{\text{cluster}}]\,(p_T^Z, |y^Z|)/N_{\text{gen}}(p_T^Z, |y^Z|)$. Since the statistics per bin is sufficiently large, the number of signal events were counted instead of fitting each spectrum. The expected number of events can exactly be reproduced over almost the entire p_T^Z-$|y^Z|$ range. However, the high p_T Z-events show a systematic excess of corrected events over the expectation. Obviously, the correction factor ε_Z is slightly underestimated for high-momentum Z's. The reason for this behaviour is currently not known. Even if this effect is quite small ($< 1\%$), it will be accounted for in the systematic uncertainties.

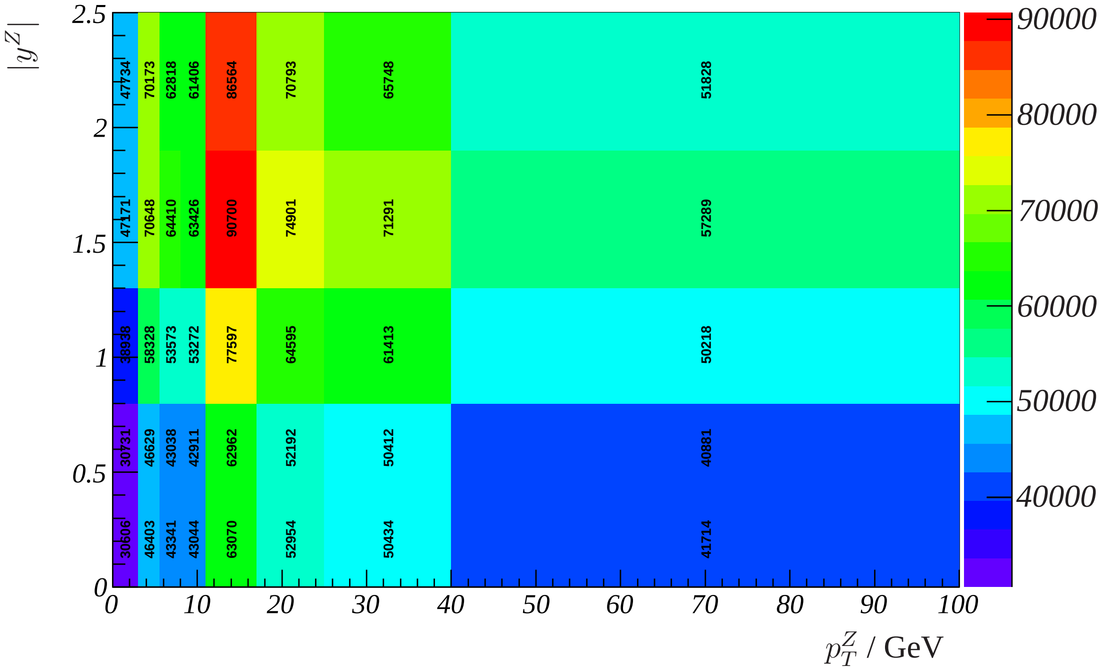

Figure 7.8: Generated number of events from the signal-only sample, full statistics.

The ratio between generated events and the corrected number of events for the combined sample is showed the bottom panel of Figure 7.9. The statistical uncertainties given by the number of events per bin and the uncertainty on the fit do not permit a proper ($\lesssim 5\%$) determination of the expected number of events.

7.9 Systematic Uncertainties

The handling of systematic uncertainties has to cover a variety of factors that might have an effect on the results of the cross-section measurement, which will be presented in Section 7.10. In the following, the various contributing uncertainties for the four “ingredients” of a cross-section measurement are going to be discussed. These four categories are

- signal selection
- efficiency correction
- acceptance
- integrated luminosity

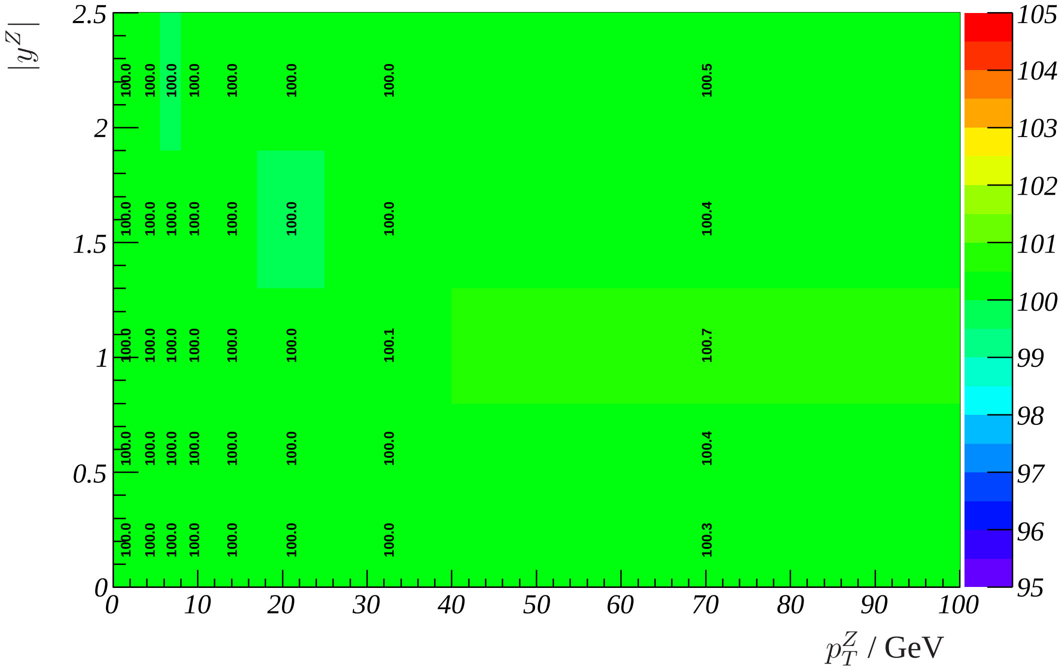

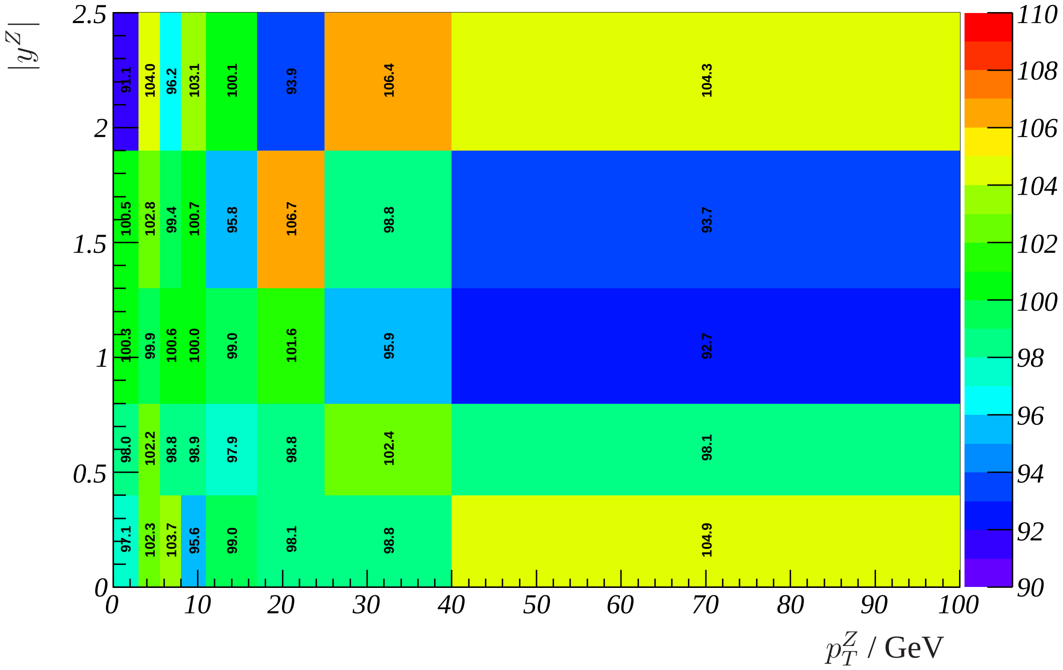

Figure 7.9: Ratio of generated and corrected number of events, see text for details. Top: signal-only sample, full statistics without fitting; the statistical errors are $\ll 1\%$. Bottom: combined sample, $L = 100$ pb^{-1}; the statistical uncertainties vary between 5.2% for bin with high statistics and 8.4% for regions with low statistics (cf. Figure 7.8). All values are given in per cent.

For the signal selection, contributions that might have an effect on the total number of selected events as well as on the background have to be checked. Apart from the estimation of the uncertainty for the background, a variation of the energy scale and possible bin migration effects were taken into account.

The systematic uncertainties for the single-electron efficiencies were already discussed in Chapter 6. However, the uncertainty on the overall efficiency factor ε_Z that has been used in this analysis is already given by the closure test shown in the top panel of Figure 7.9. Nevertheless, the tag-and-probe efficiencies will be used as an estimator for the systematic uncertainty of the efficiency correction, as it will be justified at the end of this section.

The acceptance uncertainty $\Delta\mathcal{A}/\mathcal{A}$ is mainly given by the uncertainty of the PDFs, which will be studied in Section 7.9.3. A brief discussion of the uncertainty on the luminosity is given in 7.9.5.

Due to the lack of statistics and the re-weighing problematic for the QCD-background in connection with the event numbers derived from fitting, it is obvious that a reliable treatment of systematic uncertainties for the combined sample is hardly possible. Their possible impacts become overlapped by fluctuations from the statistical uncertainty, especially in the double differential case. For completeness, explanatory results for the combined sample are shown, as well.

7.9.1 Impact of the Energy Scale

One possible contribution to the systematic uncertainty is the energy scale, which might be different in data and simulation. In order to check the impact of possible shifts, first, the acceptance and efficiencies were determined without energy-modifications. In a second step, the energy of the electrons is altered by varying their energy as a function of particle's E_T and the standard selection-criteria were applied, including the corrections to derive N_{corr} (see Equation 7.12).

The energies of the reconstructed electrons were changed by $\pm 0.5\%$ and $\pm 1.0\%$, respectively. The transverse energies of the electrons therefore changed according to

$$E_T^{\text{shifted}} = E^{\text{shifted}} \cdot \cosh \eta \,. \tag{7.13}$$

The result of the energy scale variation is shown in Figure 7.10. On the top panel, the impact on the Z's transverse momentum shows a shift of the number of produced Z bosons towards lower (higher) p_T^Z if the energy scale is altered to lower (higher) electron energies. The effect reaches up to 2% for the lowest/highest transverse momentum bin of the Z. As one would expect, the variation only has a minor effect on the rapidity of the Z, which is shown in the middle panel of Figure 7.10. For central Z bosons ($|y^Z| \lesssim 1.0$), the number of events, and hence the cross-section, is slightly larger (smaller) ($\approx 2\%$) if

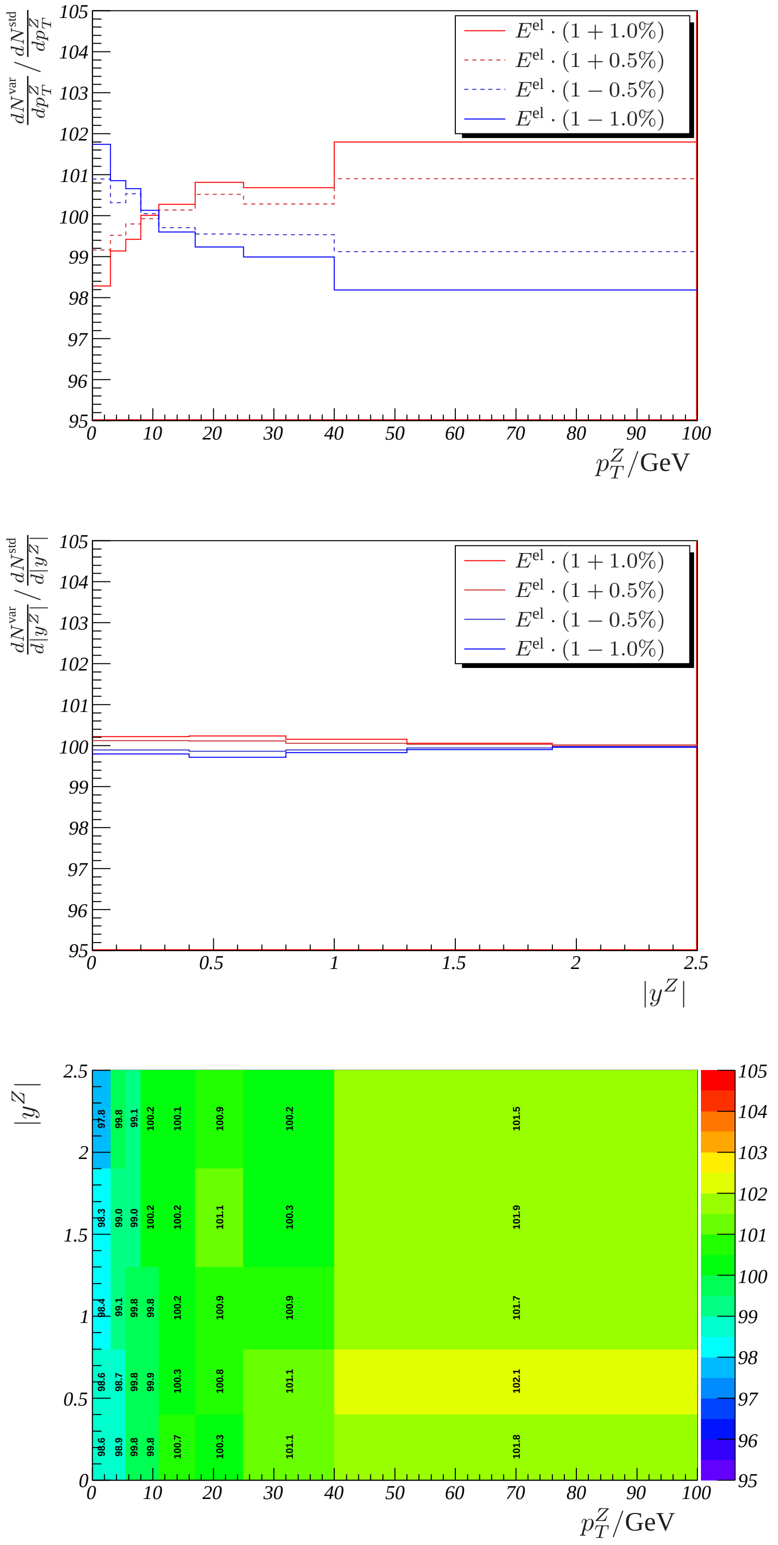

Figure 7.10: Relative systematic uncertainty due to the energy scale variation of the electron. Top: single differential versus p_T^Z. Middle: single differential versus $|y^Z|$. Bottom: $\frac{dN^{\text{var}}}{dp_T^Z d|y^Z|} / \frac{dN^{\text{std}}}{dp_T^Z d|y^Z|}$ for an energy-shift of $+1\%$. All values are given in per cent.

the energy is shifted $+1\%$ (-1%); the effect vanishes for forward Z bosons. This cross-section increase (decrease) is due to the minimal E_T cut of the electrons, which is passed for more (less) electrons.

The energy variation of $+1\%$ is exemplarily shown on the bottom panel of Figure 7.10 in bins of p_T^Z and $|y^Z|$. Obviously, the same considerations as for the single-differential distributions apply here, too. The deviation to the unbiased electron energy varies between $\approx \pm 2\%$. Inclusively, the cross-section variation caused by a shift in the energy-scale is at 0.6%.

7.9.2 Bin Migration

Independent from dealing with a simulated or a data event, one has to deal with detector imperfections and reconstruction inaccuracies in a way that a particle's location and/or energy[4] measurement might have an offset from its "real" value. The resolution studies, which were presented in Sections 6.2 and 7.3, demonstrated the effect of the reconstruction on the energy and the position of the particle of interest.

But, furthermore, the resolution effects are not only of theoretical interest, but might also have a significant impact on the analysis, itself. For example, if a Z boson is produced at a rapidity of 1.92, the reconstructed rapidity of the two electrons might be at $y = 1.89$. What seems to be a minor difference becomes a significant effect when applying the acceptance correction that is taken from Figure 7.1: Since the border of the bin is at $|y| = 1.9$, the acceptance correction that is applied is different by a factor of 2 for the given case.

This effect, called "bin migration" or "smearing", has its greatest impact on reconstructed Z bosons, as the imprecisions of both contributing electrons might add up. For completeness, the smearing on single-electron level is investigated, as well.

In order to study the bin migration between the truth-information from the simulated event and the corresponding reconstructed values, the events were pre-selected on truth level to only allow for events with a generated Z mass of 70 GeV$< M_{\text{gen}}(Z) < 110$ GeV. Each of both truth-electrons is then tried to be matched to a cluster[5] that has to pass the well-known phase-space cuts (see Section 7.2) with the minimal transverse energy cut lowered to $E_T > 10$ GeV, in order to visualise possible bin migration in and out of the acceptance region. When the cluster passes the cuts, the variable of interest (E_T or $|y|$) is filled into a histogram with its truth value on the abscissa and its reconstructed value on the ordinate. Without bin migration, the result would be a diagonal bin-population, only.

Figure 7.11 shows the results, with the expected preference for the bins on the diago-

---

[4] apart from effects due to the energy scale, which were discussed in the previous section

[5] the comparison to a reconstructed electron instead of a cluster leads to similar results, as the parameters for both are taken from calorimeter-variables

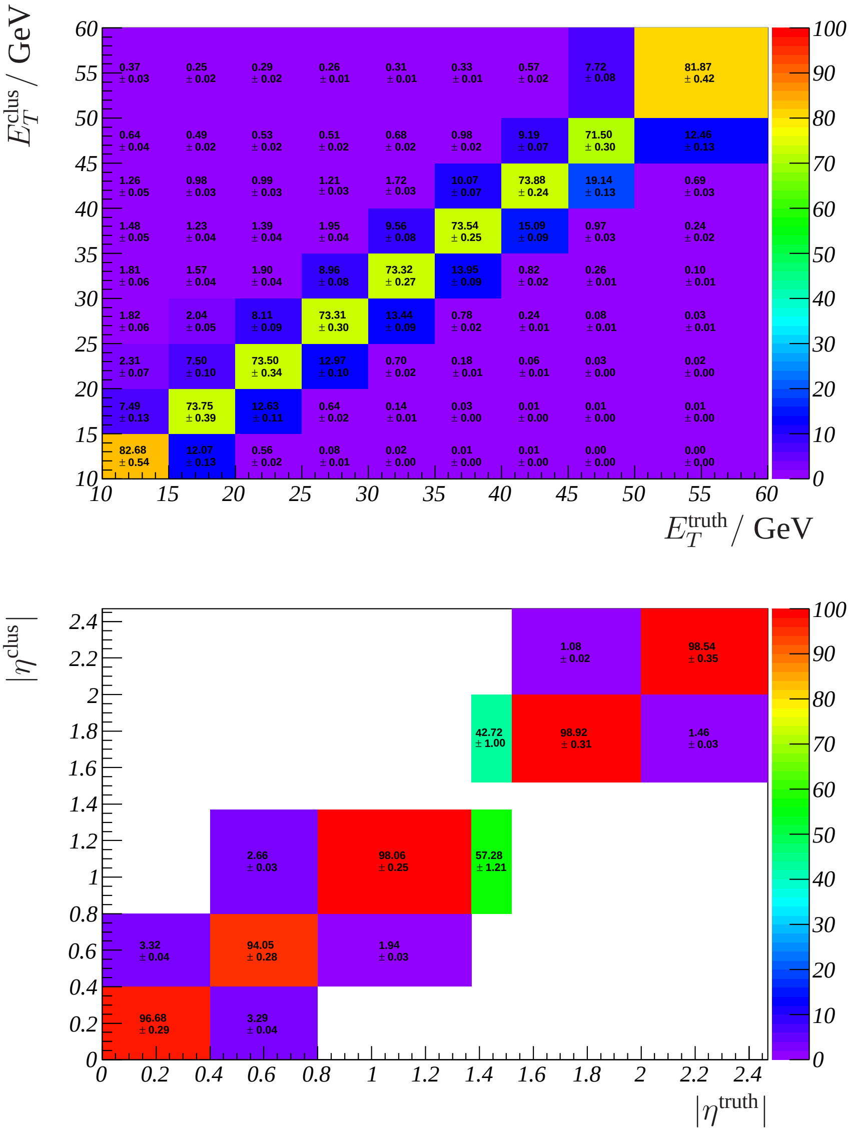

Figure 7.11: Bin migration between reconstructed clusters and associated truth electrons, including statistical uncertainties. Top: transverse energy (highest E_T-bin skipped for better illustration). Bottom: smearing in bins of $|\eta|$. All values are given in per cent.

nal. For the transverse energy distribution, however, the smearing is much more distinct as for η: Approximately three out of four clusters become reconstructed in the predetermined bin, whilst the remaining $\approx 25\%$ are almost completely shared by the adjacent bins. Due to bremsstrahlung, the sharing is biased to lower E_T-values, which can also be seen in the Figure.

The determination of the bin migration for the reconstructed Z boson uses the same algorithm as the acceptance determination given in Section 7.4: Each pair of clusters has to fulfil the truth-matching, the phase space and the invariant-mass criteria. If successful,

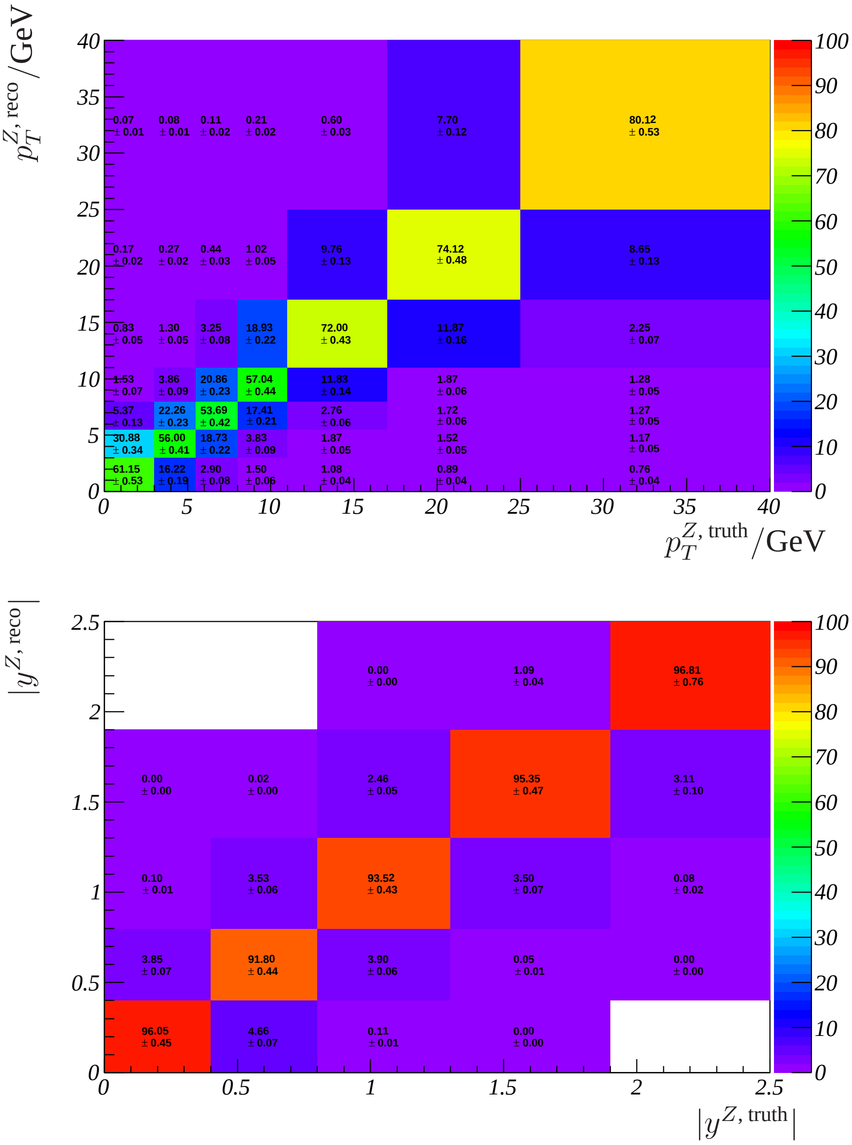

Figure 7.12: Bin migration between reconstructed and associated truth Z-bosons, including statistical uncertainties. Top: transverse momentum (highest p_T^Z-bin skipped for better illustration). Bottom: smearing in bins of Z rapidity, $|y^Z|$. All values are given in per cent.

the transverse momentum and the rapidity of the reconstructed Z is plotted versus the information from the truth-variables.

As it can be seen in Figure 7.12, the migration effect in terms of Z rapidity is quite small, at a few-percent level. The deviations in p_T^Z are significantly larger ($\approx 50\%$), however, as the acceptance distribution is pretty flat in that variable, the mis-correction due to smearing thus becomes small. To study the effects of the smearing quantitatively, the standard selection-process—as described in Section 7.2—has been altered such that the reconstructed particles were replaced by the truth particles. The corrections (efficiency and acceptance) were applied like for the standard selection and compared to the results from Section 7.8. It is obvious that there is no physical statement behind these corrections, as the efficiencies themselves would have to be adapted in order to give a meaning to the absolute numbers. The systematic uncertainty, which may arise from bin migration, however, can be estimated with this method.

The results are shown in Figure 7.13. The fluctuation for the signal-sample is in the order of $\approx 1\%$, independently from the binning in p_T^Z or Z rapidity. Only shown for comparison is the effect of bin migration for the combined sample, which is limited to an integrated luminosity of 100 pb^{-1}: As the fluctuations within the single-differential distributions are at least comparable to the ones in the signal-only case, the lack of statistics completely superimposes the effects from bin migration.

For the inclusive event selection, bin migration does not play a role obviously. However, by limiting the Z acceptance to a certain p_T^Z-rapidity window, bin migration might happen at the edges, causing Z bosons that have been generated *outside* the window to become reconstructed *inside* of it, and vice versa. The effect is found to be negligibly small ($\ll 1\%$).

Even though the total number of selected events is unaffected by smearing due to limited resolution, the weights that are applied per event might become distorted by bin migration and hence increase the systematic uncertainty on the total cross-section. By applying the previously described method, an overall uncertainty of 1.1% on the number of corrected events has been determined.

If the energy resolution in data is worse than in the simulation, the effect of bin migration will increase since both effects are correlated. With a broadened energy resolution for both electrons, the probability to reconstruct the Z in the right p_T^Z bin decreases.

With a broadened resolution in data, the energies of both electrons are measured worse, which leads to an increased probability that a Z boson is reconstructed in a different bin.

7.9.3 Parton Density Functions

Another possible source that might effect the determination of the cross-section is the choice of the Parton Density Functions (PDFs). The PDFs, which were introduced in Chapter 2, describe the fraction of the proton's momentum, that each constituent within the proton carries.

Even though the PDFs have been measured very precisely at H1 and ZEUS, the parameterisation of the PDFs in the Monte-Carlo generator suffer from the need to extrapolate these results to the energy scale at the LHC. Hence, the simulated process $pp \to \gamma^*/Z + X$ might be sensitive to imperfect description of the quark's momenta and lead to different acceptance for the Z boson.

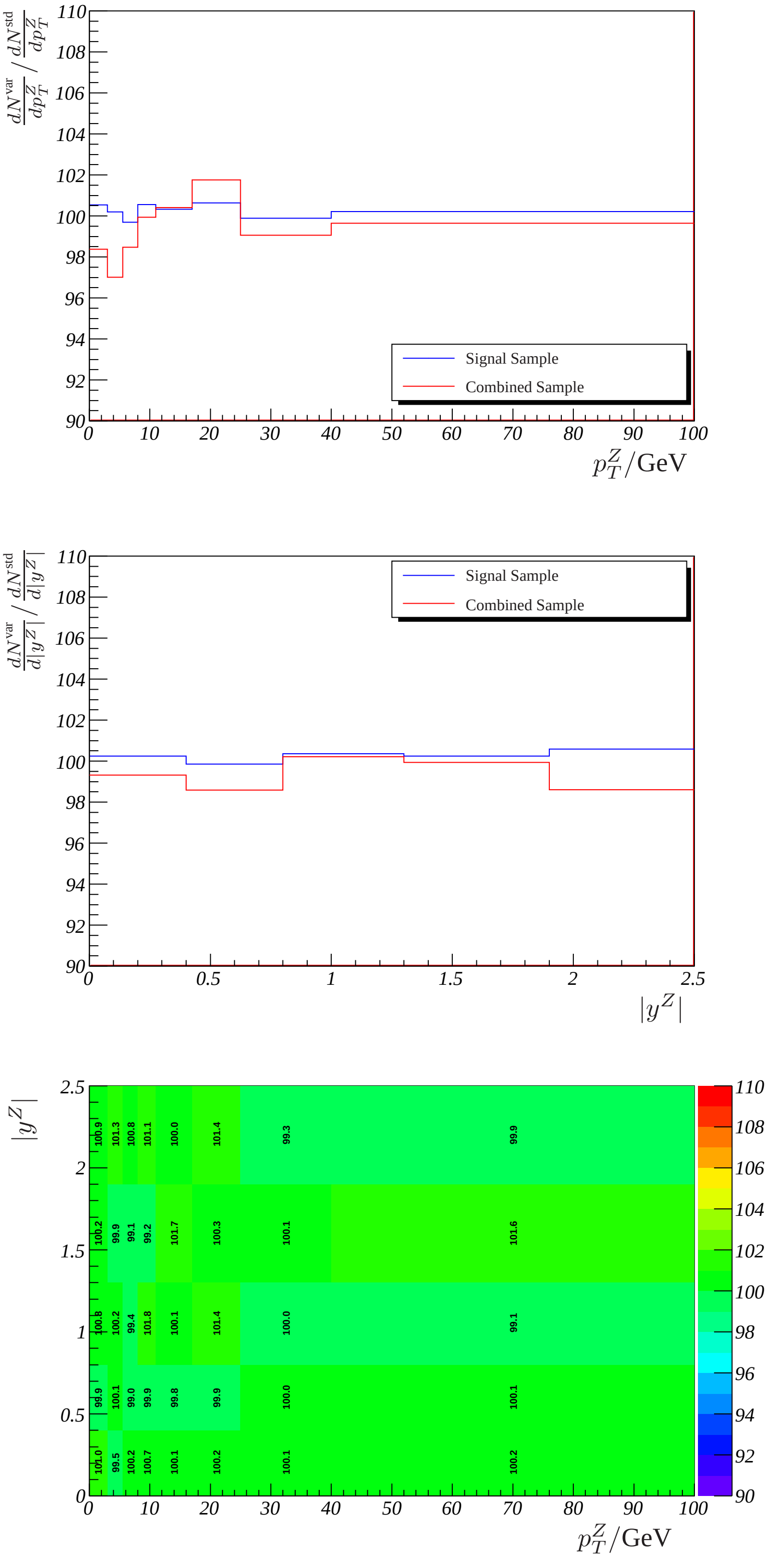

Figure 7.13: Relative systematic uncertainty from bin migration. Top: single differential versus p_T^Z. Middle: single differential versus Z rapidity. Bottom: double differential (signal only), $\frac{dN^{\mathrm{var}}}{dp_T^Z d|y^Z|} / \frac{dN^{\mathrm{std}}}{dp_T^Z d|y^Z|}$ All given values are given in per cent.

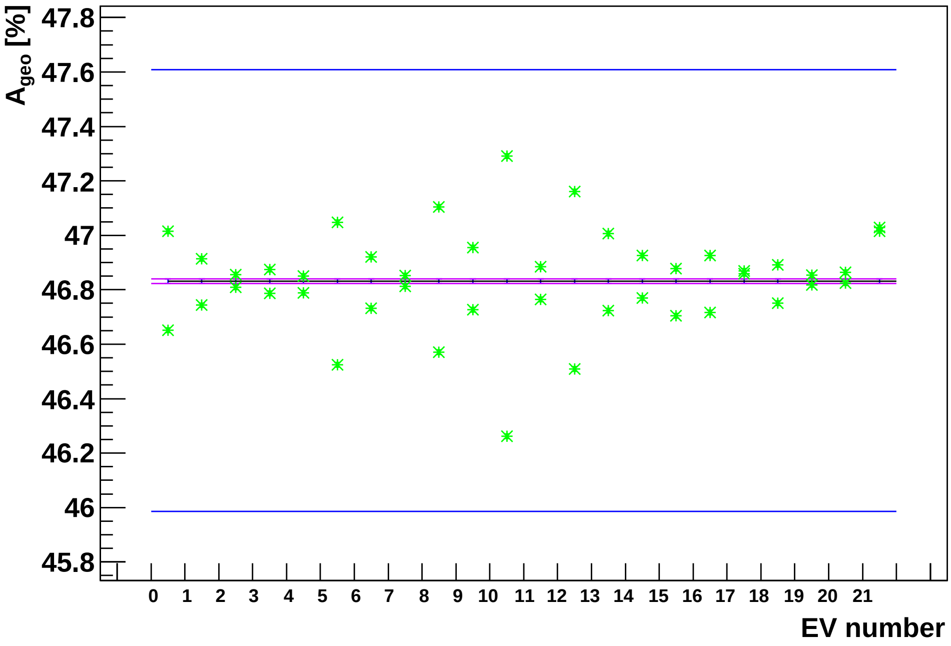

Figure 7.14: Overall Z acceptance for each variation ("up" and "down") of the eigenvectors, parametrising the PDF uncertainties. See text for details. Figure taken from [16].

In order to study the uncertainties on the acceptance that might arise from the limited knowledge of the PDFs, the acceptance was calculated for central electrons, $|\eta| < 2.47$, which were located outside the crack region, $1.37 > |\eta| > 1.52$. To reject low-momentum electrons, the minimal transverse momentum is required to be more than 15 GeV. Even if the definition of the acceptance is somewhat different from the one in this thesis, the conclusions are still applicable.

Since the leading order (LO) PDFs within MC08 lead to imperfect shapes of parameters, such as p_T and rapidity distributions, the MC09 production has been used to determine the systematic uncertainties arising from the PDFs. In this context, the results from Reference [16] are shown, since the level of detail could not be matched within this analysis, which in return also contributed to other parts of the Note.

A Monte-Carlo set with the ATLAS MC09 tune (see Reference [23]) and the NLO set CTEQ6.6 (see Reference [66]) has been produced. In order to keep the statistical error well below 0.1% for all bins, even in the double-differential illustration, the sample contains 68×10^6 events. The CTEQ-parametrisation of the uncertainties on the PDFs happens in 22 eigenvectors. Each eigenvector can be varied up and down, which gives a total of 44 error set PDFs. By calculating the acceptance for each set, its shifting in comparison to the mean value for the acceptance is a measure for the systematic uncertainty.

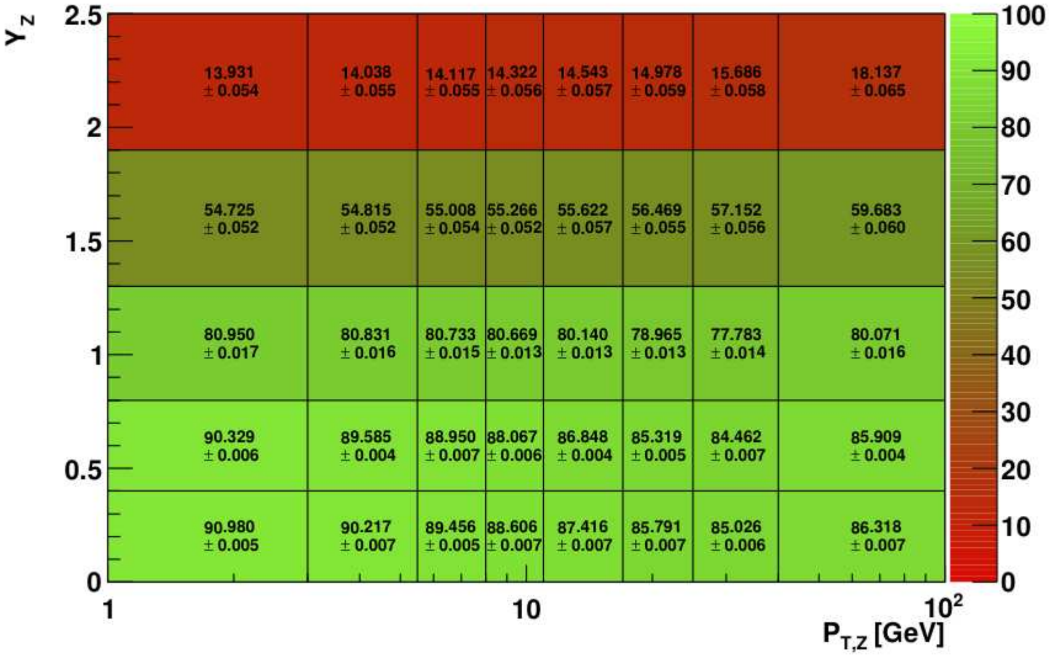

Figure 7.15: Double differential illustration of the acceptance and the absolute systematic uncertainty for two central electrons outside the crack region in bins of p_T^Z and $|y^Z|$. All values given are in percent. Figure taken from [16].

Figure 7.14 shows the result: each error set's inclusive acceptance is represented as a data point and gives two values for each eigenvector. Without the restriction to $p_T^Z < 100$ GeV and $|y| < 2.5$, respectively, 46.8% of the generated Z bosons have passed the given cuts. The magenta line shows the statistical error band, which is completely negligible. The overall systematic uncertainty of 0.8% is derived by adding in quadrature the deviations of the error sets from the mean value and is represented as blue lines in Figure 7.14. By restricting the generated Z bosons to the given values, the acceptance increases to 63.0%, whilst the systematic uncertainty decreases to 0.45%. This is due to the fact that a significant contribution to the uncertainty arises from generated Z events in the very forward direction.

In addition to the inclusive acceptance, the systematic uncertainties have also been studied for the single differential and the double differential acceptances, as well. Since for the non-inclusive cases the cross-sections will be determined including the kinematic and rapidity restriction on the Z, only corresponding uncertainties will be shown.

The absolute systematic uncertainty for the double differential acceptance is given in Figure 7.15. Although the effect of a growing uncertainty with increasing rapidity is visible, the relative error in every bin is at the per-mill level or well below, thus its contribution to the overall uncertainty in 7.9.6 can be neglected.

7.9.4 Background Estimation

As described in Chapter 4, the largest source of background comes from QCD-dijet events, that become misidentified as electrons. Even though these processes have an enormous cross-section, the jet suppression in ATLAS works so well that it is almost impossible to produce a simulated sample with sufficient amount of statistics in order to be able apply all selection criteria (see Sections 6.6.2 and 7.2). The mandatory re-weighting might distort the shape of the QCD background and lead to imperfect reproduction of total number of background events, either in the inclusive case or when binned in p_T^Z and/or $|y^Z|$.

Beyond that, the knowledge of the given QCD cross-section itself suffers from an uncertainty of $\approx 20\%$, due to the ignorance of non-pertubative corrections in the QCD models.

In order to estimate possible biases from the imperfect knowledge of the mainly contributing source of background, the impact of a $\pm 40\%$ variation of it on the resulting cross-section is studied. For the inclusive cross-section, the effect is almost negligibly small ($\lesssim 1\%$), whilst it increases for the single differential distributions to $\approx 2\%$ in all bins and becomes largest in the double differential case ($\approx 5\%$).

The systematic uncertainties in the binned distributions is averaged over all bins and is therefore applied as a constant bias for all bins of a certain distributions.

7.9.5 Luminosity Uncertainty

The description of the possible ways to measure the instantaneous luminosity has been given in Section 3.6, together with the expected uncertainty for each method. For this analysis, the uncertainty on the luminosity is assumed to be 10%, as the knowledge of the luminosity in the early data-taking stage of the ATLAS experiment will also be limited to this order of magnitude.

7.9.6 Treatment of Systematic Uncertainties

As it has already been mentioned in Chapter 6, the lack of a simulation of the process $pp \to \gamma^*/Z + X \to e^+e^- + X$ with a different generator than `PYTHIA` limits the extend of systematic uncertainty studies. In this analysis, the presented uncertainties are either considered to be fully correlated or bin-wise uncorrelated. The correlated errors deal with methodological uncertainties like detector alignment and energy calibration, whilst the uncorrelated uncertainties are given by the limited statistics of the simulation sample, e.g., the statistical uncertainty of the energy calibration. This can be estimated by determining the RMS of the derived set of cross-sections, calculated from different event-sets.

	Systematic	Uncertainty
Efficiencies	ΔR cut	$\ll 1\%$
	FSR	$\ll 1\%$
	Efficiency determination $\delta\varepsilon$	3.6%
	Tag selection	1.3%
	MC generator	0.5%
Selection	Energy scale	0.8%
	Bin migration	1.1%
	QCD cross-section	$\ll 1\%$
	Acceptance (PDFs)	0.8%
	Luminosity	10%

Table 7.4: Contributions to the systematic uncertainty of the inclusive cross-section measurement.

By varying the source of the systematic uncertainty, the resulting cross-section variation from the nominal value, σ, is determined, σ^- and σ^+. This yields the systematic uncertainties $\delta^- = \sigma^- - \sigma$ and $\delta^+ = \sigma^+ - \sigma$, which are symmetrised for simplification as $\delta = \frac{1}{2}(\delta^- - \delta^+)$. The contribution of the identification efficiency (see below) has been symmetrised in this way, for instance.

The systematic uncertainties are listed in Table 7.4 with their impact on the different contributions for the inclusive cross-section determination. They all were determined by the methods presented here and in Chapter 6. The main contribution for the differential cross-sections are given by the energy-scale and the efficiency determination.

In this context, the uncertainty on the efficiency ε_Z plays a special role. As mentioned before, usually more than one generator and hence simulated sample is needed to determine the uncertainty of the efficiency correction. This can be done by determining the efficiencies within the simulated “data” sample and use the deviations in the efficiencies from a “control” sample with respect to the simulated data sample as uncertainties (cf. Reference [16]). Within this analysis, no control sample was available. Therefore, the only way to estimate the uncertainty on ε_Z is to use the deviations between tag-and-probe method and truth efficiencies shown in Chapter 6 and calculate a systematic uncertainty on ε_Z inclusively and differentially:

$$\delta\varepsilon = \left.\frac{\varepsilon_{\text{t\&p}}}{\varepsilon_{\text{truth}}}\right|_{\text{reco}} \oplus \left.\frac{\varepsilon_{\text{t\&p}}}{\varepsilon_{\text{truth}}}\right|_{\text{ID}} \oplus \left.\frac{\varepsilon_{\text{t\&p}}}{\varepsilon_{\text{truth}}}\right|_{\text{L1}} , \tag{7.14}$$

where the relative deviation between the single-electron efficiencies determined by the tag-and-probe method and the truth efficiencies are added in quadrature.

In the early phase of data taking, the main contribution to the systematic uncertainty comes from the measurement of the luminosity. Later on, the luminosity measurement is expected to become improved to a level of $\sim 5\%$.

7.10 Expected Accuracy of the Cross-Section(s)

As it was stated several times in this chapter, that the initial formula (Equation 7.1) to determine cross-sections is simplified. Neither does the formula account for corrections on event level, nor does it include possible binning in variables of the Z boson.

In the recent sections, the different ingredients needed to calculate the cross-section were determined and their systematic uncertainties have been discussed. At this stage, and starting from Equation 7.1, all parameters are known:

$$\sigma(p_T^Z, |y^Z|) = \frac{1}{\mathcal{A} \cdot \varepsilon_F \cdot \mathscr{L}} \sum_{\text{events}} \left[\frac{w}{\varepsilon_Z}(p_T^Z, |y^Z|) \right] \cdot \beta(p_T^Z, |y^Z|)\,. \tag{7.15}$$

This representation of the double-binned cross-section simplifies to the single-differential cross-sections by integrating over p_T^Z or $|y^Z|$, respectively, and results in the total cross-section when integrating over both. The parameter β in Equation 7.15 is the correction factor that accounts for the bin size, thus, in the double-differential case, is expressed as $\beta(p_T, |y|) = 1/(\Delta p_T^Z \cdot \Delta |y^Z|)$ and is $\equiv 1$ for the total cross-section, trivially.

In the following sections, the final results of the cross-section reproduction will be presented.

7.10.1 Total Cross-Section

The total cross-section measurement has to ensure that the number of events generated by the Monte-Carlo simulation and thus the cross-section can be reproduced in case of the signal-only sample as well as for the combined sample that, additionally, went through re-weighting, rescaling and fitting processes.

In total, $3{,}023{,}412$ events were available, which corresponds to an integrated luminosity of $\mathscr{L} = 2.846$ fb^{-1}. As stated before, the signal sample makes use of all the statistics available, whilst the combined sample is limited to 100 pb^{-1}, in order to reflect measurements during early data-taking of the experiment.

After selection, $760,017$ events remained in case of the background-free signal sample. After re-weighting on event level to account for acceptance and efficiencies, as well as luminosity and filter corrections, the following cross-section has been derived:

$$\sigma_{\text{signal}}(pp \to \gamma^*/Z + X \to e^+e^- + X; p_T^Z < 100\ \text{GeV}, |y^Z| < 2.5) = (856.0 \pm 0.8_{\text{stat}})\ \text{pb}\,. \tag{7.16}$$

The whole analysis was based on the restricted invariant mass window. Thus, by considering the limited acceptance a_l, the total input cross-section can perfectly be reproduced:

$$\sigma_{\text{signal}}(pp \to \gamma^*/Z + X \to e^+e^- + X) = (1147.0 \pm 1.0_{\text{stat}})\ \text{pb}\,. \tag{7.17}$$

The agreement on this level was expected, as both, the corrections and the selected events originate from the same, background free, Monte-Carlo sample.

More interesting is the extraction of the cross-section in case of the combined sample. Subsequent to the selection process, the signal and each background sample have been scaled to the same integrated luminosity in order to create a data-like combined sample. A fitting algorithm than had to extract the amount of signal and background events. With this method, the following result was obtained:

$$\sigma_{\text{combined}}(pp \to \gamma^*/Z + X \to e^+e^- + X) = (1162.2 \pm 18.0_{\text{stat}} \pm 48.5_{\text{syst}} \pm 116.2_{\text{lumi}})\ \text{pb}\,. \tag{7.18}$$

The deviation of 1.3% from the input value of 1147.0 pb lies within the statistical uncertainty.

7.10.2 Single Differential Cross-Sections

The resulting single differential cross-sections are shown in Figure 7.16 and Figure 7.17, respectively. These have been calculated using Equation 7.15 whilst integrating over the remaining variable. Each plot shows the cross-section on generator level, the reproduced cross-section for the signal sample with full statistics as well as the combined sample for an integrated luminosity of 100 pb^{-1}. The associated ratio gives the ratio of the combined sample and the expectation from the generator, together with the statistical and combined systematical uncertainty. The Z acceptance is limited to $p_T^Z \leq 100$ GeV and $|y^Z| \leq 2.5$.

Figure 7.16 shows a very good reconstruction of the cross-section versus the transverse momentum of the Z. The distribution shows the expected behaviour with a decreasing cross-section with increasing p_T^Z, and the except for the first, most central bin, which has a significantly lower cross-section. The fluctuation is well covered by the statistical uncertainty and the integral of the distribution gives

$$\sum \frac{d\sigma}{dp_T} \Delta p_T^Z = (859.6 \pm 8.8_{\text{stat}})\ \text{pb}\,. \tag{7.19}$$

as a crosscheck to Equation 7.16. The main contribution to the systematic uncertainty comes from the effects in the identification efficiency at low E_T.

The same considerations as for the transverse-momentum analysis also hold for the cross-section measurement versus the rapidity of the Z (Figure 7.17). The corrections work perfectly for the signal-only case, where the generated spectrum is exactly reproduced. The combined sample also shows a very good agreement within the statistical

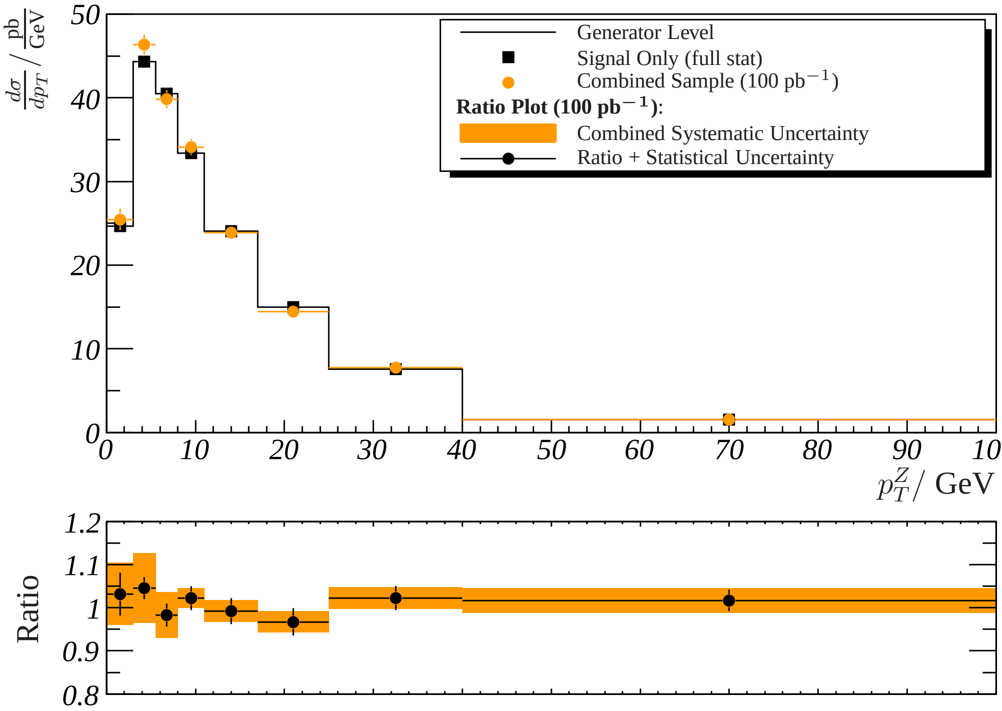

Figure 7.16: Single differential cross-section determination versus p_T^Z with the cross-section on generator level in comparison to the signal-only and the combined determination. The bottom plot gives the ratio between generator level and combined sample as well as the appropriate errors.

uncertainty. This underlines the possibility to measure the cross-section accurately with an integrated luminosity of only $100\ \text{pb}^{-1}$. The total cross-section can also be reproduced very accurately:

$$\sum \frac{d\sigma}{d|y^Z|}\Delta|y^Z| = (862.9 \pm 7.1_{\text{stat}})\ \text{pb}\,. \tag{7.20}$$

The statistical errors are calculated by error propagation from the statistical uncertainty per bin and the uncertainty on the fit parameters.

7.10.3 Double Differential Cross-Section

The cross-section on generator level shows Figure 7.18. As for the single differential cross-sections it has been derived by counting the number of generated Z bosons per p_T^Z-$|y^Z|$ bin on truth level, thus, without any cuts besides the limitation to the acceptance.

In Figure 7.19 shown is the double differential cross-section as determined from the combined sample that was limited to $100\ \text{pb}^{-1}$. In order to enhance the readability, the binning was chosen to be equidistant, rather than to represent the actual scale as in 7.18.

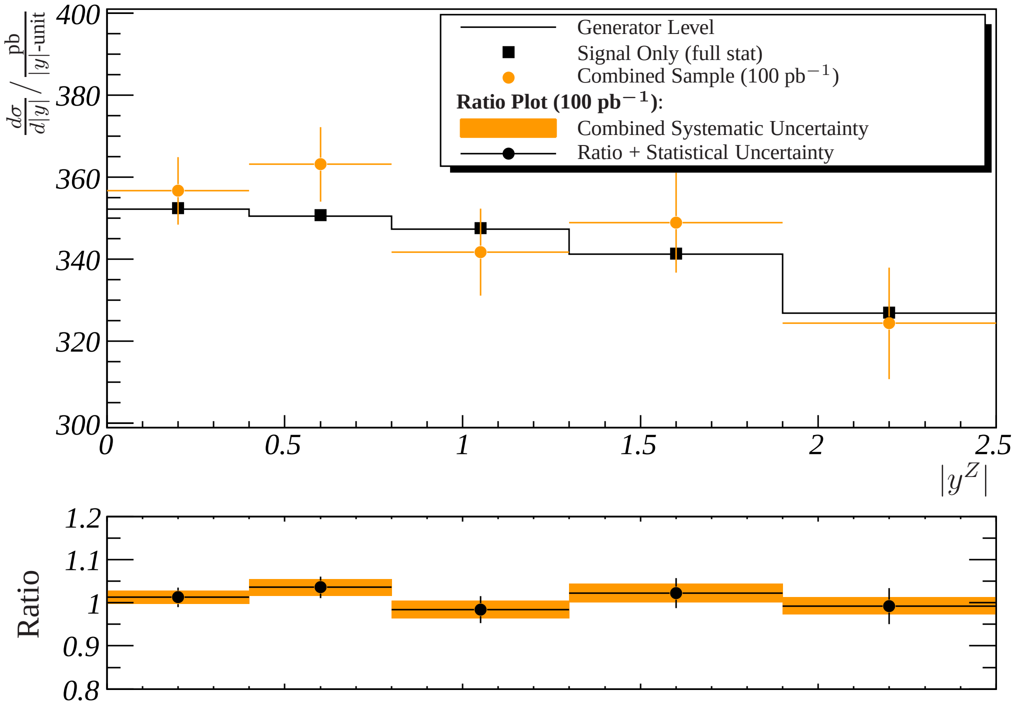

Figure 7.17: Single differential cross-section determination versus $|y^Z|$ with the cross-section on generator level in comparison to the signal-only and the combined determination. The bottom plot gives the ratio between generator level and combined sample as well as the appropriate errors.

With the information available from the simulation (see Section 7.7) an accurate reproduction of the cross-section can be accomplished. However, the variation due to the statistical fluctuations can reach almost 10 percent for some bins. Given that the corrections as well as the signal events originate from the same simulation, the deviation can be considered as large. The errors given in Figure 7.19 are the combined statistical and systematical uncertainties. They reflect the difficulty to derive a meaningful cross-section double differentially for a sample containing $100\ \text{pb}^{-1}$. For completeness, the double-integral reproduces nicely the total cross-section as given in Equation 7.16, which confirms the statistical origin of the deviations:

$$\sum\sum \frac{d^2\sigma}{dp_T^Z d|y^Z|} \Delta p_T^Z \Delta|y^Z| = (856.4 \pm 10.2_{\text{stat}})\ \text{pb}\,. \tag{7.21}$$

7.11 Summary

In this chapter, the procedure to determine inclusive and differential cross-sections has been demonstrated. From the analysis point of view, no *a priori* differentiation between a

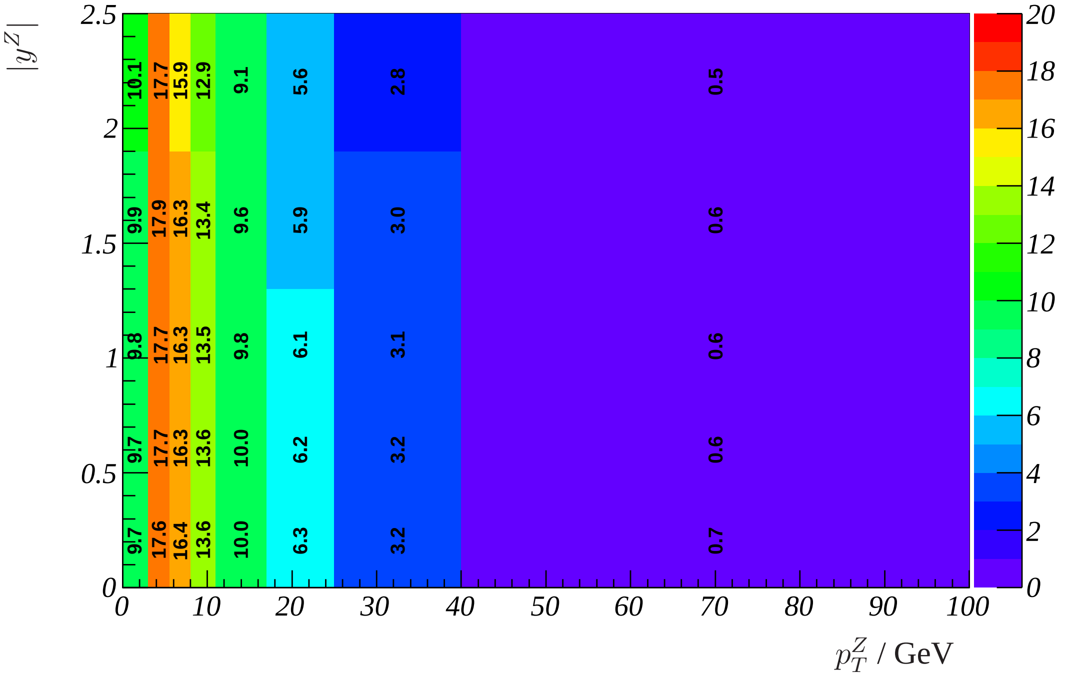

Figure 7.18: Double differential cross-section $d^2\sigma/(dp_T^Z d|y^Z|)$ in bins of p_T^Z and $|y^Z|$ on generator level. All values given are in $\mathrm{pb}/(\mathrm{GeV}\cdot y\text{-unit})$.

simulation-based analysis and an analysis with first data from the ATLAS experiment has been made. Instead, the necessary steps to derive the cross-section were introduced and special aspects for a simulation-based analysis were discussed separately. In later stages of the ATLAS experiment, especially when the centre-of-mass energy provided by the LHC is at its design value of $\sqrt{s} = 14$ TeV, some parameters in the event selection will have to become adjusted, e.g., in order to account for pile-up.

With the results shown in the previous section it has been demonstrated that an inclusive and a single differential cross-section measurement with data corresponding to $\lesssim 100\ \mathrm{pb}^{-1}$ is possible. The systematic uncertainties are a few per cent and agree well with similar analysis like given in References [50] and [16]. The limiting factor will especially during the period of early data-taking will be the poor knowledge of the integrated luminosity, which will become improved over time. In summary, the expected uncertainties on the cross-section determination for the combined sample are:

$$\frac{\Delta\sigma(pp \to \gamma^*/Z + X \to e^+e^- + X)}{\sigma(pp \to \gamma^*/Z + X \to e^+e^- + X)} = 1.5\%_{\text{stat}} \pm 4.2\%_{\text{syst}} \pm 10\%_{\text{lumi}}\,. \tag{7.22}$$

However, with the improvement on the knowledge of the luminosity, which is expected to reach $\sim 5\%$ in the future, an improvement of the systematic uncertainty is desirable. One contribution in order to minimise the systematic uncertainty might be an advanced

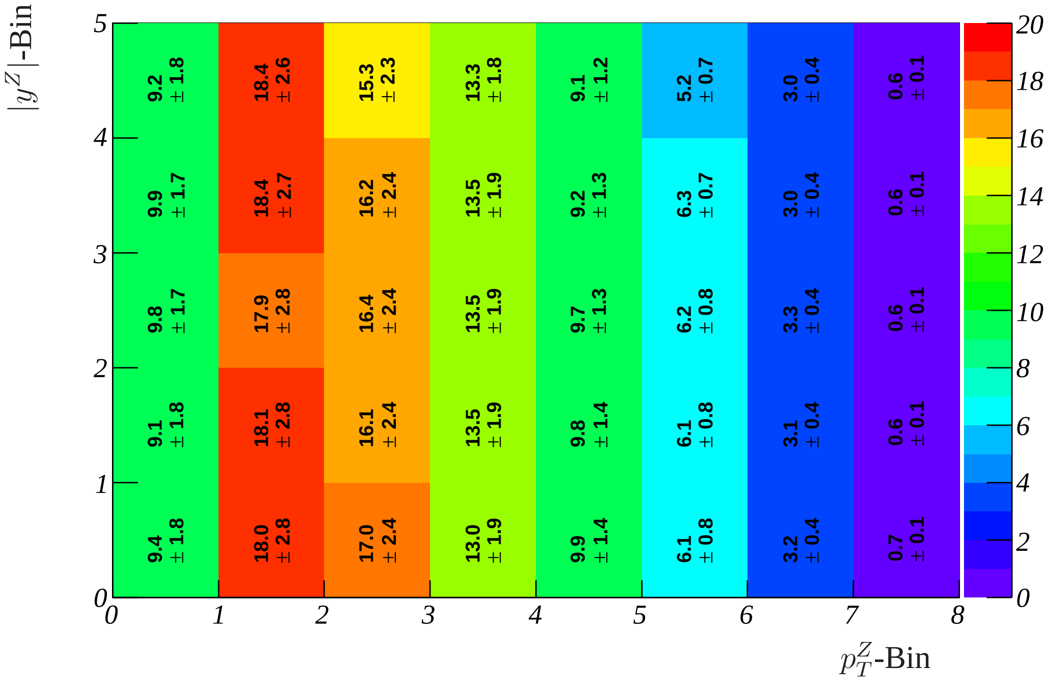

Figure 7.19: Double differential cross-section $d^2\sigma/(dp_T^Z d|y^Z|)$ in each bin of p_T^Z and $|y^Z|$ for the combined sample with an integrated luminosity of 100 pb^{-1}. The errors shown are the combined statistical and systematical uncertainties, the uncertainty on the luminosity is not included. All values given are in pb$/(\text{GeV} \cdot y\text{-unit})$.

efficiency determination that will be introduced in the next chapter.

8

Calculation of the Efficiency Correction

8.1 Introduction

In Chapter 6 the single-electron efficiencies have been determined via two independent methods. The truth efficiencies can only be derived from simulation studies, whilst the tag-and-probe method can be applied to data in order to determine the efficiencies independently from inaccurate detector description within the simulation. As it was shown, the truth efficiencies can be reproduced very accurately with the tag-and-probe method for most parts of the E_T-η plane, which underlines the functioning of this data-driven method.

In order to make use of the single-electron efficiencies to calculate a cross-section like shown in Equation 7.1, the various contributions have to be combined to a single correction factor. The aim in this context is to find a method that is also applicable to data, rather than only relying on simulation-based methods. In order to avoid any additional effects arising from combinatorial background, the studies presented in the following are based on truth-matched signal events.

8.2 Standard Approach

The idea behind this commonly used approach (cf. References [71], [50]) is to use the two-dimensional single-electron efficiencies derived in Chapter 6 to calculate the overall efficiency that will be applied to correct each selected Z event. The advantage of this method is its applicability on data with very low integrated luminosity, since the electrons are treated separately to determine the correction factor. The method will now be outlined, briefly.

After selection of a suitable Z candidate, the electrons' transverse energies and η positions are used to look up the individual efficiencies of the electrons. By treating them independently from each other, possible correlations between the particles are being

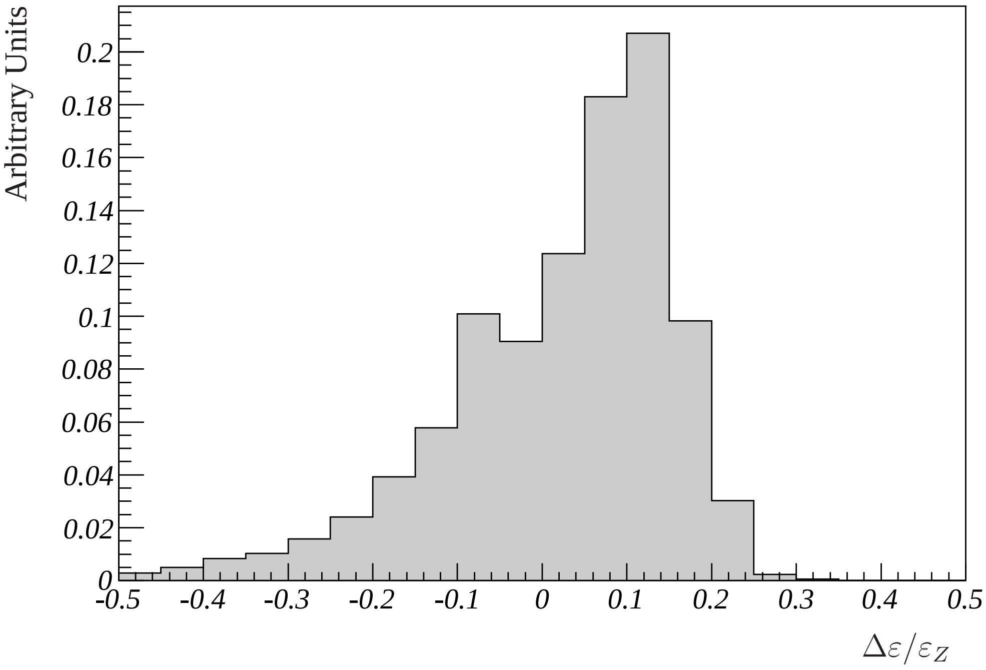

Figure 8.1: Relative deviation between the efficiency factors $\varepsilon_{\text{corr}}$ and ε_Z as described in the text, $(\varepsilon_{\text{corr}} - \varepsilon_Z)/\varepsilon_Z$.

neglected. Hence, the overall efficiency can be calculated by factorising[1] the individual contributions:

$$\varepsilon_{\text{corr}} = \varepsilon_{\text{el1}}^{\text{reco}} \cdot \varepsilon_{\text{el2}}^{\text{reco}} \cdot \varepsilon_{\text{el1}}^{\text{ID}} \cdot \varepsilon_{\text{el2}}^{\text{ID}} \cdot \varepsilon_{\text{el1}}^{\text{q}} \cdot \varepsilon_{\text{el2}}^{\text{q}} \cdot \left(\varepsilon_{\text{el1}}^{\text{L1}} + \varepsilon_{\text{el2}}^{\text{L1}} - \varepsilon_{\text{el1}}^{\text{L1}} \cdot \varepsilon_{\text{el2}}^{\text{L1}}\right) , \tag{8.1}$$

with $\varepsilon_{\text{el1,2}}^{i} = \varepsilon_{\text{el1,2}}^{\text{i}}(E_T, |\eta|)$. This factorisation can be used if all the requirements are equally applied to both electrons, except for the trigger efficiency. As only one of the electrons is required to have an associated level-1 object (see Section 7.2), the efficiency is calculated from the probability that at least one electron fires the trigger.

If N is the number of generated Z events within the acceptance, then, after applying the selection criteria as also outlined in Section 7.2, the efficiency-corrected number of Z events, N_{corr}, should equal N in order to determine a cross-section. With the application of the event-based correction with $\varepsilon_{\text{corr}}$, the result yields

$$\frac{N_{\text{corr}} - N}{N} \approx 0.9\% , \tag{8.2}$$

which shows that the correction seems to work. However, the correction factor that has been calculated in Equation 8.1 can be compared to an overall correction factor, ε_Z, for both electrons within the event, which is computed simply by mirroring the selection steps within the simulation and has been used for the cross-section determination in the previous Chapter (see Section 7.5).

---

[1] see Section 7.5 for details

The result of this comparison is shown in Figure 8.1. The distribution is distorted compared to the Gaussian-like behaviour that one would naively expect. The maximum is shifted towards higher correction factors, with a long tail for events where the correction is too small. This distinct tail is responsible for the fact that the integral over this distributions favours an overall-deviation close to zero. Thus, Equation 8.2 gives the correct number ($\mathcal{O}(\Delta N/N)1\%$) of (corrected) events. Obviously, the underlying correlations mostly cancel out for the inclusive treatment of $\varepsilon_{\text{corr}}$.

The behaviour of $varepsilon_{\text{corr}}$ that has been demonstrated in Figure 8.1 raises some questions to the use of Equation 8.1. In order to study this in more detail, the correction factor $\varepsilon_{\text{corr}}$ is calculated and compared to ε_Z in bins of p_T^Z and $|y^Z|$. This is an essential test if one wants to calculate single or double differential cross-sections.

Again, the event-by-event correction factor from Equation 8.1 is compared to an overall factor for both electrons, which is derived by mirroring the standard-selection steps. This time, the relative deviation is sub-divided in bins of p_T^Z and $|y^Z|$ (see Section 7.3), leading to the result shown in Figure 8.2, where the shape of the distribution

$$\frac{\varepsilon_Z(p_T^Z, |y^Z|) - \varepsilon_{\text{corr}}(p_T^Z, |y^Z|)}{\varepsilon_Z(p_T^Z, |y^Z|)}$$

strongly varies over the p_T^Z-$|y^Z|$ plane. Only a few bins show an acceptable replication of the efficiency correction ε_Z. Especially bins in mid-rapidity regions ($0.4 < |y^Z| \leq 1.3$) have a double-dip structure, where possibly correlations between the two electrons might have an impact.

It is obvious that there are underlying effects preventing the efficiencies to become reproduced correctly. As one can see in Figure 8.3, which shows the ratio N_{corr}/N double differentially, the effect leads to quite massive deviations from the expected number of events per bin in the order of up to 10%. This makes it impossible to determine the correct number of events—and hence the cross-section(s)—with this approach.

Under the assumption that the occurring effects are indeed related to correlations between the final-state electrons, the efficiencies have to be based on information from *both* electrons, rather than considering them separately. In the next Section, a new ansatz that is inspired by work (cf. Reference [51]) from the ATLAS collaboration is presented to account for possible correlation effects.

8.3 4 Dimensional Efficiencies

In the previous Section, the correction factor $\varepsilon_{\text{corr}}$, which included all efficiency correction for a cross-section determination, was introduced. It was shown that this correction does

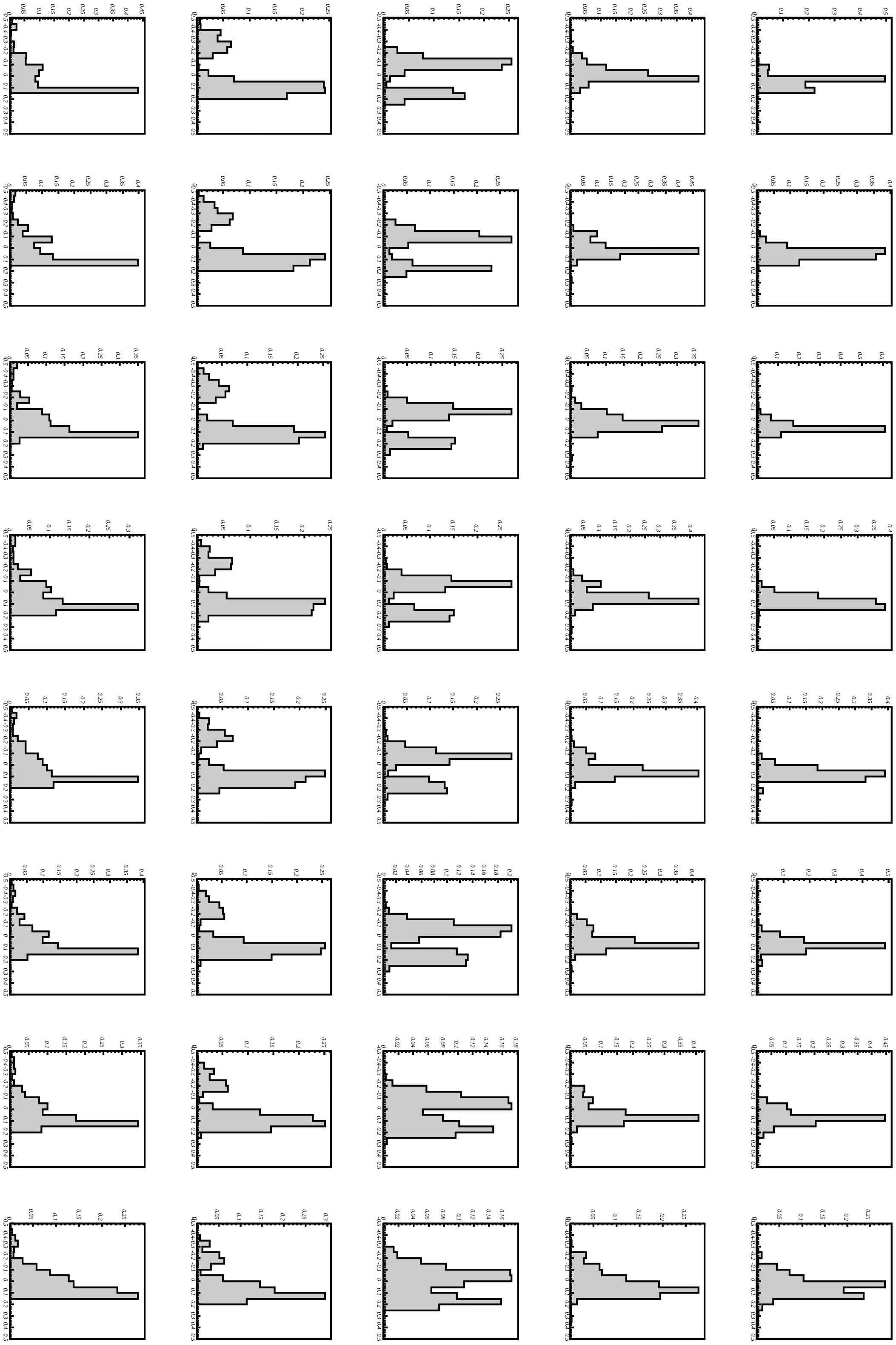

Figure 8.2: Relative deviation of the efficiency factor $\varepsilon_{\text{corr}}$, $\Delta\varepsilon/\varepsilon_Z$, in bins of p_T^Z and y^Z (given in Equation 7.4), axis labeling and range of the x axis are the same as in Figure 8.1. Picture is rotated 90 degrees clockwise.

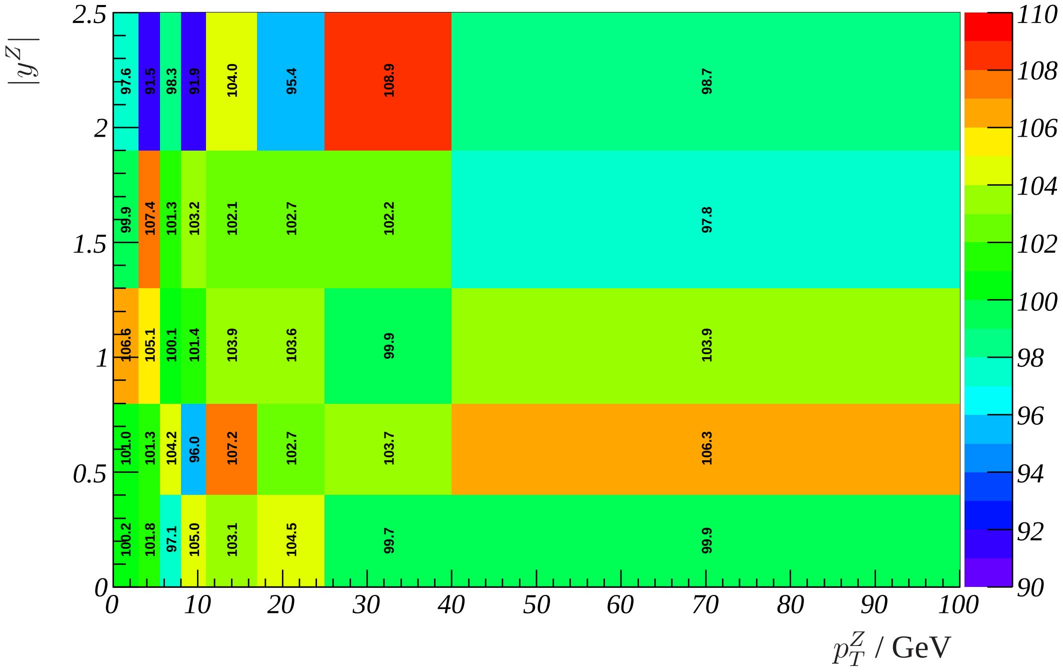

Figure 8.3: Ratio of the corrected number of events and expected number of events per p_T^Z-$|y^Z|$ bin after applying the correction via Equation 8.1. The statistical error for each bin is well contained at $\lesssim 1\%$. All values are given in per cent.

not allow to reproduce the right number of Z events. Rather than dealing with a variety of efficiencies at once, the determination of the appropriate efficiency correction factor per event is, for simplification, reduced to the correct handling of just one efficiency. The determination of the remaining efficiencies shall be deemed to be a matter of generalisation and should in principle work accordingly.

The goal for this part of the analysis is therefore to determine the (medium) identification efficiency, $\varepsilon^{\text{ID, medium}}$, in a way to reproduce the invariant mass spectrum of a selected Z candidate *before* the medium identification requirements for both electrons, with the spectrum *after* the cuts and the appropriate weight for the event from the factor $\varepsilon^{\text{ID, medium}}$. The spectrum reconstruction ensures the reproduction of the correct number of events for the cross-section determination.

If the assumption applies that correlations between the electron and the positron from the Z decay are responsible for the improper correction, the efficiency for a single electron cannot longer be determined independently from its partner. The first ansatz is therefore to define the formerly used, two-dimensional truth and tag-and-probe efficiencies in four dimensions, respecting also the partner's location and momentum, such that

$$\begin{aligned} \varepsilon_{\text{truth}}^{\text{ID, medium}}(E_T^{\text{truth}}, |\eta^{\text{truth}}|) &\rightarrow \varepsilon_{\text{truth}}^{\text{ID, medium}}(E_T^{\text{partner}}, |\eta^{\text{partner}}|, E_T^{\text{truth}}, |\eta^{\text{truth}}|)\ , \\ \varepsilon_{\text{tag and probe}}^{\text{ID, medium}}(E_T^{\text{probe}}, |\eta^{\text{probe}}|) &\rightarrow \varepsilon_{\text{tag and probe}}^{\text{ID, medium}}(E_T^{\text{tag}}, |\eta^{\text{tag}}|, E_T^{\text{probe}}, |\eta^{\text{probe}}|)\ . \end{aligned} \tag{8.3}$$

In addition to this four-dimensional ansatz, the standard approach to correct the mass spectrum with the two-dimensional efficiency is also used. The correction is applied by weighting each event that enters the spectrum with a factor of $1/w_i$. In total, five different ways to correct the spectrum have been considered:

- standard approach, 2-dimensional efficiency
  - truth, single electron efficiency

    $$w_1 = \varepsilon_{\text{truth}}^{\text{ID, medium}}(E_T^{\text{el1}}, |\eta^{\text{el1}}|) \cdot \varepsilon_{\text{truth}}^{\text{ID, medium}}(E_T^{\text{el2}}, |\eta^{\text{el2}}|)$$

  - single electron efficiency determined by the tag-and-probe method

    $$w_2 = \varepsilon_{\text{tag and probe}}^{\text{ID, medium}}(E_T^{\text{probe, el1}}, |\eta^{\text{probe, el1}}|) \cdot \varepsilon_{\text{tag and probe}}^{\text{ID, medium}}(E_T^{\text{probe, el2}}, |\eta^{\text{probe, el2}}|)$$

  - two-electron efficiency, gives an overall weighting-factor per event (for details, see Section 7.5)

    $$w_3 = \varepsilon_Z(p_T^Z, |y^Z|)$$

- 4-dimensional approach
  - truth, single electron efficiency

    $$w_4 = \varepsilon_{\text{truth}}^{\text{ID, medium}}(E_T^{\text{el1}}, |\eta^{\text{el1}}|, E_T^{\text{el2}}, |\eta^{\text{el2}}|) \cdot \varepsilon_{\text{truth}}^{\text{ID, medium}}(E_T^{\text{el2}}, |\eta^{\text{el2}}|, E_T^{\text{el1}}, |\eta^{\text{el1}}|)$$

  - tag-and-probe method, single electron efficiency

    $$\begin{aligned} w_5 &= \varepsilon_{\text{tag and probe}}^{\text{ID, medium}}(E_T^{\text{tag}}, |\eta^{\text{tag}}|, E_T^{\text{probe}}, |\eta^{\text{probe}}|) \\ &\cdot\ \varepsilon_{\text{tag and probe}}^{\text{ID, medium}}(E_T^{\text{probe}}, |\eta^{\text{probe}}|, E_T^{\text{tag}}, |\eta^{\text{tag}}|) \end{aligned}$$

The results for the various corrections are shown in Figure 8.4. The difference between the number of dimensions is clearly visible: For lower-mass Z candidates, the correction is heavily underestimated ($\approx 20\%$) and overestimated for $M_{\text{el1, el2}} \gtrsim M(Z)$ in case of the 2-dimensional efficiencies. The worst correction gives, as one would expect, the correction factor w_3, since it does not differentiate between the leptons. However, as this efficiency mirrors the selection-steps to find a Z candidate, the integral of the corrected spectrum by definition gives the number of events before applying the identification cut.

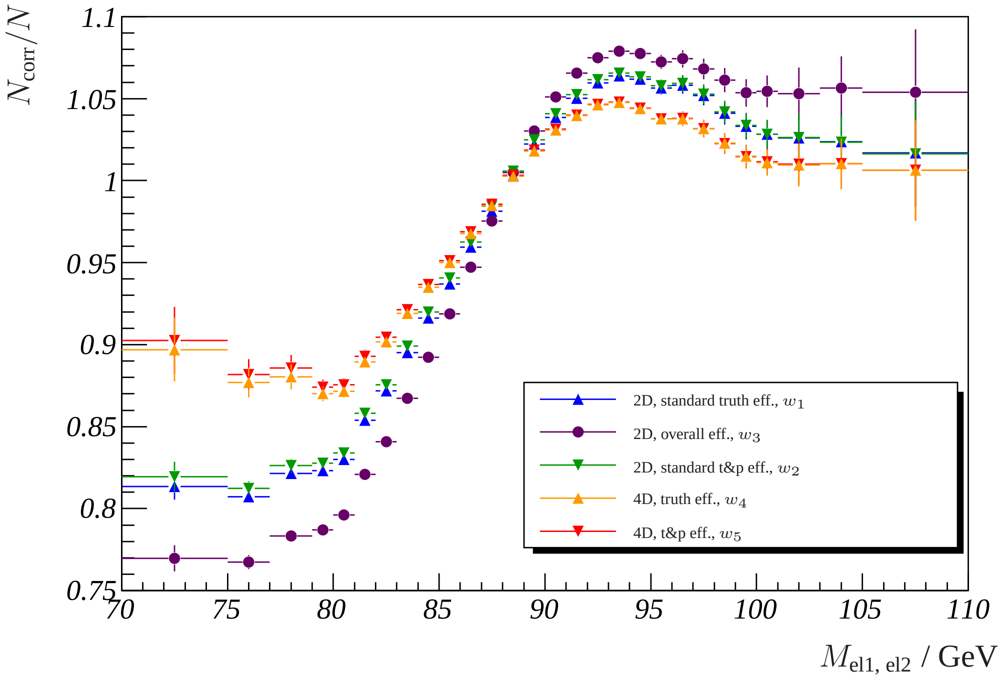

Figure 8.4: Ratio of the invariant mass spectra with and without identification cut and correction. Five different corrections have been applied, three in two dimensions and two in four dimensions.

The 4-dimensional corrections show a better reproduction of the invariant-mass spectrum before the identification cuts. Taking into account the second involved lepton obviously has an impact on the correction and reduces the deviations by roughly a factor of two.

Apparently, all five distributions show the same behaviour with the underestimation (overestimation) at the low-mass (high-mass) region. Furthermore, they all seem to share the same inflection point at 88 GeV $< M_{\text{el1, el2}} \leq 89$ GeV, with $N_{\text{corr}}/N \approx 1$. That means that the correlation is completely negligible for electron-positron pairs close the Z mass. Since the correction varies strongly with the invariant mass of the Z boson, it seems natural to extend the two and four dimensional descriptions of the efficiencies with another dimension which covers the combined mass of the two leptons.

8.4 Correction Factors Including the Invariant Mass

As it has been shown in the previous section, the inclusion of the second lepton's parameters to derive an event-based correction factor improved the picture to some extent.

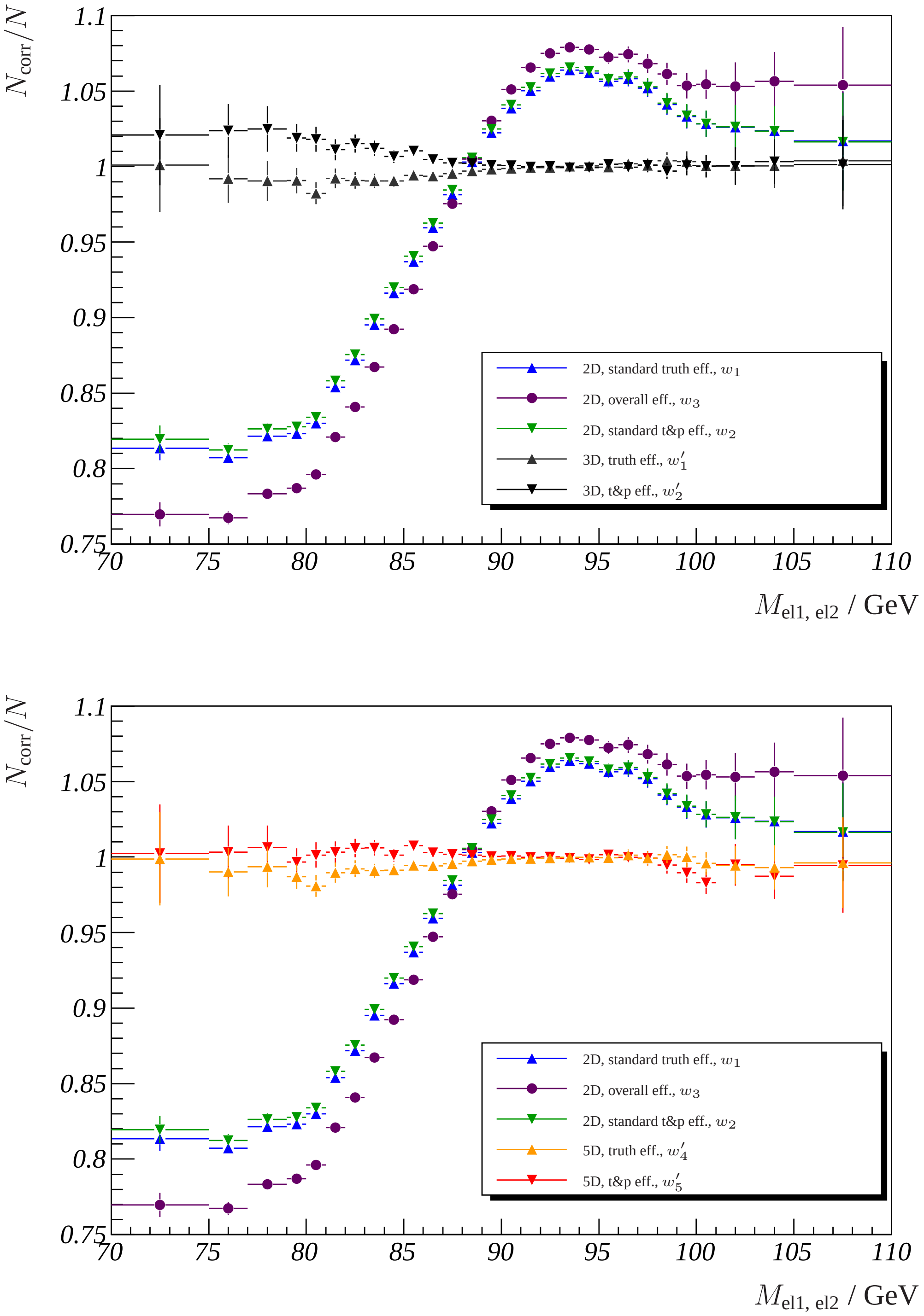

Figure 8.5: Ratio of the invariant mass spectra with and without identification cut and correction. Top: corrections in two dimensions compared to the three-dimensional ansatz. Bottom: two and five dimensional approaches in comparison.

However, as the deviation in the spectrum still heavily varies with the invariant mass of the Z, the obvious extension of the previous model would be to respect also the (reconstructed) invariant mass of both leptons, so that the factors w_1, w_2, w_4 and w_5 read now as

$$\begin{aligned} w_1' &= \varepsilon_{\text{truth}}^{\text{ID, medium}}(E_T^{\text{el1}}, |\eta^{\text{el1}}|, M_{\text{el1, el2}}) \\ &\cdot\ \varepsilon_{\text{truth}}^{\text{ID, medium}}(E_T^{\text{el2}}, |\eta^{\text{el2}}|, M_{\text{el1, el2}}) \end{aligned}$$

$$\begin{aligned} w_2' &= \varepsilon_{\text{tag and probe}}^{\text{ID, medium}}(E_T^{\text{probe, el1}}, |\eta^{\text{probe, el1}}|, M_{\text{tag, probe}}) \\ &\cdot\ \varepsilon_{\text{tag and probe}}^{\text{ID, medium}}(E_T^{\text{probe, el2}}, |\eta^{\text{probe, el2}}|, M_{\text{tag, probe}}) \end{aligned}$$

$$\begin{aligned} w_4' &= \varepsilon_{\text{truth}}^{\text{ID, medium}}(E_T^{\text{el1}}, |\eta^{\text{el1}}|, E_T^{\text{el2}}, |\eta^{\text{el2}}|, M_{\text{el1, el2}}) \\ &\cdot\ \varepsilon_{\text{truth}}^{\text{ID, medium}}(E_T^{\text{el2}}, |\eta^{\text{el2}}|, E_T^{\text{el1}}, |\eta^{\text{el1}}|, M_{\text{el1, el2}}) \end{aligned}$$

$$\begin{aligned} w_5' &= \varepsilon_{\text{tag and probe}}^{\text{ID, medium}}(E_T^{\text{tag}}, |\eta^{\text{tag}}|, E_T^{\text{probe}}, |\eta^{\text{probe}}|, M_{\text{tag, probe}}) \\ &\cdot\ \varepsilon_{\text{tag and probe}}^{\text{ID, medium}}(E_T^{\text{probe}}, |\eta^{\text{probe}}|, E_T^{\text{tag}}, |\eta^{\text{tag}}|, M_{\text{tag, probe}}) \end{aligned}$$

Apart from the additional dimension in these Equations the same considerations and steps as in the previous Section were taken into account in Figure 8.5. It shows the commonly used, 2-dimensional approach in comparison to the three and five dimensional efficiency corrections with a mass binning of

$$M_{\text{el1, el2}} = \{70, 75, 77, 79, 80, 81, \ldots, 99, 100, 101, 103, 105, 110\}\ /\ \text{GeV}\,.$$

Apparently, the quality of the correction strongly depends on the invariant mass of the leptons' mother particle, which cannot be neglected if one wants to properly reconstruct the spectrum and hence the correct number of events. As it can be seen in Figure 8.5, the three dimensional approach nicely reproduces the spectrum for $M_{\text{el1, el2}} \gtrsim 87$ GeV whilst especially the tag-and-probe correction seems to overestimate the lower mass region at a 2-3% level. When looking at the five-dimensional approach (bottom panel of Figure 8.5), the offset for low-mass pairs almost vanishes.

The question is: How many events are needed to reach the accuracy of the five-dimensional approach as presented in Figure 8.5? This can be approximated by the total number of bins used to derive appropriate correction factors. For each lepton, the binning as given in Expression 6.6 is used. This already results in $9^2 \cdot 5^2 = 2{,}025$ bins. Moreover, the mass-binning adds another 28 bins, as described above. In total, $56{,}700$ bins were taken into account in this analysis.

It is obvious that not each of the bins is occupied by the same amount of statistics, due to kinematic and geometric constraints. In Figure 8.6 shown is the population density

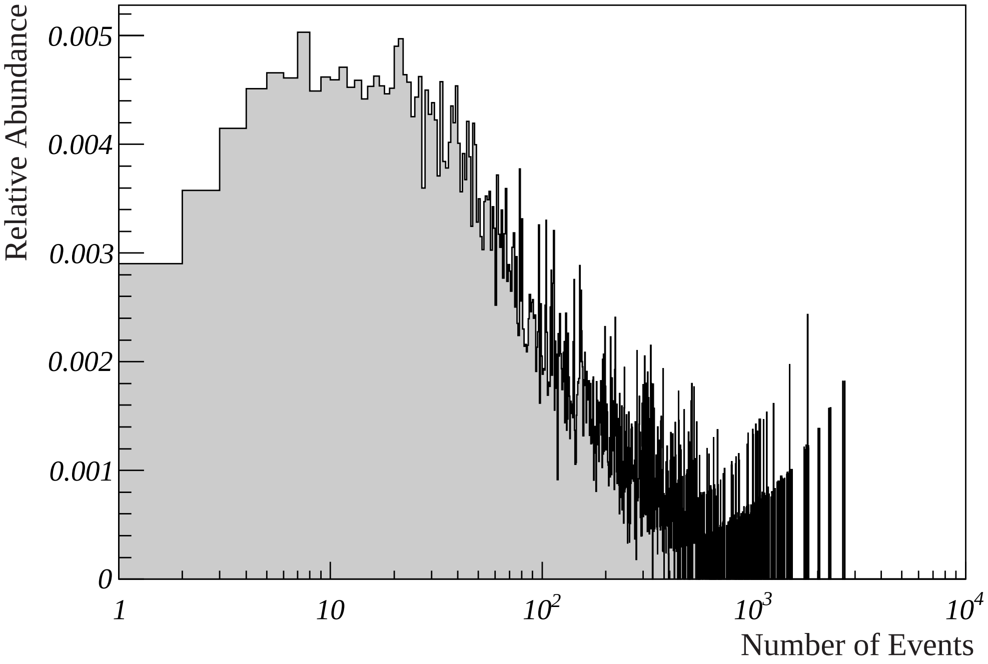

Figure 8.6: Relative abundance of number of events entering the denominator of each bin in order to calculate the 5-dimensional tag-and-probe efficiency.

of events in the denominator for the efficiency bins. It reflects the non-negligible number of correction factors based on a poor number of events per bin ($\lesssim 20$). It is therefore recommended to use either more statistics (> 3 fb^{-1}) or a somewhat coarser binning. However, for the mass binning the latter would result in a worsened reproduction of the spectrum and can therefore not be justified.

8.5 Comparison and Summary

After introducing the problems arising from the “classic”[2] factorisation ansatz in Equation 8.1, the task of finding one correction factor for all efficiencies was simplified to correctly describe one efficiency, first. The generalisation is reserved for further, more detailed analysis, but should, in principle, not deviate from the given path.

In this final Section, the implications of the ≥ 2 dimensional approaches on the differential cross-section measurements are outlined briefly. As it was previously shown in this Chapter, the invariant mass spectrum can not be reproduced appropriately when looking at the electrons from the Z decay independently. The extension to three and five dimensions, where the invariant mass of the two leptons is taken into account, allows a proper

---

[2] i.e. with two-dimensional factors

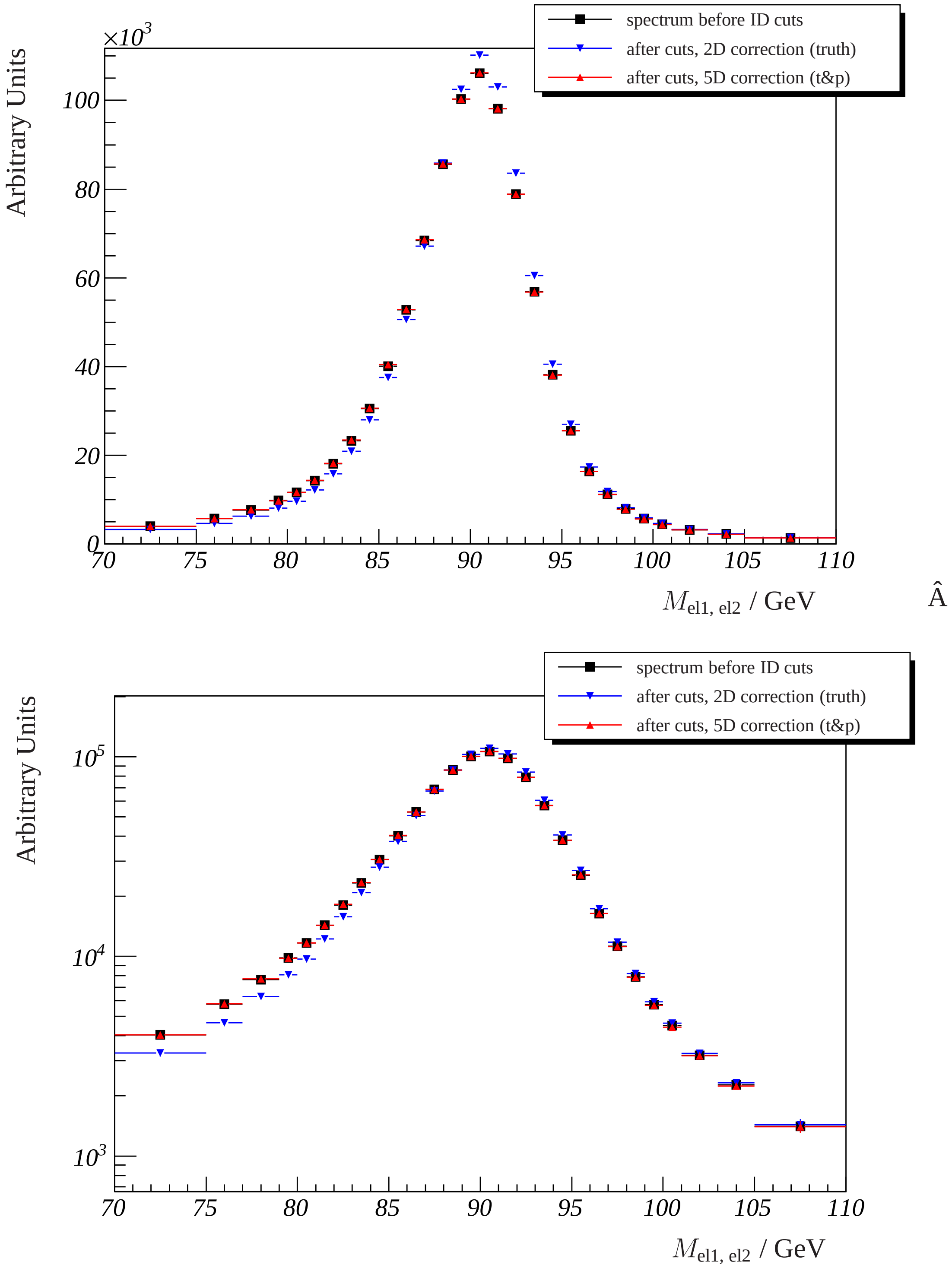

Figure 8.7: Invariant mass spectrum of a selected pair of electrons before the identification cuts, as well as after both cuts including the correction. Linear (top) and logarithmic (bottom) representation.

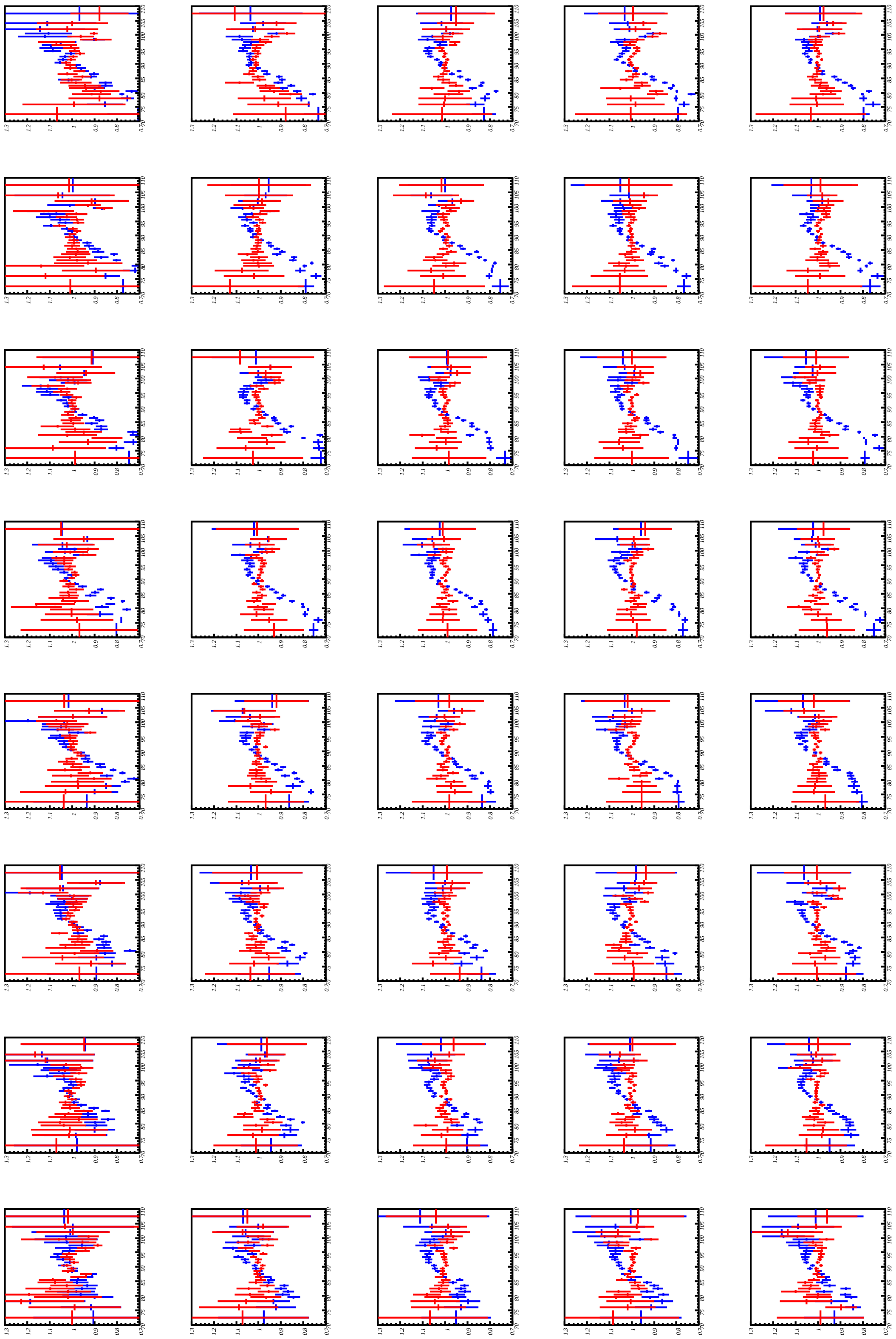

Figure 8.8: Invariant mass spectrum correction in 8 bins of p_T^Z and 5 bins of $|y^z|$ (see bin definition in Expression 7.4). Ratio of spectrum after the 2D (5D) correction and the spectrum before the ID cuts in blue (red). The range of the x (y) axis is $[70\text{ GeV}; 110\text{ GeV}]$ ($[0.7; 1.3]$). The Figure is rotated 90 degrees counter-clockwise.

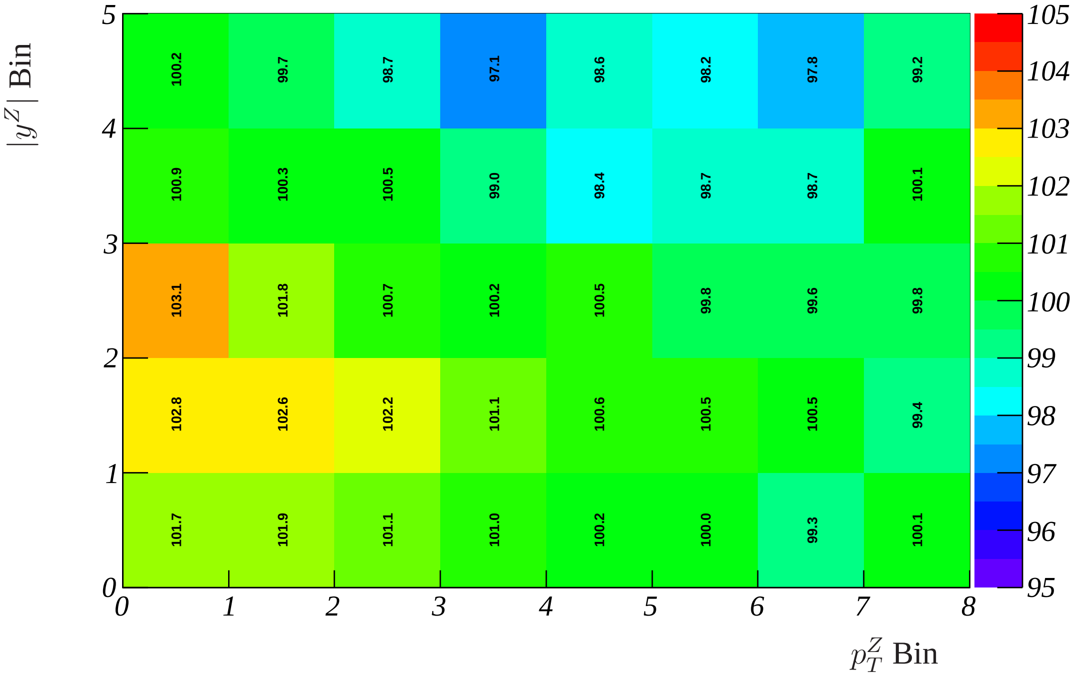

Figure 8.9: Relative deviation between the integrated two-dimensional invariant-mass correction and the integrated invariant mass before the identification criterion. For better illustration, all bins were given an equal size, the actual boundaries are given in Expression 7.4. The statistical uncertainties are $\sim 1\%$ in each bin. All values are given in per cent.

reconstruction of the spectrum (see Figure 8.7).

As already mentioned before, the impact of the mis-reconstructed spectrum is quite small for the inclusive cross-section measurement, since the integral deviates by only $\sim 1\%$ from the theoretical value. However, when it comes to the single or double differential treatment of the corrections, Equation 8.1 breaks down entirely. In the following, the behaviour of the 5-dimensional efficiency in comparison to the classic method with respect to differential distributions is subject of the considerations.

This can be studied by splitting up the spectrum that is shown in Figure 8.7 in bins of p_T^Z and $|y^Z|$. As it can be seen in Figure 8.8, the 5-dimensional tag-and-probe correction results in an fundamentally improved spectrum reconstruction in each kinematic and geometric regime of the Z boson.

Even with the low amount of statistics in the low and high mass region the initial spectrum is much better described by the 5-dimensional tag-and-probe method than with the 2-dimensional efficiency. However, some subsets of the 5-dimensional correction show also some possible biases beyond statistical fluctuations (like panel $[8, 4]$ in Figure 8.8, for instance), which might be resolved by a narrower binning in one or more of

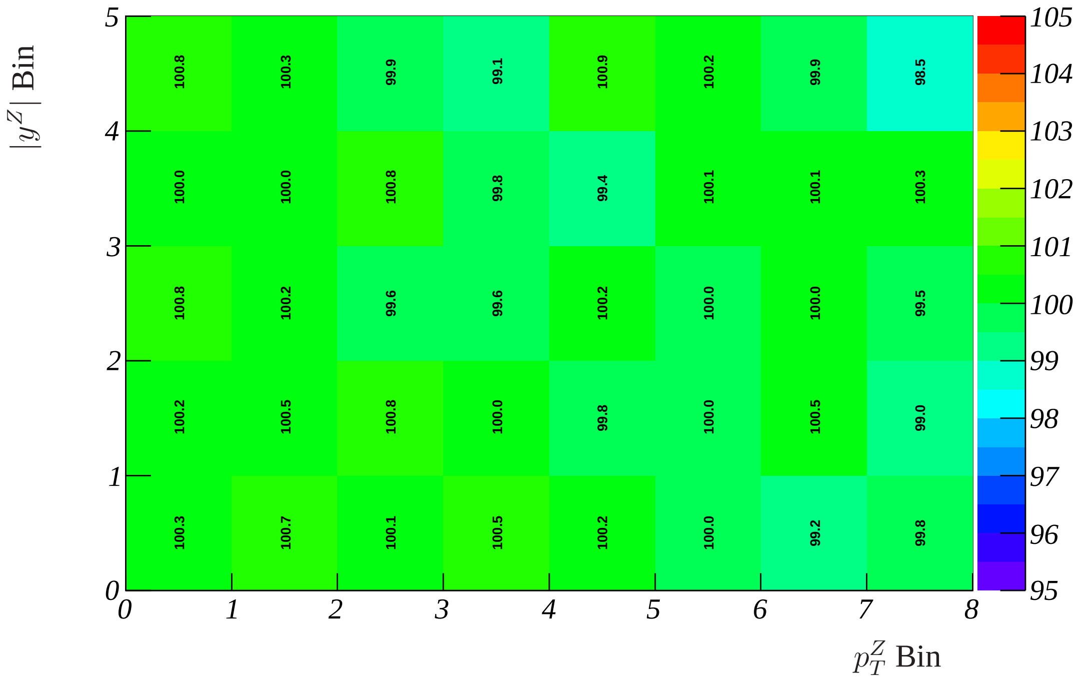

Figure 8.10: Relative deviation between the integrated five-dimensional invariant-mass correction and the integrated invariant mass before the identification criterion. For better illustration, all bins were given an equal size, the actual boundaries are given in Expression 7.4. The statistical uncertainties are $\lesssim 1\%$ in each bin. All values are given in per cent.

the variables or by adding another dimension. This should be subject of another, more detailed analysis.

The advantage of the 5-dimensional over the 2-dimensional correction can best be demonstrated by comparing the integral of the invariant-mass spectra before and after the correction. As it is shown in Figure 8.9, the factorisation in two dimensions,

$$w_1 = \varepsilon^{\text{ID, medium}}_{\text{truth}}(E_T^{\text{el1}}, |\eta^{\text{el1}}|) \cdot \varepsilon^{\text{ID, medium}}_{\text{truth}}(E_T^{\text{el2}}, |\eta^{\text{el2}}|)$$

obviously overestimates Z bosons with low p_T and underestimates significantly high-rapidity Z's. The deviations for the identification efficiency already reach the three-percent level. Thus, by also including the remaining efficiencies appearing in Equation 8.1, an overall fluctuation and deviation as shown in Figure 8.2 seems reasonable. Even if the fluctuation is sometimes quite extreme between adjacent bins, integrating over p_T^Z or $|y^Z|$ results in the same overestimated and underestimated areas, which would directly affect the single differential cross-section measurements.

In comparison, Figure 8.10 is showing the discrepancy to the expected number of events per bin for the 5-dimensional tag-and-probe method,

$$\begin{aligned} w'_5 &= \varepsilon^{\text{ID, medium}}_{\text{tag and probe}}(E_T^{\text{tag}}, |\eta^{\text{tag}}|, E_T^{\text{probe}}, |\eta^{\text{probe}}|, M_{\text{tag, probe}}) \\ &\cdot\ \varepsilon^{\text{ID, medium}}_{\text{tag and probe}}(E_T^{\text{probe}}, |\eta^{\text{probe}}|, E_T^{\text{tag}}, |\eta^{\text{tag}}|, M_{\text{tag, probe}}) \end{aligned}$$

The fluctuations are within the statistical uncertainty at $\lesssim 1\%$. Moreover, there is no region in $p_T^Z, |y^Z|$ favoured in any way. This is a confirmation that the method is working well.

However, there is a price for the efficiency-treatment in five dimensions. The amount of statistics needed to reach the accuracy presented in this analysis is ≈ 3 fb^{-1}, corresponding to ~ 3 years of initial LHC-running. On the bright side, the tag-and-probe method allows the efficiency determination from data, rather than to rely on simulated events, only. It should be emphasised in this context that the results presented here are an overview of the possibilities the 5-dimensional treatment of the efficiencies give.

The alternative to use the three-dimensional ansatz looks very promising, since it already reproduces the spectrum perfectly for higher masses of the Z and requires obviously much less statistics than the treatment in five dimensions. A more detailed analysis of binning and the remaining efficiencies should confirm the working of the three and five dimensional approaches to derive an overall efficiency, which includes reconstruction, trigger and further efficiencies that can be derived by the tag-and-probe method as well.

≪Was wir wissen ist ein Tropfen, was wir nicht wissen, ist ein Ozean.≫

Sir Isaac Newton ($^{*}1643$, $^{\dagger}1727$)

9

Summary and Outlook

In the thesis the production of the Z boson in proton-proton collisions at the ATLAS experiment has been investigated. Its subsequent decay into an electron-positron pair serves as a standard candle for the calibration and understanding of the ATLAS detector due to the clean signature given by the two isolated leptons in the final state. The total cross-section of ~ 1 nb leads to a large yield of Z bosons in the early phase of the experiment. This allows for first LHC studies of parton density functions.

After the incident at the LHC in September 2008, it became clear that the design centre-of-mass energy of 14 TeV would not be available at the restart of the experiment. During production of the Monte Carlo simulations on which this analysis is based on, an energy of 10 TeV was in the discussion for LHC startup. As it turned out, the decision was to run with $\sqrt{s} = 7$ TeV initially, leading to the fact that no exact predictions can be made within this thesis. The concepts, however, will be the same since the cross-section of the process $pp \rightarrow \gamma^*/Z + X \rightarrow e^+e^- + X$ does not change significantly. It was therefore the aim of this thesis to test the concepts used in early data-taking to measure the inclusive and differential cross-sections for the Z production.

In preparation for the cross-section measurement, the single-electron efficiencies have to be considered. Therefore, an in-depth comparison between the simulation-based “truth” and the data-driven “tag and probe” technique has been shown. They coincide within a few percent for all considered efficiencies. However, low-E_T electrons obviously suffer from effects like bremsstrahlung, leading to deviations of $\mathcal{O}(10\%)$ between truth and tag-and-probe method regarding the identification efficiency. With a combined sample of signal and background, which was limited to 100 pb^{-1} of data in order to reflect early data-taking in ATLAS, the possibility of an efficiency measurement for single electrons with the data-driven technique has been demonstrated.

The focus of this thesis has been to outline the inclusive and differential cross-section measurement with an amount of data corresponding to an early phase of the ATLAS experiment. The statistical and systematic uncertainties have been estimated. For the inclusive cross-section determination, the expected statistical uncertainty is 1.5% and the systematic uncertainty is 4.2%. Similar studies for the inclusive (see Reference [50]) and differential case (see Reference [16]) dealt with a limitation to 200 pb^{-1}, thus twice as many events as for this analysis. Their results are in good agreement with this analysis. Even if the combined uncertainty is $< 5\%$, the dominating contribution to the overall uncertainty comes from the luminosity. Its uncertainty during early data-taking is expected to be of the order of 10%.

An important aspect of this analysis has been to measure the differential cross-sections. The single-differential cross-section with respect to p_T depends on QCD radiation in the initial state including soft QCD processes, hence it might be sensitive to non-pertubative effects in pQCD. Furthermore, the rapidity distribution of the Z boson gives access to the PDFs of the protons. This is due to the fact that, at leading order, the involved partons' momentum fractions are related to the rapidity.

With the results for the single-differential cross-sections given in this analysis, the transverse momentum as well as the rapidity distributions for the Z boson can be reproduced well (better than 5%) within the statistical uncertainty for 100 pb^{-1}. It has to be stated, though, that in data it is essential to describe the shapes of signal and background very accurately in order to derive the correct cross-section per bin.

The double-differential cross-section can be reproduced a little worse than single-differential cross-seciotns. The discrepancies to the expectation per bin almost reach 10%. The overall error per bin is totally dominated by the statistical uncertainty. It is therefore not recommended to measure this distribution with a low amount of data as given by 100 pb^{-1}.

As it has been presented, the formerly used factorisation ansatz to combine the various, two-dimensional single-electron efficiencies to a common correction factor is not applicable to differential cross-section analysis, neither from simulation nor from a data-driven method. Failing to reproduce the invariant-mass spectrum before the medium identification cuts with the two-dimensional identification efficiency was demonstrated. By including the E_T and η parameters of the other lepton and the invariant-mass of both as additional dimensions in the efficiency correction, it was shown that the spectrum could be reproduced accurately and that the correction allows for a proper reconstruction of the cross-sections per bin.

However, the description in five dimensions would require several years of ATLAS' data taking. The possibility to study the efficiency correction in just three instead of five dimensions was also examined in this analysis. It has been shown for the very first time that the three-dimensional approach already reproduces the spectrum quite well, making it possible to derive the several efficiencies needed and combine them to a correction factor via the data-driven tag-and-probe method. As an educated guess, an integrated luminosity of ≈ 200 pb^{-1} would be sufficient to calculate ε from the three-dimensional electron efficiencies.

As some of the techniques and methods demonstrated in this analysis are already adopted in current data taking at ATLAS, it would make sense to study the efficiency determination in much more detail. Since only the identification efficiency has been studied in the multi-dimensional ansatz, the applicability for reconstruction and trigger efficiencies, for example, still needs to be proven. Moreover, detailed studies are needed to optimise binning effects and additional corrections that might be needed in data.

The first cross-section measurements of the $\gamma^*/Z \rightarrow e^+e^-$ production with the ATLAS detector at $\sqrt{s} = 7$ TeV have been published recently (see Reference [5]). The results are based on an integrated luminosity of $L = 316$ nb^{-1} with 70 observed Z-boson candidates yielding $68.8 \pm 8.4_{\text{stat}} \pm 0.4_{\text{syst}}$ background-subtracted signal events. With the efficiencies and the acceptance derived from Monte-Carlo simulation, the total production cross-section within an invariant-mass window of 66 GeV $< M_{ee} < 116$ GeV is derived as $\sigma^{\text{tot}}_{\gamma^*/Z} = (0.75 \pm 0.09_{\text{stat}} \pm 0.08_{\text{syst}} \pm 0.08_{\text{lumi}})$ nb. This first measurement is within 1.5σ from the theoretical value ($\sigma^{\text{NNLO}}_{\gamma^*/Z} = (0.96 \pm 0.05)$ nb) that is based on NNLO QCD corrections using the programs FEWZ [19] and ZWPROD (see References [59] and [74]).

In conclusion, the study of the Z boson production is one of the most central tasks during the first period of data taking at the ATLAS experiment. It helps to understand aspects of QED and QCD, and improves the understanding of the ATLAS' detector performance and its response. In later stages of the experiment, the knowledge gained by studying the process $pp \rightarrow \gamma^*/Z + X \rightarrow e^+e^- + X$ also has an impact on the discovery of the much anticipated Higgs boson as well as for discovering physics beyond the Standard Model.

List of Figures

2.1 Combination of α_s measurements. Left: Measurements and world average at $\mu = M_Z$. Right: Measurements of $\alpha_s(\mu)$ at different energy regimes. Results are obtained from the τ width, Υ decays, deep inelastic scattering, JADE and TRISTAN experiments, Z width and further e^+e^- event shapes. A fit on the data and its $\pm1\sigma$ error band is included. Figures taken from [67]. 18

2.2 Proton structure function $F_2^p(x, Q^2)$ as a function of the momentum transfer, $Q^2 = -\boldsymbol{q}^2$, with data from fixed-target experiments (SLAC, BCDMS, E665, NMC) and collider experiments (H1, ZEUS). See text for details. Figure taken from [67]. 20

2.3 Parametrisation of the parton distributions by the MRST group. Left: Proton structure function $F_2^p(x, Q^2)$ for two given values of $Q^2 = -\boldsymbol{q}^2$ versus the scaling variable x. Right: Contributions of the gluons and different quark flavours to the structure functions for $\mu^2 = 10$ GeV^2 and $\mu^2 = 10$ TeV^2. All figures taken from [67]. 21

2.4 Illustration of the expected cross-sections for various processes versus centre-of-mass energy. The evolutions for the weak gauge bosons are highlighted. 25

2.5 Illustration of the Drell-Yan process: hadron-hadron (h_A and h_B) interaction via quark anti-quark annihilation, intermediate γ^*/Z state and its subsequent decay into a lepton anti-lepton pair (cf. Reference [61]). . . . 27

3.1 Schematic view of the Large Hadron Collider and its four major experiments. Figure taken from [24]. 32

3.2 Illustration of a LHC dipole-magnet and its components. Figure taken from [24]. 33

3.3 Illustration of the ATLAS detector. Figure taken from [24]. 35

3.4 Illustrations of ATLAS' Inner Detector. Figures taken from [24]. 37

3.5 Simulated material distribution in terms of radiation length (X_0) at the exit of ATLAS' Inner Detector envelope. Figure taken from [3]. 39

3.6 Cut-away view of the ATLAS calorimetry. Image taken from [24]. 40

3.7 Sketch of the three-layer structure (and the granularity of each layer) of the electromagnetic calorimeter. Also shown is the size of the *trigger towers* that will be discussed in Section 3.4. Image taken from [3]. 42

3.8 Sketch of the mechanical assembly of the tile calorimeter. Image taken from [3]. 43

3.9 Cross-section of the muon spectrometer. Left: x-y plane perpendicular to the beam axis (non-bending plane). Right: x-z plane (bending plane). Images taken from [3]. 44

3.10 Predicted bending power of the muon spectrometer versus rapidity for two different azimuthal angles ϕ. Image taken from [3]. 45

3.11 Schematic overview of the ATLAS trigger system that consists of three stages: Level 1, Level 2 and Event Filter. 46

3.12 Block diagram of the ATLAS L1 trigger. Image taken from [22]. 48

3.13 Tracking reconstruction chain. The boxes in the top represent data objects, whilst the second-row boxes show the algorithms working on the them. Figure taken from [11]. 50

3.14 Cluster finding scheme with the data objects on the top and the algorithms in the second row. Figure taken from [11]. 51

4.1 Data flow in the simulation chain. Rounded rectangles show objects in the event data model, whilst rectangles represent processing stages. Figure taken from [3]. 56

5.1 Left: track reconstruction efficiencies for electrons with a given p_T as functions of $|\eta|$. Right: energy resolution of electrons in the electromagnetic calorimeter for different values of $|\eta|$. Figures taken from [4]. 62

5.2 L1 trigger towers. Left: representation of a 4×4 window of trigger towers; right: sliding-window algorithm to find a “region of interest”. Figure taken from [4]. 64

5.3 Trigger menu for an instantaneous luminosity of 10^{31} cm^{-2}s^{-1} during early data taking at ATLAS. Table taken from [3]. 67

5.4 Signal ($Z \to e^+e^-$ sample with $E_T > 15$ GeV and $|\eta| < 2.4$) and hadronic-background separation for two discriminating variables. Left: cluster-width in second sampling of the electromagnetic calorimeter. Right: leakage of electromagnetic clusters in the first compartment of the hadronic calorimeter. Figures taken from [2]. 70

6.1 Left: example of a fit within a certain E_T^{truth}-η^{truth} bin with the Crystal-Ball function; $\sigma = (2.327 \pm 0.025) \times 10^{-2}$, reduced $\chi^2 = 101.3/86$. Right: resulting E_T resolution for different values of $|\eta|$. 77

6.2 Spatial resolution for electrons in the electromagnetic calorimeter. Left: example of a resolution fit with the normal distribution; $\sigma = (3.255 \pm 0.038) \times 10^{-2}$, reduced $\chi^2 = 20.8/26$. Right: η^{calo} resolution for different E_T. 78

6.3 Spatial resolution for electrons in the tracking system. Left: example of a resolution fit with the normal distribution; $\sigma = (7.512 \pm 0.093) \times 10^{-4}$, reduced $\chi^2 = 27.1/24$. Right: η^{track} resolution for different E_T. 79

6.4 Probability that a cluster is matched to a truth electron from the $Z \rightarrow e^+e^-$ decay, including statistical errors. All values are given in per cent. . 83

6.5 Examples of cuts to select a tag-and-probe pair, signal-only case. Left: distance between probe cluster and the regions of interest (RoIs). Right: E_T spectrum of the probe cluster. 90

6.6 Invariant mass of the tag-and-probe pair after preselection. Top: signal-only sample. Bottom: combined sample with contributions from different backgrounds. 92

6.7 Invariant mass spectra (60 GeV $< M_{\text{tag,probe}} < 120$ GeV) in bins of E_T (horizontal) and $|\eta|$ (vertical) to determine the reconstruction efficiency via the tag-and-probe method. By fitting, the contribution of signal (orange) and background (grey) in each bin is determined (cf. Equation 6.14). Top: double-differential denominator. Bottom: double-differential numerator. 95

6.8 Fits to determine the inclusive efficiencies via the tag-and-probe method (signal-only case). From left to right: electron reconstruction, medium identification and level 1. First row: denominator. Second row: numerator. 98

6.9 Fits to determine the inclusive efficiencies via the tag-and-probe method for the combined sample (first row: denominator, second row: numerator). From left to right: electron reconstruction, medium identification and level 1. In order to demonstrate the background-suppression for the ID criterion, the range of the y axis has been kept constant for all plots. . . 99

6.10 Single-differential reconstruction efficiencies for truth, as well as for the tag-and-probe method with and without truth-matching. Left: versus cluster-E_T (logarithmic scale). Right: versus $|\eta|$ of the cluster. 100

6.11 Single-differential medium identification efficiencies for truth, as well as for the tag-and-probe method with and without truth-matching. Left: versus cluster-E_T (logarithmic scale). Right: versus $|\eta|$ of the cluster. 100

6.12 Single-differential level-1 trigger-efficiencies for truth, as well as for the tag-and-probe method with and without truth-matching. Left: versus cluster-E_T (logarithmic scale). Right: versus $|\eta|$ of the cluster. 101

6.13 Double differential reconstruction efficiencies. Top: truth efficiency. Middle: relative deviation of the truth-matched tag-and-probe method (full statistics) and the truth efficiency. Bottom: relative deviation of the tag-and-probe method (combined sample, 100 pb^{-1}) and the truth efficiency. All values are given in per cent. 102

6.14 Double differential identification efficiencies. Top: truth efficiency. Middle: relative deviation of the truth-matched tag-and-probe method (full statistics) and the truth efficiency. Bottom: relative deviation of the tag-and-probe method (combined sample, 100 pb^{-1}) and the truth efficiency. All values are given in per cent. 103

6.15 Double differential level-1 trigger-efficiency. All values are given in per cent. 104

6.16 Ratio of truth efficiencies derived from the $Z \rightarrow e^+e^-$ and the $W \rightarrow e\nu$ sample, $\frac{\varepsilon_{W\rightarrow e\nu}}{\varepsilon_{Z\rightarrow e^+e^-}}$, versus E_T (top) and $|\eta|$ (bottom). Both samples were reconstructed with the same software release (14.2.20.4). All values are given in per cent. 106

6.17 Relative deviation between `MC@NLO` and `PYTHIA` generators. Left: Single electron truth reconstruction efficiency. Right: Single electron truth identification efficiency. All values are given in per cent. Figures taken from [16]. 107

6.18 Ratio of the reconstruction (identification) efficiency determined with a varied ΔR cut and the according efficiency derived with the standard cut-value, versus E_T (left) and versus η (right). All values are given in per cent. 108

6.19 Ratio of single-electron efficiencies with and without final-state radiation versus E_T and $|\eta|$. All values are given in per cent. 108

6.20 Ratio of the modified single-electron tag-and-probe efficiencies and the standard tag E_T-cut versus E_T and $|\eta|$. All values are in per cent. 109

7.1 Resolution for the reconstructed Z bosons after selection in bins of truth p_T^Z and $|y^Z|$. Top: relative transverse momentum resolution, $\sigma(p_T^Z) \times 10^3$. Bottom: absolute rapidity resolution, $\sigma(y^Z) \times 10^2$. 115

7.2 Kinematic and geometric acceptance for two clusters in bins of p_T^Z and $|y^Z|$, errors are statistical. All values are given in per cent. 116

7.3 Correction factor $\varepsilon_Z(p_T^Z, |y^Z|)$. The statistical uncertainties vary between 0.2% and 0.6% All values are given in per cent. 118

7.4 Filter efficiency on Monte Carlo generator level. One particle has to fulfil the requirement $|\eta| < 2.8$. For better illustration, the highest E_T-bin was not drawn, its efficiency is essentially 100%. All values are given in per cent. 121

7.5 Fit of the inclusive, truth e^+e^- invariant mass before reconstruction, linear (left) and logarithmic illustration (right). See text for details. 122

7.6 Fit of the inclusive, reconstructed e^+e^- invariant mass, linear (left) and logarithmic illustration (right). In order to clean the sample from combinatorial background, the reconstructed leptons were matched to the truth particles. See text for details. 123

7.7 Number of reconstructed signal events after efficiency and acceptance correction for the signal-only sample (full statistics) and for the combined sample (100 pb^{-1}). Top: versus the transverse momentum of the Z. Bottom: versus Z rapidity. 126

7.8 Generated number of events from the signal-only sample, full statistics. . 128

7.9 Ratio of generated and corrected number of events, see text for details. Top: signal-only sample, full statistics without fitting; the statistical errors are $\ll 1\%$. Bottom: combined sample, $L = 100$ pb^{-1}; the statistical uncertainties vary between 5.2% for bin with high statistics and 8.4% for regions with low statistics (cf. Figure 7.8). All values are given in per cent. 129

7.10 Relative systematic uncertainty due to the energy scale variation of the electron. Top: single differential versus p_T^Z. Middle: single differential versus $|y^Z|$. Bottom: $\frac{dN^{\text{var}}}{dp_T^Z d|y^Z|} / \frac{dN^{\text{std}}}{dp_T^Z d|y^Z|}$ for an energy-shift of $+1\%$. All values are given in per cent. 131

7.11 Bin migration between reconstructed clusters and associated truth electrons, including statistical uncertainties. Top: transverse energy (highest E_T-bin skipped for better illustration). Bottom: smearing in bins of $|\eta|$. All values are given in per cent. 133

7.12 Bin migration between reconstructed and associated truth Z-bosons, including statistical uncertainties. Top: transverse momentum (highest p_T^Z-bin skipped for better illustration). Bottom: smearing in bins of Z rapidity, $|y^Z|$. All values are given in per cent. 134

7.13 Relative systematic uncertainty from bin migration. Top: single differential versus p_T^Z. Middle: single differential versus Z rapidity. Bottom: double differential (signal only), $\frac{dN^{\text{var}}}{dp_T^Z d|y^Z|} / \frac{dN^{\text{std}}}{dp_T^Z d|y^Z|}$ All given values are given in per cent. 136

7.14 Overall Z acceptance for each variation (“up” and “down”) of the eigenvectors, parametrising the PDF uncertainties. See text for details. Figure taken from [16]. 137

7.15 Double differential illustration of the acceptance and the absolute systematic uncertainty for two central electrons outside the crack region in bins of p_T^Z and $|y^Z|$. All values given are in percent. Figure taken from [16]. . . 138

7.16 Single differential cross-section determination versus p_T^Z with the cross-section on generator level in comparison to the signal-only and the combined determination. The bottom plot gives the ratio between generator level and combined sample as well as the appropriate errors. 143

7.17 Single differential cross-section determination versus $|y^Z|$ with the cross-section on generator level in comparison to the signal-only and the combined determination. The bottom plot gives the ratio between generator level and combined sample as well as the appropriate errors. 144

7.18 Double differential cross-section $d^2\sigma/(dp_T^Z d|y^Z|)$ in bins of p_T^Z and $|y^Z|$ on generator level. All values given are in pb$/($GeV $\cdot$ y-unit$)$. 145

7.19 Double differential cross-section $d^2\sigma/(dp_T^Z d|y^Z|)$ in each bin of p_T^Z and $|y^Z|$ for the combined sample with an integrated luminosity of 100 pb^{-1}. The errors shown are the combined statistical and systematical uncertainties, the uncertainty on the luminosity is not included. All values given are in pb$/($GeV $\cdot$ y-unit$)$. 146

8.1 Relative deviation between the efficiency factors $\varepsilon_{\text{corr}}$ and ε_Z as described in the text, $(\varepsilon_{\text{corr}} - \varepsilon_Z)/\varepsilon_Z$. 148

8.2 Relative deviation of the efficiency factor $\varepsilon_{\text{corr}}$, $\Delta\varepsilon/\varepsilon_Z$, in bins of p_T^Z and y^Z (given in Equation 7.4), axis labeling and range of the x axis are the same as in Figure 8.1. Picture is rotated 90 degrees clockwise. 150

8.3 Ratio of the corrected number of events and expected number of events per p_T^Z-$|y^Z|$ bin after applying the correction via Equation 8.1. The statistical error for each bin is well contained at $\lesssim 1\%$. All values are given in per cent. 151

8.4 Ratio of the invariant mass spectra with and without identification cut and correction. Five different corrections have been applied, three in two dimensions and two in four dimensions. 153

8.5 Ratio of the invariant mass spectra with and without identification cut and correction. Top: corrections in two dimensions compared to the three-dimensional ansatz. Bottom: two and five dimensional approaches in comparison. 154

8.6 Relative abundance of number of events entering the denominator of each bin in order to calculate the 5-dimensional tag-and-probe efficiency. . . . 156

8.7 Invariant mass spectrum of a selected pair of electrons before the identification cuts, as well as after both cuts including the correction. Linear (top) and logarithmic (bottom) representation. 157

8.8 Invariant mass spectrum correction in 8 bins of p_T^Z and 5 bins of $|y^z|$ (see bin definition in Expression 7.4). Ratio of spectrum after the 2D (5D) correction and the spectrum before the ID cuts in blue (red). The range of the x (y) axis is $[70$ GeV$; 110$ GeV$]$ ($[0.7; 1.3]$). The Figure is rotated 90 degrees counter-clockwise. 158

8.9 Relative deviation between the integrated two-dimensional invariant-mass correction and the integrated invariant mass before the identification criterion. For better illustration, all bins were given an equal size, the actual boundaries are given in Expression 7.4. The statistical uncertainties are $\sim 1\%$ in each bin. All values are given in per cent. 159

8.10 Relative deviation between the integrated five-dimensional invariant-mass correction and the integrated invariant mass before the identification criterion. For better illustration, all bins were given an equal size, the actual boundaries are given in Expression 7.4. The statistical uncertainties are $\lesssim 1\%$ in each bin. All values are given in per cent. 160

List of Tables

2.1 Listing of all Standard Model particles. For each particle exists an anti-particle. 9

2.2 Leading order (LO) and higher order ((N)NLO) cross-sections for Z production in pp collisions at 14 TeV and its subsequent decay into an electron-positron pair. The invariant mass of the lepton-pair is restricted to $M_{\ell\ell} > 60$ GeV. 26

3.1 Performance goals of the ATLAS experiment for the different detector parts. The performance of the muon spectrometer is given for high-p_T muons without taking the Inner Detector into account. The unit of p_T and E is GeV. Table taken from [3]. 36

4.1 Summary of the Monte Carlo samples used within this analysis. Each sample is generated for $\sqrt{s} = 10$ GeV. 59

5.1 Listing of the electron-identification criteria, leading to the classification *loose*, *medium* and *tight*. The given set of definitions is applicable to release 14 of the ATLAS reconstruction software. The specific cut criteria are mostly η and/or ϕ dependent, see Reference [14] for details. 71

5.2 Signal efficiency (from a simulated $Z \to e^+e^-$ sample) for electrons with $E_T > 17$ GeV, and jet rejection. Numbers taken from [3]. 72

6.1 Cuts to select the electron-positron pair on generator level. 88

6.2 Cuts and requirements to determine the truth efficiencies. 89

6.3 Cuts to determine the efficiencies with the tag-and-probe method. 93

6.4 Inclusive electron efficiencies. The truth and truth-matched efficiencies utilise the full statistics of the signal sample, the signal-only (including combinatorial background) and the combined samples are limited to 100 pb^{-1}. The errors are statistical errors, only. All values are given in per cent. 98

7.1 Cut requirements for two reconstructed electrons to select Z-boson candidates. 113

7.2 Remaining number of events after applying the given cut criteria. The QCD sample is split-up into flows with and without the identification criterion. All numbers given are with respect to the available statistics of each sample and therefore not normalised to a common integrated luminosity. 119

7.3 Comparison of the total numbers of generated events and reconstructed Z events after corrections. In order to study the stability of the fitting algorithm and minimise the uncertainty on the fit parameters, the corrected number of events for the combined sample is averaged over 30 runs (see Section 7.6.2 for details). 127
7.4 Contributions to the systematic uncertainty of the inclusive cross-section measurement. 140

Bibliography

[1] G. Aad et al. ATLAS Pixel Detector Electronics and Sensors. JINST, 3:P07007, 2008.

[2] G. Aad et al. Expected Performance of the ATLAS Experiment; Detector, Trigger and Physics. 2008. CERN-OPEN-2008-020.

[3] G. Aad et al. The ATLAS Experiment at the CERN Large Hadron Collider. JINST, 3:S08003, 2008.

[4] G. Aad et al. Expected Performance of the ATLAS Experiment. 2009. `http://arxiv.org/abs/0901.0512`.

[5] G. Aad et al. Measurement of the $W \to \ell\nu$ and $Z/\gamma^* \to \ell\ell$ Production Cross Sections in Proton-Proton Collisions at $\sqrt{s} = 7$ TeV with the ATLAS Detector. arXiv, (1010.2130), 2010.

[6] E. Abat. The ATLAS TRT Barrel Detector. JINST, 3:P02014, 2008.

[7] E. Abat. The ATLAS TRT End-Cap Detectors. JINST, 3:P10003, 2008.

[8] E. Abat et al. The ATLAS Transition Radiation Tracker (TRT) Proportional Drift Tube: Design and Performance. JINST, 3:P02013, 2008.

[9] A. Abdesselam et al. The Barrel Modules of the ATLAS Semiconductor Tracker. Nucl. Instrum. Meth., A568:642–671, 2006.

[10] A. Abdesselam et al. The ATLAS Semiconductor Tracker End-Cap Module. Nucl. Instrum. Meth., A575:353–389, 2007.

[11] D. Adams et al. The ATLAS Computing Model. 2005. CERN-LHCC-2004-037/G-085.

[12] M. R. Adams et al. Proton and Deuteron Structure Functions in Muon Scattering at 470 GeV. Phys. Rev., D54:3006–3056, 1996.

[13] S. Agostinelli et al. GEANT4: A Simulation Toolkit. Nucl. Instrum. Meth., A506:250–303, 2003.

[14] M. Aharrouche et al. Electron Performance in the ATLAS Experiment. ATL-COM-PHYS-2010-208.

[15] M. Aharrouche et al. Response Uniformity of the ATLAS Liquid Argon Electromagnetic Calorimeter. Nucl. Instrum. Meth., A582:429–455, 2007.

[16] M. Aharrouche et al. Double Differential Z, W Cross Sections and Their Ratios in the Electron Channels. 2010. ATLAS Note.

[17] M. Aleksa et al. Construction, Assembly and Tests of the ATLAS Electromagnetic End-Cap Calorimeters. JINST, 3:P06002, 2008.

[18] G. Altarelli and G. Parisi. Asymptotic Freedom in Parton Language. Nucl. Phys., B126(298), 1977.

[19] C. Anastasiou, L. J. Dixon, K. Melnikov, and F. Petriello. High Precision QCD at Hadron Colliders: Electroweak Gauge Boson Rapidity Distributions at NNLO. Phys. Rev., D69(094008), 2004.

[20] M. Arneodo et al. Measurement of the Proton and Deuteron Structure Functions, F_2^p and F_2^d, and of the Ratio $\sigma(L)/\sigma(T)$. Nucl. Phys., B483:3–43, 1997.

[21] A. Artamanov et al. The ATLAS Forward Calorimeter. JINST, 3:P02010, 2008.

[22] ATLAS Collaboration. `https://twiki.cern.ch/twiki/bin/view/Atlas/LevelOneCaloDiagrams`.

[23] ATLAS Collaboration. ATLAS Monte Carlo Tunes for MC09. ATL-PHYS-PUB-2010-002.

[24] ATLAS Collaboration. Image Pool. `http://www.atlas.ch/photos/index.html`.

[25] ATLAS Collaboration. ATLAS Liquid Argon Calorimeter: Technical Design Report. 1996. CERN-LHCC-96-41.

[26] ATLAS Collaboration. ATLAS Inner Detector: Technical Design Report. 2 Volumes. 1997. CERN-LHCC-97-16.

[27] ATLAS Collaboration. ATLAS Muon Spectrometer: Technical Design Report. 1997. CERN-LHCC-97-022.

[28] ATLAS Collaboration. ATLAS Level-1 Trigger: Technical Design Report. 1998. CERN-LHCC-98-014.

[29] ATLAS Collaboration. ATLAS High-Level Trigger, Data Acquisition and Controls: Technical Design Report. 2003. CERN-LHCC-2003-022.

[30] B. Aubert et al. Construction, Assembly and Tests of the ATLAS Electromagnetic Barrel Calorimeter. Nucl. Instrum. Meth., A558:388–418, 2006.

[31] A. C. Benvenuti et al. A High Statistics Measurement of the Proton Structure Functions $F_2(x, Q^2)$ and R from Deep Inelastic Muon Scattering at High Q^2. Phys. Lett., B223:485, 1989.

[32] J. D. Bjorken. Asymptotic Sum Rules at Infinite Momentum. Phys. Rev., 179(5):1547–1553, 1969.

[33] R. Blair et al. The ATLAS High Level Trigger Region of Interest Builder. JINST, 3:P04001, 2008.

[34] O. Buning, (Ed.) et al. LHC Design Report. 1. The LHC Main Ring. 2004. CERN-2004-003-V-1.

[35] N. Cabibbo. Unitary Symmetry and Leptonic Decays. Phys. Rev. Lett., 10(12):531–533, 1963.

[36] M. Cattaneo et al. A Precise Determination of the Number of Families with Light Neutrinos and of the z Boson Partial Widths. Physics Letters B, 235(3-4):399–411, 1990.

[37] J. H. Christenson, G. S. Hicks, L. M. Lederman, P. J. Limon, B. G. Pope, and E. Zavattini. Observation of Massive Muon Pairs in Hadron Collisions. Phys. Rev. Lett., 25(21):1523–1526, 1970.

[38] V. Cindro et al. The ATLAS Beam Conditions Monitor. JINST, 3:P02004, 2008.

[39] J. C. Collins and D. E. Soper. The Theorems of Pertubative QCD. Ann. Rev. Nucl. Part. Sci., 37:383–409, 1987.

[40] G. Corcella et al. HERWIG 6.5: An Event Generator for Hadron Emission Reactions with Interfering Gluons (Including Supersymmetric Processes). JHEP, 01, 2001.

[41] C. L. Cowan, F. Reines, F. B. Harrison, H. W. Kruse, and A. D. McGuire. Detection of the Free Detection of the Free Neutrino: a Confirmation. Science, 124(3212), 1956.

[42] R. Devenish and A. Cooper-Sarkar. Deep Inelastic Scattering. Oxford Univ. Press, 2004.

[43] M. Dobbs and J. B. Hansen. The HepMC C++ Monte Carlo Event Record for High Energy Physics. Comput. Phys. Commun., 134:41–46, 2001.

[44] Y. L. Dokshitzer. Calculation of the Structure Functions for Deep Inelastic Scattering and e+ e- Annihilation by Perturbation Theory in Quantum Chromodynamics. Sov. Phys. JETP, 46:641–653, 1977.

[45] S. D. Drell and T.-M. Yan. Massive Lepton-Pair Production in Hadron-Hadron Collisions at High Energies. Phys. Rev. Lett., 25(5):316–320, 1970.

[46] G. Duckeck, (ed.) et al. ATLAS Computing: Technical Design Report. 2005. CERN-LHCC-2005-022.

[47] F. Englert and R. Brout. Broken Symmetry and the Mass of Gauge Vector Mesons. Phys. Rev. Lett., 13(9):321–323, 1964.

[48] L. Evans and P. Bryant. LHC Machine. JINST, 3:S08001, 2008.

[49] R. P. Feynman. Very High-Energy Collisions of Hadrons. Phys. Rev. Lett., 23(24):1415–1417, 1969.

[50] M. J. Flowerdew. Standard Model $Z/\gamma^* \rightarrow e^+e^-$ Production in Early Data at ATLAS. PhD thesis, University of Liverpool, 2009.

[51] D. Froidevaux et al. 2010. `http://http://indico.cern.ch/getFile.py/access?contribId=7&resId=1&materialId=slides&confId=77091`.

[52] J. E. Gaiser et al. Charmonium Spectroscopy from Inclusive ψ' and J/ψ Radiative Decays. Physical Review D, 34(3), 1986.

[53] L. Garren et al. 34. Monte Carlo Particle Numbering Scheme. 2009. `http://pdg.lbl.gov/2009/reviews/rpp2009-rev-monte-carlo-numbering.pdf`.

[54] M. Gell-Mann. A Schematic Model of Baryons and Mesons. Physics Letters, 8(3), 1964.

[55] S. L. Glashow. Partial Symmetries of Weak Interactions. Nucl. Phys., 22:579–588, 1961.

[56] V. N. Gribov and L. N. Lipatov. Deep Inelastic e p Scattering in Perturbation Theory. Sov. J. Nucl. Phys., 15:438–450, 1972.

[57] D. J. Gross and F. Wilczek. Ultraviolet Behavior of Non-Abelian Gauge Theories. Phys. Rev. Lett., 30(26):1343–1346, 1973.

[58] G. S. Guralnik, C. R. Hagen, and T. W. B. Kibble. Global Conservation Laws and Massless Particles. Phys. Rev. Lett., 13(20):585–587, 1964.

[59] R. Hamberg, W. L. van Neerven, and T. Matsuura. A Complete Calculation of the Order α_s^2 Correction to the Drell-Yan K Factor. Nucl. Phys., B359(343), 1991.

[60] P. W. Higgs. Broken Symmetries and the Masses of Gauge Bosons. Phys. Rev. Lett., 13(16):508–509, 1964.

[61] Hyperlink. `http://upload.wikimedia.org/wikipedia/commons/thumb/9/9f/Drell-Yan.svg/2000px-Drell-Yan.svg.png`.

[62] M. Kobayashi and T. Maskawa. CP-Violation in the Renormalizable Theory of Weak Interaction. Progress of Theoretical Physics, 49(2), 1973.

[63] H. L. Lai et al. Global QCD Analysis of Parton Structure of the Nucleon: CTEQ5 Parton Distributions. Eur. Phys. J., C12:375–392, 2000.

[64] M. L. Mangano, M. Moretti, F. Piccinini, R. Pittau, and A. D. Polosa. ALPGEN, a Generator for Hard Multiparton Processes in Hadronic Collisions. JHEP, 0307, 2003.

[65] A. D. Martin, W. J. Stirling, R. S. Thorne, and G. Watt. Parton Distributions for the LHC. Eur. Phys. J., C63:189–285, 2009.

[66] P. M. Nadolsky, H.-L. Lai, Q.-H. Cao, J. Huston, J. Pumplin, D. Stump, W.-K. Tung, and C.-P. Yuan. Implications of CTEQ Global Analysis for Collider Observables. Phys. Rev. D, 78(1), 2008.

[67] K. Nakamura et al. Review of Particle Physics. J. Phys. G, G(37), 2010.

[68] H. D. Politzer. Reliable Perturbative Results for Strong Interactions? Phys. Rev. Lett., 30(26):1346–1349, 1973.

[69] A. Rimoldi et al. The Simulation of the ATLAS Experiment: Present Status and Outlook. 2004. ATL-SOFT-2004-004.

[70] A. Salam. Weak and Electromagnetic Interactions. 1968. Originally printed in *Svartholm: Elementary Particle Lerum, Sweden*, Stockholm 1968, 367-377.

[71] M. Schott. Study of the Z Boson Production at the ATLAS Experiment with First Data. PhD thesis, LMU München, 2007.

[72] T. Sjostrand, S. Mrenna, and P. Z. Skands. PYTHIA 6.4 Physics and Manual. JHEP, 06(026), 2006.

[73] S. van der Meer. ISR-PO 68-31,KEK68-64.

[74] W. L. van Neerven and E. B. Zijlstra. The O(α_s^2) Corrected Drell-Yan K Factor in the DIS and MS Scheme. Nucl. Phys., B382, 1992.

[75] S. Weinberg. A Model of Leptons. Phys. Rev. Lett., 19:1264–1266, 1967.

[76] L. W. Whitlow, E. M. Riordan, S. Dasu, S. Rock, and A. Bodek. Precise Measurements of the Proton and Deuteron Structure Functions from a Global Analysis of the SLAC Deep Inelastic Electron Scattering Cross-Sections. Phys. Lett., B282:475–482, 1992.

[77] G. Zweig. An SU_3 Model for Strong Interaction Symmetry and its Breaking; 2 parts. (CERN-TH-401, CERN-TH-412), 1964.